PB-213 417

HEAT-ENGINE/MECHANICAL-ENERGY-STORAGE HYBRID PROPULSION SYSTEMS FOR VEHICLES

G. L. Dugger, et al

Johns Hopkins University

Prepared for:

Environmental Protection Agency

March 1972

DISTRIBUTED BY:

NTIS

National Technical Information Service
U. S. DEPARTMENT OF COMMERCE
5285 Port Royal Road, Springfield Va. 22151

PB 213 417

CP 011
MARCH 1972
Copy No. 96

APTD-1344

Air Pollution Control

HEAT-ENGINE/MECHANICAL-ENERGY-STORAGE HYBRID PROPULSION SYSTEMS FOR VEHICLES

FINAL REPORT

G. L. DUGGER, A. BRANDT, J. F. GEORGE, L. L. PERINI,
D. W. RABENHORST, T. R. SMALL, and R. O. WEISS

Contract No. N000-17-62-C-0604

Reproduced by
NATIONAL TECHNICAL
INFORMATION SERVICE
U S Department of Commerce
Springfield VA 22151

THE JOHNS HOPKINS UNIVERSITY • APPLIED PHYSICS LABORATORY

R 312

CP 011
MARCH 1972

Air Pollution Control

HEAT-ENGINE/MECHANICAL-ENERGY-STORAGE HYBRID PROPULSION SYSTEMS FOR VEHICLES

FINAL REPORT

G. L. DUGGER, A. BRANDT, J. F. GEORGE, L. L. PERINI,
D. W. RABENHORST, T. R. SMALL, and R. O. WEISS

Contract No. N000-17-62-C-0604

PREPARED FOR THE ENVIRONMENTAL PROTECTION AGENCY,
OFFICE OF AIR PROGRAMS

THE JOHNS HOPKINS UNIVERSITY • APPLIED PHYSICS LABORATORY
8621 Georgia Avenue - Silver Spring, Maryland - 20910

This report is printed on recycled paper.

BIBLIOGRAPHIC DATA SHEET

1. Report No. APTD-1344

2.

3. Recipient's Accession No. PB 213 417

4. Title and Subtitle
Heat-Engine/Mechanical-Energy-Storage Hybrid Propulsion Systems for Vehicles

5. Report Date March 1972

6.

7. Author(s)
G.L. Dugger, A. Brandt, J.F. George, L.L. Perini, et al

8. Performing Organization Rept. No. CP 011

9. Performing Organization Name and Address
The Johns Hopkins University
Applied Physics Laboratory
8621 Georgia Avenue
Silver Spring, Maryland 20910

10. Project/Task/Work Unit No.

11. Contract/Grant No.
N000-17-62-C-0604

12. Sponsoring Organization Name and Address
ENVIRONMENTAL PROTECTION AGENCY
Office of Air Programs
Research Triangle Park, North Carolina 27711

13. Type of Report & Period Covered

14.

15. Supplementary Notes **Details of illustrations in this document may be better studied on microfiche.**

16. Abstracts
An analytical study indicated that a flywheel-only propulsion system could satisfy specified performance requirements for a city bus, and that flywheel/heat engine hybrids could meet the specified requirements for cars, vans, and buses. In all cases substantial emission-free ranges could be achieved with hybrid systems by using the engine only periodically (at constant load) to recharge a large, high-energy flywheel. Experiments verified the principle of the "superflywheel" by spin tests of unindirectional materials in rod or bar rotor configurations. The better results demonstrated energy densities greater than 30 W-h/lb (max. = 48) for boron filaments and slender rods of graphite and glass composites. High-speed photographs of rotor failure showed complete pulverization of 1 pound rods in 0.6 ms as they impacted steel containment rings; only 1 to 2% of the initial stored energy was imparted to the rings. Thus, composite flywheels will be much easier to contain than metal flywheels and are promising candidates for energy storage devices.

17. Key Words and Document Analysis. 17a. Descriptors

Air pollution	Heat engines
Engines	Air pollution control equipment
Flywheels	
Hybrid propulsion	
Motor vehicles	
Buses (vehicles)	
Performance standards	
Energy storage	
Composite materials	
Design	

17b. Identifiers/Open-Ended Terms
Hybrid power train
Air pollution control

17c. COSATI Field/Group 13B, 21C

18. Availability Statement
Unlimited

19. Security Class (This Report) UNCLASSIFIED

20. Security Class (This Page UNCLASSIFIED

21. No. of Pages 312

22. Price $6.00/$0.95

- i -

FORM NTIS-35 (REV. 3-72)

THIS FORM MAY BE REPRODUCED

USCOMM-DC 14952-P72

CONTENTS

List of Illustrations . . . ix

1. Summary 1
    1.1 Experimental Study 1
    1.2 Analytical Study 4

2. Introduction 9

3. Experimental Program 15
    3.1 Introduction 15
    3.2 Tests of Small-Diameter Rods at APL . . 15
        3.2.1 Equipment and Instrumentation . . 17
        3.2.2 Selection of Candidate Test Materials . 21
        3.2.3 Test Results and Discussion . . 22
        3.2.4 Conclusions from Small-Scale Tests . 30
    3.3 Tests of 1-Pound Bars at the Naval Air Propulsion Test Center 30
        3.3.1 Facility Modifications . . . 31
        3.3.2 Selection and Procurement of Test Materials 34
        3.3.3 Test Results and Discussion . . 38
        3.3.4 Mode of Failure 48
        3.3.5 Energy Absorbed by the Containment Ring 53
    3.4 Conclusions 60

4. Flywheel System Design Considerations and Performance 63
    4.1 Introduction 63
    4.2 Rotor Configuration and Material Considerations 64
        4.2.1 Simple Comparative Illustrations of the Superflywheel Concept . . 64

Preceding page blank

CONTENTS (cont'd)

    4.2.2 Transverse Stresses in Bar Rotors Made of Unidirectional Composite Material 66
    4.2.3 The Circular Brush Rotor . . 69
    4.2.4 Radially-Fanned Brush Rotor . . 72
    4.2.5 A Laminated Composite Disk . . 77
    4.2.6 Summary of Energy Characteristics . 79

  4.3 The Effects of Flywheel Rotor Speed . . 82

    4.3.1 Bearings 82
    4.3.2 Vacuum System 85
    4.3.3 Power Losses and Run-Down Times . 86

  4.4 Factors Affecting the Allowable Stresses in Composite Material Flywheels . . . 89

    4.4.1 Flywheel System Life Cycle and Environment 89
    4.4.2 Dynamic Fatigue of Composite Materials 92
    4.4.3 Creep and Stress-Rupture of Composite Materials . . . 95
    4.4.4 Longitudinal Divergence . . . 100
    4.4.5 Future Improvements in Materials, Fabrication, and Design Techniques 102

  4.5 Vehicular Installation 107

    4.5.1 Heat Energy/Flywheel Hybrid Propulsion in a Commuter Car . . 107
    4.5.2 Flywheel Gyroscopic Torque . . 110

  4.6 Closure 113

5. Preliminary Vehicle Evaluation Studies . . . 115

  5.1 Introduction 119
  5.2 Powerplants for the Hybrid-Flywheel Vehicles 119

CONTENTS (cont'd)

- 5.2.1 Otto (SIE) Cycle 120
- 5.2.2 Diesel Engine (CIE) . . . 123
- 5.2.3 Gas Turbine (GT) Cycle . . . 126
- 5.2.4 Rankine Cycle 129
- 5.2.5 Emissions 131
- 5.2.6 Engine Performance . . . 134
- 5.2.7 Closure 139

5.3 Vehicle Requirements and Weight and Volume Considerations 140

- 5.3.1 Vehicles Specifications and Resulting Flywheel Subsystem Weights . . 141
- 5.3.2 Rotor Weight and Flywheel Subsystem Volume 148

5.4 Drivetrain Considerations . . . 152

- 5.4.1 General Considerations . . . 152
- 5.4.2 Engine-to-Flywheel (Charge) Transmission 154
- 5.4.3 Flywheel-to-Wheels Drive Transmission 155
- 5.4.4 Other Drivetrain Components and Drivetrain Layout . . . 160
- 5.4.5 Regeneration Efficiency and Operations on the DHEW Cycle . . . 163
- 5.4.6 Conclusions on Transmissions and Regeneration Efficiency . . 172

5.5 Performance and Emission Estimates . . 172

- 5.5.1 Inputs 172
- 5.5.2 Method of Analysis 176
- 5.5.3 Results 178
- 5.5.4 Sensitivities of Performance and Emission Estimates to Assumptions . 188

5.6 Closure 190

CONTENTS (cont'd)

6. Conclusions and Recommendations . . . 193

- 6.1 General 193
- 6.2 Rotor Configuration and Materials . . . 194
- 6.3 Containment of Rotors 196
- 6.4 Flywheel Systems 197
- 6.5 Evaluation Studies 201

Appendices

- A. Flywheel Shape and Biaxial Stress Considerations 203
- B. The Disk Flywheel Configuration . . . 235
- C. Estimates of Windage Losses for Flywheels . 243
- D. Survey of Available Transmissions and Proposed Concepts 253
- E. Tire and Wind Resistance of Automobiles . . 277

References 285

Acknowledgment 305

ILLUSTRATIONS

3-1 Energy Storage Capability of the Straight Filament 16

3-2 Spin Chamber for Small-Scale Tests Being Installed in Test Cell at APL . . . 18

3-3 Test Setup for Rotating Small Filaments or Composite Rods Using High-Speed Motor Inside Chamber 19

3-4 Alternative Setup with Speed Increaser Inside Chamber and 1-HP Motor Outside . . . 19

3-5 Schematic Diagrams of Spin Chamber Setup at APL 20

3-6 Remains of Graphite/Epoxy Composite in Spin Chamber after Test 28

3-7 Simulation of Circular Brush Configuration and Test Results 28

3-8 General Arrangement for 1-Pound Rod Tests at NAPTC, Philadelphia 32

3-9 General View of APL's Inner Chamber Suspended from an Assembly Platform . . 35

3-10 Inside View of Spin Chamber 36

3-11 Typical Specimens for NAPTC Tests . . 36

3-12 S-Glass/Epoxy Fragments from Test JH-1 . . 40

3-13 Graphite/Epoxy Fragments from Test JH-3 . . 40

3-14 Containment Rings after Tests, Compared to Reference Circles 43

3-15 Static Tensile Test Specimens before and after Test 46

ILLUSTRATIONS (cont'd)

3-16 Kinematics of Rod Failure (Assuming Two Equal Segments) 49

3-17 Photographs Taken before Run JH-4 and at 7 Times after Failure Tripped Photographic System 49

3-18 Photographs Taken before Test JH-2 and at Seven Intervals following Failure of S-Glass/Epoxy Bar 51

3-19 Deformation of 3/8-Inch-Thick Steel Ring; Rod Energy of 820 000 In-Lb . . . 54

3-20 One of the Impact Arcs on the Containment Ring 54

3-21 Radius of Curvature and Change in Curvature for 3/8-Inch-Thick Ring (JH-4 Test) . . 56

3-22 Assumed Initial Velocity Profile of Ring for Use in Momentum Transfer Analysis . . 58

4-1 Specific Energy Coefficients, Relative Specific Strengths, and Relative Specific Energies for Various Flywheel Shapes . . 65

4-2 Specific Energy Degradation Caused by Biaxial Stress Field in Wider Bars . . . 68

4-3 Circular Brush Configuration . . . 70

4-4 Radially Fanned Brush Rotor . . . 73

4-5 Effects of Rotor Geometry and Material Properties on Specific Energy in a Radially-Fanned Brush Rotor 76

4-6 Specific Energy and Energy Packaging Density versus T/R for Radially-Fanned Brush Rotors of S-Glass/Epoxy Elements . . 76

ILLUSTRATIONS (cont'd)

4-7 Summary of Ultimate Composite Material Flywheel Characteristics for Different Rotor Configurations 80

4-8 Effect of Rotor Configuration on Tip Speed . . 83

4-9 Typical Flywheel Cycle Requirements for a Commuter Car 91

4-10 Constant Amplitude Fatigue Tests of Boron-Epoxy Composite at Room Temperature (from Ref. 34) 93

4-11 Fatigue Tests of S-Glass and E-Glass/Epoxy Laminates at Room Temperature (from Ref. 33) 93

4-12 Probability Lines for Stress-Rupture of S-Glass/Epoxy Strands (from Ref. 39) . . 97

4-13 Time of Failure for S-Glass/Epoxy Cylinders under Pressure at Ambient and Liquid Nitrogen Conditions (from Ref. 40) . . 97

4-14 Static Fatigue Data for Silica Fibers: in Vacuum at -196°C, in Vacuum at Room Temperature, and in Air at Room Temperature (Refs. 41, 42) 99

4-15 Longitudinal Divergence of Rod-Type Rotors . 101

4-16 Characteristics of Failure Mechanisms for Metals and Composite Materials (from Ref. 36) 108

4-17 Heat Engine/Flywheel Hybrid Commuter Car . 109

4-18 Example of Family Car Encountering a Severe Roadway Obstacle at 45 MPH with 5 kW-h Hard-Mounted Flywheel 112

5-1 Ideal Cycles (T-S Diagrams), Ideal Thermal Efficiencies (η_t) and Simple Configurations of Heat Engines 121

ILLUSTRATIONS (cont'd)

5-2 Spark-Ignition Engine Characteristics . . 124

5-3 Projections of HC, CO, and NO_x (as NO_2) Emissions 133

5-4 Specific Weight versus Brake Horsepower for the Four Heat Engines 136

5-5 Comparison of Specific Weights of the Four Engines 138

5-6 Brake Specific Fuel Consumption versus Engine Size 138

5-7 Effect of Rotor Length on Rotor Weight and Total Volume, $T_c = 0.25$ Inch, $T/R = 0.125$. 149

5-8 Transmission Output Characteristics . . 156

5-9 Acceleration Parameters versus Time, Family Car 158

5-10 Flywheel Hybrid Power Control System . . 162

5-11 Commuter Car Hybrid Operating on DHEW Driving Cycle. Full Flywheel Charge at Start of Cycle; Engine Is Off during this Portion 168

5-12 Energy Disposition of Commuter Car on DHEW Cycle without Air Conditioner; 0.247 HP-H/Mile. (A 4-HP Air Conditioner Operating Continuously Represents 32% of Above Energy.) 171

5-13 Steady-State Wheel Horsepower Requirements for the Four Vehicles 174

5-14 Driving Cycles 174

5-15 Flywheel Rotor Mass Fractions Assumed . . 174

5-16 Flywheel-Only Level Road Cruise Performance . 187

5-17 Effect of Design Speed and Air Conditioner Load for Otto Hybrid Commuter Car . . 189

ILLUSTRATIONS (cont'd)

5-18 Effect of Flywheel Rotor Weight for Otto Hybrid Commuter Car 191

5-19 Effect of Drivetrain Efficiencies and External Resistance for Otto Hybrid Commuter Car . 191

6-1 Details of Recommended Working Prototype Structure 198

A-1 Constant Stress Flywheel Performance . . 209

A-2 Thickness Distributions for Constant Stress Rod Flywheels. $(t_o/t_{\alpha=2}$ = Thickness of Uniform Rod with Same Weight as $\alpha = 2$ Constant Stress Case.) 209

A-3 Effect of End Mass on Constant Stress Flywheel Performance 211

A-4 Stress Distributions in Various Rod Flywheel Configurations 211

A-5 Formulation of Rotating Bar Problem. Note that the Thin Plate or Bar Is in Plane Stress 214

A-6 Comparison of Rayleigh-Ritz Solution with Finite-Difference Solution. The Solution Is Shown as a Dashed Line (Symmetrical about x and y Axes)(Ref. 125) 218

A-7 Stress Distribution for a Graphite/Epoxy (Hercules 2002T) Bar 225

A-8 Geometric and Performance Parameters of a Constant Stress Disk Flywheel 229

A-9 Performance Parameters for Hyperbolic Disks $(r \propto 1/z)$ with a Central Hole. Inner-to-Outer Radius Ratio Equals Inner-to-Rim Thickness Ratio 229

B-1 Lamina Axes Rotation and Pseudo-Isotropic Laminated Disk 237

ILLUSTRATIONS (cont'd)

D-1 Perbury, Hayes, or Toric Type CVT's . . 255
D-2 Beier CVT's 257
D-3 Hydrostatic Transmission 262
D-4 Efficiencies for Catalogued Hydrostatic Transmissions at 2800-RPM Input Speed . . 266
D-5 Fluid Coupling Diagram and Characteristics . 268
D-6 Single-Stage Torque Converter Diagram and Characteristics 268
D-7 Schematic Diagram and Wide-Open Throttle (Acceleration) Efficiency of Sunstrand Dual-Mode, Infinitely Variable Ratio Transmission 272
D-8 Rear Axle Efficiency at Wide-Open Throttle and Road Load 276
D-9 Overall Efficiency Comparisons of Roller Traction versus Geared Planetary Drive Units 276
E-1 Vehicle Drag Coefficients for a Frontal Area of 25 ft^2 and Drag Forces at 60 MPH . . 281
E-2 Experimental Rolling Resistance Coefficients . 281
E-3 Steady Horsepower Requirements for Various Drag and Friction Estimates . . . 284

1. SUMMARY

This experimental and analytical study of high-specific energy flywheel systems for use in automotive propulsion systems had two main objectives:

1. Proof-of-principle demonstration of the use of filamentary or composite materials of high uniaxial tensile strength in rotor configurations that would have significantly higher specific energies than prior flywheels. The goal was to demonstrate a specific energy storage capability of 30 W-h/lb of rotor material.

2. Theoretical evaluation of the performance of such flywheels, alone and in combination with heat engines, in four classes of vehicles: family car, commuter car, van, and intracity bus. The interest of the Office of Air Programs (OAP) of the Environmental Protection Agency was in the potential value of such propulsion systems for reducing air pollution from such vehicles.

1.1 EXPERIMENTAL STUDY

The results of the experimental study may be summarized as follows:

1. Several filamentary or composite materials available today can exceed 30 W-h/lb at burst. The most interesting spin test results for 30-inch-long specimens spun around their mid-points are summarized in Table 1-1. Boron filaments are outstanding (48 W-h/lb demonstrated without failure) but probably will remain too costly ($100/lb) (Ref. 1) for automotive use. Glass and glass-resin composites are most attractive from a cost (< $1/lb) (Ref. 2) and availability viewpoint. A slender (0.1-inch-diameter) R-glass/polyester rod failed at 31 W-h/lb. The theoretical ultimate value for current S-glass/epoxy

Table 1-1

Results of Small Rod (or Bar) Tests of Superflywheel Concept[1]

Rod or Bar Description			Values Attained at Burst[2]		
Cross-Section, Material (source)	Density (lb/in^3)	Weight (pounds)	Rotational Speed (rpm)	Calculated Stress (psi)	Specific Energy (W-h/lb)
4-mil-diameter boron filament (AVCO Corp.)	0.094	0.00004	38 000[2]	424 000	48[2]
20-mil-diameter boron/magnesium (General Technology Corp.)	0.080	0.00075	31 500	254 000	33
1/16-inch-square graphite/epoxy (Fothergill & Harvey, Ltd.)	0.056	0.00656	33 000	194 000	36
1/8-inch-square graphite/epoxy (Hercules, Inc.)	0.057	0.0267	31 300	180 000	33
0.098-inch-diameter R-glass/polyester (PPG Industries)	0.065	0.0147	30 700	195 000	31
0.79-inch-square graphite/epoxy (Hercules, Inc.)	0.054	1.00	28 200	137 000	26
0.57-inch-square S-glass/epoxy (Hercules, Inc.)	0.075	0.73	29 000	204 000	28

[1] Each rod or bar was 30 inches long and was rotated about its mass center in an evacuated chamber at pressures between 0.001 and 0.250 torr. (1 torr = 1 mm Hg abs.)

[2] The boron filament did not fail – value limited by spin test rpm limit; all other specimens failed at indicated rpm.

material is 38 W-h/lb, and 0.57-inch-square, 0.73-pound, first-generation bars were spun to 28 W-h/lb at failure. Because some questions remain about stress-rupture and fatigue properties of glass for this application, another family of materials of great promise and excellent fatigue properties, graphite and graphite/resin composites, is a leading contender. Very slender graphite/epoxy bars (1/16-inch-square) achieved 36 W-h/lb, and 0.79-inch-square, 1-pound, first-generation bars achieved 26 W-h/lb. Costs of graphite composites are high at present ($200/lb) but are expected to come down to the $20/lb to $40/lb range in the next few years as applications in new aircraft lead to more efficient production and quality control, which will also raise performance (Ref. 1).

2. An encouraging finding from these tests with respect to the use of filamentary or composite materials for man-rated flywheel applications is the type of failure mode observed. In all tests conducted, these materials were ground to dust or small straw-like fragments upon contact with the containing structure. Post-test analysis of a containment ring used in the test of a 1-pound graphite/epoxy rod showed that only 1 to 2% of the kinetic energy of the rod was imparted to the ring.

3. As noted above and in Table 1-1, the burst strengths of the larger (in cross-section) graphite/epoxy and S-glass epoxy bars were lower than those of the very slender bars or rods. This poorer performance is attributed primarily to the inexperience of the supplier in fabricating specimens of these greater thicknesses, but basic factors related to size and flaw distribution probabilities in composite materials may limit the optimal size of individual elements used in a high-energy-density flywheel rotor. Thus, brush-like rotors (see next paragraph) comprising many slender elements may prove best from both performance and containment (see previous paragraph) viewpoints. It should be noted that the energy densities quoted in Table 1 are burst values (except for boron filaments) based on the weights of the bars or rods. In a

flywheel system, the rated value for the material used will have to be lower than its burst value by some factor of safety (including a factor for fatigue effects), and weight of accessories (hub, bearings, seals, containment, and mounting) will have to be included if one wishes to state an overall flywheel subsystem energy density.

1.2 ANALYTICAL STUDY

Theoretical studies were conducted on various potential flywheel configurations. Of particular interest are the calculated ultimate-stress performance capabilities for four classes of "superflywheels": (a) composite bars, (b) circular brushes comprising thousands of filamentary spokes potted into a hub, (c) radially fanned brushes comprising continuous filaments passed through a potting hub, and (d) composite, pseudo-isotropic disks made from many plies of uniaxial cloth cured together at specified ply angles. Composite bars, such as tested experimentally, are simplest but are inefficient with respect to packaging volume for a given stored energy. Composite disks would be far superior to bars with respect to packaging volume and would have approximately the same specific energy (E/W, W-h/lb) for a given material. Such disks were assumed for the purposes of the vehicle applications studies discussed below. The brush configurations are intermediate to bars and disks with respect to packaging volume and should require the least containment weight, because very slender elements would fail sequentially. The radially fanned brush is judged by the authors to be particularly worthy of development, because its use of slender continuous filaments or composite rods permits slightly higher specific energy than a composite disk, as well as a ready upgrading of specific energy as better materials become available.

The various materials problems (e. g. , static and cyclic fatigue) and fabrication and installation problems (e. g. , bearings, seals, and gyroscopic torques) for flywheel systems are discussed in some detail, and an example of major installation features of a flywheel/heat-engine hybrid propulsion system in a commuter car is given.

The studies of performance of flywheel-only and flywheel-hybrid propulsion systems in the four vehicle classes were undertaken before the experimental work was completed. At the outset of the program the anticipated vehicular operational date was 1980. For these studies a rated specific energy of 32 W-h/lb (at maximum rated rpm) was assumed for the rotor, and the assumed sizes and weights of the accessories and case (including containment) were related to rotor size. Although the previously summarized experimental results demonstrated with materials received early in 1971, when degraded for safety and fatigue effects, would lead to rated rotor specific energies considerably lower than 32 W-h/lb, the authors believe this value could be achieved by a prototype flywheel subsystem using a brush or disk type rotor after two or three years of active exploratory development. If the rated specific energy achieved at any particular point in time is different from 32 W-h/lb, the effect will be simply to change all factors directly related to specific energy (e. g., flywheel-only range) in proportion. With this qualification in mind, and on the basis of the other assumptions made (detailed in the report), the results of the vehicle application studies may be summarized as follows:

1. Of the vehicles studied, and within the specifications established for them by OAP, the city bus is the only one for which a flywheel-only system would appear to be able to meet all requirements. A van with approximately half of the specified 60-mile range might be possible.

2. It appears that all performance requirements for all specified vehicles could be met with flywheel/heat-engine hybrid vehicles. Regenerative braking would recover 15 to 20% of the total energy requirement on urban

driving cycles. Compared to present vehicles with automatic transmissions, however, approximately half of this gain probably would be lost to the continuously variable transmission and the clutches and speed changer postulated for the hybrids.

3. The most important aspect – the ability to reduce objectionable emissions – could not be assessed fully because of a lack of a sufficient body of self-consistent data on the optimization of heat engines to reduce emissions near design points or over limited ranges of load and speed. It is expected that substantial reductions should be achievable by proper design and operation of heat engines in these hybrid systems, where the flywheels would provide acceleration power.

4. An important advantage seen for the use of relatively large, high-specific-energy flywheels in hybrid systems is the ability to provide significant ranges with no emissions for travel through congested or specially restricted areas such as may become necessary in the future to meet air quality standards (Ref. 3). For this reason an on-off mode of engine operation, whereby the engine is used only about 20% of the time during urban driving, to recharge the flywheel, is recommended. With this mode of operation, there will be no emission penalty for idling or rapid acceleration, and no drivability penalty, if, for example, the engine is operated quite lean to reduce emissions. On the other hand, there will be an emission penalty for the periodic engine restarts; an assumption was made for this effect, but it could not be assessed quantitatively.

5. With respect to transmission systems for use in flywheel propulsion units, literature and technology reviews were conducted, and it appears that the technology is available for direct engineering design and development of a transmission for each of the vehicles studied. While there are no off-the-shelf units that specifically satisfy the requirements, a leading contender

for larger units appears to be the power-splitting, hydromechanical system (see, e.g., Ref. 4). Variable belt drives, such as used by DAF on small cars (Ref. 5), may be satisfactory for low power systems. A 72% overall transmission efficiency (engine-to-flywheel-to-drive wheels) is assumed in the foregoing studies.

6. Among the heat engines considered – spark ignition, diesel, gas turbine, and Rankine cycle – the gas turbine appears most attractive because of its low specific weight and its low inherent hydrocarbon and CO emissions. The diesel appeared unattractive for the cars and van because of its weight and size (leaving negligible allowances for flywheels within given constraints) and odor problems (Ref. 6). The diesel would remain attractive for the bus. Steam engines also appeared to rank behind spark-ignition and gas turbine engines on the basis of the limited available data, although their potentials for low emissions cannot be denied. The spark-ignition engine is a good short-term candidate by virtue of its present use and the immense current efforts to reduce its emissions.

2. INTRODUCTION

The objectives of this program were to conduct proof-of-principle tests of the "superflywheel" concept (Refs. 7 and 8) and to evaluate the use of such flywheels in automotive vehicles, both alone and in combination with heat engines, to reduce emissions of pollutants. A superflywheel may be defined as a rotor of novel design that uses a material of high uniaxial specific strength (i. e., ratio of tensile strength to density), such as glass or graphite fibers or a composite of such a material in a resin matrix, in such a way as to take maximum advantage of that uniaxial strength, and which is operated in a chamber evacuated to 10^{-5} to 10^{-6} atmosphere pressure to reduce material degradation caused by moisture or oxygen, as well as windage loss and heating effects at high rotational speeds. Such a rotor may take one of several possible configurations, ranging from simple bar shapes to various brush-like configurations.

The experimental program consisted primarily of spinning small-diameter, 30-inch-long specimens at the Applied Physics Laboratory and approximately 1-pound, 30-inch-long bars of graphite/epoxy and S-glass/epoxy at the Naval Air Propulsion Test Center, Philadelphia. The better results achieved during this program have been summarized in Table 1-1 in the Summary; details of the test equipment, testing techniques, and results are presented in Section 3. Considerations regarding design and installation of flywheel systems are discussed in Section 4. The latter section, supplemented by Appendixes A-C, also presents results of theoretical studies of advanced rotor concepts.

The evaluation studies of the applications of advanced flywheels to automotive vehicles are covered in Section 5. The objectives of this part of the program

Preceding page blank

were to explore the ways in which flywheels could be used in propulsion systems that would have low HC (hydrocarbon), CO (carbon monoxide), and NO_x (oxides of nitrogen) emissions while meeting performance criteria specified by the Office of Air Programs (OAP) of the Environmental Protection Agency (EPA) for each of four vehicle classes: commuter car, family car, city bus, and van. For each vehicle class, four heat engine types (spark-ignition, diesel, gas turbine, and Rankine cycle) were to be considered for the hybrid systems. The vehicles were to be studied on their typical urban cycles, and estimated emission levels were to be compared to the OAP 1980 research goal values that existed at the outset of this program. This program was therefore intended to probe the potential value of advanced flywheels for applications in 1980. However, Federal legislation has since established emissions standards for 1976 (Ref. 9) that are essentially the same as those earlier research goals.

Prior operational application of flywheel propulsion to land vehicles has been limited to mine engines and to the Oerlikon Gyrobuses (Refs. 8 and 10) that were used in Switzerland and Africa in the 1950's. Experimental development of the Gyreacta system for cars and buses was done in England in the 1950's (Ref. 10). All of these applications had used steel flywheels of conservative design. Some research had been done on circumferentially wound flywheels of composite materials for naval applications (Ref. 11). At the time this program was begun, OAP also was sponsoring a study of the same vehicular applications by Lockheed (Ref. 12), which was to include demonstration of state-of-art technology by testing shaped steel wheels and another type of flywheel rotor. Thus, the present program was to study the longer term prospects for advanced flywheels using the aforementioned superflywheel concept.

Two advantages of using flywheels made of filamentary or composite materials in novel rotor configurations, as contrasted to shaped metal flywheels, are seen:

1. The potential for significant improvement in specific energy (stored-energy/weight ratio), which would permit greater energy storage within a specified weight allowance for a propulsion system, and

2. The lower safety hazard or lower containment weight requirement for a given energy storage level that should follow because of the type of failure mode exhibited by such materials (as discussed in Sections 3 and 4).

While Item 2 may prove to be of interest regardless of the propulsion system approach taken, Item 1 is of particular interest in considering both flywheel-only systems and the propulsion system approach to be taken for flywheel/heat-engine hybrids. There may someday be a need to restrict operation of heat engines to certain portions of cities or congested areas that have particular difficulty in meeting air quality standards (see, e.g., Ref. 3). Therefore, a potential for dual-mode operation of a flywheel/heat-engine hybrid, whereby in urban use[1] the engine would be used only periodically to recharge the flywheel, permitting substantial operating range on the flywheel alone, is of interest. It follows that the largest practical energy storage is of interest, and this, in turn, calls for high specific energy in the flywheel. Therefore, the authors concluded that the present study should emphasize the potential future performance with such systems, thereby complementing the Lockheed study (Ref. 12), which was covering the nearer term approach to the hybrids with smaller flywheels used essentially in parallel with the heat engine.

Important questions in optimizing a system using the on-off mode of engine operation relate to the trade-off between emission-free (engine-off) range available and the total emissions produced per complete on-off cycle. These questions include the reliability of engine starting and what constitutes a "cold start," i.e., how much penalty is paid in emissions on each restart. The answers undoubtedly will vary from one engine type to another and may be affected by the particular emission controls used on the engines. Data are needed on both these points and the even more important question of just how much is to be gained by operating the engine only at nearly constant-load, constant-speed conditions so that it can be truly optimized for those conditions. Until self-consistent and pertinent sets of data become available in these areas, these crucial points cannot be answered.

---

[1] For automobiles, the engine still would be used continuously for long-range highway cruise through unrestricted areas.

Another important feature of propulsion systems using flywheels is the continuously variable transmission needed between the flywheel and the drive axle. Considerable progress is being made by industry in such transmissions (see Section 5, Appendix D, and, e.g., Refs. 4, 5, and 13 through 17) and OAP has contracted studies (following Ref. 18) addressed specifically to flywheel-hybrid vehicles. Finally, the questions of flywheel containment design and gyroscopic forces must be addressed from a safety viewpoint, and a little is said about each in Section 4.

Some features differentiating flywheels from electric energy storage systems should be kept in mind. The nominal "depth of discharge" (DOD, or removal of energy per discharge cycle) for the flywheel used in the present studies is 75%. Since the stored energy is proportional to the square of rotational speed, a 75% DOD requires only a 2:1 speed range for the flywheel (and a corresponding 2:1 speed range for the normal, constant-load operation of the heat engine used to charge it). This nominal DOD could be increased to 89%, if increasing the heat engine's operating speed range to 3:1 would not appreciably affect its emissions of air pollutants. Neither a high DOD nor a high rate of energy withdrawal for vehicle acceleration will affect the flywheel's life. A flywheel system could easily provide as great a specific power (W/lb or hp/lb) as a vehicle could profitably use. In contrast, the life, or number of useful cycles, of an electric energy storage system depends strongly on either DOD or rate of withdrawal, or both, depending on battery type (see, e.g., Ref. 19) and a drawback in designing electric propulsion systems is in determining the compromise in acceleration capability that will be accepted in order to improve range and obtain an acceptable life from the batteries. It is likely that, for propulsion systems of comparable weight providing comparable acceleration and emission-free range, a battery system would have to be replaced several times during the life of a vehicle (Ref. 20), whereas a flywheel system probably could be designed for the full vehicle life (Refs. 2 and 20). However, flywheel life will depend mainly on the life of seals and bearings, which will be subjected to stresses and strains caused by gyroscopic forces when the vehicle pitches up or down (see Section 4.5.2), and flywheel systems must be developed and tested to confirm the potential life advantage compared to battery systems.

Detailed trade-off studies and cost comparisons of mechanical and electric energy storage systems were beyond the scope of this program, and, indeed, much of the data needed for such a task are yet to be developed. Section 6 includes recommendations for some of the work needed to provide such information for flywheel energy storage systems and their applications for automotive propulsion.

3. EXPERIMENTAL PROGRAM

3.1 INTRODUCTION

The primary goal of the experimental program was to prove the principle of the "superflywheel concept" (Ref. 8) by demonstrating that unidirectional composite or filamentary materials can be spun about their centers of mass, as shown in Fig. 3-1, to develop high levels of specific energy storage. This basic development effort was to progress from tests of single filaments and slender rods of 30-inch-length to rods or bars weighing approximately 1 pound each. A goal of 30 W-h/lb of rotor material (or 30 000 rpm for a 30-inch length) was established for a 1-pound rod. This goal represented an order-of-magnitude improvement over the past flywheel propulsion units such as mentioned in Section 2. In addition, rod elongation, creep, and fatigue were to be studied so as to estimate the allowable, or rated, energy level for a vehicular system, and the mode of failure was to be studied to permit estimates of containment structure requirements for an operational system.

Thus, the experimental program was organized to (a) construct equipment and instrumentation to spin test specimens, (b) test small-diameter specimens of a variaty of candidate materials, (c) select materials and spin test larger specimens (on the order of 1 pound), and (d) study rod deformation and mode of failure so as to define the problem of rotor containment in the event of structural failure or vehicular accident.

3.2 TESTS OF SMALL-DIAMETER RODS AT APL

This section describes the experimental program conducted at APL, including the spin equipment and its instrumentation, the selection and testing of small-scale rods, and static tensile tests of rod specimens.

Preceding page blank

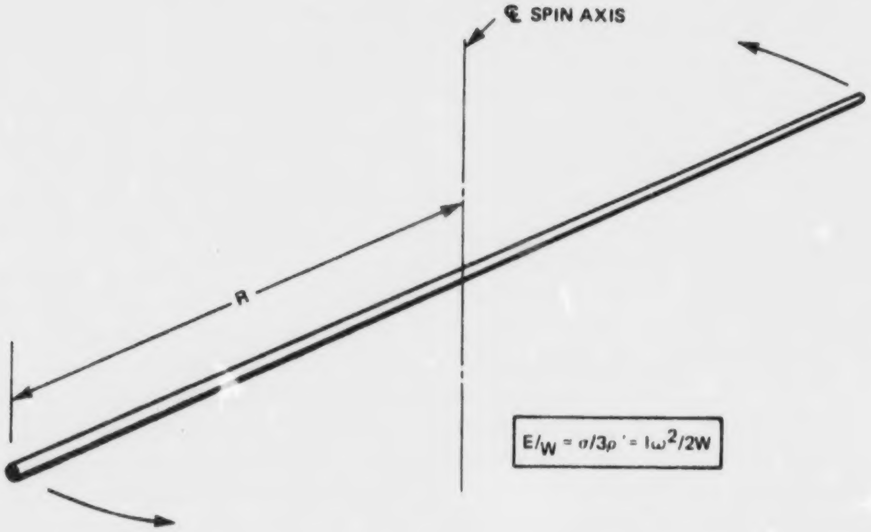

E = KINETIC ENERGY OF ROTATING ELEMENT (IN-LB)

W = WEIGHT OF ROTATING ELEMENT (EXCLUSIVE OF SHAFT AND HUB) (LB)

E/W = SPECIFIC ENERGY (IN-LB/LB) (MULTIPLY BY 0.314×10^{-4} TO CONVERT TO W-H/LB)

ω = ROTATIONAL SPEED (RAD/S)

σ = STRESS AT ROTATIONAL SPEED ω (PSI)

ρ' = MATERIAL WEIGHT DENSITY (LB/IN^3)

I = MOMENT OF INERTIA ABOUT SPIN AXIS ($IN/LB/S^2$) (FOR THIN ROD, $I = R^2W/3g$)

g = GRAVITATIONAL CONSTANT = 386 IN/S^2)

Fig. 3-1 ENERGY STORAGE CAPABILITY OF THE STRAIGHT FILAMENT

3.2.1 EQUIPMENT AND INSTRUMENTATION

Fundamental to the superflywheel concept is the provision of a very low pressure (and possibly a reduction in gas molecular weight) to reduce the windage losses associated with the high tip speeds and high drag shapes (see Appendix C). The spin-test chamber shown in Figs. 3-2 through 3-5 was designed and fabricated at APL for testing small-scale rods at pressures near 10^{-3} torr (i.e., 10^{-3} mm Hg abs, or approximately 10^{-6} atmosphere). The chamber consists of 1/4-inch-thick, steel tank closures, 32 inches in diameter, with flanges and an "O" ring seal. Four sets of opposed viewing ports permit observation of the rod tip regions. A 2-hp Heraeus mechanical roughing pump reduces the pressure to 5×10^{-2} torr, and a 500-watt Veeco diffusion pump (not shown) in series reduces it to 10^{-3} torr or less. Continuous pumping is used, because the program schedule and funding did not allow for development of a chamber that could maintain a vacuum over a long period.

Two methods of driving the rods were used. In one a fractional horsepower electric motor was used inside the vacuum chamber to drive the rod directly or drive a bearing-supported spindle holding the rod (Fig. 3-3). In the other, a 1-hp electric motor, mounted outside the vacuum chamber, transmitted power through a ferrofluidic vacuum seal to a 1:10 planetary friction-drive, speed increaser to the rod (Fig. 3-4). Both systems were capable of providing rod rotation rates above 30 000 rpm.

All spin tests were conducted remotely. The spin chamber was located in a heavy-walled concrete test cell with bullet-proof glass windows. The instrumentation was designed to measure chamber pressure, rod rotation rate, rod tip elongation, drive system vibrations, and to permit visual observation of the rod and spindle.

Figure 3-5 shows the overall instrumentation arrangement and system diagram. As the rod rotates,

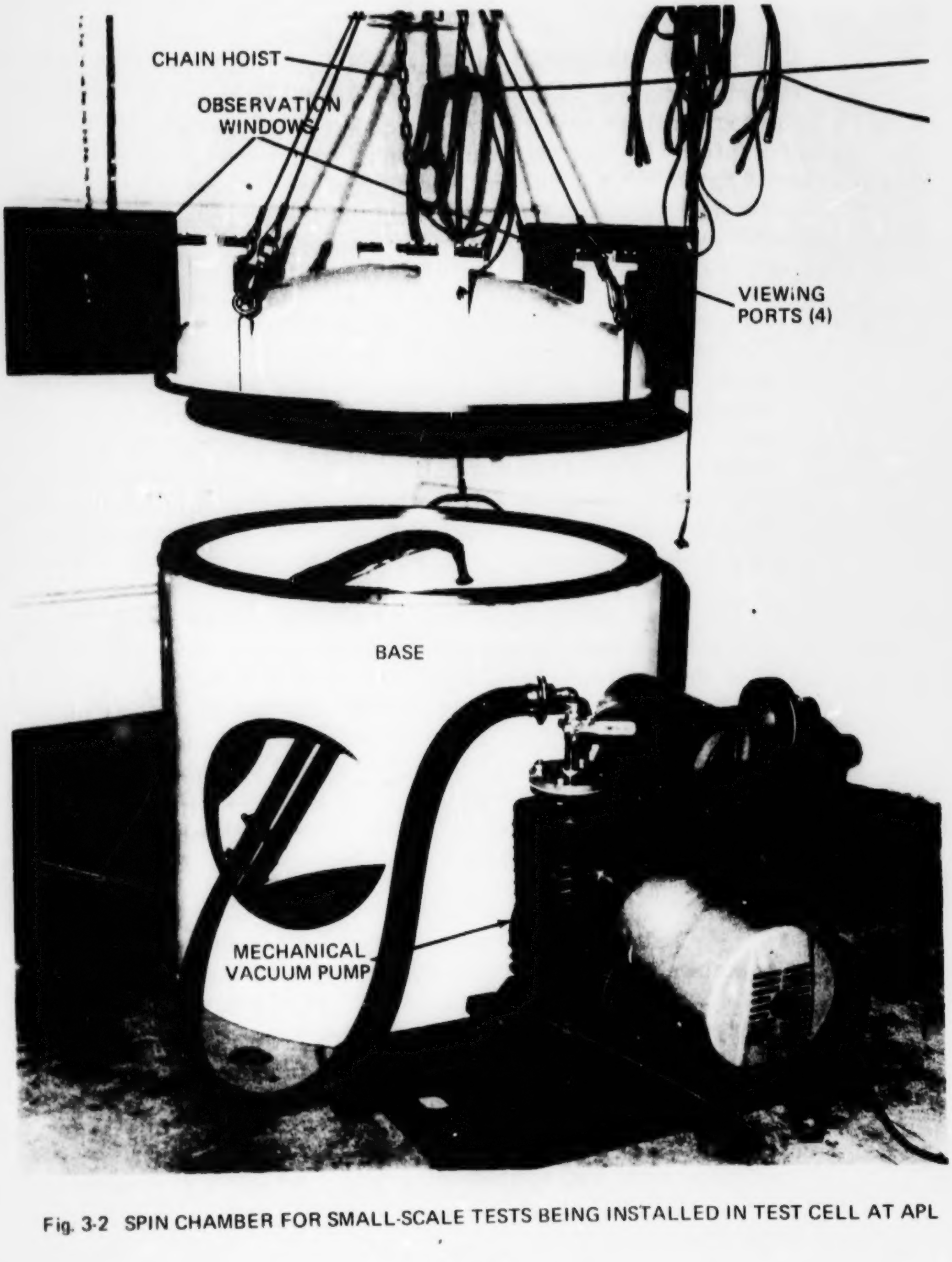
CHAIN HOIST
OBSERVATION WINDOWS
VIEWING PORTS (4)
BASE
MECHANICAL VACUUM PUMP

Fig. 3-2 SPIN CHAMBER FOR SMALL-SCALE TESTS BEING INSTALLED IN TEST CELL AT APL

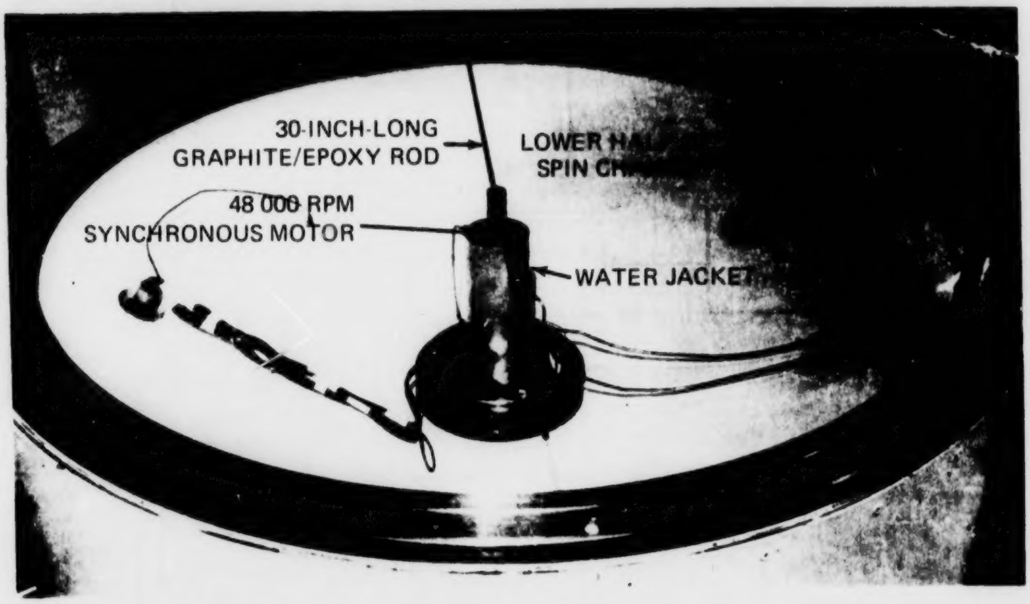
30-INCH-LONG
GRAPHITE/EPOXY ROD
LOWER HAL
SPIN CH
48 000 RPM
SYNCHRONOUS MOTOR
WATER JACKET

Fig. 3-3 TEST SETUP FOR ROTATING SMALL FILAMENTS OR COMPOSITE RODS USING HIGH-SPEED MOTOR INSIDE CHAMBER

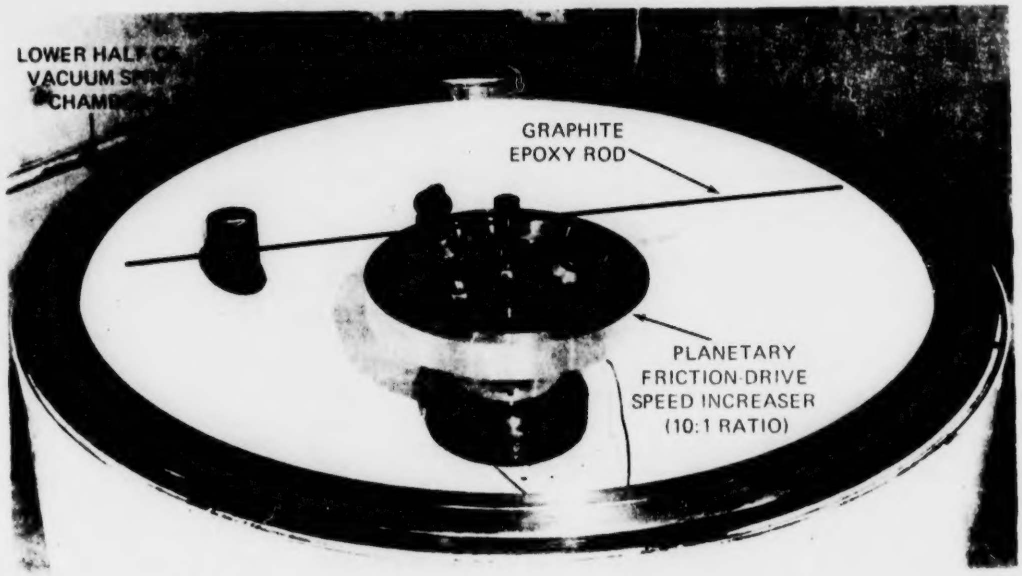
LOWER HALF
VACUUM SP
CHAMB
GRAPHITE
EPOXY ROD
PLANETARY
FRICTION-DRIVE
SPEED INCREASER
(10:1 RATIO)

Fig. 3-4 ALTERNATIVE SETUP WITH SPEED INCREASER INSIDE CHAMBER AND 1-HP MOTOR OUTSIDE

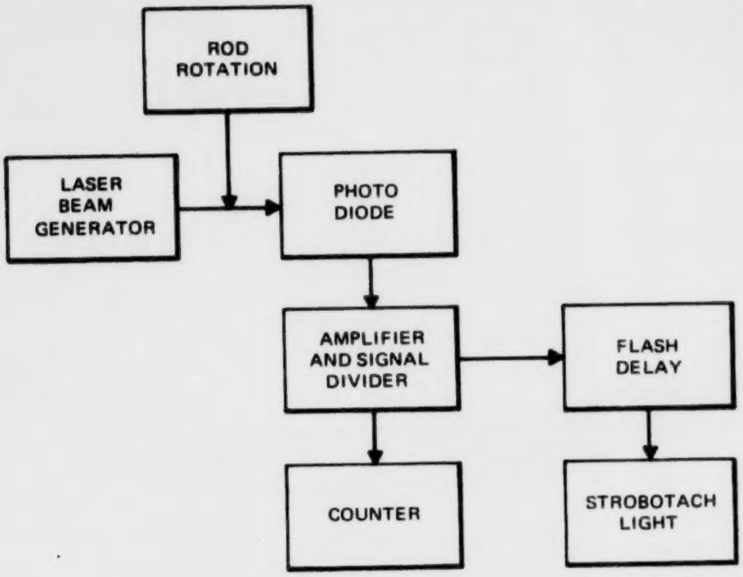
ROD ROTATION
LASER BEAM GENERATOR
PHOTO DIODE
AMPLIFIER AND SIGNAL DIVIDER
FLASH DELAY
COUNTER
STROBOTACH LIGHT

(a) BLOCK DIAGRAM OF INSTRUMENTATION FOR TIMING AND OBSERVING ROD

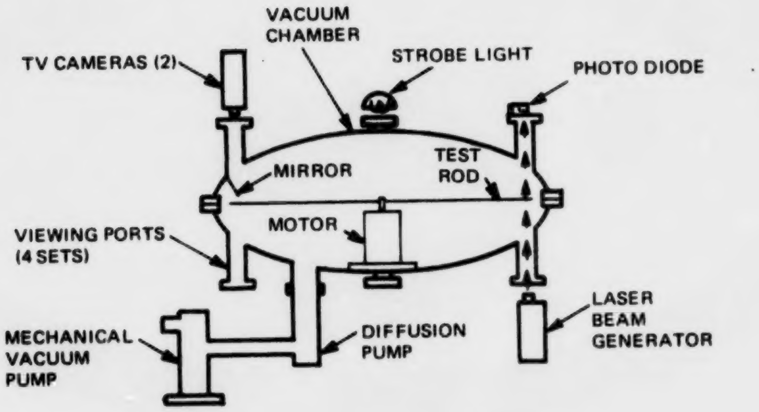
VACUUM CHAMBER
TV CAMERAS (2)
STROBE LIGHT
PHOTO DIODE
MIRROR
TEST ROD
VIEWING PORTS (4 SETS)
MOTOR
MECHANICAL VACUUM PUMP
DIFFUSION PUMP
LASER BEAM GENERATOR

(b) EXPERIMENTAL ARRANGEMENT

Fig. 3-5 SCHEMATIC DIAGRAMS OF SPIN CHAMBER SETUP AT APL

its tips interrupt the beam from a laser generator that is focused on a high-response, photo diode. The diode senses the change in energy, and the signal is amplified, divided by 2, and displayed on a digital counter in rps. The same signal triggers a strobotach flash unit, which flashes in synchronization with the instantaneous rotation rate of the rod, thereby freezing its image, which can be viewed by TV cameras and displayed in the control room. One TV camera is focused on a mirror which furnishes an overall view of the rod and hub and can be used to observe dynamic resonance of the rod and nutation of the drive spindle. The other TV camera is focused through a microscope with a reticle, so that rod elongation can be observed on the monitor. (This method of measuring elongation has not yet been used because of circuit problems with the flash delay unit, which was sent to the factory for repair and was returned to APL after the small-scale rod test program had been concluded.)

The digital counter signal activates a printer, which provides a record of rotation rate versus time (rod acceleration). Accelerometers were mounted on the drive unit housing to detect excessive vibration and resonant conditions. The chamber pressure was monitored with two thermal-conductivity vacuum gauges, and two Hastings meters, one covering the range from 1 atmosphere to 10^{-2} torr and the other from 10^{-2} to 10^{-4} torr.

3.2.2 SELECTION OF CANDIDATE TEST MATERIALS

In order to achieve a specific energy of 30 W-h/lb, a rod must have a uniaxial-tensile-strength/density ratio (σ/ρ')[1] in excess of 3 million inches. A number of composite materials meet this requirement, including boron filaments in an epoxy or magnesium matrix, graphite fibers in epoxy, and glass fibers in an epoxy or polyester matrix. In addition, free-standing filaments of boron or chemically strengthened glass satisfy the requirement and would be suitable for certain brush-type rotors (see Section 4.2). Table 3-1 lists the specimens tested at APL.

---

[1] In Sections 3 and 4, ρ' refers to the weight density of the material (lb/in^3). The symbol ρ is used in the Appendix for mass density (lb-s^2/in^4).

While other materials might also have been suitable, this group was selected because of the relatively large amount of available test data. (Data for all composites are sparse when compared to data for conventional structural alloys.) Though the costs of boron fibers and graphite/epoxy broad goods are high (near $200 per pound), fabricators and leading investigators of the field indicate that order-of-magnitude reductions, at least for graphite composites, are likely in the foreseeable future (Ref. 1). While the glass composite prices are already low enough for vehicular applications, some questions remain regarding fatigue life, but the vacuum environment will be beneficial (see Section 4.4). All of the selected materials have the potential for dissipating large amounts of energy by fracturing into very small segments at failure.

3.2.3 TEST RESULTS AND DISCUSSION

The drive system and rod mounting system used for each test also are shown in Table 3-1, because in some cases it appeared that they had a direct effect on the test results. The nominal length (spin diameter) for all samples was 30 inches, but the minor length variations have been included in the calculation of stress and stored energy. The specific energy E/W and maximum stress σ (at the center) are calculated from the equations (see symbol definitions in Fig. 3-1):

$$E/W = R^2\omega^2/6g \qquad (3\text{-}1)$$

$$\sigma = \frac{\rho' R^2 \omega^2}{2g} \qquad (3\text{-}2)$$

The calculated values do not include the effects of rod deformation as discussed by Brunelle (Ref. 21), which would increase the maximum σ and E/W values by about 2% for the glass composites but would have very little effect on graphite and boron specimens (see Section 4.4.5 for further discussion of this point).

The boron filaments were tested with the small Diehl motor (the only one available at the start of the program) whose rated speed of 3600 rpm was increased to 39 000 rpm under no-load conditions by raising the driving voltage and frequency. The maximum speed attainable with a test rod was strongly influenced by the mass of the rod and the associated increase in bearing friction caused by inherent imbalance. In fact, this drive system was not able to fail the boron test rods, all three types being intact after spin-down. Therefore, the energy levels presented do not show the maximum capabilities of these materials. The boron filament tests were conducted before the diffusion pump was added to the vacuum system, and test pressures were 4.7×10^{-2} torr for the 8-mil rod and 8.0×10^{-2} torr for the 4-mil rod. The test of the boron/magnesium rod (a "preform" material from General Technology Corp., Reston, Va.), and all subsequent tests included the diffusion pump with nominal test pressures of 1×10^{-3} torr.

Graphite/epoxy composite specimens were fabricated by Hercules, Inc., Cumberland, Md., and Fothergill & Harvey, Ltd., Lancashire, England. Both manufacturers used layers of composite tape to build up unidirectional laminate plates 30 inches long. The Hercules plate was 1/8-inch thick, while the Fothergill and Harvey material was 1/16-inch thick. These plates were cut lengthwise with a diamond wheel to form the square rods. For the most part the surface appeared smooth and free from flaws; however, this type of fabrication will inherently impart more surface imperfections than a molding

Table 3-1

Summary of Composite Materials, Rod Tests at APL

Test	Drive System[1]	Mounting System[2]	Max. Speed (rpm)	Max. Stress[3] (ksi)	E/W[3] (W-h/lb)	Remarks
AVCO Boron Filaments				W_r = 0.00035 and 0.00014 pound		
4-mil	Diehl	Tube	38 000	424	48	Rod did not fail, speed limited by motor
8-mil	Diehl	Tube	34 000	340	38	
General Technology Corp. Boron/Magnesium 20-Mil Preform				W_r = 0.00075 pound		
1	Diehl	Epoxy	31 500	254	33	No failure, speed limited
Hercules Graphite/Epoxy 1/8-Inch Square				W_r = 0.027 pound		
1	S/I	RTV	24 500	105	20	
2	G/S	RTV	19 000	66	12	
3	G/S	Epoxy	31 300	180	33[4]	
Fothergill & Harvey Graphite/Epoxy 1/16 Inch Square				W_r = 0.0066 pound		
1	S/I	RTV	22 400	91	17	
2	S/I	RTV	22 800	94	18	
3	S/I	RTV	22 400	91	17	
4	S/I	RTV	28 900	151	28	
5	S/I	RTV	26 200	124	23	
6	S/I	RTV	22 100	88	16	
7	G/S	Epoxy	33 000	195	36[4]	
PPG/BBI Type 525 E-Glass/Polyester (48% Fiber Volume) 0.098 Inch in Diameter				W_r = 0.015 pound		
1	G/S	Epoxy	23 600	116	19	
2	G/S	Epoxy	23 400	118	18	
3	G/S	Epoxy	24 000	123	19	
4	G/S	RTV	~19 800	~84	~13	Counter stopped just before rod failure
5	G/S	RTV	24 000	123	19	
6	G/S	RTV	23 200	115	18	
PPG/BBI Type 1055 E-Glass/Polyester (58% Fiber Volume) 0.098 Inch in Diameter				W_r = 0.016 pound		
1	G/S	Epoxy	27 000	165	24	
2	G/S	RTV	26 700	160	24	
PPG/BBI R-Composition Glass/Polyester (55% Fiber Volume) 0.098 Inch in Diameter				W_r = 0.015 pound		
1	G/S	Epoxy	28 900	177	28[4]	
2	G/S	Epoxy	30 700	194	31[4]	
3	G/S	RTV	<18 000	<65	<11	Failure before strobe synchronization
4	G/S	RTV	26 400	149	23	
Columbia Products (Shakespeare) E-Glass/Epoxy, 0.250 Inch in Diameter				W_r = 0.091 pound		
1	S/I	RTV	14 400	41	7	Some indications rod pulled out of holder
2	S/I	RTV	14 600	42	7	

Table 3-1 (Cont'd)

Summary of Composite Materials, Rod Tests at APL

Test	Drive System[1]	Mounting System[2]	Max. Speed (rpm)	Max. Stress[3] (ksi)	E/W[3] (W-h/lb)	Remarks
Corning Glass Rods, 0.106 Inch in Diameter, 10.9 Inches Long			W_r = 0.026 pound			
1	G/S	Acrylic	9 240	29	3	
2	G/S	Acrylic	9 480	28	3	
3	G/S	Acrylic	9 780	26	3	Failed away from point of max. stress
4	G/S	Acrylic	9 900	32	4	d. o.
5	G/S	Acrylic	9 540	30	3	
6	G/S	Acrylic	10 260	36	4	
PPG Glass Rods in Steel Holder (see Fig. 3-7)			W_{glass} = 0.0015 pound; W_{steel} = 0.32 pound			
1	G/S	Acrylic	25 100	165	14	E/W based on equivalent full circular brush (see text)

[1] Drive System:

S/I: Speed increaser
G/S: Globe motor with spindle
Diehl: Diehl motor

[2] Mounting System:

RTV: Dow Corning Silastic 734, room temperature vulcanizing
Epoxy: Armstrong epoxy
Acrylic: Acrylic cement
Tube: Stainless steel tube support with epoxy cement

[3] Stress and specific energy calculations assume constant rod cross-section, uniform mass distribution, and 30-inch length (spin diameter) except where noted. 1 ksi = 1000 lb/in^2.

[4] For the graphite/epoxy and R-glass/polyester materials, the better results were obtained with the Globe motor and epoxy mounting system.

or pultrusion[1] process. Initial trials with Hercules rods in brass holders (not listed in Table 3-1) led to early failure because of high acceleration and instability during start-up. Motor operating procedures were changed to avoid this problem. Tests of two Hercules rods and six Fothergill & Harvey rods followed with the rod mounted in the hub with Dow Corning 734 Silastic RTV. The assumption was that this material was strong enough to counter the nominal imbalance forces during spin-up but would allow the segments of a failed rod to clear the rod-holder quickly, before the resulting imbalance forces would damage the bearings. These tests produced calculated stress levels at failure ranging from 66 to 151 ksi for materials that were supposed to have 200 ksi strength.

To evaluate this problem further, some of the remaining Fothergill & Harvey rods were used for static tensile tests. The ends of the test specimens were embedded in aluminum rod grips and cemented with epoxy. Table 3-2 shows that three of the specimens failed at ~ 80% of the quoted strength, while one nearly achieved it.

Table 3-2

Static Tensile Tests of 1/16-Inch-Square Graphite/Epoxy Rods from Fothergill & Harvey, Ltd.

Specimen	Failure Stress (ksi)	Gauge Length (inches)
S1	158	5
S2	154	5
S3	163	5
S4	195	2

---

[1] In the pultrusion process the fibers and resin are pulled through a die into a mold, insuring a finished composite with uniform properties along the length, correct fiber alignment, and a smooth, dense surface.

In general, the spin test results are lower than the static test results. The manufacturer suggested that fiber misalignment and surface flaws were responsible. This hypothesis is somewhat verified by the higher strength of the short-gauge-length specimen, a characteristic of materials with random imperfections.

At this time in the program tests of 0.25-inch-diameter glass/epoxy rods gave evidence that the rods may have pulled out of the RTV mounting and failed by bending as they hit the side of the chamber. For this reason, the remaining two graphite/epoxy rods were hard-mounted with epoxy cement, and better performance was indeed realized: both rods exceeded 30 W-h/lb. The calculated stress was within 20% of the manufacturers claim for the 1/8-inch rod and within 3% for the 1/16-inch rod.

Twelve glass/polyester rods were furnished by PPG Industries, Pittsburgh, Pa., as examples of the kind of specimens that could be pultruded with the existing equipment of BBI, Inc. of Pittsburgh. The fiber volume is relatively low (45 to 55%) and could be increased to obtain higher strengths. The E and R-glass fibers are formulated for use in electrical applications, and the substitution of S-glass fiber, a high strength formulation, should also raise the composite strength level by 10 to 20%. Nevertheless, the tests of these glass/polyester rods were encouraging. The failure levels were quite consistent. For E-glass there is no clear-cut effect of using an RTV mounting adhesive, though one rod did fail at a low level. For R-glass rods, the epoxy mounting gave better results.

The glass and graphite composite rods were completely destroyed after failing at high rpm. The graphite rods were pulverized to fine particles, as shown in Fig. 3-6. The steel chamber was hardly scratched at impact, suggesting that a significant portion of the rod energy was dissipated by the microfracturing of the rod itself. The low-level vacuum meter indicated a sudden rise in pressure

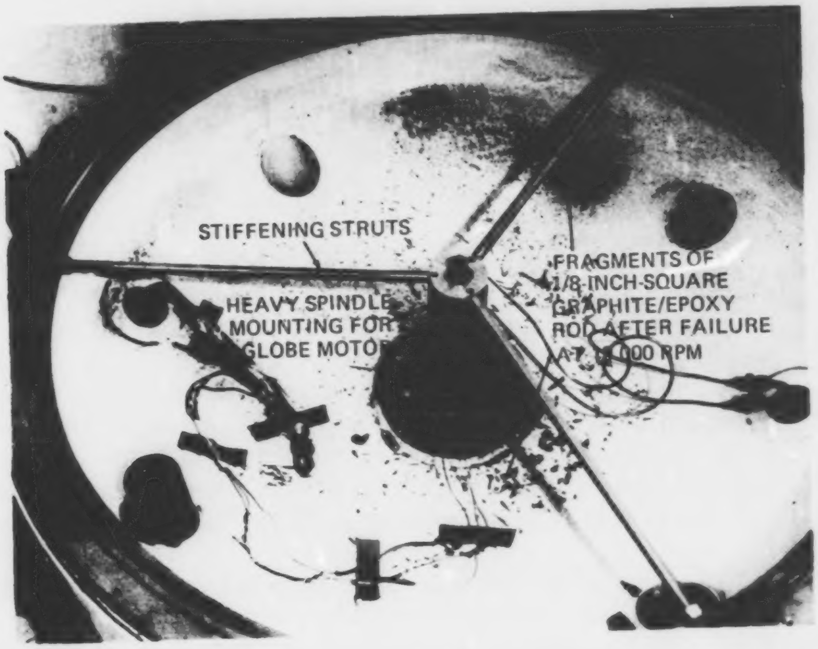
STIFFENING STRUTS
HEAVY SPINDLE MOUNTING FOR GLOBE MOTOR
FRAGMENTS OF 1/8-INCH-SQUARE GRAPHITE/EPOXY ROD AFTER FAILURE AT [illegible] 000 RPM

Fig. 3-6 REMAINS OF GRAPHITE/EPOXY COMPOSITE IN SPIN CHAMBER AFTER TEST

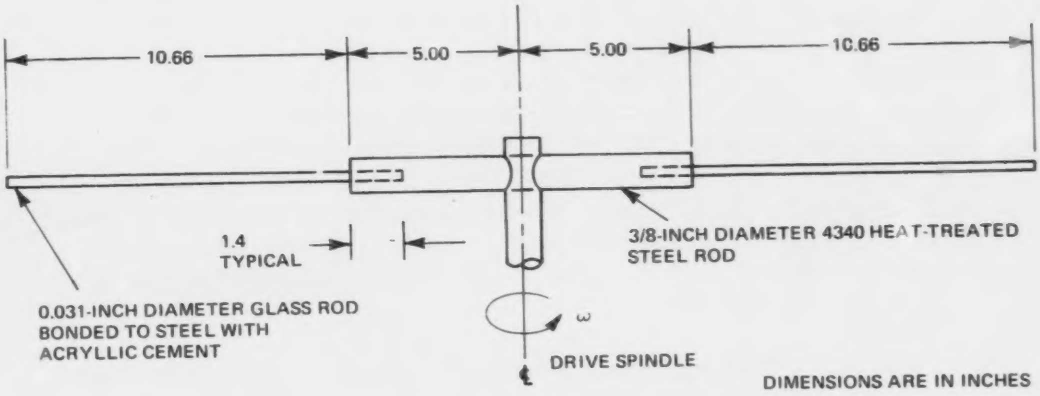
10.66
5.00
5.00
10.66
1.4 TYPICAL
3/8-INCH DIAMETER 4340 HEAT-TREATED STEEL ROD
0.031-INCH DIAMETER GLASS ROD BONDED TO STEEL WITH ACRYLLIC CEMENT
ω
DRIVE SPINDLE
℄
DIMENSIONS ARE IN INCHES

MAXIMUM SPEED AT FAILURE: 25 100 RPM
AVERAGE DENSITY OF GLASS RODS: 0.090 LB/IN^3
MAXIMUM STRESS AT ROOT OF GLASS ROD: 165 000 PSI
EQUIVALENT CIRCULAR BRUSH ENERGY DENSITY: $\frac{14.3\text{ W-h}}{\text{LB}}$

Fig. 3-7 SIMULATION OF CIRCULAR BRUSH CONFIGURATION AND TEST RESULTS

from 10^{-3} to > 10^{-2} torr. We did not determine the exact magnitude of the pressure rise, since the continuous pumping system quickly returned the chamber to the nominal operating pressure. In fact, it is not certain whether the increase in indicated pressure is a valid reading (resulting, probably, from heat generation and vaporization of the matrix material) or whether the sudden increase in small particles affects the thermal-conductivity vacuum gauge so as to indicate an increase in pressure. The preliminary indications were, however, that the break-up of the composite materials occurred in a way that would minimize damage to any surrounding chamber.

Another series of tests evaluated chemically-strengthened glass for use in brush-type rotor configurations (see Sections 4. 2. 3 and 4. 2. 4). Six 0. 100-inch-diameter rods were furnished by the Corning Glass Company. They were chemically cleaned and etched to remove surface impurities and then covered with an acrylic coating. At APL the rods were mounted in aluminum holders with acrylic cement and spun to destruction. All rods broke at low speeds with a maximum energy storage of 4 W-h/lb. Two of them failed away from the hub at points of lower stress, indicating flaws in the material at these locations. The specimens were returned to Corning for examination, and their engineers reported that the points of fracture were indeed flaws which should be correctable with better production controls.

PPG Industries supplied similarly coated glass specimens that were 0. 036-inch diameter and approximately 16 inches long. Two of these were cut to length and cemented in opposite ends of a 10-inch-long, 3/8-inch-diameter, hardened steel rod, as shown in Fig. 3-7. This model simulated two opposite elements in a circular brush rotor (see Section 4. 2. 3) which would have a steel hub 10 inches in diameter and thousands of closely spaced glass rods. The two-element model was spun to destruction at 25 000 rpm. This speed produced a maximum stress of 165 000 psi in the glass rods, which is equivalent to a specific energy of 14 W-h/lb for a full brush rotor, including the weight and energy of the steel hub. The steel rod of the failed model impacted the vacuum chamber with force sufficient to gouge a 1/4-inch-deep hole into the 2-inch-thick steel mating flange, damaging the "O" ring seal.

3.2.4 CONCLUSIONS FROM SMALL-SCALE TESTS

These small-scale rod tests at APL provided valuable information on selection of materials for later tests as follows:

1. The spin and vacuum systems were adequate, though a more powerful drive system, with bearings on each side of the specimen, would be desirable. The instrumentation system was versatile and well-suited to this exploratory program.
2. The better test results for the composite materials, obtained with the Globe motor/spindle drive system and epoxy mounting, demonstrated ultimate specific energy storages of 31 W-h/lb for R-glass/polyester and 33 to 36 W-h/lb for graphite/epoxy. A 4-mil boron filament demonstrated 48 W-h/lb without failure. The selection of materials for scaled-up rotors will depend on specific system requirements and rotor types.
3. Upon failure, the composite rods appear to dissipate a significant portion of their kinetic energy by microfracture or vaporization of the matrix material.

3.3 TESTS OF 1-POUND BARS AT THE NAVAL AIR PROPULSION TEST CENTER

The Naval Air Propulsion Test Center (NAPTC) operates a large vacuum spin chamber at the Philadelphia

Naval Base. Under contract from the NASA Lewis Research Center, they study the modes of failure of turbine rotors and blades in order to develop design techniques for sizing containment structures for turbojet engines[1]. Discussions with the NAPTC staff indicated that the facility could be modified to test 1-pound composite bars and to observe the mode of failure and the consequent distortion of a steel containment ring. The following sections discuss the facility modifications, the test results, and containment analysis.

3.3.1 FACILITY MODIFICATIONS

The main spin chamber at NAPTC has a 10-foot-diameter test section, as shown in Fig. 3-8. In March 1971 it was operating at pressures near 1 torr. Its photographic system (Ref. 22) consists of a high-speed Beckman & Whitley camera with a loop of film, a high-intensity strobe light system, and a large front-surface mirror to reflect the light to the test section. The procedure is to darken the test cell and bring the camera up to speed before the spin test begins. Then the test rotor is accelerated, and when failure occurs the first fragment to strike the containment ring closes a circuit between the ring and a small trigger wire, activating the strobe lights for a period just long enough to expose the loop of film. This photographic system and operating technique appeared directly applicable to the APL test program with only a minor modification to the trigger wire to account for the use of nonconducting rotor materials such as the S-glass/epoxy composite.

---

[1] NASA also funds the Aeroelastic and Structures Research Laboratory of MIT in a complementary program to develop a computerized dynamic structural model of a containment ring for use in extending experimental results and preliminary design. The program can compute deformations of multilayer, multimaterial rings; however, correlation between results of tests and analyses has thus far been limited to steel rings.

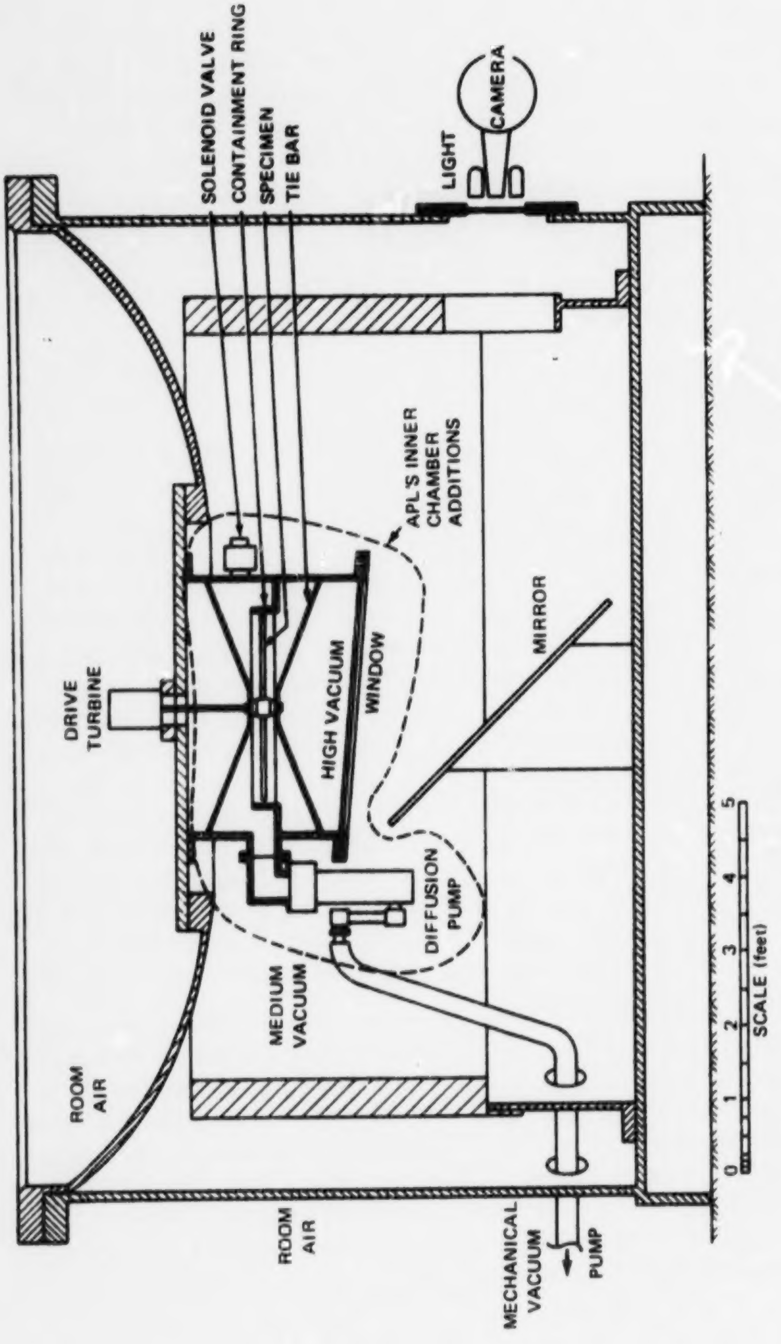
ROOM AIR
ROOM AIR
MECHANICAL VACUUM PUMP
MEDIUM VACUUM
DIFFUSION PUMP
DRIVE TURBINE
HIGH VACUUM
WINDOW
MIRROR
APL'S INNER CHAMBER ADDITIONS
SOLENOID VALVE
CONTAINMENT RING
SPECIMEN
TIE BAR
LIGHT
CAMERA
0
1
2
3
4
5
SCALE (feet)

Fig. 3-8 GENERAL ARRANGEMENT FOR 1-POUND ROD TESTS AT NAPTC, PHILADELPHIA

There were two areas of concern about spinning the 1-pound rods with the NAPTC equipment. First the pressure in the chamber would be 2 to 3 orders of magnitude higher than that envisioned for a superflywheel system. The temperatures at the tips of the rods would reach 600° to 800°F at the end of a rapid acceleration to 30 000 rpm ($\dot{\omega} \simeq 1500$ rpm/s). These temperatures would be sufficient to start a charring process in the ablative resin materials, and in the high acceleration field (400 000 g's at the tip) it is likely that pieces of the rod would fly off, causing premature triggering of the lighting system or destruction of the rotor by imbalance.

The second concern was one of critical speed of the rotor itself. The NAPTC drive system consists of an air turbine mounted on top of the vacuum chamber lid, and a long, thin spindle shaft is cantilevered downward to drive the rotor. In the case of symmetrical disk rotors the critical speed (equivalent to the first lateral natural frequency) is low, and the rotor is driven through it before excessive deflections develop. After passing this critical speed the system is stable until the rotor fails. However, NAPTC personnel pointed out that a rod-type rotor might have different stability characteristics. Simple tests at APL of rods supported by thin, flexible drive shafts confirmed this problem. The markedly different inertias in the two directions perpendicular to the spin axis of a rod apparently create a "band" of critical speeds that is difficult to traverse before developing unstable deflections, and the rod wobbles out-of-plane and bends the drive spindle.

To solve these two problems a secondary, inner chamber was fabricated (at APL) to permit the desired higher vacuum and to provide support for additional bearings on each side of the test rod to prevent instability during spin-up. Figure 3-8 includes this secondary chamber and the diffusion-type vacuum pump that was mounted from it to exhaust through a flexible hose to a mechanical roughing pump outside the main chamber (the same vacuum equipment used at APL). To permit use of the existing photographic system, a plexiglass window was used on the bottom of the secondary chamber (canted 15° to reduce reflections), and tension tie bars were used to hold the bearings in place. A solenoid valve was installed to permit equalization of the pressure inside and outside the secondary chamber during the initial evacuation of the main chamber, thereby allowing the window to be designed to resist only a small pressure differential.

Figure 3-9 shows APL's inner chamber while it was suspended from an assembly platform at NAPTC. Figure 3-10 is a view through the window up into the chamber, showing the specimen, bearing supports, tie bars, containment ring, trigger wire, and drive spindle. The containment ring rests on three metal tabs and is constrained from vibration during spin-up by three small C-clamps.

3.3.2 SELECTION AND PROCUREMENT OF TEST MATERIALS

In the small-scale tests at APL, boron filaments and boron/magnesium, graphite/epoxy, and R-glass/polyester composites had achieved specific energies in excess of 30 W-h/lb. After discussion with OAP it was decided to test 1-pound rotors of two material types (rather than one as originally planned) to offer a comparison in strength levels and modes of failure. Glass composites are, in general, the best documented and are obvious candidates for operational systems because of their low cost. Although they are prone to fatigue and stress rupture, the vacuum environment proposed for a flywheel system (10^{-2} to 10^{-3} torr, void of moisture and oxidants that cause stress corrosion on the surface of glass) will improve their fatigue and stress-rupture characteristics (see Section 4.4). Therefore, this class of material was considered the primary choice, and the strongest and most fatigue-resistant material in this class is S-glass fiber in an epoxy matrix, which was selected.

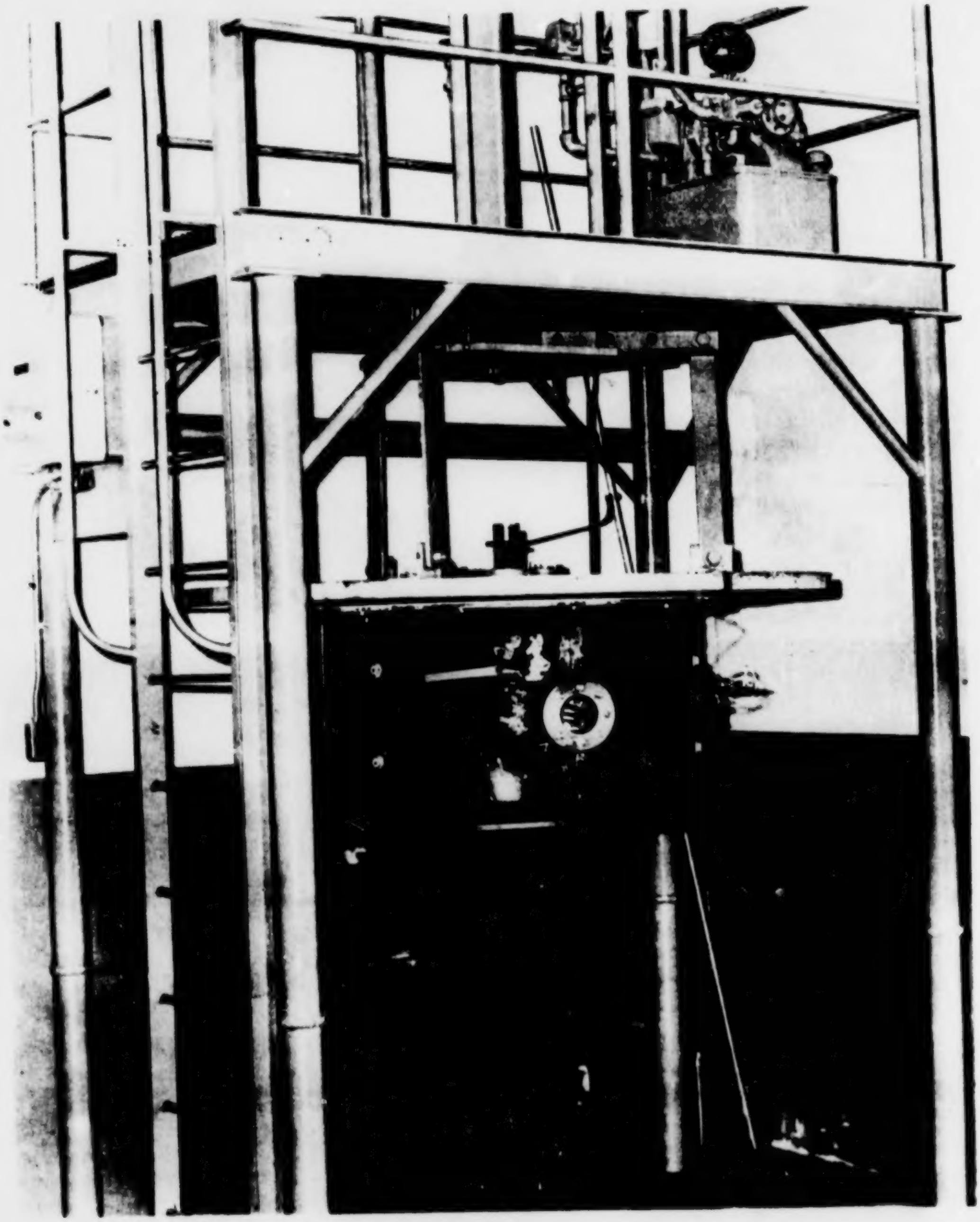

Fig. 3-9 GENERAL VIEW OF APL'S INNER CHAMBER SUSPENDED FROM AN ASSEMBLY PLATFORM

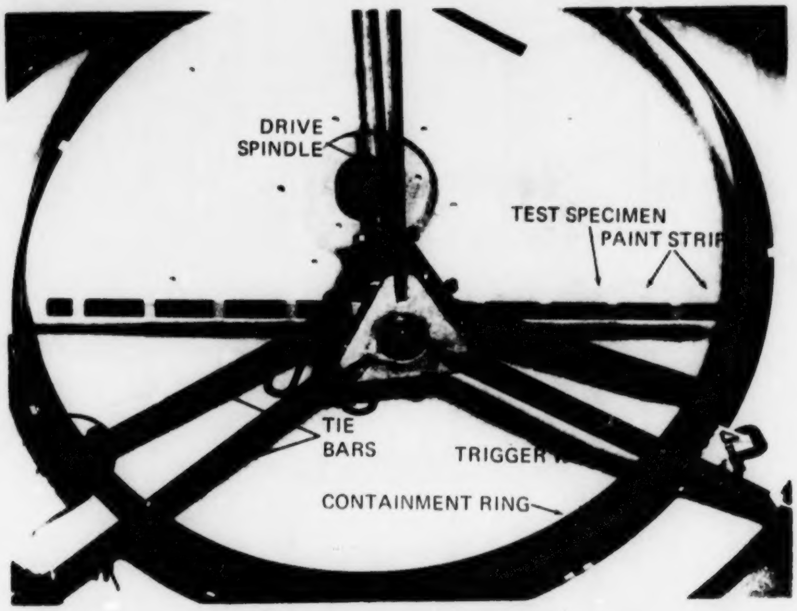
DRIVE
SPINDLE
TEST SPECIMEN
PAINT STRIP
TIE
BARS
TRIGGER W
CONTAINMENT RING

Fig. 3-10 INSIDE VIEW OF SPIN CHAMBER

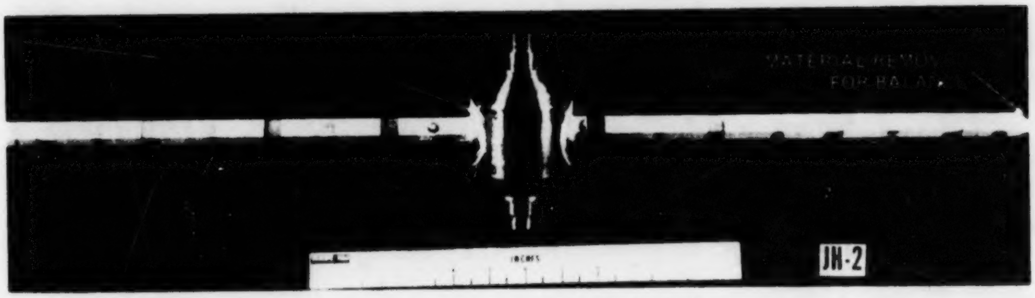
MATERIAL REMOVED
FOR BALANCE
INCHES
JH-2

(a) S-GLASS/EPOXY ROD POTTED INTO HUB

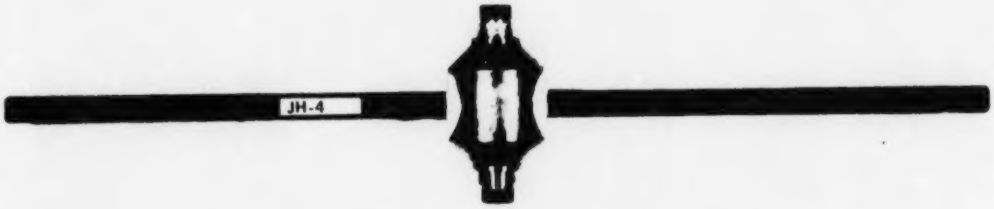

(b) GRAPHITE/EPOXY TEST ROD

Fig. 3-11 TYPICAL SPECIMENS FOR NAPTC TESTS

Boron and graphite composites were considered for the second material. Both are excellent in their resistance to fatigue and are logical alternatives to glass for this reason. Boron has been in service longer, and its properties are more completely characterized; however, the trend in use appears to be toward the new graphite fiber with its equal or superior strength and more rapidly decreasing price. Therefore, graphite/epoxy composite was selected as the second material for the 1-pound tests.

Three bars of each composite material were ordered from Hercules, Inc. Fabrication of the bars by the process of net-molding[1] was considered but discarded because of the costs required for tooling. This process eliminates machining of the part and usually results in significant increases in strength compared to a machined part. To meet the desired schedule at reasonable cost Hercules elected to fabricate the bars by laying up the composite tape to the required thickness and forming a plate from which three square bars could be cut. A problem evolved because Hercules was in the process of shifting production of composite materials from their Cumberland, Md., plant to their Magna, Utah plant. Their equipment was expected to be in operation in Utah in time to meet the schedule for this program, but it was not, and they had to procure the tapes from another source. The S-glass/epoxy tape (Scotchply 1009-26S) was procured directly from 3-M Corporation. Hercules furnished the graphite fiber and resin used in their 2002T system to 3-M, who made the graphite/epoxy tape.

All of the actual laying-up of the tape laminae, curing, and machining of the bars was done by Hercules. Lack of experience with the Scotchply tapes resulted in the S-glass/epoxy plate curing-out at less than the desired thickness, and the bars cut from it weighed only

---

[1] A process where the part is pressurized and cured to the final dimensions in a mold, eliminating the need for final machining operations.

3/4 pound each. The graphite/epoxy rods were of the proper size and weighed 1 pound. The rods were cut with a diamond wheel to minimize damage to the surfaces; however, some bruising and scraping was evident, particularly with the glass composite. Tensile test specimens also were provided from the material used to make the bars. The glass composite was expected to have an ultimate tensile strength of 260 000 psi and a density of 0.075 lb/in^3; the graphite, 200 000 psi and 0.054 lb/in^3. If these strengths had been realized in the spin tests, the specific energy storages would have been between 36 and 39 W-h/lb. Figure 3-11 shows one bar of each type mounted in its spindle holder.

3.3.3 TEST RESULTS AND DISCUSSION

A shakedown test (designated JH-1) of the modified equipment at NAPTC was conducted with a 1.1-pound, 0.81-inch-diameter, pultruded E-glass/epoxy bar that was available as a free sample from PPG Industries, Inc. Because of its glass type and its low fiber content this bar was not expected to achieve 30 000 rpm but was useful for a first test. It was cemented with epoxy into an aluminum adapter piece, which was cemented in the 2-inch-diameter hole that runs through the center of the spindle holder. This assembly was dynamically balanced at NAPTC by drilling holes in the spindle (a procedure that was modified later).

Because leaks in the main chamber system (probably in the turbine drive spindle seal) permitted large quantities of humid ambient air to enter the secondary vacuum system, large amounts of water were absorbed in the oil in the pumps. It was necessary to clean and flush the pumps between runs and to limit their operating times during prerun preparation. During the pump-down for the test of the trial specimen the solenoid valve remained closed, though power was applied to open it. As a result, air trapped in the secondary chamber created an excessive pressure differential across the plexiglass window, and it burst downward, destroying the mirror. Fortunately the test specimen was not damaged. The test procedure was revised to require verification that the solenoid valve was in the open position before pump-down of the main chamber was begun. In the next trial, with a vacuum level of 1.8×10^{-2} torr in the secondary chamber, the bar was observed while it was accelerated to ~ 5000 rpm and then slowed down. No vibrations or instabilities were observed. The bar was then spun to destruction at 19 900 rpm. All equipment worked well, and the check-out run was considered successful. The 5/8-inch-thick containment ring showed no damage other than mild abrasion where fragments of the bar contacted the trigger strip. The bar disintegrated into straw-like fragments upon impact.

The next test, JH-2, was of the S-glass/epoxy bar (Fig. 3-11a). A different balancing procedure was used on this and all subsequent specimens to minimize forces that would tend to pull the bar out of the spindle or adapter. First, the heavy steel spindle was balanced by drilling prior to insertion of the bar. The square bar was clamped and cemented between the two halves of an aluminum adapter that had been carefully sized to grip the specimen. The adapter was then cemented into the steel spindle, and the spindle-bar assembly was balanced by removing material from one end of the bar. During the five tests there was no evidence that the bar had pulled from the adapter before fracture, and the adapter always remained in the spindle after bar failure.

The pressure in the secondary chamber was 6.3×10^{-2} torr when the bar was accelerated at an average rate of 335 rpm/s. Failure occurred after 87 seconds at 29 100 rpm, equivalent to 28 W-h/lb for the bar. The photographic system operated well, except that the light-colored bar did not offer sufficient contrast to produce high-quality pictures. The bar fractured into a straw-like mass (Fig. 3-12).

Reproduced from best available copy.

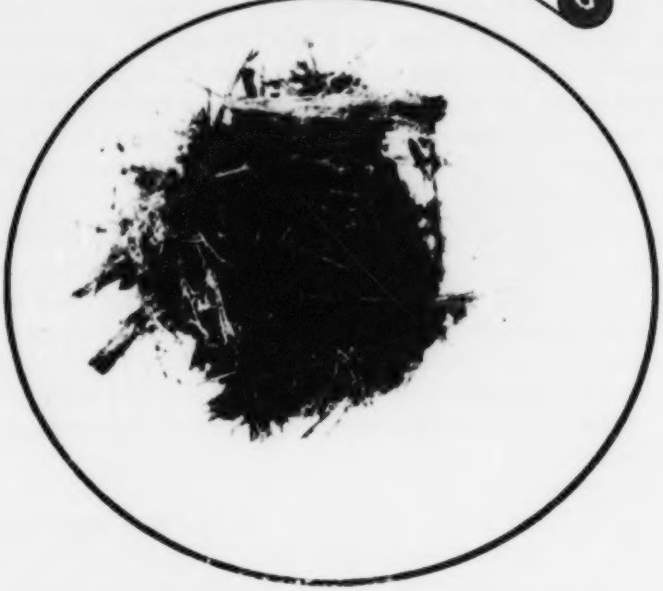

Fig. 3-12 S-GLASS/EPOXY FRAGMENTS FROM TEST JH-1

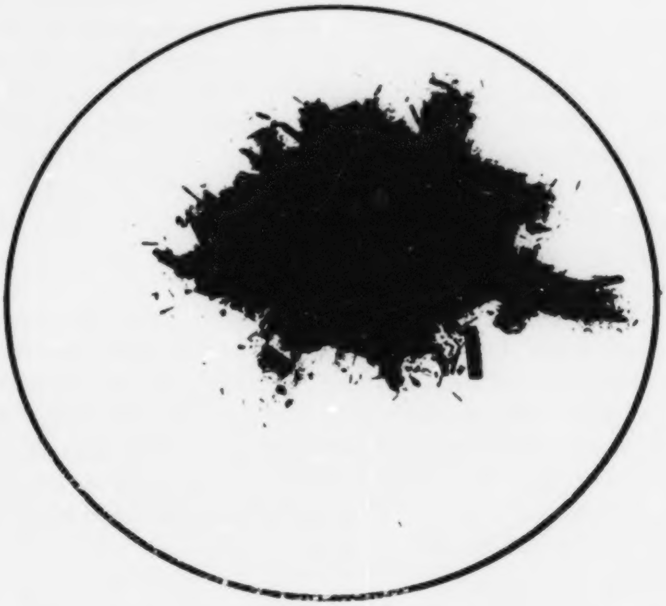

Fig. 3-13 GRAPHITE/EPOXY FRAGMENTS FROM TEST JH-3

Another S-glass/epoxy bar was set up for test, but after the main chamber vacuum pump had been operating for about 15 minutes there was a sudden implosive failure of the glass window that serves as the camera port. Pieces from the window shattered the mirror and damaged the lights. The small solenoid relief valve could not compensate for the large flow of air into the main chamber, and after another 2 or 3 seconds the plexiglass window imploded into the secondary chamber, breaking the specimen. Fortunately, there were no people near the camera port at the time of failure, and only material damage resulted. There was no explanation for the failure other than possible fatigue of the window after many chamber evacuations. The window was replaced with an identical unit, and testing was resumed.

The next test, JH-3, was the first test of a graphite/epoxy bar. In spite of cleaning and flushing the pumps, the vacuum system could only evacuate the secondary chamber to 0.17 torr. The bar accelerated smoothly for 71.3 seconds, failing at 28 000 rpm (26 W-h/lb). The two halves of the failed bar impacted a 1/4-inch-thick containment ring and were pulverized as shown in Fig. 3-13. The ring suffered more damage than did the similar ring in the glass-composite test, JH-2, as shown in Figs. 3-14a and 3-14b. This may be due to the fact that the graphite bar fails suddenly and both ends impact the ring simultaneously, whereas the glass bar breaks up more slowly. Also, the graphite bar contained 28% more energy by virtue of its greater mass.

In Test JH-4 the second graphite/epoxy rod achieved 28 200 rpm, or 26.5 W-h/lb. The pressure during this test was 0.25 torr, the highest value experienced. Continued attempts to seal possible leaks had no effect. This vacuum was adequate, however, for the short-duration test, and the bending stresses induced in the rod by aerodynamic drag were less than 50 psi. Since a 3/8-inch-thick containment ring was used, the permanent deformation of the ring (Fig. 3-14c) was less than observed in Test JH-3.

The final test (JH-5) made use of the third S-glass/epoxy bar, which was judged by Hercules to be the poorest in quality of the three because of observable surface defects. They applied an extra coating of epoxy over the entire rod in an effort to improve its integrity, but the effectiveness of this treatment is doubtful. At the start of this test the pressure was 0.19 torr. The rod was accelerated to 27 200 rpm (24.7 W-h/lb), at which time the camera lights were actuated, and the drive turbine was decelerated. Visual inspection from outside the chamber did not reveal rod damage, and it was concluded that either the lights were actuated from a spurious signal, as sometimes happens, or a small piece of the rod tip triggered the system. Because a small film of oil was seen on the inner surface of the plexiglass window, and the drive shaft vacuum seal was its probable source, the chamber pressure was checked and was found to be dropping rapidly. Apparently the act of spinning the rod caused the shaft seal to "wear in" and improve the seal, though the result is not conclusive. The pressure finally stabilized at 2.6×10^{-3} torr, and the rod was accelerated again. It failed at 24 200 rpm, somewhat verifying the assumption that failure had begun at 27 200 rpm during the previous run. The impact damage to the 1/4-inch-thick ring is shown in Fig. 3-14d.

Results of these tests are summarized in Table 3-3. The calculated stresses at failure (and energy densities) were less than expected. The best S-glass/epoxy test, JH-2, achieved 79% of the expected 260 ksi strength. These differences can hardly be attributed to additive bending stresses caused by aerodynamic drag and rod acceleration, which were always quite small (< 1%) compared to the axial stresses resulting from centrifugal forces.

The tensile specimens mentioned earlier were loaded to failure in a Universal Testing Machine at APL. Foil strain gauges were applied on opposite surfaces of each specimen to detect bending stresses caused by eccentric

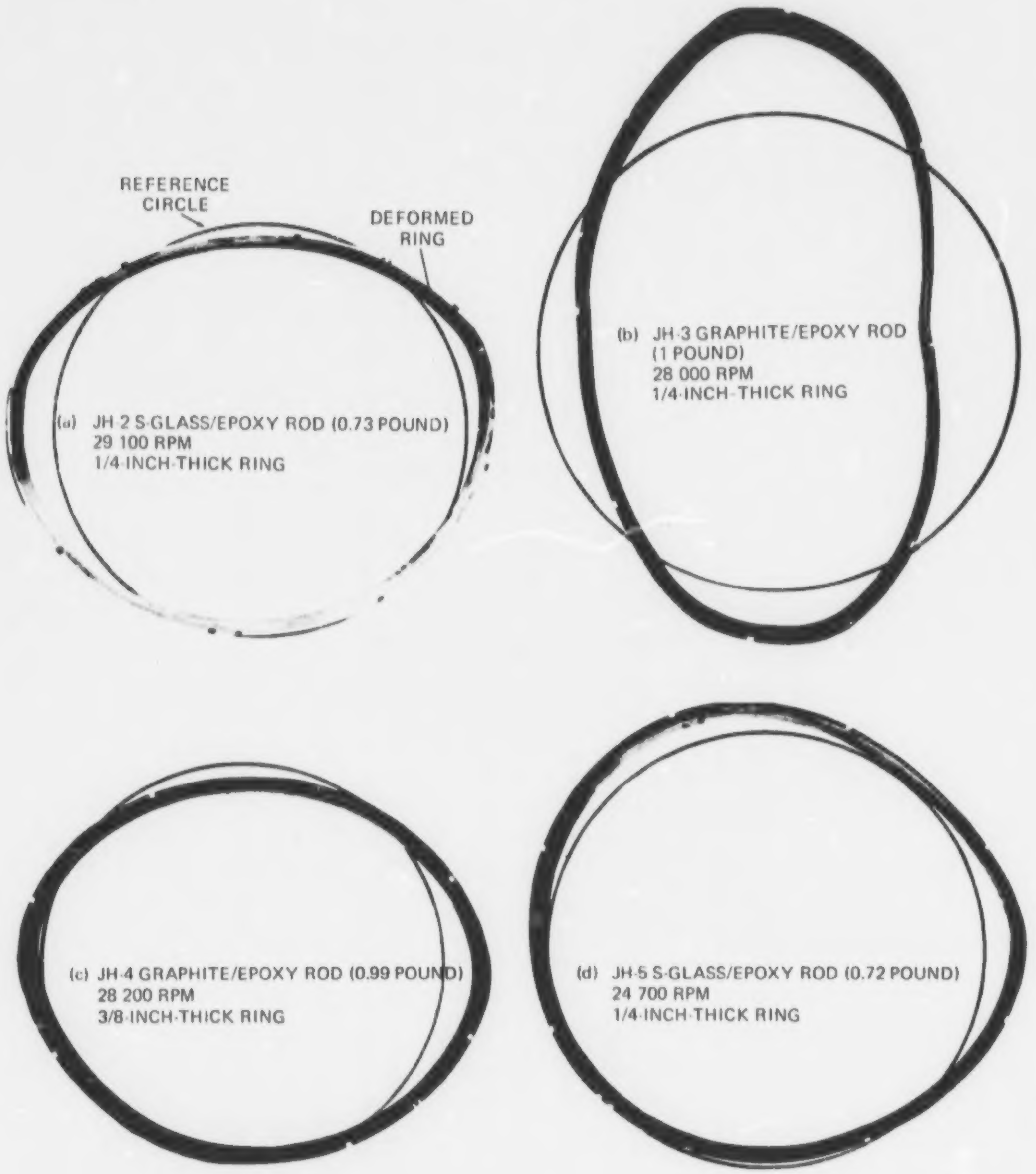

(a) JH-2 S-GLASS/EPOXY ROD (0.73 POUND)
29 100 RPM
1/4-INCH-THICK RING

(b) JH-3 GRAPHITE/EPOXY ROD
(1 POUND)
28 000 RPM
1/4-INCH-THICK RING

(c) JH-4 GRAPHITE/EPOXY ROD (0.99 POUND)
28 200 RPM
3/8-INCH-THICK RING

(d) JH-5 S-GLASS/EPOXY ROD (0.72 POUND)
24 700 RPM
1/4-INCH-THICK RING

Fig. 3-14 CONTAINMENT RINGS AFTER TESTS, COMPARED TO REFERENCE CIRCLES

Table 3-3

NAPTC Test Results: Speed, Stress, and Specific Energy at Failure

Test	Material	Cross Section	Weight (pounds)	Speed (rpm)	Stress[1] (ksi)	Stress[1] (%)	E/W (W-h/lb)
JH-1[2]	E-Glass/Polyester	13/16 inch diameter	1.10	19 900	89	--	13.2
JH-2	S-Glass/Epoxy	0.57 inch square	0.73	29 100	204	79	28.2
--	S-Glass/Epoxy	0.56 inch square	0.72	No test (facility failure)			
JH-3	Graphite/Epoxy	0.79 inch square	1.00	28 000	136	68	26.1
JH-4	Graphite/Epoxy	0.78 inch square	0.99	28 200	137	69	26.5
JH-5	S-Glass/Epoxy	0.57 inch square	0.72	27 200[3]	178	69	24.7

[1] Percentage of expected value quoted by Hercules

[2] Facility and instrumentation check-out

[3] Test aborted at this speed. Rod subsequently failed at 24 700 rpm.

loading (see Fig. 3-15a); differences in strain readings from the pairs of gauges remained less than 2% for all specimens, and it was concluded that the specimens were in proper alignment throughout the tests. Two of the failed specimens are shown in Fig. 3-15b, and the results are given in Table 3-4.

Table 3-4

Failure Stresses for Tensile Test Specimens

Specimen	Cross Sectional Area (in^2)	Load (pounds)	Stress (ksi)	Stress (%)
Graphite -1	0.0187	3050	164	82
Graphite -2	0.0192	3220	168	84
Graphite -3	0.0187	3230	173	87
S-Glass -1	0.0218	5690	261	100
S-Glass -2	0.0218	6070	279	107

For graphite/epoxy, the average stress, 168 ksi, is 84% of the expected value of 200 ksi, with a variation of ±3%. A probable explanation for this lower strength is the fact that the prepreg tape was produced by another firm (because of the previously discussed scheduling problems) and yielded only 53% fiber volume instead of the normal 59%. The S-glass samples exceeded the requested ultimate strength of 260 ksi.

For graphite/epoxy, the average spin test stress from Table 3-3 is 81% of the average tensile-test stress from Table 3-4. For S-glass epoxy, this percentage is 71%.

There are several possible reasons for the differences in achieved strength between the bars and the tensile specimens. First, the bars required the fabrication of plates that were large, particularly in thickness, by current composite material demands. As thickness increases it is more difficult to maintain fiber alignment

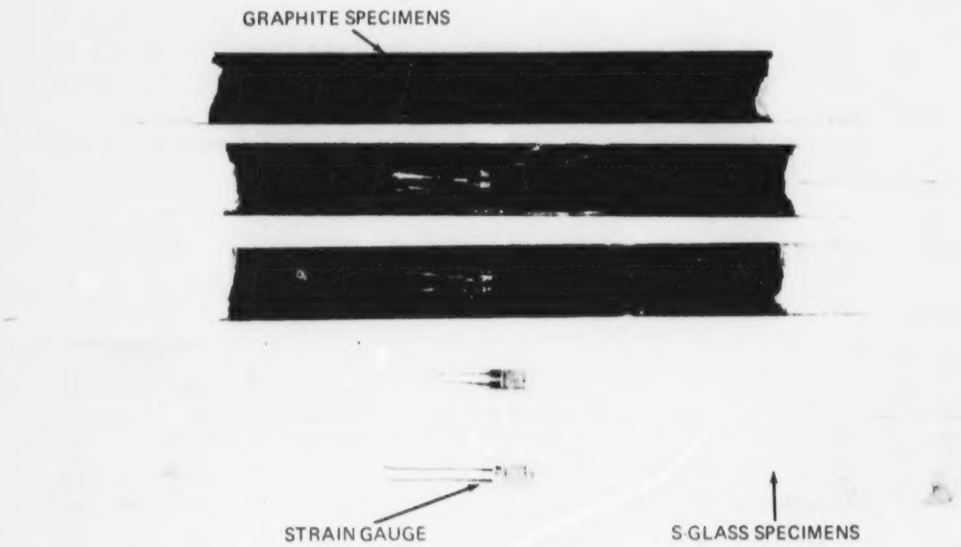
GRAPHITE SPECIMENS
STRAIN GAUGE
S-GLASS SPECIMENS

(a) SPECIMENS BEFORE TEST

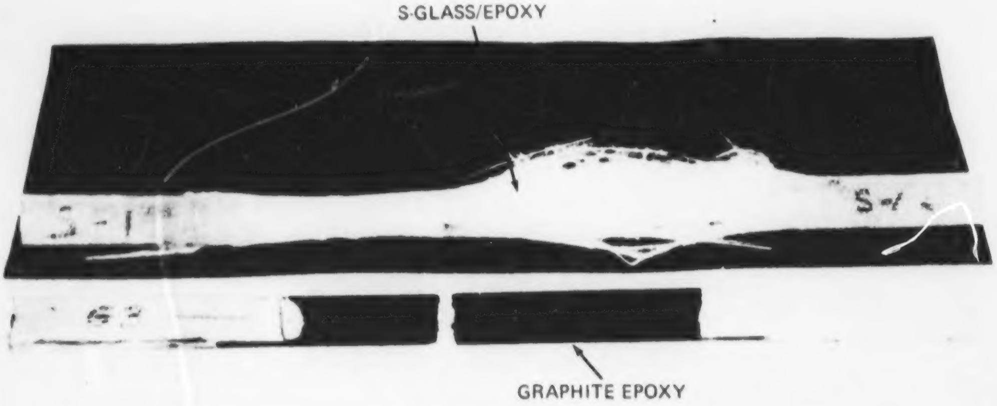
S-GLASS/EPOXY
S-1
GRAPHITE EPOXY

(b) FAILED TEST SPECIMENS

Fig. 3-15 STATIC TENSILE TEST SPECIMENS BEFORE AND AFTER TEST

(a problem that could be overcome with the use of individual bar molds). Also, large sizes require special cure cycles to achieve uniform properties, free of voids, and with the desired fiber content. The current program involved only a single fabrication and cure for each of the materials, and it is not surprising that Hercules encountered some difficulties, particularly with the use of different prepreg tape material.

Another degrading effect on the bar strength was the surface machining required to cut them from the larger plate. This process is certain to damage or cut fibers, and any vibration of the bars during spin testing would aggravate the problem of stress transfer around these discontinuities. The cut surfaces of the S-glass bars were noticeably bruised and abraded, and the graphite bars showed some delamination. Again, the use of an individual molding process would eliminate the requirement for machining.

Another possible reason for the low spin test results is that the dynamic environment developed transient vibrations that were damaging to the composite materials, though the limited amount of instrumentation used was not effective in detecting a problem of this type. A fourth possibility is that the differences result from a "size effect," common to brittle structural materials, wherein the probability of encountering a critical flaw increases with the volume of material stressed. This is a real effect that is observed in all structural materials, and it is true that the strength of large elements will be less than that of smaller ones. However, the principal flaws in composite materials are a direct result of manufacturing processes, and it is judged that major differences in strength with respect to size will be eliminated when the experience and control required to fabricate large pieces approaches the techniques now available to form tensile specimens.

3.3.4 MODE OF FAILURE

The photographic system at NAPTC gave us the first definitive evidence of the mode of failure of the rods. Because of the favorable indications for containment (safety), the presentation of these data, their analysis, and discussion is considered to be one of the more important results of the current program.

It has been postulated that the kinematics of rod failure would be as shown in Fig. 3-16. This behavior is demonstrated clearly in Fig. 3-17 for a graphite/epoxy rod test (JH-4) and Fig. 3-18 for an S-glass/epoxy rod test (JH-2). Figure 3-17b shows the two halves of the graphite/epoxy rod impacting the containment ring, and their orientations indicate forward angular velocities. The fact that the two halves struck diametrically opposite points of the ring at approximately the same time means that (a) failure occurred near the spin axis and (b) maximum bending moments were imposed on the ring. The subsequent frames show the pulverizing of the rod tips as they grind into the containment ring.

For the S-glass/epoxy rod (Fig. 3-18) one end failed first, possibly by fraying or interlaminar shear, and the other end remained essentially attached to the hub through one half of a revolution. The effect was to "spread" the energy release over the perimeter of the containment ring, reducing ring deformation. The effect can be judged by comparing the deformations of the 1/4-inch-thick rings shown in Figs. 3-14a and 3-14d (S-glass rods) with those for the 1/4-inch and 3/8-inch-thick rings in Figs. 3-14b and 3-14c (graphite rods).

A significant feature seen in both sets of failure photographs is that the rod is essentially destroyed in less than 1 ms and before motion of the ring is detected. This is in sharp contrast to failure of metal disks against containment rings in which the ring "follows" the segments of the disk until the ductile limit is reached (ring failure)

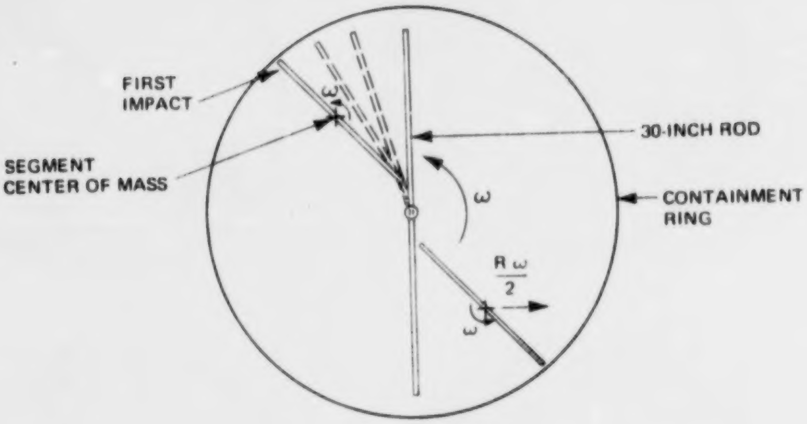
FIRST IMPACT
SEGMENT CENTER OF MASS
30-INCH ROD
CONTAINMENT RING
ω
$\frac{R\omega}{2}$
ω
ω

Fig. 3-16 KINEMATICS OF ROD FAILURE (ASSUMING TWO EQUAL SEGMENTS)

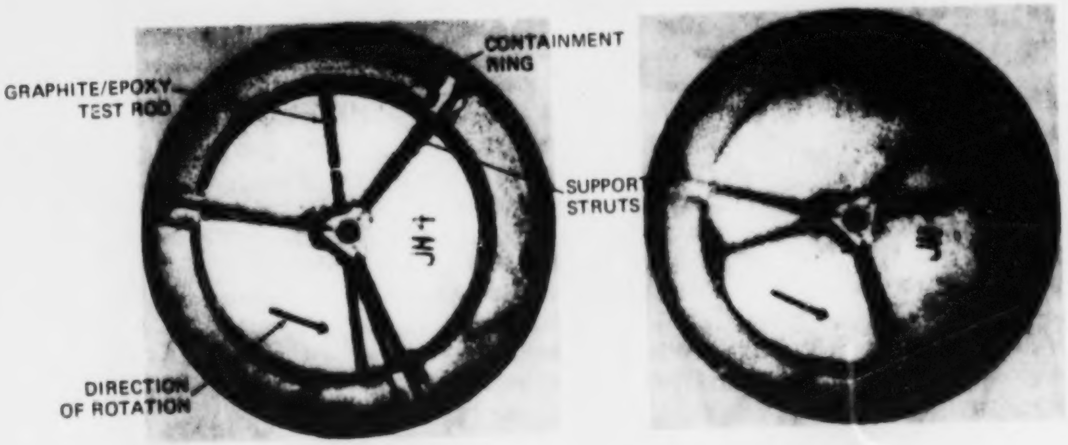
CONTAINMENT RING
GRAPHITE/EPOXY TEST ROD
SUPPORT STRUTS
DIRECTION OF ROTATION
JH-4

(a) PRETEST PHOTO

(b) TIME = + 41 μs

Fig. 3-17 PHOTOGRAPHS TAKEN BEFORE RUN JH-4 AND 7 TIMES AFTER FAILURE TRIPPED PHOTOGRAPHIC SYSTEM

Reproduced from best available copy.

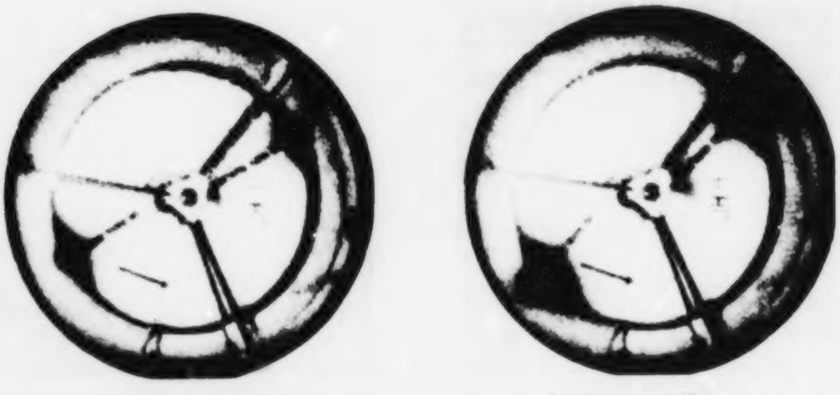

(c) TIME = + 123 µs

(d) TIME = + 205 µs

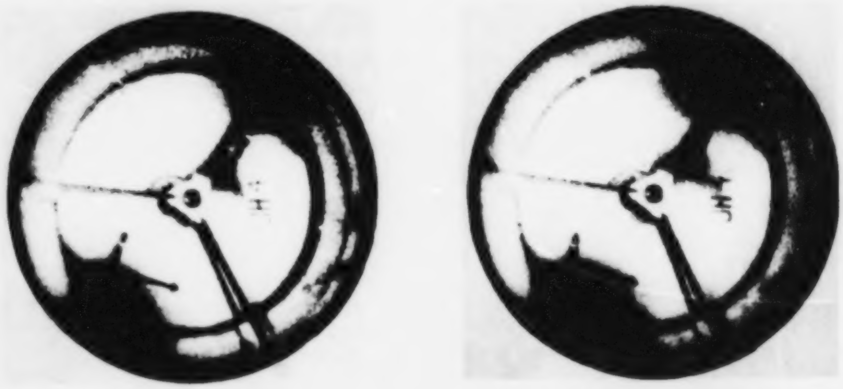

(e) TIME = + 287 µs

(f) TIME = + 369 µs

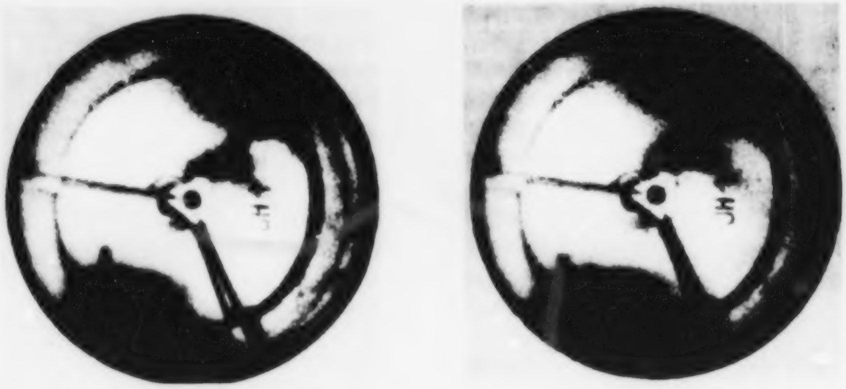

(g) TIME = + 451 µs

(h) TIME = + 533 µs

Fig. 3-17 (Cont'd) PHOTOGRAPHS TAKEN BEFORE RUN JH-4 AND 7 TIMES AFTER FAILURE TRIPPED PHOTOGRAPHIC SYSTEM

Reproduced from best available copy.

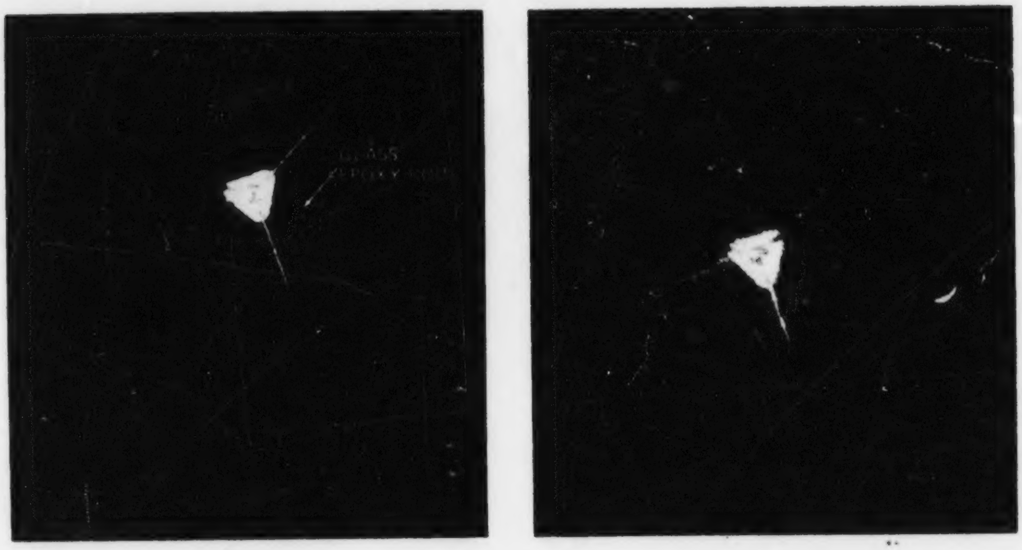

(a) PRETEST

(b) TIME = + 53 µs

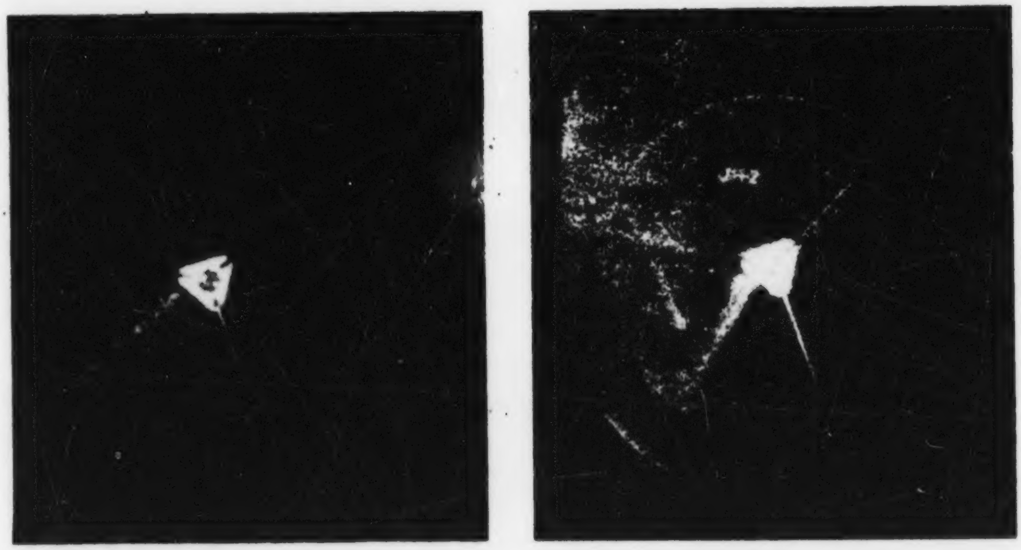

(c) TIME = + 159 µs

(d) TIME = + 265 µs

Fig. 3-18 PHOTOGRAPHS TAKEN BEFORE TEST JH-2 AND AT SEVEN INTERVALS FOLLOWING FAILURE OF S-GLASS/EPOXY ROD

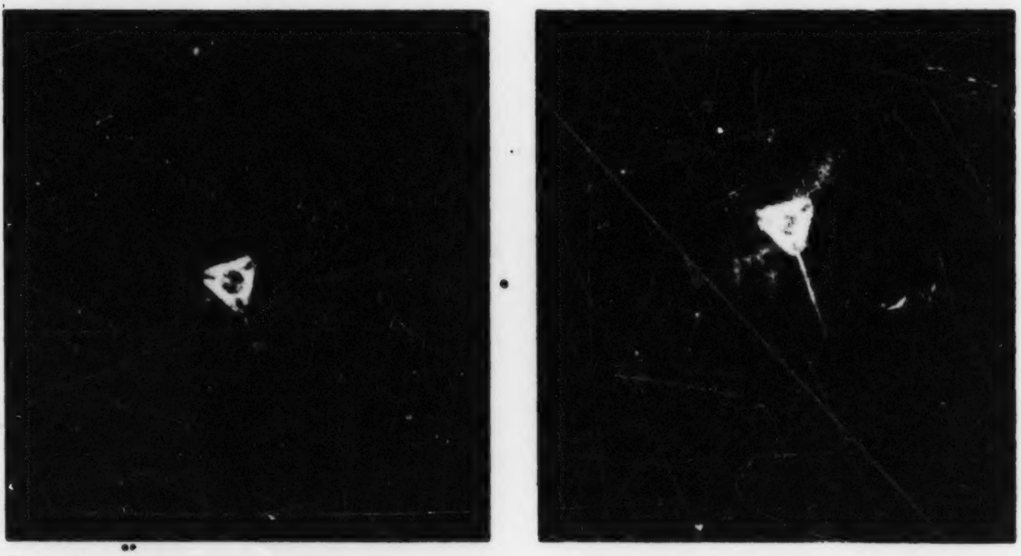

(e) TIME = + 371 μs

(f) TIME = + 476 μs

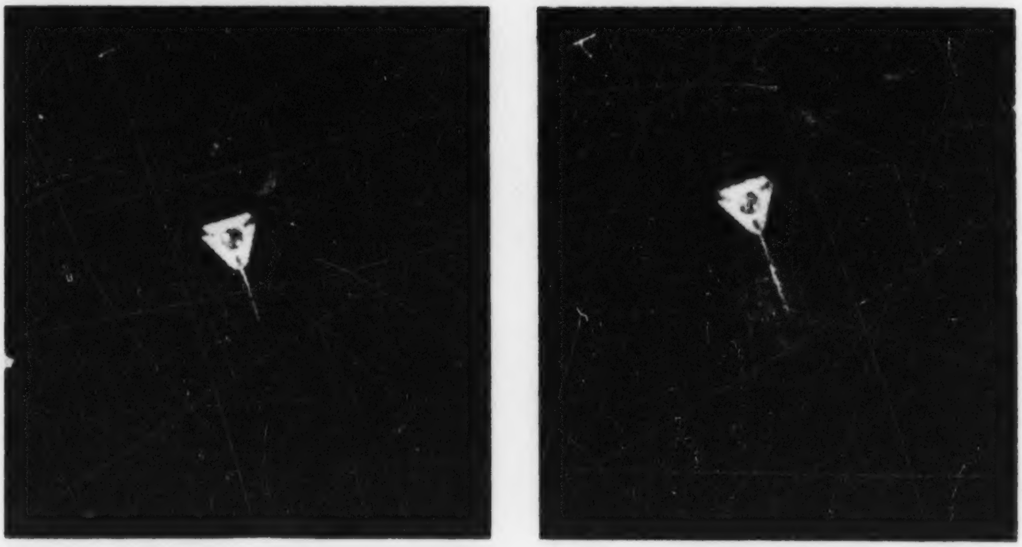

(g) TIME = + 586 μs

(h) TIME = + 795 μs

Fig. 3-18 (Cont'd) PHOTOGRAPHS TAKEN BEFORE TEST JH-2 AND AT SEVEN INTERVALS FOLLOWING FAILURE OF S-GLASS/EPOXY ROD or until a sufficiently-resistive force field develops (containment) (Ref. 22). In all tests at NAPTC the rods were completely destroyed, as shown in Figs. 3-12 and -13. This is again contrasted with typical disk failures in which no appreciable damage occurs to the large disk segments while the rings are being severely distorted or ruptured. In fact, the relative rates of rod destruction and containment ring response limit the energy that can be transferred from the rod to the ring. Techniques are available to study the energy transfer by means of a computer program (Ref. 23), but this is beyond the scope of the current project.

3.3.5 ENERGY ABSORBED BY THE CONTAINMENT RING

The graphite/epoxy Test JH-4, shown in Fig. 3-17, resulted in a very regular pattern in the deformation of the 3/8-inch-thick steel ring, as shown in Fig. 3-19. Since the deformed shape was nearly a perfect ellipse, it appeared that the theory of plasticity might be used to estimate the energy dissipated during the deformation process. There was no detectable stretching of the nominal 31.38-inch-diameter mid-plane of the ring, only bending deformation. The deformed major axis measured 34.62 inches, and the minor axis measured 28.62 inches. There was very little bulging of the ring in the depth direction at the points of impact, and the sides remained essentially cylindrical. One of the impact points is shown in Fig. 3-20.

Let us assume that the deformed ring is elliptical and that the mid-plane can be defined by the polar coordinate equation:

$$r^2 = a^2 b^2/(a^2 \sin^2 \theta + b^2 \cos^2 \theta) , \qquad (3\text{-}3)$$

where a = 14.31 inches, and b = 17.31 inches. The radius of curvature r_D is defined by:

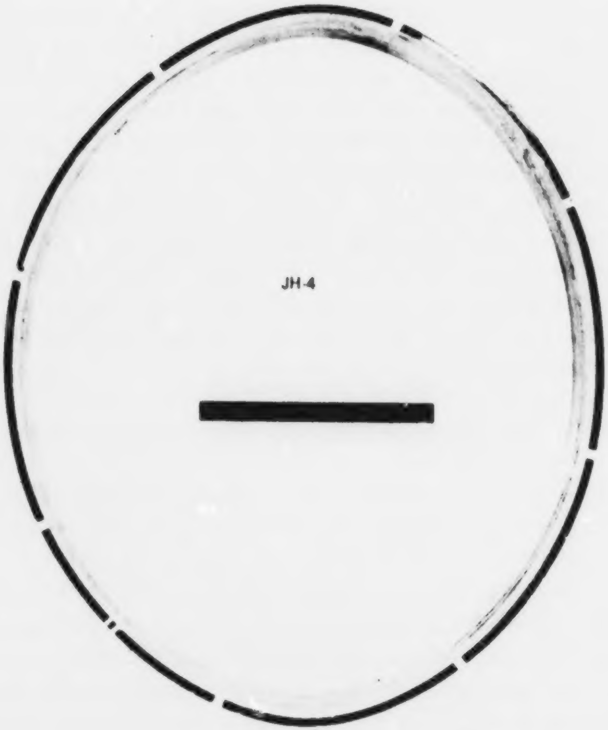

Fig. 3-19 DEFORMATION ON OF 3/8-INCH-THICK STEEL RING; ROD ENERGY OF 820 000 IN-LB

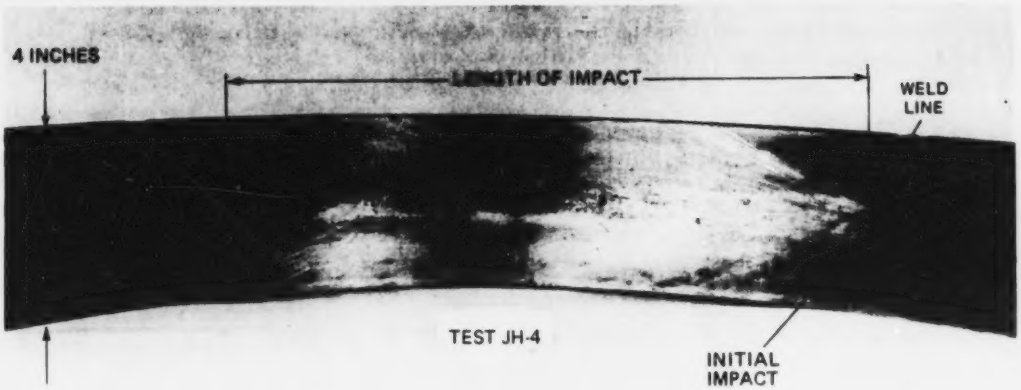
4 INCHES
LENGTH OF IMPACT
WELD LINE
TEST JH-4
INITIAL IMPACT

Fig. 3-20 ONE OF THE IMPACT ARCS ON THE CONTAINMENT RING

$$r_D = \frac{[r^2 + (dr/d\theta)^2]^{3/2}}{r^2 + 2\,(dr/d\theta)^2 - r\,(d^2r/d\theta^2)} \,. \qquad (3\text{-}4)$$

Figure 3-21 compares r_D, calculated from these equations, with the original radius of the undeformed ring. In the theories of plasticity and limit analysis (Ref. 24) the energy dissipated internally during the permanent deformation of a beam by bending is assumed to be:

$$W_i = \int_S (\text{Change in curvature})\; M_o \, ds \,, \qquad (3\text{-}5)$$

where M_o is the "yield moment" of a "fully-plastic" beam (i.e., the stresses in the beam do not vary linearly across the depth of the beam as assumed in elastic theory, but take on limit or yield values of tension and compression on each side of the neutral axis). The yield moment is determined from

$$M_o = bt^2\sigma_o/4 \,, \qquad (3\text{-}6)$$

where b is the width of the beam, t is the thickness, and σ_o is the limit or yield stress of the material.

The rings were made from AISI C1018 cold drawn steel plates whose static σ_o is 54 000 psi. Dynamic straining usually results in some increase in yield strength, though this type of steel should not be particularly strain-rate sensitive. For $b = 4$ inches and $t = 3/8$ inch the static yield moment given by Eq. (3-6) is 7600 in-lb.

The curvature is defined as the reciprocal of the radius of curvature, and Fig. 3-21 includes a plot of the absolute value of change in curvature of the ring. Integrating the area under this curve and multiplying by 4 for the other quadrants,

$$\int_S (\Delta\ \text{Curvature})\, ds = 1.25 \left(\frac{\text{rad}}{\text{in}}\right) (\text{in}) \,. \qquad (3\text{-}7)$$

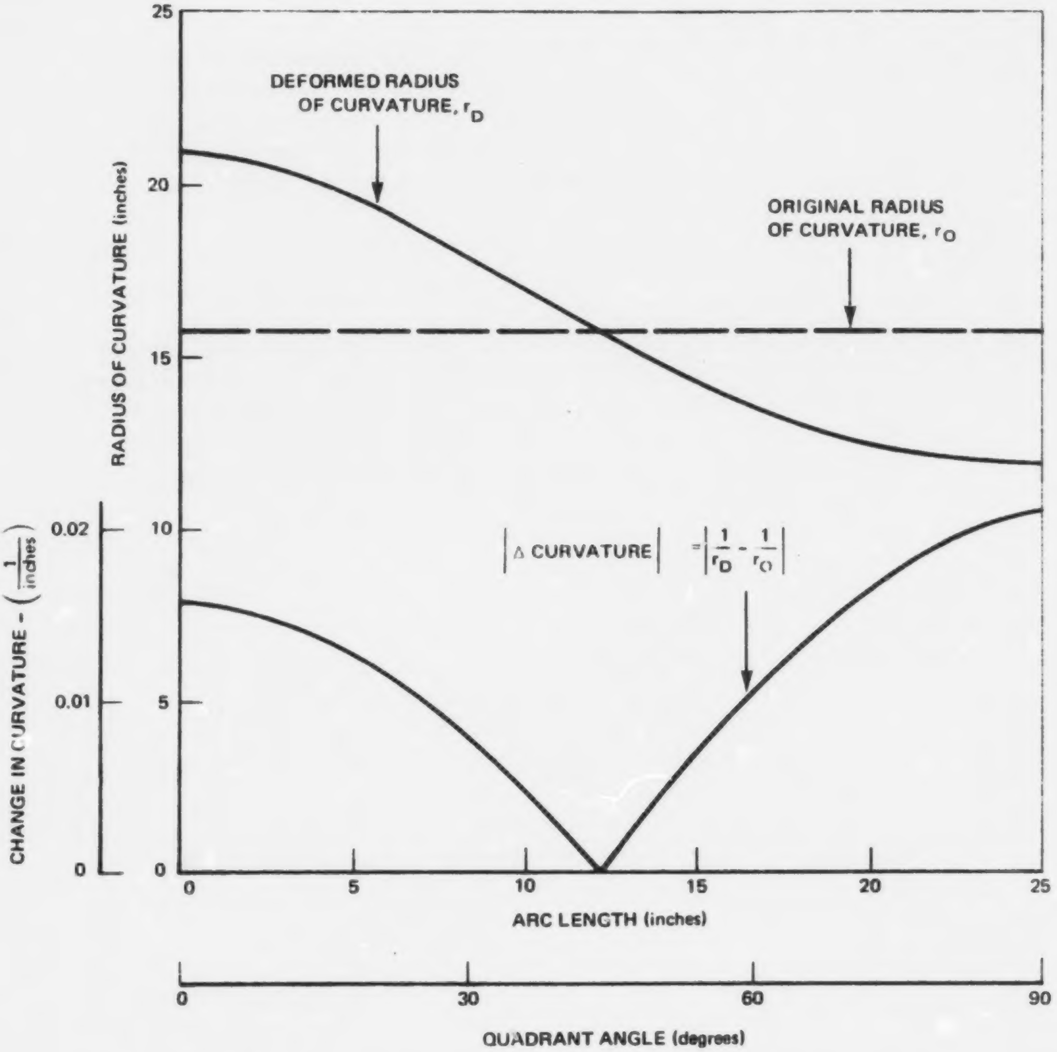

Fig. 3-21 RADIUS OF CURVATURE AND CHANGE IN CURVATURE FOR 3/8-INCH-THICK RING (JH-4 TEST)

The energy dissipated internally during this plastic deformation is, then

$$E_{i_{\text{ring}}} = 1.25\,(7600) = 9500 \text{ in-lb} . \qquad (3\text{-}8)$$

Undoubtedly there is residual elastic strain energy in the ring which has not been accounted for, and dynamic effects will increase the calculated values, but these increments should be small compared to the energy dissipated in the permanent deformation process. Also, the transverse bending energy at the points of impact has been neglected, but this too should be small, as evidenced by Fig. 3-20. The accuracy of the preceding assumptions could be verified experimentally by loading a similar ring at opposite points and measuring the force-deflection function required to produce a permanent deformation of this type. However, time did not permit this in the current program.

Another approach is to assume that a complete transfer of momentum occurs when the rod strikes the ring, an approach often used in ballistic studies. A velocity profile of the ring is then assumed (Fig. 3-22) and the total momentum is used to determine the velocity values. (The assumed shape is often not too important as long as it satisfies the physical conditions of the problem.)

For the rod in Test JH-4 the momentum at failure was:

$$MV = \frac{WR\omega}{2g} = \frac{(0.99)\,(15)\,(2950)}{2(386)} = 57 \text{ lb-s} . \qquad (3\text{-}9)$$

The average velocity of the ring is 2/3 the maximum velocity, V_o. Therefore:

$$\frac{2}{3} V_o \left(\frac{W_{\text{ring}}}{g}\right) = 57 \text{ lb-s} , \qquad (3\text{-}10)$$

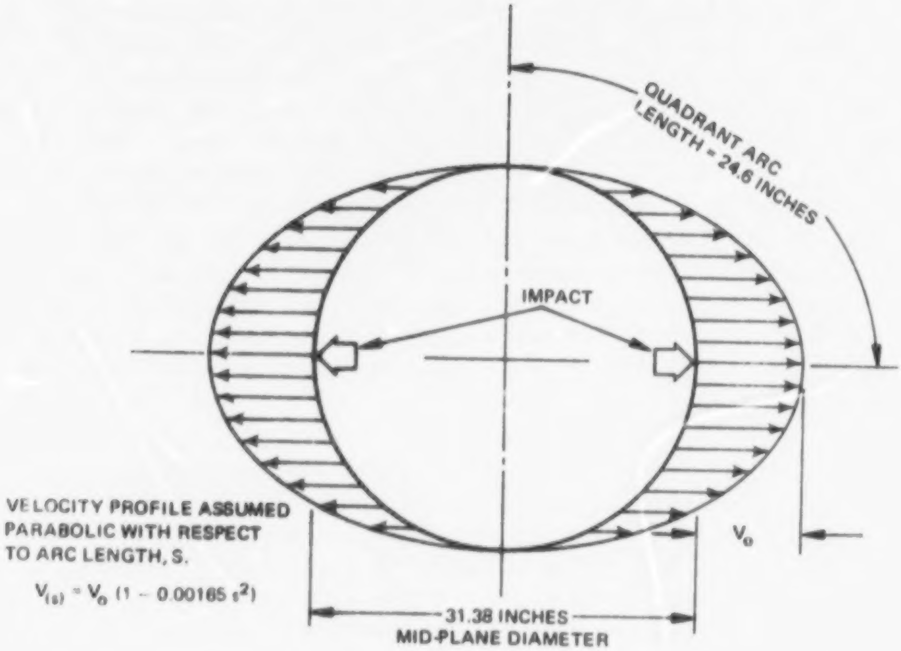
QUADRANT ARC
LENGTH = 24.6 INCHES
IMPACT
VELOCITY PROFILE ASSUMED
PARABOLIC WITH RESPECT
TO ARC LENGTH, S.
$V_{(s)} = V_0 (1 - 0.00165 s^2)$
V_0
31.38 INCHES
MID-PLANE DIAMETER

Fig. 3.22 ASSUMED INITIAL VELOCITY PROFILE OF RING FOR USE IN MOMENTUM TRANSFER ANALYSIS

which yields V = 782 in/s. The assumed velocity profile (see Fig. 3-22) is:

$$V = 782\,(1 - 0.00165\,s^2)\,. \qquad (3\text{-}11)$$

The energy in the ring at the moment of impact is:

$$E_{i_{ring}} = \frac{1}{2}\int_{Vol} V^2 dm = 4 \times \frac{1}{2} \times \frac{bt\rho'}{g}\int_0^{24.6} V^2 ds\,, \qquad (3\text{-}12)$$

Substituting b = 4 inches, t = 3/8 inch, ρ' = 0.268 lb/in^3, g = 386 in/s^2, and Eq. (3-11) for V, we find $E_{i_{ring}}$ = 18 000 in-lb.

Since the maximum kinetic energy of the rod at failure was 820 000 in-lb, the foregoing two estimates of $E_{i_{ring}}$ represent only 1.2 and 2.2% of this rod energy, respectively. Thus, only a small fraction of the energy of the composite rod was transferred to the steel ring.

The momentum-transfer method shows that the energy transferred to the ring is dependent on the relative mass values of the rod and ring. Therefore, the very low fraction of energy transferred may not hold as the mass of the rod increases relative to the mass of the ring. (This is somewhat borne out by Test JH-3 in which a graphite/epoxy rod with comparable mass and energy impacted a 1/4-inch-thick ring (1/3 less mass) to produce much larger deformations, as shown in Fig. 3-14b.) However, the momentum-transfer method does not include the pulverizing process, which can account for a significant portion of the energy absorption for brittle materials (Ref. 25). The preferred approach would be to use the computer program mentioned earlier (Ref. 23), with velocity and deformation data measured in further experimental studies.

3.4 CONCLUSIONS

The small-scale, materials test program in the APL spin chamber demonstrated the principle of rotating filamentary and composite materials to achieve high specific energy storage. It was observed that these materials were likely to have a desirable mode of failure. The small-scale test chamber is a versatile arrangement that will continue to be useful in evaluating materials for use in composite flywheels.

The test program at NAPTC was successful in demonstrating the use of a secondary vacuum chamber to obtain required operating pressures (though some work needs to be done with the drive shaft seal), the use of a dual bearing support to avoid rod instability, the use of high-speed photography to observe the mode of rod failure, and the effect of composite rods striking steel containment rings.

For the first set of laminated, wheel-cut, composite bars ever made by the supplier in these sizes, the best demonstrated ultimate specific energy storage levels were 28 W-h/lb for 3/4-pound, 30-inch-long S-glass/epoxy bars and 26.5 W-h/lb for 1-pound, 30-inch-long graphite/epoxy bars. The calculated stresses at failure were only 79 and 69%, respectively, of the values expected by Hercules, who are confident that development and quality control in the manufacturing process will raise the performance of such bars above 30 W-h/lb.

The high-speed photography system at NAPTC showed that the composite rods did indeed fail in a manner that did minimum damage to the containment rings. The bars initially parted into two segments by failure very near the spin axis, and then each segment was pulverized within 0.7 ms by rubbing against the containment ring. This pulverization process was completed before ring deformation caused by energy transfer began. Subsequent approximate analysis of the deformed rings by two approaches – plastic deformation and momentum transfer –

revealed that 1.2 to 2.2% of the kinetic energy of the rod was transferred to the ring. This result, especially when combined with the prospect of a brush-type rotor configuration (two of which are described in Section 4.2), is most encouraging. It offers the hope of developing high-energy composite rotors that could be contained in the event of failure or vehicle accident. The writers judge that if the advantages seen for flywheel-only or flywheel-hybrid propulsion systems are ever adopted on an appreciable scale, this safety aspect alone may lead to the choice of composite-material flywheels as opposed to all-metal ones.

4. FLYWHEEL SYSTEM DESIGN CONSIDERATIONS AND PERFORMANCE

4.1 INTRODUCTION

The practical application of flywheel power in vehicle propulsion will entail the design, development, and integration of all of the components required in the energy storage system in such a way as to meet both the performance requirements and the constraints imposed by the vehicle and its missions. Design constraints will tend to lower the energy storage capacity of the flywheel system relative to the ultimate values, but the amount of degradation will be highly dependent upon the particular application. This section discusses the following major design considerations:

1. Rotor configuration and related material considerations, including preliminary theoretical (ultimate performance) analysis of four specific types of advanced rotor configurations that would take advantage of the properties of composite materials (supported by Appendixes A and B).

2. Effects of flywheel rotor speed, including effects on bearings, the need for an evacuated housing (supported by Appendix C), power losses, and rundown times.

3. Factors affecting the allowable stresses in composite-material flywheels, including cyclic and static fatigue and related problems, as well as the potential for improvements in materials that will offset and may eventually far outweigh these effects relative to the 32 W-h performance level that has been assumed in the system studies subsequently discussed in Section 5.

Preceding page blank

4. Vehicular installation, including an example illustration for a commuter car and a brief discussion of the gyroscopic torque problem with an example for a family car.

Section 5 presents further discussion of weight and volume considerations for the vehicles specified by OAP (commuter car, family car, van, and city bus), and particularly the effects of engine choice for hybrid systems on maximum allowable flywheel system weight, as well as powertrain installation, including the necessary continuously variable transmission (supported by Appendix D). Section 6 includes the description of a flywheel demonstration system, designed to establish operating parameters for an energy storage unit of usable size.

4.2 ROTOR CONFIGURATION AND MATERIAL CONSIDERATIONS

4.2.1 SIMPLE COMPARATIVE ILLUSTRATIONS OF THE SUPERFLYWHEEL CONCEPT

The simplest superflywheel rotor is a rod or bar composed of a high-strength, unidirectional composite material. Though the coefficient of specific energy storage of such a rotor is lower than that of a more conventional disk or rimmed flywheel, the ability to take advantage of the ultra-high-strength/density ratio of uniaxial composite materials more than offsets the geometric penalty. This point is demonstrated in Fig. 4-1.

In all cases the ultimate specific energy, E/W, is related to the ultimate specific strength (the ultimate-tensile-strength/density ratio σ/ρ') by a geometric coefficient K. The coefficients shown in Fig. 4-1 for the shaped disk and rod are not the truly optimal ones (see Appendix A) but represent configurations that can be fabricated easily. The values of relative specific strength assume that the biaxial stress patterns in the disks require the use of an isotropic material, such as steel or titanium,

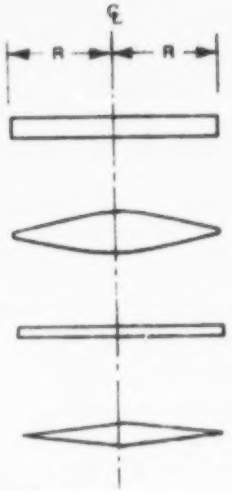

SHAPE	SPECIFIC ENERGY COEFFICIENT	RELATIVE SPECIFIC STRENGTH	RELATIVE SPECIFIC ENERGY
CONSTANT THICKNESS DISK	0.61	1[2]	1.0
SHAPED DISK	0.93[1]	1[2]	1.5
○ □ THIN ROD OR BAR	0.33	3.5[3]	1.9
⊠ THIN DOUBLE PYRAMID	0.45	3.5[3]	2.6

NOTES

1. THIS COEFFICIENT RELATES TO A SHAPED DISK WITH A HUB THICKNESS FOUR TIMES THE RIM THICKNESS. SEE APPENDIX A.3.
2. ASSUMES ISOTROPIC MATERIAL WITH $\sigma/\rho' = 1 \times 10^6$ INCHES (STEEL OR TITANIUM).
3. ASSUMES UNIDIRECTIONAL MATERIAL WITH $\sigma/\rho' = 3.5 \times 10^6$ INCHES (GRAPHITE OR S-GLASS COMPOSITES).

Fig. 4-1 SPECIFIC ENERGY COEFFICIENTS, RELATIVE SPECIFIC STRENGTHS, AND RELATIVE SPECIFIC ENERGIES FOR VARIOUS FLYWHEEL SHAPES

while the uniaxial rod stresses will permit the use of boron, graphite, or glass composites. The performance of these rotors in terms of ultimate specific energy storage (normalized with respect to the constant-thickness disk) shows the rods to be superior to the disks – which is the essence of the superflywheel concept. However, as discussed in Section 3. 3. 4, another virtue of rotors made of composite materials – an inherent ability to absorb the major portion of failure energy by microfracture (and possibly vaporization) of the matrix material and progressive fracturing of the brittle filaments – may prove even more important.

4. 2. 2 TRANSVERSE STRESSES IN BAR ROTORS MADE OF UNIDIRECTIONAL COMPOSITE MATERIAL

Since the superflywheel is assumed to be encased in a container evacuated to approximately 10^{-3} torr, flywheel subsystem weight and volume will also include the weights of the case, shaft, seals, and bearings. To minimize weight of these items, one wants the rotor to be relatively compact. Thus, one wishes to increase the lateral dimensions of a bar-like rotor to improve the energy packaging efficiency, E/V. However, a rotating bar of appreciable width will be in a state of biaxial stress because of the component of the centrifugal forces acting normal to the bar centerline, and the transverse properties of the composite material must be considered in determining the energy storage capability.

The rotating bar is assumed to be in a state of plane stress (no normal stresses perpendicular to the spin plane), and the equations of elasticity have been formulated for an anisotropic material (see Appendix A. 2). The numerical method of collocation (see Appendix A. 2) was used to obtain a solution to the governing equations and thence the stresses acting in the bar[1].

---

[1] During the progress of this contract, another project within APL was developing a capability to use the NASTRAN program, a multipurpose, master structural analysis program sponsored by the National Aeronautics and Space

When stresses exist in more than one direction it is usually necessary to use some form of interaction relationship in order to use available materials test data to predict structural failure because the majority of these data are developed for a single state of stress. An often used relationship is the Hill (Ref. 27) (or generalized von Mises) criterion, which employs ratios of the actual longitudinal, transverse, and shearing stresses to the allowable single-stress test data of these material properties. This criterion was used to predict the rotational speed ω at which failure of the bar would occur. Figure 4-2 shows the resulting specific energy degradation factor versus the bar half-width/radius ratio T/R for three candidate composite materials. Here E/W is referenced to the thin-rod, uniaxial stress value, $[E/W]_o$, for each material. The absolute value of E/W for any T/R can be determined by multiplying the appropriate $[E/W]_o$ by the degradation factor. Therefore, the graphite/epoxy composite (Hercules 2002T system) is the superior performer over the range of aspect ratios shown, though glass and boron composites are near-equals for thin-rods. As an example of the effect of the transverse stresses, a graphite/epoxy composite bar with width-to-length ratio of 0.10 will have an ultimate specific energy equal to ~ 94% of that of a thin rod of the same material.

This analysis has considered only unidirectional composite materials. Since the allowable transverse stress for a material of this type is only a fraction (~ 1/17 for graphite/epoxy and ~ 1/35 for S-glass epoxy) of the allowable longitudinal stress, a modest number of cross or angle plies might increase the transverse strength of the laminate enough to overcome the attendant loss in

---

Agency. The bar flywheel was programmed as a trial problem by members of the other project, and the resulting stresses were essentially identical to those obtained by the numerical method of collocation. The NASTRAN solution also develops a displacement function at all points in the bar, and these data are referred to in later sections on the design of the rotor hub.

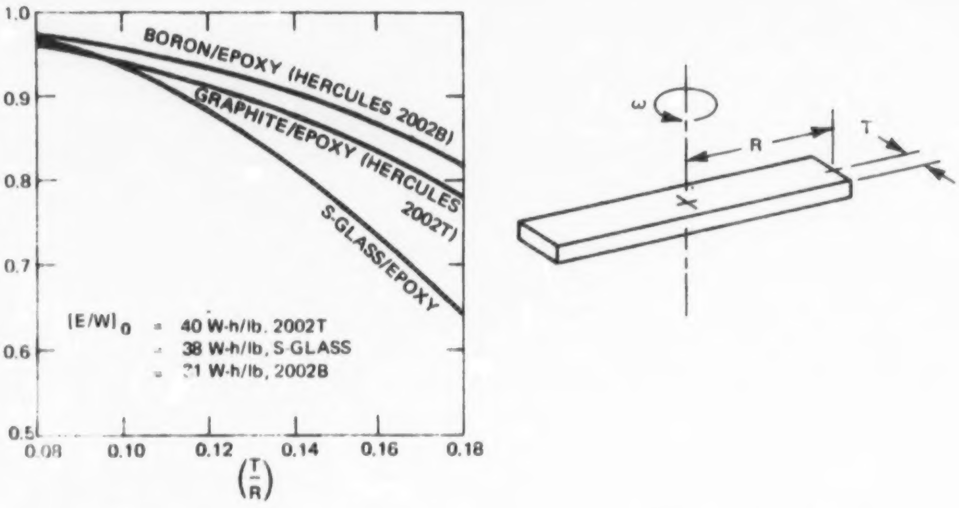

Fig. 4-2 SPECIFIC ENERGY DEGRADATION CAUSED BY BIAXIAL STRESS FIELD IN WIDER BARS

longitudinal efficiency. Since it has also been shown that angle and/or cross plies improve the material resistance to fatigue (Ref. 26), this seems to be a particularly fruitful path to reduce the specific energy degradation while improving volumetric efficiency.

4.2.3 THE CIRCULAR BRUSH ROTOR

Another concept with theoretically improved energy packaging efficiency (E/V) is depicted in Fig. 4-3. The "circular brush" rotor comprises a large number of individual elements mounted in a hub in a manner that allows the free length of each element to lie along a radial line from the spin center. The elements can be glass or graphite/epoxy composite rods that are pultruded to avoid fiber misalignment and fiber damage at the surface, or they can be individual filaments such as boron or chemically-strengthened bulk glass rods. The relatively small size of the elements and the controlled processing techniques available for this type of element should result in maximum allowable strengths. The elements are imbedded into the hub only as far as is required to develop a bond strength sufficient to transfer the centrifugal forces to the hub. The hub can be made of high-strength steel, or possibly of layers of composite material that sandwich the layers of rods. The hub diameter must be limited so that the combination of loads transmitted from the brush and the inertial body forces within the hub do not over-stress it.

The equations for maximum rod stress, rotor energy, rotor specific energy, and energy packaging efficiency follow. The subscripts R and H refer to rod and hub values, respectively. The parameter α is the ratio of hub diameter to brush diameter, while β is the ratio of the sum of the rod cross-sectional areas to the cross-sectional area of the perimeter of the hub (an index of the brush element spacing at the hub interface). The equations assume that the maximum stress in the rods governs the rotation speed, which is usually true for $\alpha \leq 1/3$.

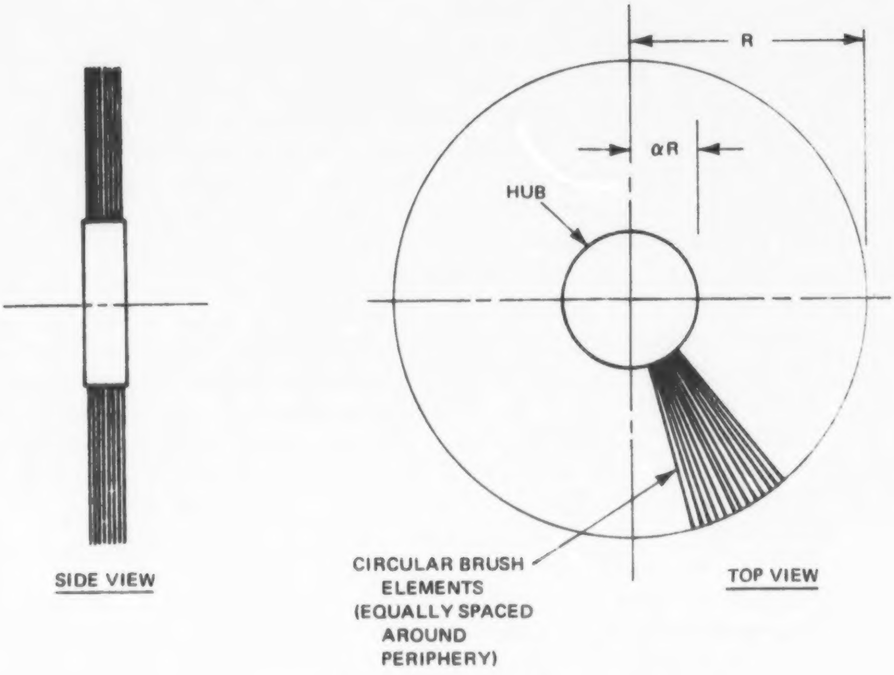
R
αR
HUB
SIDE VIEW
CIRCULAR BRUSH ELEMENTS (EQUALLY SPACED AROUND PERIPHERY)
TOP VIEW

Fig. 4-3 CIRCULAR BRUSH CONFIGURATION

The equation for the stresses at the root of each rod is similar to Eq. (3-2) for a simple rod, except that it is modified to account for the hub radius.

$$\sigma_R = \frac{\rho'_R(1 - \alpha^2)R^2\omega^2}{2g} \qquad (4\text{-}1)$$

The stored energy in the brush flywheel is the product of one-half the moment of inertia of the hub and elements (taken about the spin center) and the square of the rotation rate.

$$E = \frac{\pi R^4\omega^2}{12g}\left[4\rho'\beta\alpha(1 - \alpha^3) + 3\rho'_H\alpha^4\right] \qquad (4\text{-}2)$$

The specific energy (E/W) and the energy packaging efficiency (E/V) can then be formulated by combining the weight and volume equations of the brush rotor with Eq. (4-2), and using Eq. (4-1) to put them in terms of the rod σ/ρ' ratio.

$$\frac{E}{W} = \frac{\sigma_R}{6\rho'_R(1 - \alpha^2)}\,\frac{4\beta\rho'_R(1 - \alpha^3) + 3\rho'_H\alpha^3}{2\beta\rho'_R(1 - \alpha) + \rho'_H\alpha}\,; \qquad (4\text{-}3)$$

$$\frac{E}{V} = \frac{\sigma_R}{6\rho'_R(1 - \alpha^2)}\left[4\rho'_R\beta\alpha(1 - \alpha^3) + 3\rho'_H\alpha^4\right]. \qquad (4\text{-}4)$$

The above formulations include the energy and the weight of the hub. It should be noted that these equations include the effect of hub weight for the circular brush configuration, whereas estimates for the other types of rotor configurations discussed here in Section 4 have neglected hub weight. Therefore, relative comparisons presented later will be unfair to the circular brush to some degree, even though its hub will probably be heavier than the hub of a bar, fanned brush, or composite disk rotor.

Table 4-1 presents values of ultimate specific energy and energy packaging density as a function of rotor geometry. For reference, a value of $\beta = 0.20$ is equivalent to rods spaced in a square pattern 2 diameters on center; $\beta = 0.35$, a 1.5-diameter spacing; and $\beta = 0.50$, a 1.25-diameter spacing. E/W is a strong function of β, while E/V depends on both α and β.

Table 4-1

Theoretical Ultimate Performance for Circular Brush Rotors Using S-Glass/Epoxy Filaments and a Steel Hub[1]

Parameter	$\alpha = 0.2$			$\alpha = 0.3$		
	$\beta = 0.20$	0.35	0.50	0.20	0.35	0.50
E/W (W-h/lb)	17.9	24.4	29.0	17.6	24.0	28.1
E/V (kW-h/ft^3)	0.50	0.84	1.18	0.97	1.49	2.01

[1] Assumptions: The small-diameter, pultruded filaments have $\sigma_{ultimate} = 300$ ksi and $\rho' = 0.075$ lb/in^3; hub stresses do not control rotor speed.

Aside from an improvement in theoretical energy packaging density relative to a bar-type rotor, the circular brush rotor offers two other advantages: (a) it should be feasible, if required, to gimbal a steel hub at its connection to the shaft, permitting the vacuum case to pitch and roll about the stable rotor; and (b) in the event of a rotor failure or accident, the individual rods could fail successively and distribute their energy over the entire containment case, which should permit a lighter containment structure.

4.2.4 RADIALLY-FANNED BRUSH ROTOR

This configuration is shown in Fig. 4-4.[1] The elements are continuous from one side of the hub to the

---

[1] A straight element, brush-type rotor was originally considered, but an analysis showed that bending stresses in the rods were too high.

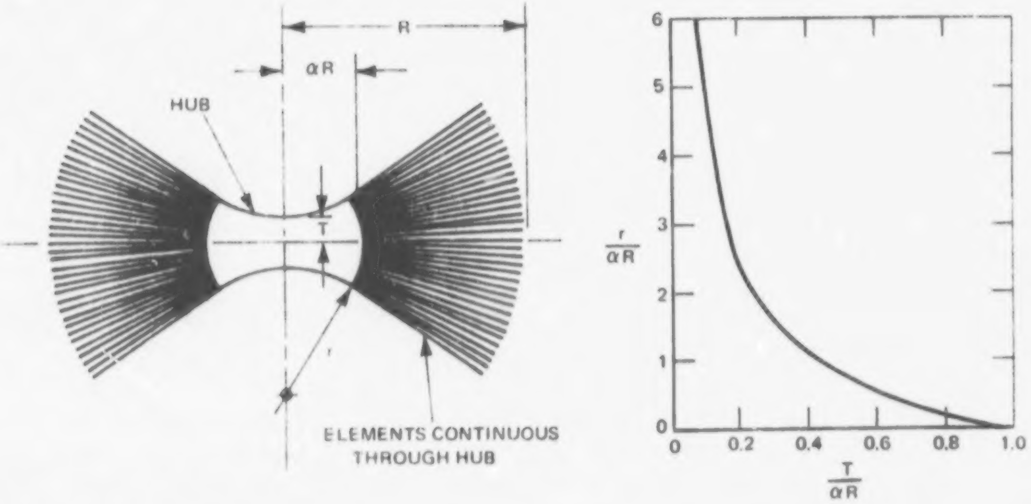
R
αR
HUB
T
r
ELEMENTS CONTINUOUS
THROUGH HUB
6
5
4
3
2
1
0
$\frac{r}{\alpha R}$
0
0.2
0.4
0.6
0.8
1.0
$\frac{T}{\alpha R}$

Fig. 4-4 RADIALLY FANNED BRUSH ROTOR

other, with balancing longitudinal components of centrifugal force. The transverse components of centrifugal force must be reacted through the hub structure. The elements are held in the radially-fanned configuration by a potting adhesive (such as epoxy) whose strength is sufficient to transfer the normal components of force acting on the elements.

The stress in the free-standing portion of an element is pure tension; however, in the curved portion a bending stress also exists and is additive to the tensile stress. The resulting maximum stress in an element, which controls the allowable speed of the rotor, is:

$$\sigma_{max} = \underbrace{\frac{\rho' R^2 \omega^2}{2g}}_{\text{tensile}} + \underbrace{\frac{E_m d}{2r}}_{\text{bending}} \tag{4-5}$$

where d is the element diameter, r is its radius of curvature, and E_m is its elastic modulus.

To achieve the radial alignment of the outermost element at the edge of the hub, the hub radius of curvature, r, becomes a direct function of the hub length, $2\alpha R$, and width, 2T, as shown in Fig. 4-4. Thus, the maximum operating speed (determined from Eq. (4-5)) and the specific energy are related to the rotor width and packaging efficiency in a manner similar to the bar rotor. Neglecting the weight and energy of the hub and the potting material, the energy per unit thickness of the brush is:

$$\frac{E}{t} = \sim (0.91) \frac{2R^3 \omega^2 T \rho'}{3g} , \tag{4-6}$$

where T is the half-width (transverse direction) of the hub at the spin axis. The factor 0.91 assumes a dense rod packing arrangement, and the energy formulation neglects rod curvature. In terms of geometric parameters, the specific energy is the same as for a thin rod,

$$\frac{E}{W} = \frac{R^2 \omega^2}{6g} \; . \qquad (4\text{-}7)$$

However, in terms of materials properties the effect of bending stresses modifies the thin rod values according to

$$\frac{E}{W} = \frac{\left(\sigma - \frac{E_m}{2r}\right)}{3\rho'} \qquad (4\text{-}8)$$

The energy packaging density is given by:

$$\frac{E}{V} = (0.91) \left(\frac{4}{3\pi}\right) \left(\sigma - \frac{E_m}{2r}\right) \left(\frac{T}{R}\right) \; . \qquad (4\text{-}9)$$

The specific energy is shown in Fig. 4-5 as a function of brush width-to-length ratio for four different rotor configurations. All rotors have a 30-inch spin diameter ($R = 15$ inches) and have a 12-inch-long hub ($\alpha = 0.4$). Results are given for a graphite/epoxy brush with 0.100-inch-diameter rods and S-glass/epoxy brushes with rods of three different diameters. The effect of the elastic modulus of the rod is clearly shown by the rapid drop-off in specific energy of the graphite/epoxy rod ($E_m = 21.5 \times 10^6$ psi) when compared to the S-glass/epoxy rod of the same diameter ($E_m = 8 \times 10^6$ psi). Other things being equal, a low-modulus material and small-diameter elements are desirable for the radially-fanned brush application. Even with the small rod diameters, the energy storage capacity drops off sharply as the geometric limit ($T/R \rightarrow \alpha$) is approached. Nevertheless, the energy degradation with increasing width is not as severe as for the wide bar.

Figure 4-6 shows the effect of the hub length/rotor diameter ratio, α, on the energy functions. The longer hub results in a 50% improvement in energy packaging density over the shorter one. It must be remembered,

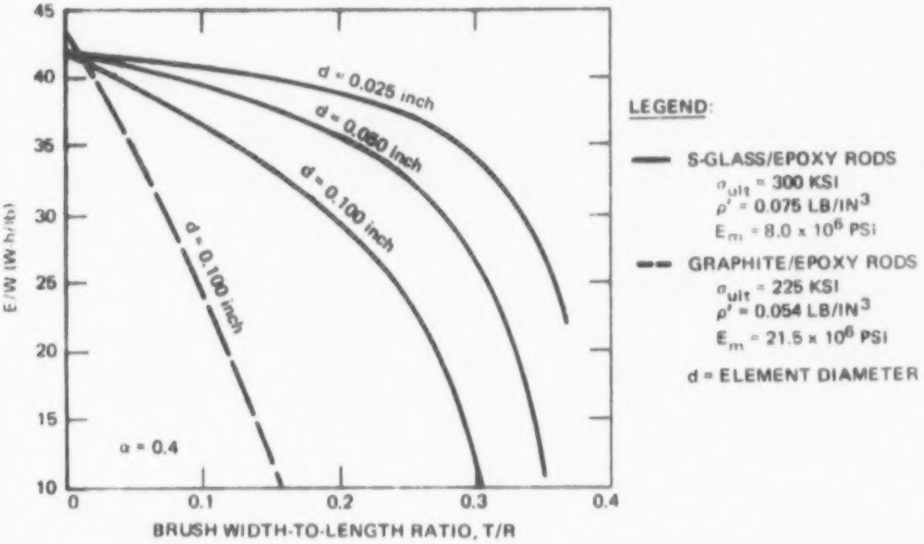

Fig 4-5 EFFECTS OF ROTOR GEOMETRY AND MATERIAL PROPERTIES ON SPECIFIC ENERGY IN A RADIALLY-FANNED BRUSH ROTOR

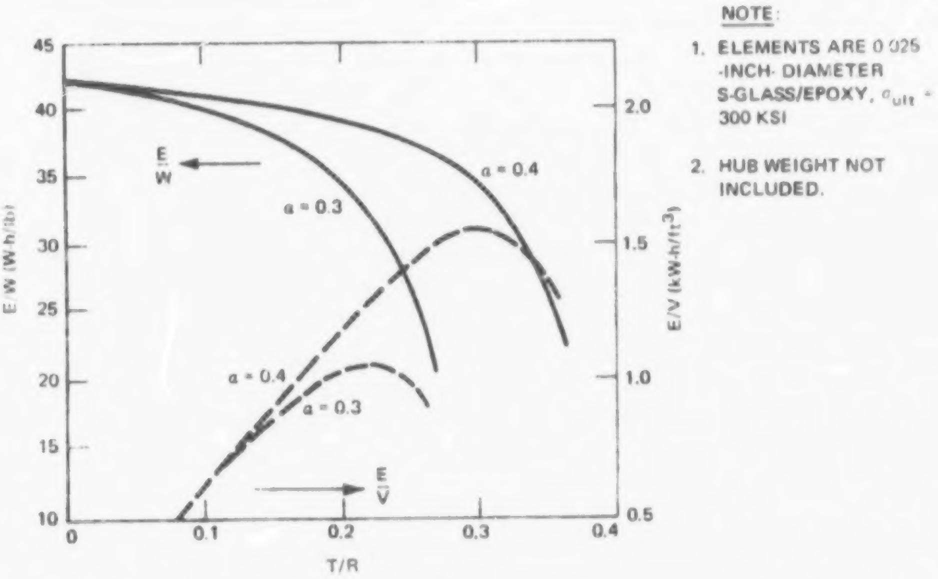

Fig. 4-6 SPECIFIC ENERGY AND ENERGY PACKAGING DENSITY VERSUS T/R FOR RADIALLY-FANNED BRUSH ROTORS OF S-GLASS/EPOXY ELEMENTS

however, that the weight of the hub and potting material have not been included in this analysis, and the increase shown would certainly diminish in an absolute comparison.

The outer elements, with their higher portions of bending stress, control the speed (and energy) of the rotor. It should be possible to shorten them to reduce the pure tension portion of their stress. In fact, the lengths of all of the rods could be adjusted so that their combined bending plus axial stresses would be equal. This would reduce the moment of inertia of the rotor but would allow higher operating speeds; it is likely that shaping of this type would result in some improvements in E/W for the higher values of T/R.

4.2.5 A LAMINATED COMPOSITE DISK

In Section 4.2.1 the geometric coefficients of specific energy were discussed, and it was pointed out that the biaxial state of stress in disk rotors requires the use of an isotropic material. By the very nature of the manufacturing process, composite laminae are nonisotropic, however they can be oriented in patterns to produce laminates whose properties are theoretically independent of direction for plane stress applications. Composite laminates of this type are referred to as quasi-isotropic, and the lamina orientation patterns are usually +60/0/-60 or +90/+45/0/-45 degrees. (Any pattern with three or more equally spaced angles of orientation will give the same result by the method of analysis used, see Appendix B.) The strength of such a laminate is only a fraction of the unidirectional strength of the reinforced material, but the biaxial stress capability may qualify it for use in a disk rotor where the geometric energy coefficient is nearly double that of a wide bar.

The finite-element, direct-stiffness method of structural analysis was used to evaluate the stresses and deformations in a constant thickness rotating disk, as discussed in Appendix B. The results of the analysis showed that all patterns except the 0/90 produced isotropic-case stress resultants with zero shear stress. The laminate properties of S-glass, graphite, and boron/epoxy were determined from uniaxial tensile test data in the 0° and 90° orientations. These base data were transformed and summed for different lamination patterns. The ultimate material stresses for the biaxial stress field were determined by the Hill criterion (Ref. 27), and these values were used to establish the maximum rotor speed and kinetic energy. The results are given in Table 4-2 for three composite materials.

Table 4-2

Theoretical Ultimate Performance of Disk Rotors Made from Quasi-Isotropic (+60/0/-60) Composite Laminate

Material			Laminate Properties		
Type	σ_1 (ksi)	ρ' (lb/in^3)	σ_u (ksi)	E/W (W-h/lb)	E/V (kW-h/ft^3)
Boron/Epoxy	212	0.075	112	30	3.7
Graphite/Epoxy	204	0.054	105	37	3.4
S-Glass/Epoxy	264	0.072	136	36	4.5

The theoretical results are extremely good with respect to both E/W and E/V. However, certain assumptions used in the analysis will require experimental verification: First, the method of transforming lamina properties and summing the values from all of the laminae to form average laminate properties is a rational and necessary approach because strength and deformation data are available only for principal laminae directions. Some researchers (Ref. 28) feel that the pseudo-isotropic allowable stress will be closer to 40% of the uniaxial value rather than the ~ 52% determined by the transformation.

Secondly, the validity of the interaction criterion becomes very important, since the radial and tangential stresses are equal at the center of the disk. Third, a practical method of attaching hubs to the disk will have to be developed. Finally, the ability of the matrix to resist the interlaminar shear forces that develop between the laminae will have to be demonstrated. Nevertheless, this approach offers the theoretical potential of achieving high specific energy storage within a compact unit, while providing the inherent safety of composite construction (though this, too, should be verified by experiment).

4.2.6 SUMMARY OF ENERGY CHARACTERISTICS

The superflywheel concept of using filamentary composite materials, stressed along the primary axis of the material, has been presented, and examples of three different configurations – the bar, the circular brush, and the radially-fanned brush – have been given. In addition, the use of pseudo-isotropic composite laminates in constant-thickness-disk flywheels has been investigated.

Figure 4-7 compares the specific energy (E/W) and energy packaging density (E/V) characteristics of these rotor configurations. As noted in Section 4.2.3, the E/W values for the circular brush include hub weight, whereas values for the other rotors (which would have somewhat lower hub weight fractions) do not include hub weight and should be lowered slightly for a fair comparison to the circular brush.

Bar rotor curves are shown for S-glass/epoxy and graphite/epoxy unidirectional composites. For these constant-cross-section bars, the results are nearly identical for the two materials, yielding a maximum E/V of ~ 0.65 kW-h/ft^3 at an E/W of 32 W-h/lb. This is the simplest of the superflywheel configurations and should be considered for use in applications where the volume constraints are not severe. Optimization of lamina orientation should improve these values a modest amount, while also improving

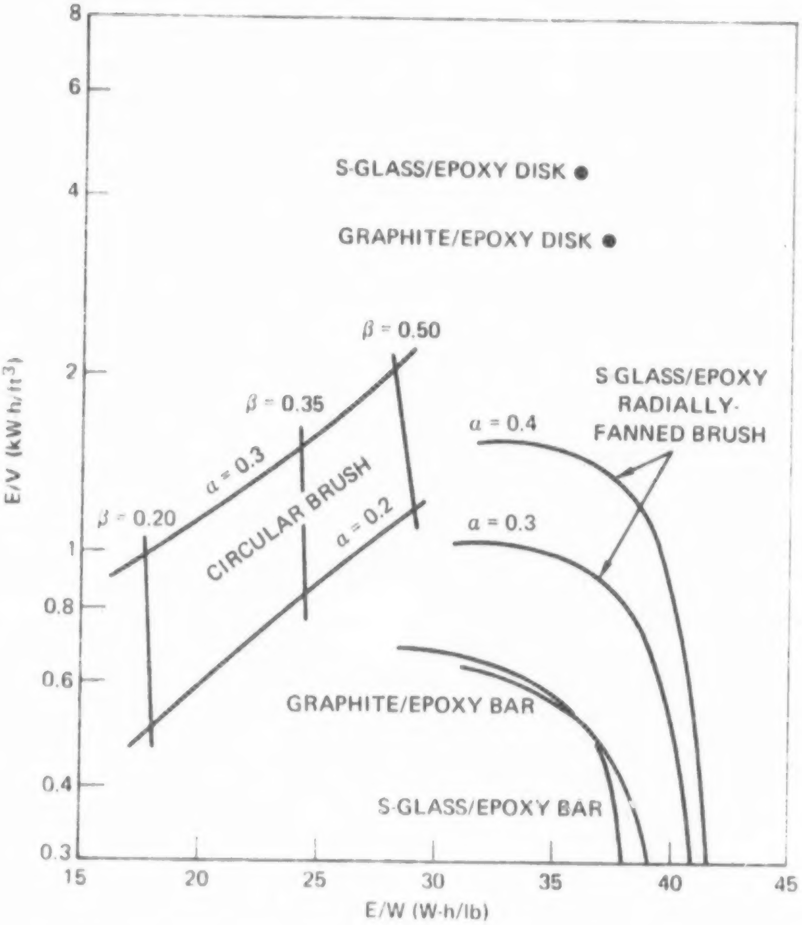

Fig. 4-7 SUMMARY OF ULTIMATE COMPOSITE MATERIAL FLYWHEEL CHARACTERISTICS FOR DIFFERENT ROTOR CONFIGURATIONS

resistance to fatigue, thereby partially compensating the probable derating needed for life and safety margin considerations, as discussed in following subsections.

The radially-fanned brush has similar, though apparently improved, characteristics. The higher E/W at low E/V is directly attributed to the assumption that small-diameter, pultruded rod elements will achieve higher strength than composite laminates.

However, it must be remembered that the hub and potting material weights are not included, and the hub length of the best example ($\alpha = 0.4$) is probably 30 to 50% longer than the hub of a wide bar rotor. Also, the hub must be strong enough to resist the transverse components of centrifugal force. Nevertheless, a brush rotor should achieve a 50 to 100% improvement in E/V over a bar rotor for a comparable E/W, and its containment requirements probably would be lower because of both timewise and spacewise distribution of failure energy of the thousands of rod elements. A disadvantage is the increased complexity of working with the many elements and fitting them in the hub. Analysis and experiments must be conducted to verify that the potting material will be capable of resisting the lateral force components and maintaining the fanned arrangement.

The circular brush is ideal for containment design because of its intrinsic ability to distribute energy to the absorbing structure. Its E/W is a strong function of the rod element spacing, and a spacing no more than 1.5 diameters ($\beta = 0.35$) is desirable. Though E/V improves with increased hub diameter, $\alpha = 0.3$ is an approximate limit to prevent overstressing the hub. An arrangement that gives E/V = 1.5 kW-h/ft^3 and E/W = 25 W-h/lb (including hub weight) appears reasonable. Whether this would prove superior to a fanned brush ($\alpha = 0.4$) would depend on the latter's hub weight.

Finally, the use of composite materials, formed into a quasi-isotropic, laminated, constant-thickness disk, may prove to be the most effective way of achieving high E/V and E/W while retaining the inherent safety of the composite materials. There are assumptions in the analysis techniques used, but knowledge of the behavior of these materials is steadily growing, and sufficient test data should soon be available to improve the estimates.

4.3 THE EFFECTS OF FLYWHEEL ROTOR SPEED

The flywheels being considered in this program have lower inertias but much higher rotational speeds than those of previous flywheel systems. Figure 4-8 shows tip speed versus specific energy for constant-thickness disk, thin rod, and circular brush configurations, and the tip-speed scale is equated to the speed of rotation for a 30-inch-diameter rotor. These curves merely relate tip speed ($R\omega$) and specific energy according to the equation:

$$\frac{E}{W} = \frac{K}{g}(R\omega)^2 , \tag{4-10}$$

where K is determined by the rotor configuration but not the strength of the materials. However, each configuration will be limited in E/W and tip speed by the materials used, and data points from Fig. 4-7 have been added to indicate the current limits of interest. The curve for a radially-fanned brush will lie between those of the bar and circular brush. It is probable that a disk rotor, with its higher coefficient of E/V, would be smaller in diameter than a bar, effectively increasing its relative rate of rotation over the values shown. Some of the effects of these speeds are discussed briefly in the following sections.

4.3.1 BEARINGS

The rotor bearings will be selected by the requirements of radial load capacity, operating speed, life, and minimum no-load friction losses. Operating speeds of interest will range between 20 000 and 40 000 rpm for the rotor sizes of interest. If we assume the use of bearings

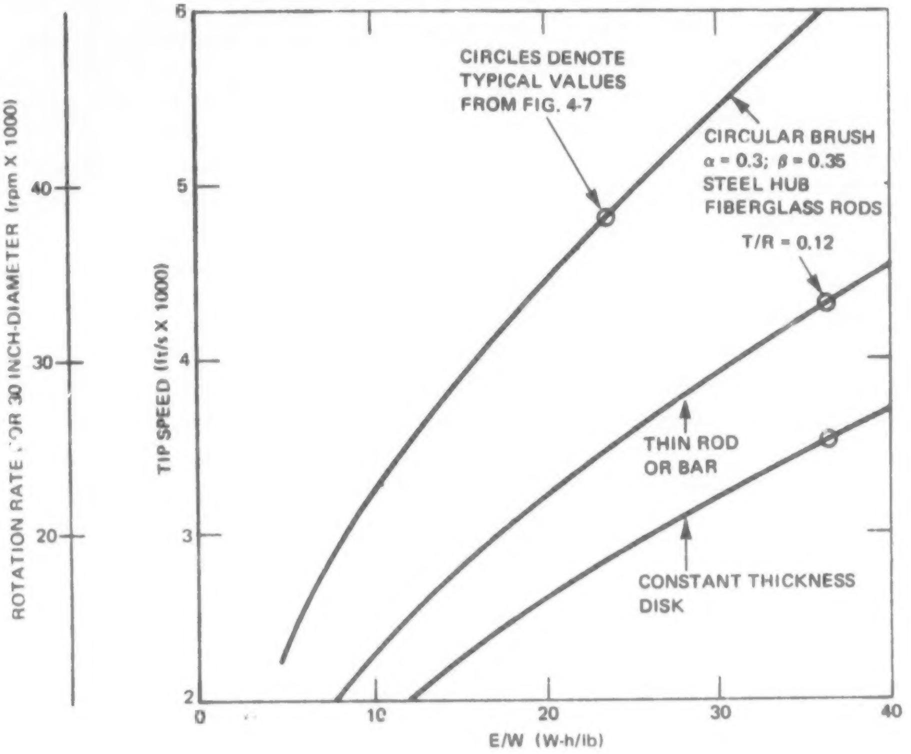

Fig. 4-8 EFFECT OF ROTOR CONFIGURATION ON TIP SPEED

whose bore dimension is 30 to 45 mm in diameter, the DN rating (bearing bore in millimeters times shaft speed in rpm) will be approximately 0.6 to 1.8 million.

Ball bearings in current production aircraft turbine engines operate in the DN range of 1.5 to 2.0 million, and engine designers anticipate that DN values for turbine bearings will have to increase to 2.5 to 3.0 million by 1980 (Ref. 29). Thus, ball bearings of the types used and to be used in modern turbo-machinery appear to be adequate for flywheel rotors from the standpoint of DN rating. The rated life of these bearings can exceed 10 000 hours at maximum rpm, particularly when the fatigue-resistant, high-temperature, M-50 tool steel is substituted for standard bearing material. Longer life would be expected when the speed continually varies between full and 1/2 or 1/4 speed. Tests at DN values between 1.25 and 1.5 million with bearings made from M-50 steel and using special lubricants demonstrated an operating life at least 14 times the AFBMA[1] rated life for similar bearings of standard material (Ref. 30). A DN value of 0.5 million is about the present limit for grease-lubricated bearings; therefore, a flywheel system will probably have some type of positive lubrication such as oil jet, spray, or mist lubrication.

The principal drawback to the use of ball bearings is that their no-load friction torque may reduce flywheel run-down times to undesirable levels, as shown in Section 4.3.3. An alternative is the use of air bearings with lower power losses. Their use, however, has often been limited by low load capacity and whirl instability. Tests have been conducted to determine the effect of air supply pressure ratio on bearing stiffness and fractional-frequency whirl of a rotor (Ref. 31), and additional experiments of this type would be required to determine similar parameters for a flywheel rotor with large gyroscopic effects. Another alternative to ball bearings is the magnetic fluid bearing (Ref. 7), which also incorporates the vacuum seals. These low-friction bearing systems, along with conventional mechanical bearings, must be designed to resist the intermittant radial loads resulting from flywheel gyroscopic torques (though Section 4.5.2 illustrates that this should not be a critical requirement for ball bearings).

---

[1] Antifriction Bearing Manufacturer's Association.

4.3.2 VACUUM SYSTEM

The high rotation rates and blunt aerodynamic configurations of most of the rotors dictates operating at air pressures between 10^{-3} and 10^{-2} torr (see Appendix C). From a reliability and maintenance standpoint it would be desirable to evacuate and seal the flywheel unit at the factory and never open it again (or possibly just once for a mid-life service at ~ 50 000 miles). After an initial period of outgassing, while the unit is being maintained under vacuum and a slightly elevated temperature at the factory, a case with no rotating-seal penetrations could be sealed and the system would maintain this pressure level (modest by modern aerospace vacuum system standards) for an acceptable period. This assumes an increase in the level of mass-produced vacuum system technology, however.

The problem is that, for most power transmission methods – and in order to place the bearings outside of the vacuum can to provide for active lubrication – we require a rotating vacuum seal(s). A seal that will satisfy all of the requirements of the system is not available on the market today. The Ferrofluidic Corporation produces rotary vacuum seals that use a magnetic fluid to resist the pressure differential (a unit of this type was used in the APL vacuum spin chamber, discussed in Section 3.2). Currently Ferrofluidics has units that operate at DN = 0.3 million for > 5000 hours, and they are working on DN = 1.0 million. These units require active water cooling, which would be undesirable for an operational flywheel system, but they feel there is a possibility of developing a high-thermal-conductivity magnetic fluid that would eliminate this requirement.

DN values for the seals also could be reduced by locally reducing the shaft diameter. Therefore, technology areas exist whereby rotor seal development for a prototype flywheel system, with active cooling and reduced seal life, appears to be possible. Friction drag of these magnetic fluid seals is relatively high, equal or greater than that of the bearings. This is a drawback for a flywheel system where the reduction of parasitic losses is very important. This type of seal, however, could be acceptable in a demonstration model.

The use of magnetic couplings, harmonic drives, or an electric motor inside the vacuum case would eliminate the need for rotating vacuum seals if the bearings could be placed inside the case. Again, the development of a combination fluid bearing and seal would be highly desirable. The use of a rubbing seal with an auxiliary vacuum pump to make up for leakage around the seal is also a possibility, though it increases system complexity and could present problems in spinning up the flywheel after long periods of vehicle storage because of the small pump displacement that would be used for economy.

4.3.3 POWER LOSSES AND RUN-DOWN TIMES

Windage losses are discussed in more detail in Appendix C, and an example is shown where a 0.68-kW-h bar-type flywheel would run down to one-half its maximum speed of 30 000 rpm in 49 hours, assuming an air atmosphere at 10^{-3} torr and no seal or bearing losses. This does not account for the swirling of the air inside of the can which will have the effect of reducing the relative velocity between the bar and the air and could double the value quoted above (i.e., ~ 4 days). The main purpose of this section is to investigate the mechanical power losses and their effect on run-down times, and therefore the windage losses will be neglected for the time being.

The no-load bearing friction torque T, in ft-lb, is given by Eq. (15) of the SKF Engineering Data Book (Ref. 32) as follows:

$$T = 1.183 \times 10^{-6} f_o (\nu N)^{2/3} d_m^3 , \qquad (4\text{-}11)$$

where

f_o = viscous torque factor,
ν = lubricant kinematic viscosity in centistokes at the operating temperature,
N = speed in rpm, and
d_m = bearing mean diameter in inches.

For single row, angular contact, ball bearings and oil mist lubrication the torque factor $f_o = 1.0$. This is the minimum value for this type of bearing; an oil bath system of lubrication results in a factor of 2.0.

Equation (4-11) can be expressed as:

$$T = K \omega^{2/3} , \qquad (4\text{-}12)$$

where ω = rotation rate in rad/s (= $2\pi N/60$), and for a flywheel rotor with n friction elements:

$$K = 5.33 \times 10^{-6} f_o n \nu^{2/3} d_m^3 . \qquad (4\text{-}13)$$

The rate of run-down caused by the friction elements is expressed as:

$$d\omega/dt = - T/I = - K\omega^{2/3}/I . \qquad (4\text{-}14)$$

Solving this equation for t, with the condition that $\omega = \omega_o$ at $t = 0$, we obtain:

$$t = 3I(\omega_o^{1/3} - \omega^{1/3})/K . \qquad (4\text{-}15)$$

The time (in seconds) to run-down to half speed ($\omega = \omega_o/2$):

$$\Delta t_{1/2} = 0.62\ I\omega_o^{1/3}/K\ . \qquad (4\text{-}16)$$

Since:

$$E_o = \frac{1}{2} I\omega_o^{2}\ ,$$

$$\Delta t_{1/2} = 1.24\ E_o/K\omega_o^{5/3}\ , \qquad (4\text{-}17)$$

where E_o is expressed in ft-lb.

If we now assume a rotor supported with two angular contact ball bearings ($n = 2$) of 30 mm bore ($d_m = 1.81$ inches) and lubricated with an oil mist ($f_o = 1$), Eq. (4-13) yields:

$$K = 63 \times 10^{-6}\ \nu^{2/3}\ .$$

Standard bearings of this type operate at oil temperatures near 125°F with $\nu = 85$ centistokes. The use of high-temperature M-50 tool steel for the bearing components, and special lubricants operating near 300°F, will reduce ν to ~ 3 centistokes (Ref. 30). Using this value:

$$K = 63 \times 10^{-6}\ (3)^{2/3} = 1.31 \times 10^{-4}\ (\text{ft-lb})\ (\text{second})^{2/3}$$

Then, assuming $\omega_o = 3142$ rad/s (30 000 rpm):

$$\Delta t_{1/2} = \frac{1.24\ E_o}{1.31 \times 10^{-4}\ (3142)^{5/3}} = 0.0141\ E_o\ (\text{seconds})$$

For a family car with a 163-pound rotor:

$$E_o = (163\ \text{lb})\ (30\ \text{W-h/lb})\ (2656\ \text{ft-lb/W-h}) = 13 \times 10^{6}\ \text{ft-lb},$$

and

$$\Delta t_{1/2} = 0.0141\,(13 \times 10^6) = 0.18 \times 10^6 \text{ seconds} = 50 \text{ hours}$$

It may be seen that the run-down time is directly proportional to the initial energy and inversely proportional to the number of friction elements. Therefore smaller flywheel systems will run down faster, and the inclusion of seal friction, which will likely be greater than the bearing friction, will further reduce run-down time. Thus bearing and seal friction are likely to be more important than windage losses for the types of components (and internal pressure, 10^{-3} torr) assumed in this analysis. Again the need for a high-speed, low-friction bearing/seal unit is apparent, for the use of large flywheel rotors in hybrid vehicles will be practical only if friction losses can be minimized.

4.4 FACTORS AFFECTING THE ALLOWABLE STRESSES IN COMPOSITE MATERIAL FLYWHEELS

For any structural application, the allowable stresses depend on (a) the prescribed life cycle and environment of the structure, (b) a criterion of desired reliability of the structure (and this may be based on economics of replacement, personnel safety, operational requirements, etc.), and (c) the material characteristics, which, in addition to strength and physical properties, include manufacturing controls and size effects. The following sections discuss the effects of these factors for flywheels made of composite materials.

4.4.1 FLYWHEEL SYSTEM LIFE CYCLE AND ENVIRONMENT

As presently envisioned, the flywheel system for a hybrid vehicle would be factory-assembled, hermetically-sealed, and operated under controlled vacuum conditions at predictable stress levels. All of these factors will tend to lower the effective "factor of safety" applied to materials test data, particularly with respect to the vacuum environment. The flywheel life cycle is primarily a function of the vehicle operational requirements and the size of the flywheel. Rotor configuration (windage losses) and bearing and seal friction have secondary influences.

As an example, a commuter car with a 2 kW-h flywheel (70-pound rotor with E/W = ~ 30 W-h/lb) operating on the DHEW driving cycle will cover ~ 7 miles per charge. For a vehicle design life of 100 000 miles this equates to ~ 14 000 charges, plus the additional charges (full or partial) required because of run-down between operating periods. If these amounted to an average of one additional charge per day for 8 years (12 500 miles per year), the total number of cycles would amount to ~ 2×10^4. If the flywheel stored only 0.5 kW-h, or 1/4 of the former example (which is probably a minimum size to establish history-independent performance; i.e., three complete accelerations per charge without engine assist), the number of charge cycles in a vehicle lifetime would be 4 x 14 000, plus possibly two additional charges per day (because of faster run down), for ~ 7×10^4 cycles. These examples are shown in Fig. 4-9a. Also shown (Fig. 4-9b) is an example of emission-free driving in the central business district, as discussed in Section 5. Note that the charge and discharge rates are quite low compared to the loading rates used in developing fatigue test data. This is beneficial, for it eliminates heating of the composite materials caused by rapid straining, a factor which sometimes results in loss of strength in the matrix. Also, the stresses in the flywheel rotor range from the rated tensile stress to zero, with no compressive stresses. Data of composite materials tests by Boller (Ref. 33) show that stress cycles involving only tensile stresses result in much longer fatigue lives (orders of magnitude more) than for stress cycles with alternating tension and compression.

Another material characteristic that interacts with the rotor size and system losses is the stress-rupture or

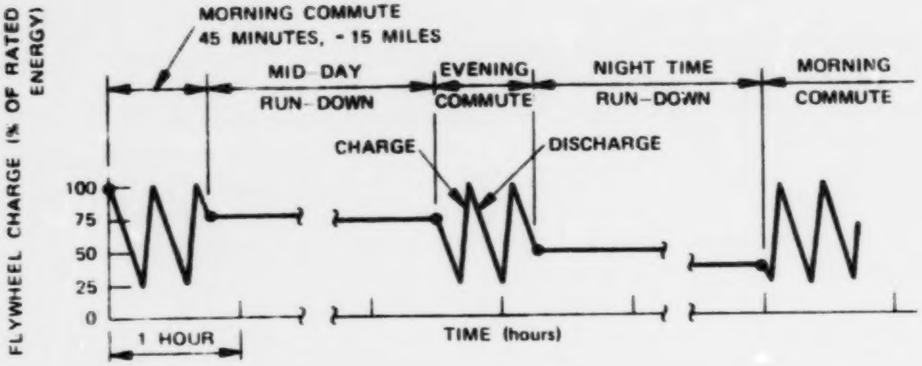

(a) EXAMPLE OF HYBRID COMMUTER CAR ON DHEW DRIVING CYCLE (2 kW-h FLYWHEEL; AIR CONDITIONER OPERATING)

	2 kW-h FLYWHEEL (AS ILLUSTRATED)	0.5 kW-h FLYWHEEL (ALTERNATIVE)
•CHARGE TIME (minutes)	6	1.5
•DISCHARGE TIME (minutes)	16	4
•ASSUMED RUN–DOWN TIME TO HALF SPEED (hours)	24	6
•LIFE REQUIREMENTS (cycles)	2×10^4	7×10^4

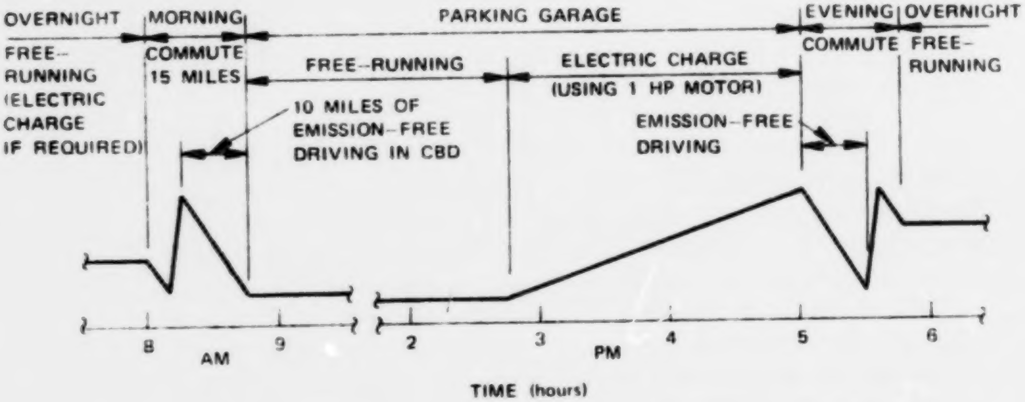

(b) EXAMPLE OF EMISSION–FREE DRIVING OPTION IN THE CENTRAL BUSINESS DISTRICT (CBD) (COMMUTER CAR WITH 2 kW-h FLYWHEEL; A/C NOT OPERATING)

Fig. 4-9 TYPICAL FLYWHEEL CYCLE REQUIREMENTS FOR A COMMUTER CAR

static fatigue life of the material at various stress levels. A large rotor with low system losses and long times to run down will be stressed over this longer period even though the vehicle is not operating. Conversely, a rotor that has a short run-down period will be stressed primarily while the flywheel system is being used to propel the vehicle. Since the allowable stress is a function of time under load, a flywheel with the desirable characteristic of low losses imposes operating stress limits because of the long time under load.

4.4.2 DYNAMIC FATIGUE OF COMPOSITE MATERIALS

The high-modulus composite materials, graphite and boron, have excellent resistance to fatigue loading, and are superior in this respect to many of the high-performance metals that are used in aerospace applications. A notable example is the recent retrofit of a boron/epoxy doubler panel to increase the fatigue resistance of the D6A steel wing pivot structure on the F111 aircraft. In general, boron and graphite/epoxy composites endure more than 10^7 cycles of tension-zero-tension at maximum stress levels equal to 70% of their static ultimate values (Refs. 34 and 35). A data sheet from Ref. 34 is reproduced in Fig. 4-10, which shows that boron/epoxy endures 10^5 cycles at ~ 90% of the static ultimate.

Conversely, glass-reinforced composites have usually been characterized as having relatively poor fatigue resistance. Data from Ref. 33 are reproduced in Fig. 4-11, which show endurance to 10^7 cycles at ~ 40% of static ultimate stress, and endurance to 10^5 cycles at ~ 50% of static ultimate. These data clearly show the effect of compressive stresses (lower mean stress) in degrading the fatigue life of the material. The tests were conducted at ambient temperature and 50% relative humidity, which are typical conditions for fatigue tests reported in the literature.

Thus, there apparently are large differences in the abilities of the various composite materials to endure

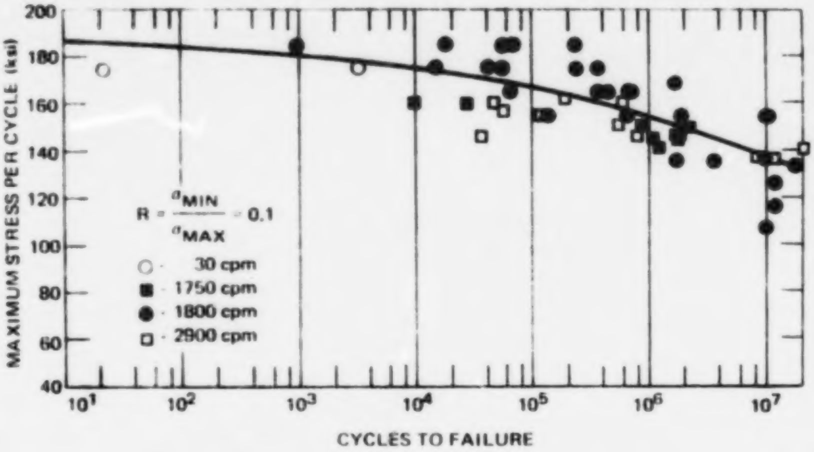

Fig. 4-10 CONSTANT AMPLITUDE FATIGUE TESTS OF BORON-EPOXY COMPOSITE AT ROOM TEMPERATURE (FROM REF. 34)

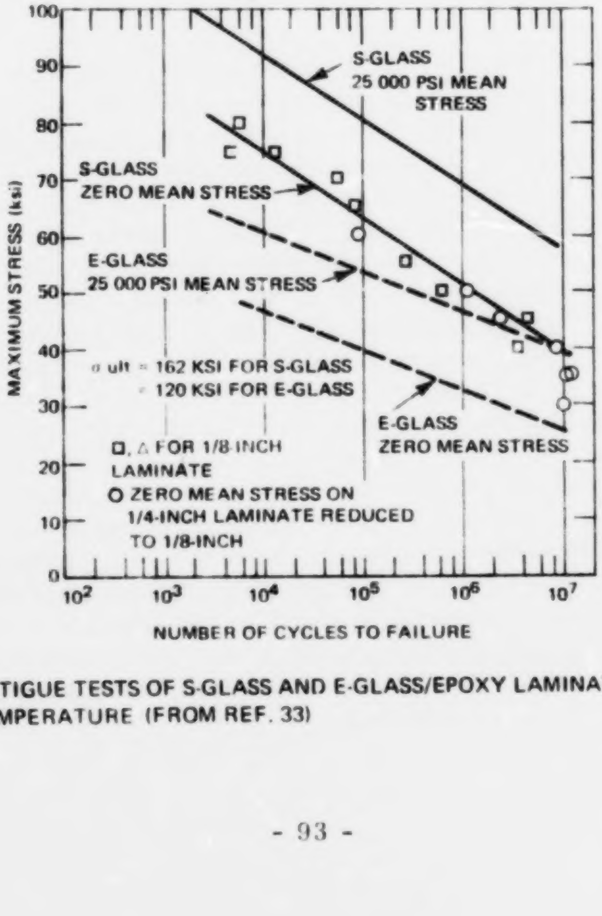

Fig. 4-11 FATIGUE TESTS OF S-GLASS AND E-GLASS/EPOXY LAMINATES AT ROOM TEMPERATURE (FROM REF. 33)

cyclic loading. These differences are often explained by comparing the stiffness-to-strength ratios (ultimate strains) of the materials (Ref. 36), as shown in Table 4-3.

Table 4-3

Ultimate Strains of Composite Materials

Composite Material	Ultimate Tensile Strength (psi)	Elastic Modulus (10^6 psi)	Ultimate Strain (in/in)
Boron/Epoxy	210 000	30.3	0.007
Graphite/Epoxy (high-strength type)	200 000	21.5	0.009
S-Glass/Epoxy	260 000	7.6	0.034

The theory is that the matrix resin develops a nonlinear stress-strain behavior above strain elongations of 1/2 to 1%, and repeated cycles above these levels can cause cracking or crazing of the matrix resulting in an inability to transfer stresses from one fiber to another. The values in the table show that the ultimate strain in the glass composite is on the order of 4 to 5 times the ultimate strain in the high-modulus composite materials. Therefore, the glass is usually limited to a lesser fraction of its ultimate strength in order to reduce matrix damage under cyclic loading. Another, and probably related reason for reduced endurance of the glass composites is that, when the resin matrix cracks or crazes under stress, the glass fibers are exposed to atmospheric moisture which is known to degrade their strength (Ref. 37). There are no known dynamic fatigue test data of glass composites in a vacuum, though static fatigue data for glass and glass composites tested in the absence of air and moisture (see Section 4.4.3) show a marked improvement over similar materials tested under ambient conditions.

4.4.3 CREEP AND STRESS-RUPTURE OF COMPOSITE MATERIALS

Creep is a time- and stress-dependent phenomenon in which the material continues to deform after the stresses have reached a stable value. The rate of deformation is a function of the stress level and the accumulated strain, and the process terminates in rupture of the material. (Homogeneous, isotropic materials also are affected.) It is of interest because it generally limits the amount of stress a material can resist for a specified time or the amount of time a specified stress level may be endured. Stress-rupture is sometimes referred to as creep-rupture or static fatigue, and there are similarities between the behavior of materials under dynam[illegible] fatigue and long-term loading.

There are not many data available on the stress-rupture and creep characteristics of boron and graphite composites, primarily because these materials have usually been considered for applications where short-term cyclic or vibratory loads are more important. The fibers have very linear stress-strain relationships to failure, and creep would not be expected to be a major concern. Graphite/epoxy composites were discussed by Soliman (Ref. 38), and it was concluded that if the fibers are aligned with the load direction, the creep strain will be negligible compared to the instantaneous elastic deformation. Such is not the case for off-axis loading, where it was found that fiber orientation is the most influential factor in determining the creep characteristics (i.e., the fibers do not creep but the matrix does). The laminae orientation effects the linearity of the stress-strain relations, which will be important for rotors with biaxial stress states such as the wide bar and the pseudo-isotropic disk. However, from the foregoing it seems reasonable to assume that the high-modulus composites, graphite and boron, can provide satisfactory endurance for long-term loading.

Boller (Ref. 37) and others have reported that glass composites are susceptible to stress-rupture and creep in a manner analogous to their problems in dynamic fatigue. Very recently, Chiao and Moore (Ref. 39) published an interim report on their tests of the stress-rupture of S-glass/epoxy strands at Lawrence Radiation Laboratory using 1500 specimens.

Tests are being conducted at room temperature and 20 to 60% relative humidity in air at six different load levels, with the three highest levels completed. The results of the first series of tests are shown in Fig. 4-12, where the cumulative percentage of strands failed is plotted versus time-to-failure for these three load levels. The spread in the data clearly illustrates a stress rupture problem with this material. The time-to-break at any given load level scatters over three orders of magnitude with a coefficient of variation over 100%, while the ultimate tensile strength data were reported to have had very little scatter with a coefficient of variation of only 3. 6%.

The spread in the data suggests that the stress-rupture may be produced by progressive corrosion from moisture in the atmosphere, with some strands being degraded more rapidly than others. A study that lends support to this hypothesis is one by Hanson (Ref. 40), who has tested glass filament-wound pressure vessels in both ambient and cryogenic environments. Figure 4-13 shows time-to-failure for 13 S-glass/epoxy cylinders, 11 under ambient conditions and 2 in liquid nitrogen. Both cryogenic tests were halted as the result of test equipment malfunctions, but they sustained periods under load far in excess of the other cylinders. The data are ratioed to the single-cycle burst strength at test temperature, which takes into account the increase in ultimate-tensile strength of the glass composite at low temperatures.

A recent survey by Weiderhorn (Ref. 41) reviews the large body of knowledge that has been accumulated on

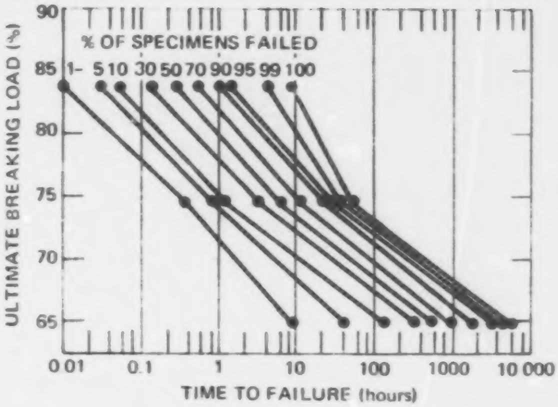

Fig. 4-12 PROBABILITY LINES FOR STRESS-RUPTURE OF S-GLASS/EPOXY STRANDS (FROM REF. 39)

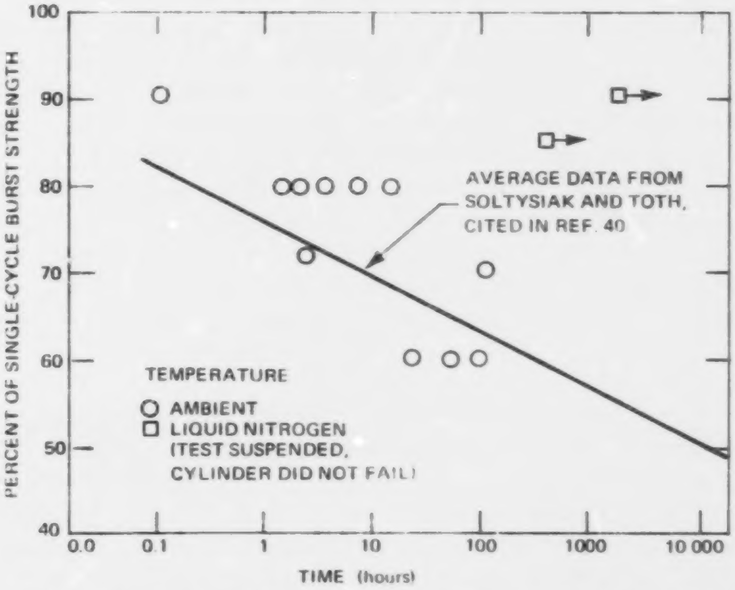

Fig. 4-13 TIME OF FAILURE FOR S-GLASS/EPOXY CYLINDERS UNDER PRESSURE AT AMBIENT AND LIQUID NITROGEN CONDITIONS (FROM REF. 40)

environmental stress corrosion cracking of glass. This well-referenced document clearly states that (a) the ultimate strength of glass is directly related to the perfection of its surface and not the size of the specimen, as was once believed; (b) phenomenal increases in strength can be obtained by the removal of surface flaws (for example, bulk glass can be improved from 5000 to 500 000 psi by chemical polishing with hydrofluoric acid, and silica rods can be flame-polished to obtain strengths to 2 million psi); (c) despite the inert character of glass and its use to resist chemical attack, the material is highly susceptible to stress-corrosion cracking, known as static fatigue; (d) this phenomenon is caused by water in the environment; (e) glass that is baked out and tested in vacuum shows little fatigue, and similar results are obtained for tests conducted in liquid nitrogen; (f) tests conducted in water or air can result in static fatigue failures within time intervals as short as 10 ms at high stress levels; and (g) comparison of cyclic and static tests demonstrate that the time to failure depends on the magnitude and total duration of the load, but not its cyclic nature. Reference 41 notes that the most extensive study of static fatigue of silica glass fibers was conducted by Proctor, Whitney, and Johnson (Ref. 42), and data from their experiments are shown in Fig. 4-14. Static fatigue was observed in air, but not in the liquid nitrogen environment. The fatigue effects noted for the fibers tested in vacuum was attributed to residual moisture adsorbed on the glass surface.

It is the authors' opinion that the foregoing data and discussion on the fatigue characteristics of glass fibers are encouraging with respect to the application to a flywheel system environment. Problems may still exist in composite materials of glass fibers and a resin matrix because of excessive matrix deformation; however, it seems clear that controlled processing, fabrication, and environment can significantly reduce fatigue degradation of these materials.

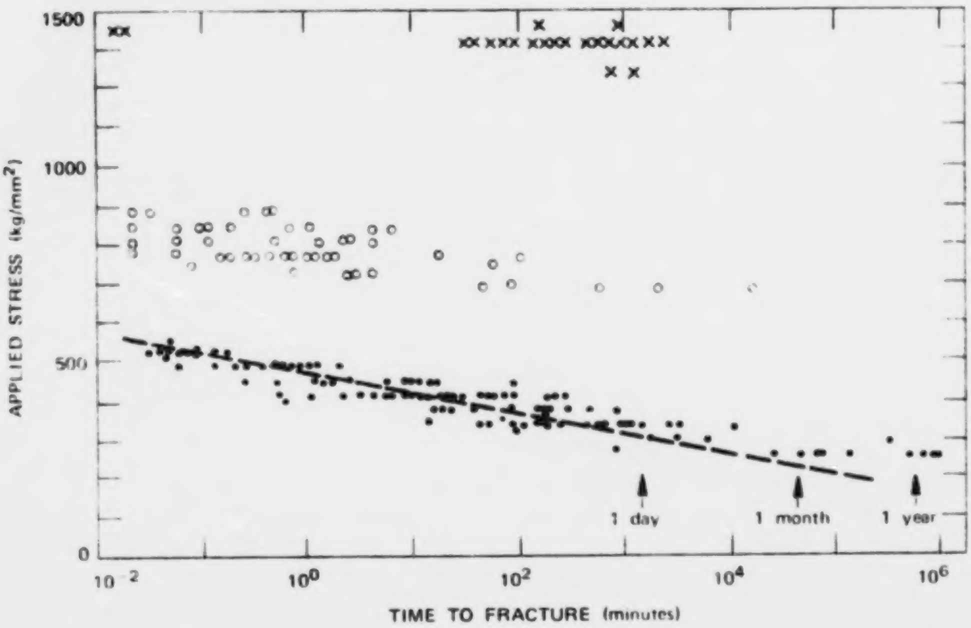

Fig. 4-14 STATIC FATIGUE DATA FOR SILICA FIBERS, x IN VACUUM AT −196° C, o IN VACUUM AT ROOM TEMPERATURE, ● IN AIR AT ROOM TEMPERATURE (REFS. 41, 42)

4.4.4 LONGITUDINAL DIVERGENCE

The theoretical upper limit to energy storage in a rod-type flywheel has been discussed by Brunelle (Ref. 21), who has shown that a condition of inertio-elastic instability exists for certain combinations of rotor tip speed, elastic modulus, and material density. He has termed this condition longitudinal divergence, and the critical tip speed for divergence ($R\omega_D$) is given by the equation:

$$R\omega_D = (\pi/2)(gE_m/\rho')^{1/2} \qquad (4\text{-}18)$$

For rotational speeds higher than the critical value (ω_D), the rod elongation becomes divergent. Also, using Eq. (3-2), the maximum tip speed compatible with the ultimate strength of the material can be written:

$$R\omega_{max} = (2g\,\sigma_{max}/\rho')^{1/2}\,. \qquad (4\text{-}19)$$

Equation (4-18) is plotted in Fig. 4-15, and the area below and to the right of the curve represents the region of longitudinal divergence. A given material can be located on the plot by fixing its ordinate with the elastic modulus/density ratio and its abcissa using Eq. (4-19). Points for graphite/epoxy, S-glass/epoxy, boron filaments, and a future high-strength fused silica material are shown. The indications are that there is no problem with longitudinal divergence for the range of materials that we are considering. It would be desirable, once the creep characteristics of the candidate materials are defined more accurately for vacuum use, to extend this divergence criterion to consider visco-elastic behavior of the material, which may establish more practical limits.

Brunelle also pointed out that the extension of the rotating rod adds to its kinetic energy, and this increase can be formulated as:

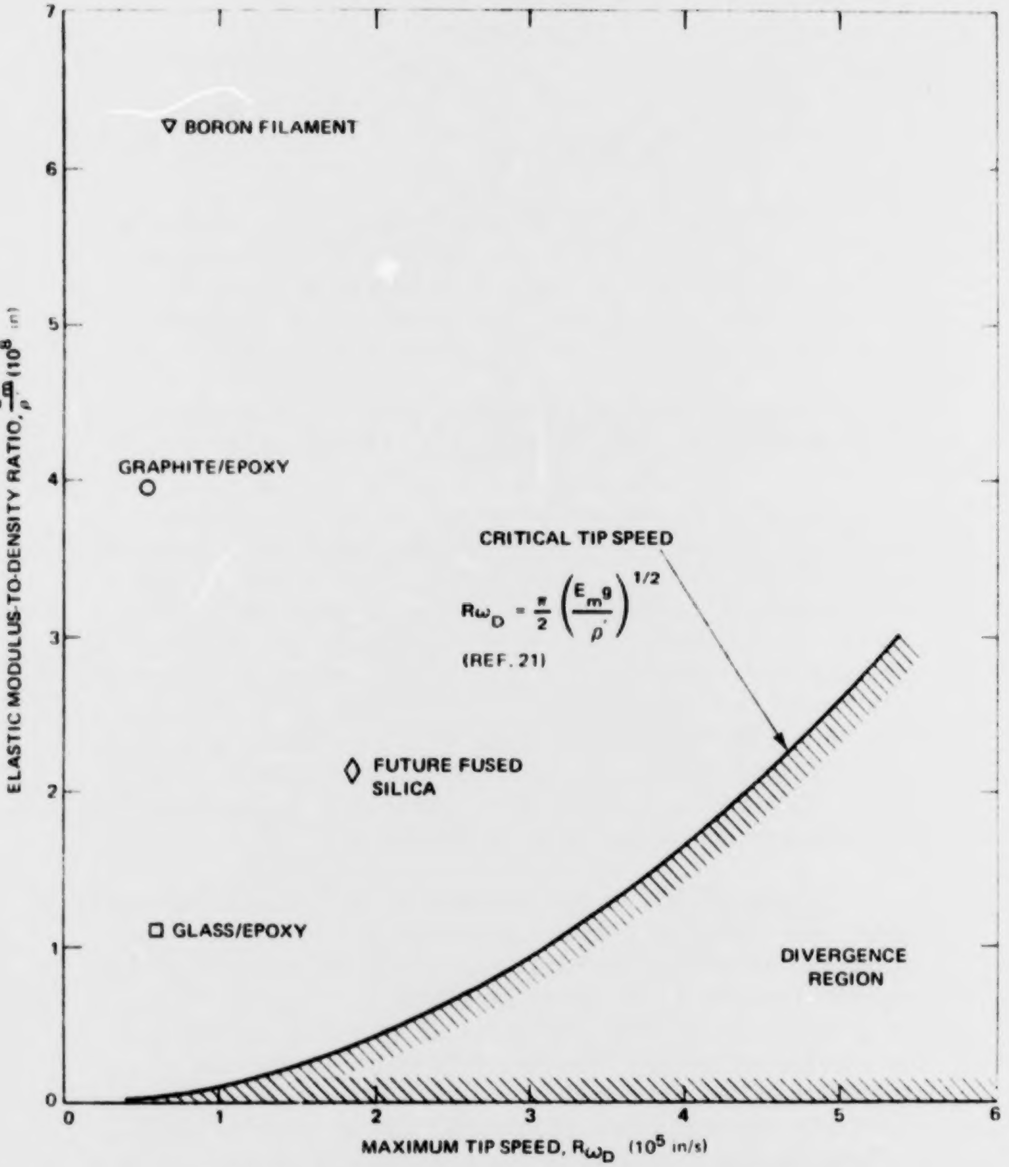

Fig. 4-15 LONGITUDINAL DIVERGENCE OF ROD-TYPE ROTORS

$$\frac{E + \Delta E}{E} = \frac{3(2k - \sin 2k)}{4\,k^3 \cos^2 k}\ , \tag{4-20}$$

where

$$k = \rho'\, R^2\, \omega^2 / gE_m\ . \tag{4-21}$$

For a 30-inch-long glass/epoxy composite rod spinning at 30 000 rpm, this yields a kinetic energy increase of only 2%, and the effect would be even smaller for the higher modulus materials. Therefore, it has been neglected in all energy calculations presented herein.

4.4.5 FUTURE IMPROVEMENTS IN MATERIALS, FABRICATION, AND DESIGN TECHNIQUES

A study of the predicted future improvements in materials indicates that there may be many with strength-to-density ratios (σ/ρ') several times the values of the best materials currently available. These findings are in part corroborated by work the Russians are doing in the field of mechanical energy storage, wherein they forecast future rotor specific energies of 200 to 300 W-h/lb (Ref. 43). Significant improvements are expected with composites of glass and graphite, boron filaments, bulk glass, high-purity fused silica, and other new materials, as discussed in the following paragraphs.

Fiberglass. Improvements in σ/ρ' of unidirectional fiberglass will result from improved glass formulations, increased glass-to-resin ratios, and (perhaps most of all) improved manufacturing and handling techniques. With the present techniques, the strength of the glass fibers in the composite seldom reaches 50% of the virgin fiber strength for two principal reasons: (a) the fibers are physically damaged during manufacturing, and (b) they are chemically damaged by the presence of water during the manufacture of the filament and in the ambient environment. The Russians apparently have developed a method of protecting the glass filament from both physical damage and water damage by applying a protective coating of epoxy/polysulfide at the instant the glass filament is formed at the bushing during drawing (Ref. 44). They claim that with this procedure they can make unidirectional composites wherein 90% of the virgin strength of the glass is usable in the laminate. It is generally agreed that future glass fibers will have virgin strengths of 800 000 psi. If 90% of this can be recovered in a unidirectional laminate with 75% fiber volume, the resulting laminate strength would be 540 000 psi. This is twice the strength currently achievable with S-glass/epoxy systems.

Graphite/Epoxy. The strength of currently available graphite filaments has steadily improved with at least two manufacturers quoting values of 400 000 psi (Ref. 34). Bowman and Branan (Ref. 45a) report that laboratory-produced samples of filament have exceeded 500 000 psi, and that graphite whiskers have been produced with strengths on the order of 3 million psi. Fabricators are now beginning to talk about graphite/epoxy laminates with tensile strengths of 250 000 psi, compared to the 200 000 psi level seen in most data books. This improvement is believed to result from the use of a superior matrix material to increase the interlaminar shear strength, which has been one of the weakest links in the graphite/epoxy system. It seems reasonable to predict at least a 50% increase in performance over current laminates, including both fiber and matrix improvements. The price of high-strength graphite fiber is ~ 50 times the price of S-glass fiber, but it is expected to diminish rapidly in future years as the rate of production increases and plants are opened in different countries. Eventually prices are expected to be less than $10/lb.

Boron. Line and Henderson (Ref. 45b) report that the measured strength capability of pure boron is three times the current production average of 450 000 psi for the $250/lb boron/tungsten filament. Future boron filaments are expected to be stronger and lower in cost,

\$100/lb. The cost reduction is expected to result from a faster plating method, plus the substitution of a silica substrate for the more expensive and 10 times heavier tungsten substrate currently used. Thus, filament strength may approach 800 000 psi while density is reduced to $\sim$ 0.083 (instead of the present 0.093), resulting in a 100% improvement in σ/ρ.

A distinct advantage of boron is that the filaments are large enough and stiff enough so that they can be used alone without a matrix, which becomes an enormous advantage in the brush type-configurations. For example, an existing boron-magnesium composite only has a strength of 300 000 psi, whereas the boron alone would have a strength of 450 000 psi average, a 50% improvement.

Bulk Glass. About 10 years ago laboratory tests demonstrated that common soda glass could be used to make rods with a strength of 500 000 psi (Ref. 46) using acid to etch away the micro-cracks on the surfaces. As in any of the filament materials, the principal reason the finished product is only about 1/4 to 1/3 the theoretical strength is because of the surface cracks and impurities. In the case of the bulk glass rods these surface discontinuities are smoothed out by the acid etch. High strength can also be obtained by chemically treating the surface to induce a compressive stress of greater magnitude than the expected tensile stresses. Perry (Ref. 47) has forecast strengths of 300 000 psi by 1980 and up to 500 000 psi in the future. This technique would be applicable to a solid disk rotor.

Bulk glass has several intrinsic advantages over fiberglass, which warrants interest. First, the rods can be used as is, without the need for a matrix material to complicate the installation and reduce σ/ρ'. Its cost should be much less than fiberglass/epoxy, because its diameter is 100 times that of the glass fibers, which means less assembly and handling is required, and handling is much easier.

The glass rods would be made much the same as the high strength fiberglass. They would be protected by a polymer coating instantly when made, and, of course, the flywheel vacuum environment would protect against water damage, as well as against further mechanical damage. The raw material from which these rods would be made costs on the order of 15¢/lb. Thus, the bulk glass rods offer the potential of σ/ρ' of 5 to 9 million (inch) for the least cost among the common materials available.

Quartz and Fused Silica. High-purity, or high-silica glass is generally agreed to be that which contains 95%+ SiO_2. Natural quartz has an even higher purity, having about 99.95% SiO_2. High-silica glass is chiefly made by leaching impurities out of ordinary glass by appropriate acid rinses. The leaching also reduces the weight of the remaining glass, which can be as low as 0.063 lb/in^3, compared with 0.09 for S-glass. Quartz is slightly heavier at 0.079 lb/in^3.

Hillig of General Electric (Ref. 48) and a group of scientists from Rolls Royce, Ltd, have tested fused silica rods to greater than 1 million psi (some tests approached 2 million psi). The theoretical strength of this material is 4 800 000 psi, and it is reasonable to expect that future applications of high silica rods may demonstrate strengths in excess of 2 million psi.

Other New Materials. New organic fibers are being produced that offer combinations of high strength and high density. DuPont is in the process of documenting data on a proprietary fiber material designated PRD49 Type 1, that is reported to have a simple filament σ/ρ' of 7 to 10 million (inch) and an elastic modulus of 20 million psi (3 to 4 times that of S-glass) (Ref. 49). This material offers the promise of high energy storage performance and good fatigue resistance due to its high modulus. DuPont projects costs to $20/lb as demand increases. In addition to new organic fibers, a large variety of whisker-based materials should be applicable to various superflywheel configurations. Milewski (Ref. 45c) projects widespread use of these materials, particularly in conjunction with more conventional fibers to form "whiskerized" systems. Plants having a capacity of 200 000 lb/yr are on the drawing board, and whisker costs are projected at less than $5/lb for larger volumes.

Other Sources of Improvement. Along with improvements in the basic materials and their fabrication, we can expect improvements in our ability to analyze the composite materials and select allowable stresses that will result in efficient, reliable, and safe structures. It has been seen that considerable scatter exists in materials' property data (Figs. 4-10, -11, -12, and -13 for example), and a simple factor-of-safety approach to design is no longer appropriate. However, using statistical methods, reasonable reliability limits can be obtained on properties such as fatigue life, stress endurance, and ultimate strength. As an example, Weibull statistics can be used to describe the distribution of the measured data (Ref. 39). A very extensive treatment of Weibull statistics in structural design applications is given by De Salvo (Ref. 50), who determines allowable material strengths and reliability factors for several structural problems.

The flywheel life cycle shown in Fig. 4-9 combines effects of cyclic fatigue with long-term stress-rupture. Broutman and Sahu (Ref. 51) are developing methods to predict damage to composite materials resulting from cumulative effects of this type.

It must be emphasized that the failure process of most composite materials is quite different than that of a metallic material. In the case of metals, most of the life is spent in developing the first flaw, and there is little or no change in strength or stiffness during this period. After the flaw develops it usually propagates rapidly and the metal fails. By contrast, composite materials may exhibit several modes of damage, some occurring early in life and progressing at a very low rate until failure. The damage can include delamination, matrix crazing and cracking, void growth, fiber failure, or a combination of these. These differences are shown qualitatively in Fig. 4-16 by Salkind (Ref. 36).

It is expected that composite materials will be more damage-tolerant than metals. They exhibit good fracture toughness and, unlike metals, increase in fracture toughness with increasing tensile strength (Ref. 36). The inspection threshold for composites occurs much earlier in the life cycle and occupies a wider band; for metals there may be little time between the threshold of inspection and the propagation to fracture, requiring more frequent inspections to assure reliability and safety. In composites the stiffness often changes during the life cycle, and this offers a promising method of assessing remaining life by nondestructively determining the static resonances or dynamic damping of the structure.

4.5 VEHICULAR INSTALLATION

There are a number of concepts available for installing the propulsion equipment in each of the vehicles, but this program has not dealt with this subject in much detail, since the system factors described above have yet to be selected. An example for a commuter car is presented to illustrate the fact that a flywheel hybrid propulsion system can be adapted to common vehicles in a straightforward manner. Gyroscopic effects for large flywheels also will require considerable study, and the results of only a brief examination are presented here.

4.5.1 HEAT ENERGY/FLYWHEEL HYBRID PROPULSION IN A COMMUTER CAR

Figure 4-17 shows the general details of a hybrid propulsion system for a commuter car. This car has a curb weight of only 1400 pounds, and the loaded weight of 1700 pounds accounts for the driver and one passenger. This vehicle is among those studied in Section 5.

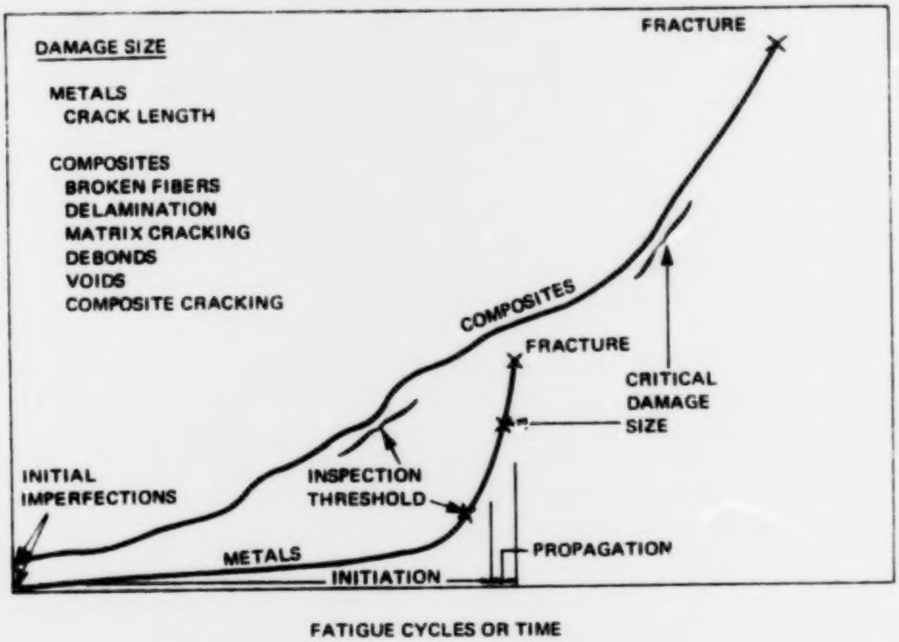
DAMAGE SIZE
METALS
CRACK LENGTH
COMPOSITES
BROKEN FIBERS
DELAMINATION
MATRIX CRACKING
DEBONDS
VOIDS
COMPOSITE CRACKING
FRACTURE
COMPOSITES
FRACTURE
CRITICAL
DAMAGE
SIZE
INITIAL
IMPERFECTIONS
INSPECTION
THRESHOLD
METALS
PROPAGATION
INITIATION
FATIGUE CYCLES OR TIME

Fig. 4-16 CHARACTERISTICS OF FAILURE MECHANISMS FOR METALS AND COMPOSITE MATERIALS (FROM REF. 36)

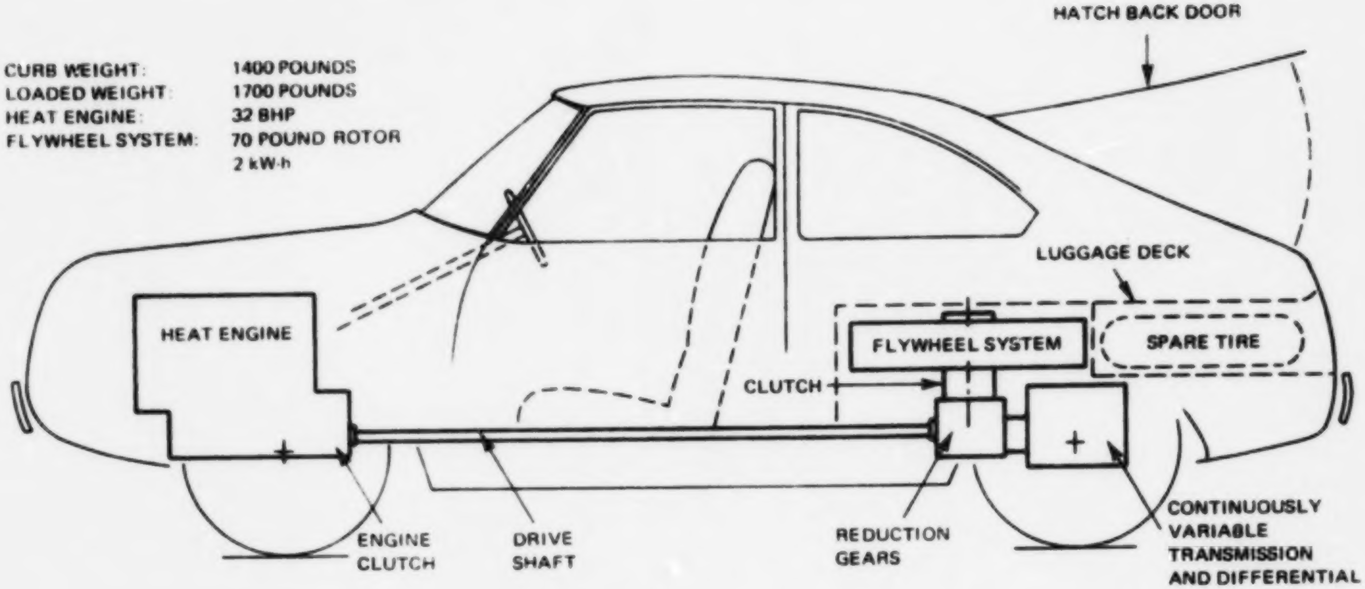
HATCH BACK DOOR
LUGGAGE DECK
HEAT ENGINE
FLYWHEEL SYSTEM
SPARE TIRE
CLUTCH
ENGINE CLUTCH
DRIVE SHAFT
REDUCTION GEARS
CONTINUOUSLY VARIABLE TRANSMISSION AND DIFFERENTIAL

CURB WEIGHT:	1400 POUNDS
LOADED WEIGHT:	1700 POUNDS
HEAT ENGINE:	32 BHP
FLYWHEEL SYSTEM:	70 POUND ROTOR 2 kW·h

Fig. 4-17 HEAT ENGINE/FLYWHEEL HYBRID COMMUTER CAR

For a series power train (discussed later in Section 5.4.4 and shown schematically in Fig. 5-10) it is desirable to locate the flywheel, gear box, and transmission in close proximity. This can be accomplished as shown in Fig. 4-17 by placing the heat engine and associated equipment in the front of the car and the flywheel-transmission system in the rear, essentially equalizing the weight distribution. The continuously variable transmission is integrated with the differential, and all of the powertrain components in the rear of the car are rigidly connected to one another and are shock-mounted on the sprung mass, the rear wheels being independently suspended. This arrangement will provide space for a disk flywheel with $E_0 = 2$ kW-h or a bar of approximately 1.5 kW-h, though the use of a system with this amount of energy will depend upon the ability to contain the rotor, acceptable vehicle handling characteristics, and the development of low-friction seals and bearings.

4.5.2 FLYWHEEL GYROSCOPIC TORQUE

When the axis of a rotating element is pitched, a torque is produced perpendicular to the axis of rotation and the plane of the pitch according to the formula:

$$T = I\omega\dot{\phi}\ , \qquad (4\text{-}22)$$

where $\dot{\phi}$ is the pitch rate. Since $E = I\omega^2/2$, Eq. (4-22) may be written:

$$T = 2E\dot{\phi}/\omega\ . \qquad (4\text{-}23)$$

This equation shows that torque increases with the level of flywheel system energy (vehicular operational criteria) and pitch rate (a function of the vehicle suspension and road characteristics), but reduces as rotor speed increases. Therefore, all other things being equal, a flywheel configuration with low inertia and operating at high rpm will produce lower gyroscopic torques than a slower, high-inertia system.

Nevertheless, an attempt was made to assess the degree of the problem associated with gyroscopic forces. Dynamic data for a typical family car (a 1963 Ford Galaxie 4-door sedan) were obtained from McHenry (Ref. 52) and used as inputs to the APL vehicle dynamics program (APLDYN). This vehicle was assumed to have a 5 kW-h flywheel system (164-pound rotor at ~30 W-h/lb: see Table 5-10b). The vehicle mass remained the same, assuming that flywheel system weight additions were balanced by heat engine and other weight reductions. The flywheel system was (for simplicity) hard-mounted to the sprung mass.

The vehicle was programmed over a 3½-inch high, transverse bump in the roadbed while traveling at 45 mph. The bump profile and the resulting displacements are shown in Fig. 4-18. In the upper graph, the dashed lines are for a nonrotating flywheel, and it is seen that there is no roll induced by the transverse bump. When the flywheel is spinning at 30 000 rpm to produce 5 kW-h, the pitching of the vehicle induces a roll component nearly twice as large as the pitch. The vertical deflections are the same for both cases. The maximum roll angle is only 2°.

It should be emphasized that these results are illustrative of the problem but not necessarily quantitatively relevant. For instance, no shock mounting was provided between the flywheel system and the sprung mass, and this would be an obvious way to reduce flywheel system rates. Also, the particular vehicle does not appear to have much damping in the roll mode,and it would be expected that a flywheel-tailored suspension system would improve the rideability. The bump is severe at this speed, producing a pitch rate of 20 deg/s. Rice (Ref. 53) notes that pitch rates in excess of 20 deg/s are rarely encountered on real-life roadways.

The peak value of the flywheel torque is 4000 ft-lb, resulting in a radial bearing load of ~ 4000 pounds. Other

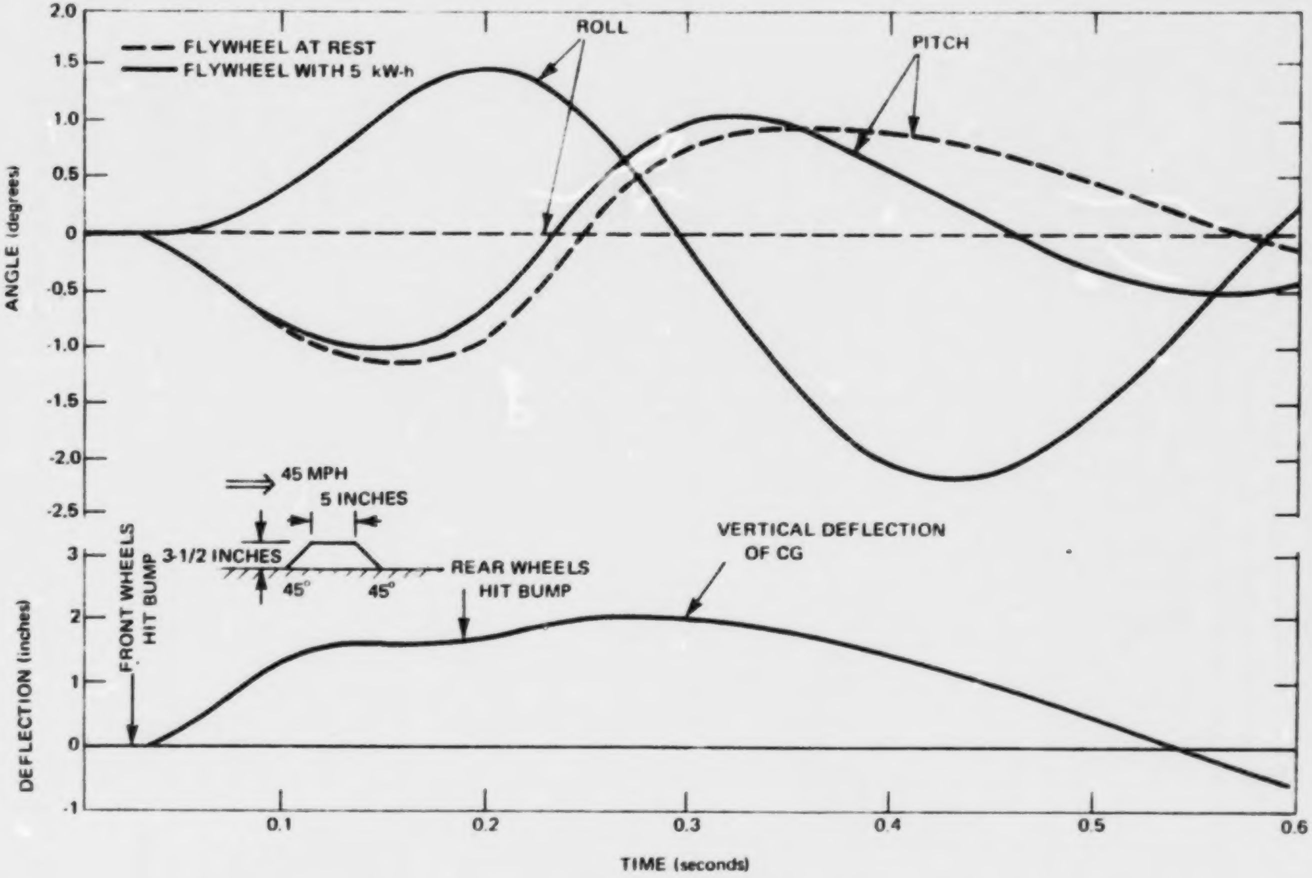

Fig. 4-18 EXAMPLE OF FAMILY CAR ENCOUNTERING A SEVERE ROADWAY OBSTACLE AT 45 MPH WITH 5 kW-h HARD-MOUNTED FLYWHEEL

studies using this dynamic program have verified that the induced roll is linear with respect to the flywheel momentum. Computer programs at Cornell Aeronautical Laboratory, Inc. have the capability of assessing the problem of flywheel gyroscopic torques with the use of human response factors incorporated in the programs (Ref. 52).

4.6 CLOSURE

Several flywheel rotor configurations offer the potential of achieving high specific energy by using filamentary or composite materials. These rotors are sufficiently compact for use in vehicular propulsion systems.

System components such as bearings, seals, and vacuum equipment demand development in order to realize the full potential of the superflywheel concept.

Composite materials are rapidly emerging as prime candidates for high-performance structural systems. Their characteristics are improving and becoming more reliable while costs are decreasing (Ref. 54). They have the unique ability to match reinforcement to the structural load paths. The apparently favorable aspects of operating in a vacuum environment (Refs. 41 and 42) need further definition for they could open the way to the use of low-cost glass materials in flywheel systems. In any event, forecasts indicate that materials will be developed that will have performance characteristics superior to our current exploratory materials. Predictions of specific energy storage several times the values assumed in these studies have already been made (Ref. 43).

5. PRELIMINARY VEHICLE EVALUATION STUDIES

5.1 INTRODUCTION

The objective of the analytical evaluation studies that are presented in this section was to investigate the feasibility of using flywheels alone or in combination with heat engines to reduce HC (hydrocarbon), CO (carbon monoxide), and NO_x (oxides of nitrogen) emissions from vehicles, while essentially retaining current vehicle performance as defined in criteria furnished by OAP at the start of the program (July 1970). It should be emphasized that the purpose was to explore, in a broad sense, the potential of a flywheel-only or flywheel-hybrid propulsion system for meeting this objective, and that most of the inputs to the analysis were based on forecast improvements in flywheel system technology. Indeed, the analysis effort conducted at APL was intended to be complementary to the Lockheed effort (Refs. 2 and 12) in that it would look toward future rotor materials and configurations for advanced flywheels for application in the 1980 period, while the Lockheed work emphasized state-of-the-art materials and an early prototype evaluation.

The studies are based on certain basic assumptions of operating modes, engine emissions characteristics, and flywheel system performance. First of all, it was assumed that there was merit in a capability to operate the vehicle in an emission-free mode all or part of the time. This assumption is explicit in the flywheel-only evaluation where the vehicle is charged between trips by an outside power source, but the authors believe it to have merit for the flywheel-hybrid case whereby a vehicle with a large, high-specific-energy flywheel could operate in an emission-free mode for a significant range in the central business district or other severely polluted regions of a large metropolitan area. The possible need

Preceding page blank

for limiting or banning emission-producing vehicles from such areas has been discussed by others (Ref. 3), and the ability for a flywheel-hybrid vehicle to provide such an emission-free mode is a feature well worth considering.

Consistent with the above idea is the further assumption of a series-type power train for a flywheel-hybrid system whereby the heat engine would be operated in an on-off mode; that is, all energy required to operate the vehicle would come from the flywheel and the engine would remain off while the wheel discharged 75% of its stored energy (2:1 speed range), at which time the engine would be activated to recharge the flywheel to its maximum rated energy level before shutting down again. For urban driving the engine would operate ~15 to 30% of the time, depending on the type of vehicle and its driving requirements. Alternatively, a hybrid vehicle could use a parallel-type-power train in which the engine operated continuously to power the vehicle with a much smaller flywheel providing supplemental power during acceleration (Ref. 12). The size of the heat engine would not be affected appreciably by the choice between these two approaches, since it must be large enough to provide continuous power for cruise conditions in both cases, and cruise power is not strongly affected by modest weight changes.

The scope of this program did not include any original work on emissions from heat engines, and OAP supplied curves of emissions versus horsepower for each type of engine (spark-ignition, diesel, gas turbine, and Rankine cycle) to be considered in the hybrid studies. These data were very preliminary and do not include possible gains that may be achievable by optimizing a heat engine to run only under the constant-load, limited-speed-range conditions associated with on-off operation for flywheel-charging in a hybrid system. No credit is taken for such gains in the emission ratios presented later, but the authors feel that they should be substantial. In Ref. 55, 60% reductions in HC and CO and a 25%

reduction in NO_x were obtained for an electric hybrid "Minicar," and the first recommendation of that report was: "Since the ICE (internal combustion engine) did not operate at extremely high A/F ratios during the hybrid mode, these tests should be repeated using an engine that has been developed on a test stand for this type of operation." In Ref. 56 an appreciable effect of engine speed on NO_x emission from diesel engines was found, and this effect of engine speed remained when water injection (which sharply reduced NO_x) was used.

On the other hand, an on-off mode of operation will result in start-up emission penalties, though data have not been published on these effects for a typical 20-minute cooldown period between engine charge cycles. An allowance for HC and CO emission penalties has been included in the analysis, but the effect of multiple starts on NO_x emission has been assumed to be negligible. The large flywheel would be expected to have plenty of reserve energy after overnight parking to use in restarting the cold engine, and with flywheel "cranking" and properly sequenced (computer-controlled) fuel injection, emission penalties for the initial cold-start may also be reduced.

The evaluation studies were started at the same time as the experimental, proof-of-principle, test program began and, in fact, they were essentially completed at a time when only five of 41 rod tests (reported in Section 3) had been made. Furthermore, studies of rotor configurations, seals, and bearings, and containment had yet to be made. The assumptions on flywheel system performance that were used in the evaluation studies were not, therefore, based on test results or studies of system components, but rather on the type of system the authors believed achievable through active development and the type of system that would be required to permit significant emission-free driving range. The basic assumptions follow:

1. **A rated specific energy capability of 32 W-h/lb of rotor material (at maximum rpm) independent of rotor size.**

2. **A 2:1 operating speed range that will permit withdrawal of 75% of the rated energy of the system (24 W-h/lb per cycle).**

3. A disk-like rotor shape and a density equivalent to a glass composite material for volume considerations.

4. A favorable failure mode that will permit a containment case of nominal weight (equivalent in weight to 3/8-inch of armor steel).

5. Very low parasitic losses (windage and bearing/seal friction) which are negligible compared to vehicle power requirements.

6. A weight allowance for the flywheel rotor hub, bearings, and seals equivalent to 10% of the rotor weight.

Results of the experimental program (Section 3) and the configuration and component studies (Section 4) point to some problems that must be solved in order to achieve the assumed performance; at the same time, however, projected increases in materials strength and reliability offer hope of realizing these characteristics for use by 1980 if a vigorous development program is undertaken. As a single example, researchers at the Naval Ordnance Laboratory, White Oak, Md., forecast (Ref. 47) the availability of surface-compressed silicate glass with a strength of 300 000 psi by 1980. If this material were used in a shaped disk rotor it would provide a compact flywheel system with an ultimate specific energy density of 96 W-h/lb of rotor material, allowing a factor of safety of three compared to the rated value assumed in these studies. The radially fanned brush configuration discussed in Section 4.2 could take advantage of even more advanced glass-like materials (e.g., fused silica), if they become economically feasible, and might produce an even safer design (because of the favorable failure mode already demonstrated; see Section 3.3) with the rated specific energy assumed here.

The flywheel system assumptions above have very little direct effect on the calculated level of vehicle emissions; however, the value of the on-off mode of operation with respect to flywheel-only range would be diminished if the usable rotor specific energy achieved were very far below the assumed 32 W-h/lb, or the required net increase in vehicle weight to assure rotor containment far exceeded the estimates used. In such a case, the parallel hybrid mode (Ref. 12) might be chosen, permitting use of a flywheel of only 1/10 to 1/4 the weight considered herein for any particular application while giving up the possibility of appreciable emission-free range.

5.2 POWERPLANTS FOR THE HYBRID-FLYWHEEL VEHICLES

This section presents the characteristics of the four heat engines considered in the flywheel-hybrid studies:

1. The spark-ignition, four-stroke Otto cycle engine (SIE),
2. The compression-ignition, four-stroke Diesel engine (CIE),
3. The open-cycle gas turbine Brayton cycle engine (GTE), and
4. The steam Rankine cycle engine (SRE).

For each, the ideal cycle efficiency, configuration, and current characteristics are briefly described, and, since brake specific fuel consumption (bsfc, lb_m/bhp-h) is inversely proportional to thermal efficiency η_t, the major parameters affecting η_t are discussed. Then the emission estimates supplied by the OAP are presented. Finally, the two performance parameters required for the analysis, the ratio of specific weight to brake horsepower ratio (lb/bhp), and the bsfc are covered.

5.2.1 OTTO (SIE) CYCLE

The ideal Otto cycle is composed of isentropic compression and expansion with constant-volume heat addition and rejection (Fig. 5-1a). Its thermal efficiency (Fig. 5-1a) is given by:

$$\eta_{t_{ideal}} = 1 - r_v^{1-\gamma}, \qquad (5\text{-}1)$$

where r_v is the adiabatic compression ratio and γ is the ratio of specific heats. Increasing r_v beyond 10 yields only small improvements in $\eta_{t_{ideal}}$, which is theoretically independent of the load. A carburetor supplies a fuel-air mixture to the engine intake at a relatively constant fuel/air ratio not far from stoichiometric. Engine output (load) is controlled by varying (throttling) the air flow. Combustion efficiencies are high (~ 98%). Average cylinder temperatures are high, generally 5000°R, and the combustion process can be described as a flame propagating through the mixture. Final combustion pressures are generally near 1000 psia, as the combustion is essentially completed at constant volume before expansion begins.

The engine, at a fixed throttle setting, delivers a relatively constant torque, and its output is roughly proportional to engine speed (rpm). A typical (Ref. 57) wide-open throttle (WOT) performance map is shown in Fig.

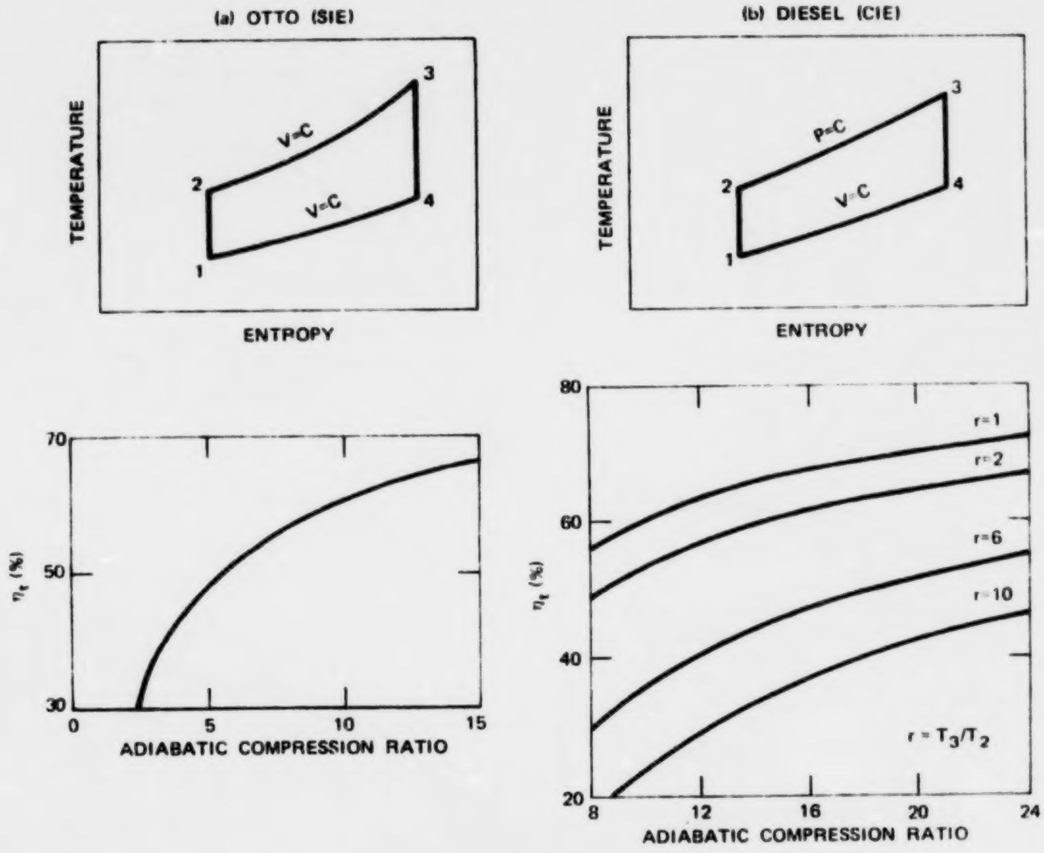

FOUR-CYCLE OTTO OR DIESEL

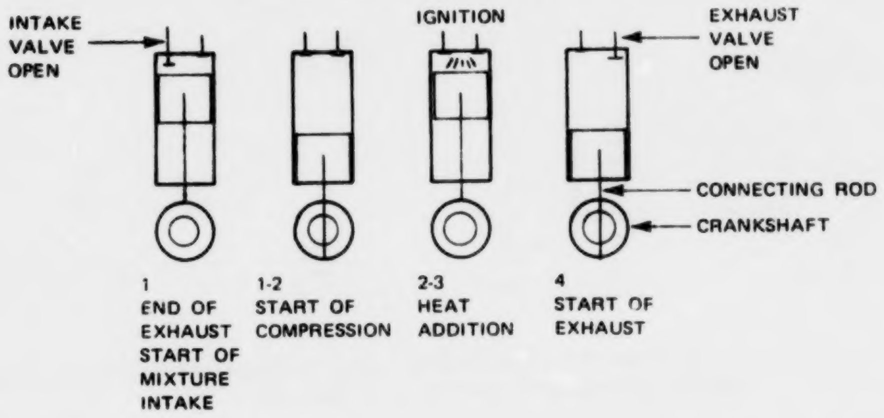
INTAKE VALVE OPEN
IGNITION
EXHAUST VALVE OPEN
CONNECTING ROD
CRANKSHAFT
1
END OF EXHAUST
START OF MIXTURE INTAKE
1-2
START OF COMPRESSION
2-3
HEAT ADDITION
4
START OF EXHAUST

Fig. 5-1 IDEAL CYCLES (T-S DIAGRAMS), IDEAL THERMAL EFFICIENCIES (η_t) AND SIMPLE CONFIGURATIONS OF HEAT ENGINES

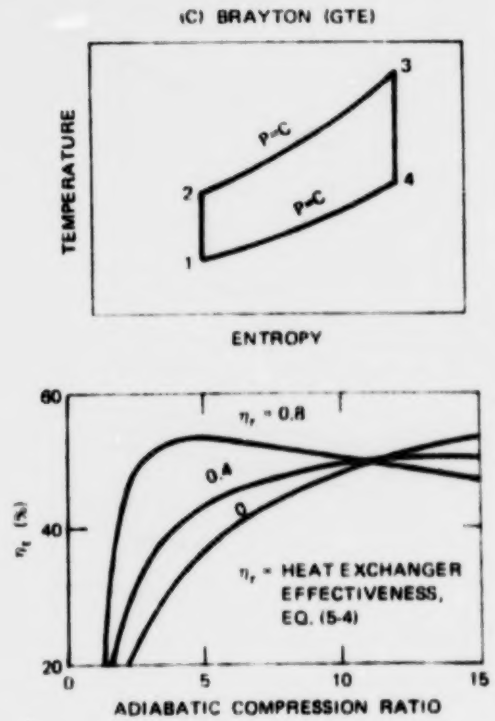

SINGLE-SHAFT GAS TURBINE CYCLE WITH REGENERATOR

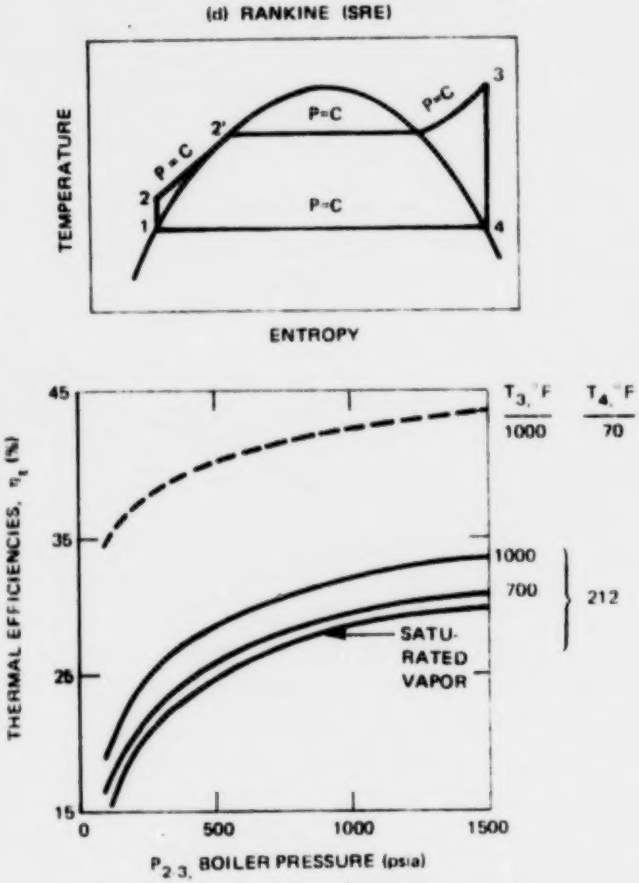

SIMPLE RANKINE CYCLE; EXPANDER IS EITHER TURBINE OR RECIPROCATOR

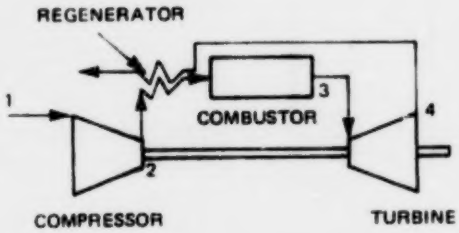
REGENERATOR
1
2
3
4
COMBUSTOR
COMPRESSOR
TURBINE

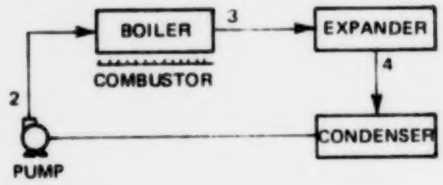
BOILER
3
EXPANDER
COMBUSTOR
4
2
PUMP
CONDENSER

Fig. 5-1 (Cont'd) IDEAL CYCLES (T-S DIAGRAMS), IDEAL THERMAL EFFICIENCIES (η_t) AND SIMPLE CONFIGURATIONS OF HEAT ENGINES

5-2a. The SIE characteristics normally quoted are the maximum values of bhp and torque (at the output shaft) and the minimum value of bsfc for the WOT conditions. However, the engine seldom operates at those conditions and is, in fact, not capable of sustained operation there; the bhp_{max} indicates instead the acceleration capability of the engine. A performance map of a six-cylinder SIE (Ref. 58) for four throttle angle settings (80° throttle is the WOT) is shown in Fig. 5-2b. Also shown, by a plus, is the operating point for a 4500-pound vehicle cruising at 60 mph. The minimum bsfc curve generally corresponds closely to the WOT curve, and the bsfc increase (η_t decreases) as the throttle is closed. As evident from the 60-mph point, the SIE generally is operated at relatively low load; it may be operated at less than 10% full load for 90% of its life (Ref. 59).

Most of the current SIE's for vehicle application (Ref. 60) use 4, 6, or 8 cylinders in in-line, opposed, or V-type cylinder arrangements. Compression ratios range from 8.3 to 11.3; maximum powers from 90 to 460 bhp; and peak rotational speeds, from 4000 to 6000 rpm.

5.2.2 DIESEL ENGINE (CIE)

The ideal CIE cycle is characterized by isentropic compression and expansion with constant-pressure heat addition and constant-volume heat rejection (Fig. 5-1b). For this cycle, $\eta_{t_{ideal}}$ (Fig. 5-1b) is influenced by the compression ratio r_v and a parameter variously termed the "fuel cutoff ratio" or "isentropic ratio" r, defined as the heat-addition temperature ratio, $r \equiv T_3/T_2$:

$$\eta_{t_{ideal}} = 1 - r_v^{1-\gamma} [r^{1-\gamma}/\gamma(r-1)] \, . \tag{5-2}$$

Thus, $\eta_{t_{ideal}}$ differs from that for the Otto cycle by the bracketed term in Eq. (5-2), which is always greater

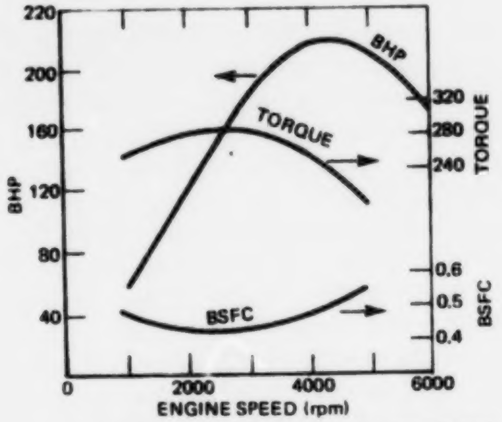

(a) WIDE-OPEN-THROTTLE CHARACTERISTICS

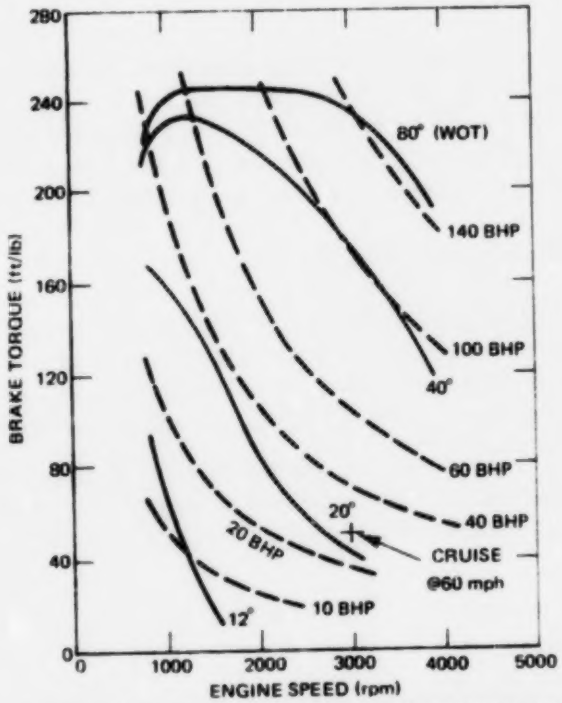

(b) TORQUE, POWER, AND SPEED VERSUS THROTTLE ANGLE

Fig. 5-2 SPARK-IGNITION ENGINE CHARACTERISTICS

than one and is related to the load (i. e., heat addition). For the equivalent r_v the SI cycle is more efficient than the CI cycle; however, in practice r_v for the CIE is 15 to 20 as compared to 8-10 for the SIE, so that CIE's generally have the lower bsfc's.

Mechanically, the 4-cycle arrangement in Fig. 5-1a also is used for the CIE. Air only is inducted through the intake valve (the air supply is unthrottled) with fuel being injected into the cylinder at the end of the compression stroke. The output is controlled by varying the amount of fuel injected. Combustion is initiated by self-ignition as a result of the high r_v. The combustible mixture is heterogeneous, and the combustion process can be described as one of localized burning at a number of points (i. e., wherever the fuel is) throughout the cylinder. The localized burning probably is at nearly stoichiometric conditions although the overall air/fuel ratios are quite lean, varying from 100 at idle to 20 at full load.

The CIE is built heavier than the SIE because its more rapid pressure rise results in higher stresses and vibration (final pressures in the two engines are essentially equivalent). It also has a higher initial cost because of its fuel injection system and its design for durability. For industrial vehicles its high initial cost is outweighed by its lower operating and maintenance costs. Its marine use is attributed primarily to its lower fire hazard (hence, lower insurance costs) because of the use of less volatile fuels (Ref. 57). Its tendency to smoke can be eliminated by proper fuel injector adjustment, but its objectionable odor remains a problem (Ref. 6).

Current "off-the-shelf" CIE's (Ref. 60) have from 1 to 18 cylinders and are rated from 8 to 400 bhp. Compression ratios vary from 10 to 34 with maximum engine speeds up to 4200 rpm. Over 400 models are available. Only eight production passenger cars (all European) are offered with CIE's.[1] The Mercedes Benz model 200 passenger car can be purchased with a CIE (model 200D) or SIE (model 200). Both are 4-cylinder, in-line engines, and they have equal displacements. The CIE is rated at 65 bhp at 4200 rpm; the SIE, 116 bhp at 5000 rpm. The CIE-powered car is 150 pounds heavier, takes 46% longer to pass a 50 mph vehicle (Ref. 61), and has a 20-mph lower maximum speed (Ref. 62).

5.2.3 GAS TURBINE (GT) CYCLE

The GT (Brayton) (Fig. 5-1c) is composed of isentropic compression and expansion with constant-pressure heat addition and rejection. For the simple Brayton cycle:

$$\eta_{t_{\text{ideal}}} = 1 - \frac{1}{\theta} . \qquad \theta = r_v^{(\gamma-1)/\gamma} . \qquad (5\text{-}3)$$

The GT cycle, for aircraft and vehicular applications, is generally an open cycle and consists, in its simple form, of a compressor and turbine mounted on a common shaft with a combustion chamber between them. Engine output is reduced by reducing the amount of fuel, thereby resulting in a lower heat addition, a lower rotational speed, and hence a decrease in r_v and thus in $\eta_{t_{\text{ideal}}}$ per Eq. (5-3). It is this unfortunate characteristic, the increase in bsfc as the load is decreased, that has stymied the acceptance of the open-cycle gas turbine for vehicular use. To increase η_t at part load, the waste heat in the exhaust gas (at temperature T_4) is transferred via a heat exchanger (Fig. 5-1c) to the compressor exit (temperature T_2). Defining the heat exchanger effectiveness η_r as the fraction of the temperature difference transferred:

---

[1] The Land Rover (Great Britain), the Volga Rover, and MZMA-Scaldia (Soviet Union), Mercedes 200-D (Germany), Peugeot-204 (France), and the ISUZU-Bellett 1800D, Datsun 2L130 and Nissara Cedric Q130 (Japan) (Refs. 60 and 62).

$$\eta_r \equiv (T_4 - T_2)_{\text{tran}} / (T_4 - T_2)_{\text{max}} \quad . \qquad (5\text{-}4)$$

the ideal thermal efficiency (Fig. 5-5b) for the regenerative Brayton cycle is:

$$\eta_{t_{\text{ideal}}} = \left(1 - \frac{1}{\theta}\right) \left[1 - \frac{\eta_r}{\theta} \frac{(T_3/T_1) - \theta^2}{(T_3/T_1) - \theta}\right]^{-1} \quad , \qquad (5\text{-}5)$$

where T_3 is the combustor exit temperature, and T_1 is the freestream ambient temperature. When $\eta_r = 0$, i.e., no regeneration, Eq. (5-5) reduces to Eq. (5-3). For $r_v \gtrsim 10$, regeneration is ineffective (η_t drops in Fig. 5-1c for $\eta_r = 0.8$).

Two types of heat exchangers have been developed, recuperative (stationary) and regenerative (rotary). The latter type is smaller but suffers from sealing difficulties. Heat exchangers increase the complexity, cost, weight, and size of the engine but improve the fuel economy (particularly at part load) and reduce the exhaust temperatures and hence the turbine noise (Ref. 63). Effectiveness ratios η_r are as high as 0.90 (Ref. 64).

The combustor is normally a simple can with fuel being injected, in a cone-shaped spray, into the primary air that enters through holes in the can's head-end dome. The local fuel-air equivalence ratios (ER's) are generally from 0.8 to 1.2 in the primary combustion zone. Secondary air is injected into the burned mixture through larger holes to reduce the combustor exit temperature to a level (~ 1700°F) dictated by turbine material limitations. Resulting overall ER's range from as low as 0.05 at idle to 0.20 at full load. Combustion efficiencies are generally high (98 to 99%). Considerable research has been done on emissions (Refs. 65 through 73).

Over twenty firms (Ref. 74) have developed GTE's for vehicular application over the past decade, but not until 1971 was a plan for mass-production for trucks and buses announced (Ref. 75). Various cycle modifications have been used to improve part-load economy. In addition to a heat exchanger, all vehicular units developed to date use a separate turbine (the power turbine) mounted on an independent shaft, so that the main turbine is not strongly influenced by load variation. Intercooling between multiple compressor stages and reheat between multiple turbines have also been used (e. g., Ford, Ref. 76). The power turbine has also been equipped with variable blades (e. g., Chrysler, Ref. 77) in an effort to improve acceleration response and for engine braking. Great care is taken to reduce weights of rotating members to improve acceleration response (i. e., minimize inertia). The GTE is strongly influenced by the ambient temperature T_1 — the output drops sharply as T_1 is increased, because compressor work is increased and the net work/turbine work ratio is low (Ref. 57). General Motors Corp., for example, designs and rates their engine at 100°F.

An added problem to the development of a small GTE is the effect of small scale on component efficiencies, which decrease as size is decreased, due largely to the greater surface-area/mass-flow ratio, which increases friction loss. In addition, rotational speeds increase as size decreases, resulting in smaller manufacturing tolerances on the rotating parts to reduce unbalancing forces (Ref. 78). Compressors are, in general, of the single-stage radial type with $r_v = 3\text{-}4$ and efficiencies near 80%. Compressor and power turbines are generally of the axial type and have efficiencies near 85%.

Williams (Ref. 79) has stated that GTE's for automobiles could be developed for mass production in a form suitable for public acceptance by 1978, but others have said 1980 (Ref. 59).

5.2.4 RANKINE CYCLE

The ideal Rankine cycle is a closed thermodynamic cycle with constant-pressure heat addition (boiler) and rejection (condenser) and isentropic compression (pump) and expansion (reciprocater or turbine). The previous cycles have been discussed in terms of their idealized behavior, and the question of a working fluid did not appear, although it was assumed for the efficiency relationships that the fluid was an ideal diatomic gas with a specific heat ratio γ of 1.4. The Rankine cycle, in contrast, depends strongly on the heat of vaporization of the working fluid and the boiler and condenser temperatures. Figure 5-1d shows the cycle on the TS diagram for a fluid with the characteristic dome-shaped phase diagram (e.g., water). The region to the left of the dome represents the liquid state; to the right, superheated vapor. The region enclosed by the dome is the "wet mixture" region. Heat addition occurs at constant pressure (2-2'-3'-3). The left edge of the domed curve is the saturated liquid line; the right edge, the saturated vapor line. Heat addition occurs from 4 to 1. The thermal efficiency of the cycle is given in terms of enthalpies:

$$\eta_t = (h_3 - h_2 - h_4 + h_1)/(h_3 - h_2) \quad (5\text{-}6)$$

For steam as the working fluid (Ref. 80), the favorable effects of higher boiler pressure P_3 and boiler temperature T_3, and lower condenser temperature T_4 are shown in Fig. 5-1d.

The steam engine found an automotive application in 1769 in France (Ref. 81) and reached its heyday in the United States half a century ago. In 1930 the Doble Corp. discontinued production of its steam automobile and ended the "steamer era." Although a Senate Committee pronounced the Rankine cycle engine a "satisfactory alternative" to the SI engine in 1969 (Ref. 82), citing its low emissions of pollutants, low cost, simplicity, low noise, acceptable performance, no transmission required, and acceptable packagability for automobiles, it is, to date, the least developed of the four powerplants. Only one (GM-SE 101) (Refs. 83 and 84) working and completely installed unit has been reported in detail.

Referring to Fig. 5-1d, an external combustor heats the boiler, which is normally of a once-through monotube construction. The condenser is quite large in relation to the radiator on the SIE or CIE, mainly because of the requirement to dissipate nearly all of the waste heat (SIE and CIE radiators handle only 1/3 to 1/2 of the waste heat). Condenser size depends strongly on the condenser temperature T_4. Both size and η_t increase as T_4 is decreased. Incorporation of a condenser in standard automobile bodies requires enlargement of the front end. Condenser fan horsepower requirements are large (~ 17 hp). The condenser represents a sizable fraction of the weight and cost of the powerplant, and, if it is located where automobile radiators usually are located, a protective structure will have to be incorporated because of its susceptibility to damage in a low speed collision[1]. The expander can be of the reciprocating or turbine type. The majority of paper studies and experimental hardware programs have selected the reciprocating type (Ref. 85).

The General Motors Corp. steam automobile, GM SE-101 (Refs. 83 and 84), incorporates power steering, air conditioning, and a novel continuously variable transmission (Toric). The general conclusions with respect to emissions, fuel economy, weight, size, complexity, reliability,and performance are discouraging. American Oil Co. (Ref. 87), investigating the possible impact of the steam powerplant on the petroleum industry, has concluded that "they [automotive steam propulsion systems] would probably consume 50% more fuel than conventional gasoline engines giving the same vehicle performance." Thermo Electron, with support from OAP and the Ford Motor Co., is attempting to develop an organic Rankine cycle with a reciprocating engine for automobiles. Thermo Electron originally developed a smaller organic reciprocating engine for military application (Ref. 88). A full-scale working unit has not yet been demonstrated, and the results to date (Ref. 89) have involved analytic studies, testing of part-scale components and wood mock-ups. Unfortunately, none of the strong vocal advocates of the Rankine cycle engine (Lear, Williams, Keen, Minto, etc., Ref. 85), has adequately documented his results in the open literature.

---

[1] The vapor cycle engine developed by Minto and presently being developed by Datsun for scheduled production in 1972 (Ref. 86) uses a rotary condenser that results in a reduced size. The boiler is located under the passenger compartment.

5.2.5 EMISSIONS

The primary emissions of present concern are unburned hydrocarbons (HC), carbon monoxide (CO), and oxides of nitrogen (NO_x). In general the HC and CO emissions result from many factors (rich combustion, premature quenching by walls, insufficient reaction times, and poor mixing) all resulting basically in incomplete combustion. Consequently, their concentrations can be reduced in many ways (thermal reactors, afterburners, catalytic converters, etc.). The NO_x (basically NO) problem is a different story. Theoretically calculations based on equilibrium assumptions lead to high concentrations (~ 3000 ppm) in the combustion zone at stoichiometric conditions and very small values upon completion of the expansion to ambient pressures. However, the formation and dissipation of NO is kinetically controlled (Refs. 66 and 90); the NO equilibrium is generally not attained in the burning region because of the relatively slow NO forward reactions (Refs. 66, 73, 91, and 92). The amount that is formed is "frozen" – the reverse reactions cannot occur quickly enough upon early dilution or expansion to reduce the NO concentration. Current research is therefore directed toward methods of decreasing the effective flame temperature and the residence time. Lowering of the flame temperature via lean or rich mixtures and/or dilution by recycling exhaust gas lowers the amount of NO formed (Refs. 66, 70, and 91). Rich mixtures, however, result in increased concentrations of CO and HC. Very lean mixtures result in combustion instability with the attendant inefficient combustion and again increased CO and HC concentrations.

The use of premixed, prevaporized air-fuel mixtures (Ref. 92) and special fuel injection and mixing configurations (Ref. 93) tend to decrease NO_x emissions by allowing lean operation (Ref. 66). For the closed combustors (SIE and CIE), research is directed toward cylinder redesign (Ref. 94), more efficient mixing and, for the SIE, preheated-prevaporized fuel preparation (Ref. 95). Add-on devices (e. g. , catalytic converters) are under intense development for use on current powerplants; however, questions of durability and reliability remain (Ref. 96). It is difficult to relate the many laboratory experimental studies to a mass-produced vehicle installation.

The lowest emission estimates for HC, CO, and NO_x supplied by OAP are shown in Fig. 5-3. We have used the lowest curves supplied (based on claims for manifold reactor, carburetor modification, recirculation, thermal reactor, combustor redesign, and modern combustor technology) because of the presently conceived mode of operation (i. e. , constant-speed, constant-load, on-off mode) of the heat engine, coupled with the assumption that this allows minimum emissions, and the expected time of application (1975 or later). The data are given in brake specific units, BSPE, lb pollutant/bhp-h. An attempt was made, via the open literature, to verify the supplied values, but it became apparent that one could 'pick a number' and locate a piece of data to support it. The OAP estimates supplied are interpreted as steady-state data applicable to different size powerplants.

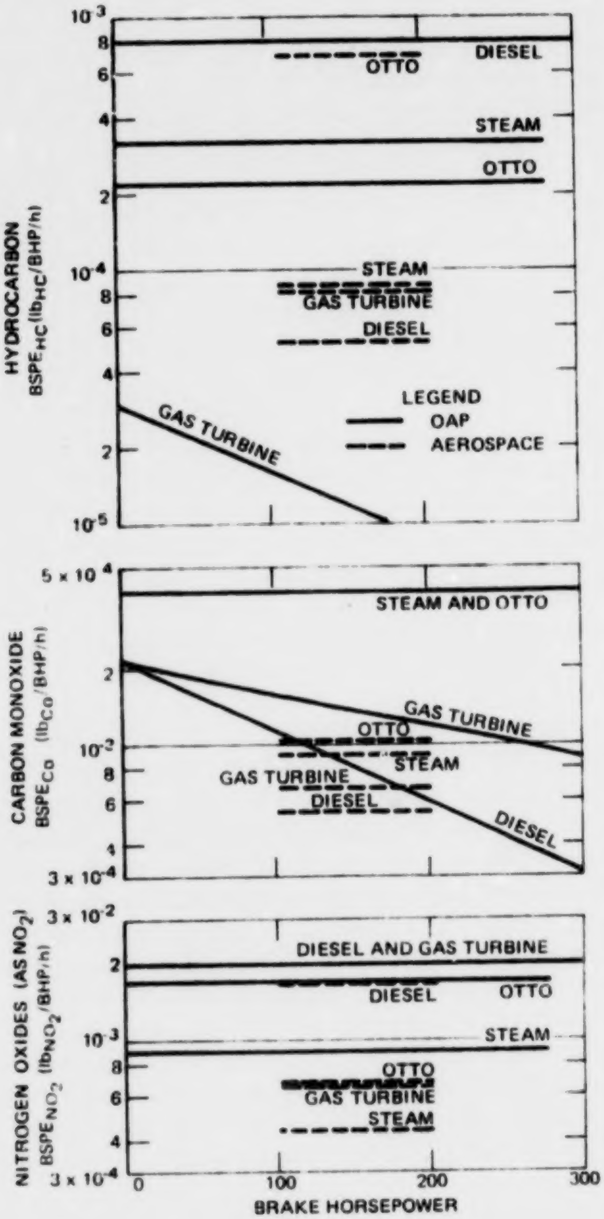

Fig. 5-3 PROJECTIONS OF HC, CO, AND NO_x (AS NO_2) EMISSIONS

Allowances for transient emissions resulting from startup have been incorporated in the computer studies as follows. The TECO data (Ref. 89), based on a continuous combustor experiment for a Rankine cycle powerplant, were used for the factors for these transient penalties, and the same factors were used for all four engines. The steady-state values of HC and CO are increased by factors of 10 and 5, respectively, for a 10-second period. During the startup the engine is fuel-rich and relatively cold, therefore not modified for the startup period. These assumptions, it must be remembered, represent only crude estimates for lack of better data; some engines used in this mode may do better, others worse.

An intensive survey has recently been completed by Aerospace Corp. (Ref. 97) on the available, published and unpublished information on exhaust pollutants from various powerplants. Their 'projected values' also are shown (by dashed curves) in Fig. 5-3 and are generally markedly lower than the values supplied by OAP, except for HC from the Otto engine. The Aerospace projections assume a fixed-speed, fixed-load operation.

The projections of emission characteristics, for the four powerplants under consideration, appear to be open to conjecture. Reference 56 presents data on ways to reduce emissions from the diesel engine, including engine speed effects, and some of these trends may apply for the SIE. Reference 92 gives optimistic projections for the SRE and GTE. The potential probably is there for each type to meet the 1975-76 standards; whether this potential can be achieved in a mass-produced automobile for the life of the vehicle, at a cost and with performance acceptable to the customer, remains to be shown. The major automobile manufacturers apparently are following the course of cleaning up the present SI engine as opposed to developing another powerplant.

5.2.6 ENGINE PERFORMANCE

The two performance parameters required for the analytic studies of the hybrid system are the engine specific weight (lb/bhp) and the brake specific fuel consumption bsfc (lb fuel/bhp-h). Since the SIE's are rated by manufacturers at the maximum bhp, we have reduced the published bhp ratings by 40% to arrive at "continuous" ratings for Fig. 5-4a. The engine weight does not include the exhaust system, radiator, battery, or fuel tank. Data (Ref. 60) for the CIE's are shown in Fig. 5-4b; since CIE's are normally rated on a "continuous" bhp basis, the published values were not modified. For each engine, only the engine weight is included.

The GT data (Refs. 64 and 74) in Fig. 5-4c are for single-shaft, double-shaft, and double-shaft-with-heat-exchanger units. For the GTE and SRE, the methods of horsepower and engine weight rating have not been defined. We have assumed that the horsepower ratings are on a "continuous" basis and that the weight includes the complete engine except for battery and fuel tank. Data for steam engines are sparse and difficult to assess because of a lack of documentation. The available information (Refs. 83, 85, 98, and 99) for experimental hardware and paper study predictions is shown in Fig. 5-4d. The curves in Figs. 5-4a - 5-4d are being used in the analytic studies; they are replotted, for comparative purposes, in Fig. 5-5. The curves for the diesel and SI engines represent the lower bounds of the data and reflect the assumptions that the lower specific weights represent better designs and that powerplants designed for a hybrid vehicle (fixed-load, relatively narrow speed range operation) will result in improved specific weights. For the Rankine cycle engines the three points quoted by Lear and Minto fall below the chosen curve. The curve for the GT specific weights is assumed to represent single shaft engines without a heat exchanger. The effects of control devices have not been considered, since it has not as yet been decided what control techniques are to be adopted. It should be emphasized that the values represent bare engine horsepowers and weights. (They are modified in the analysis to include power and weight requirements of auxiliary

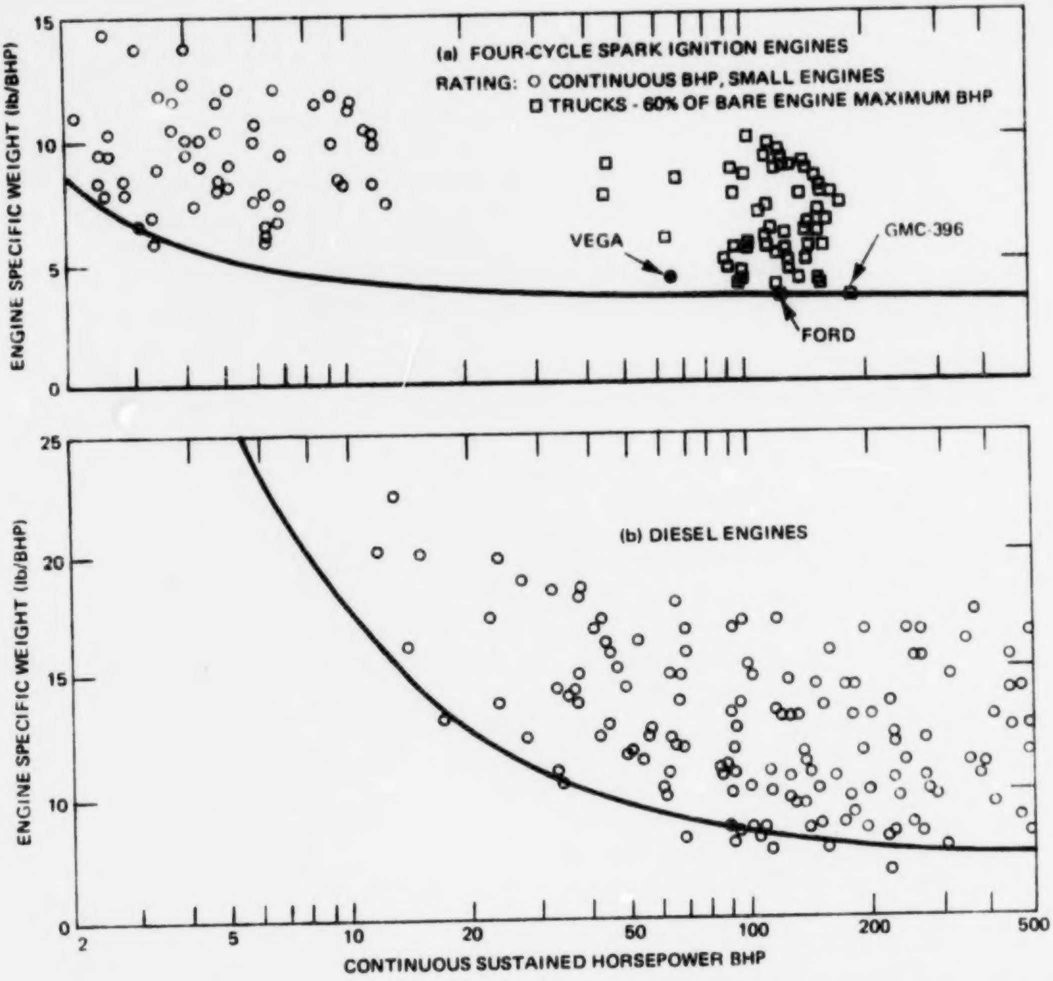

Fig. 5-4. SPECIFIC WEIGHT VERSUS BRAKE HORSEPOWER FOR THE FOUR HEAT ENGINES

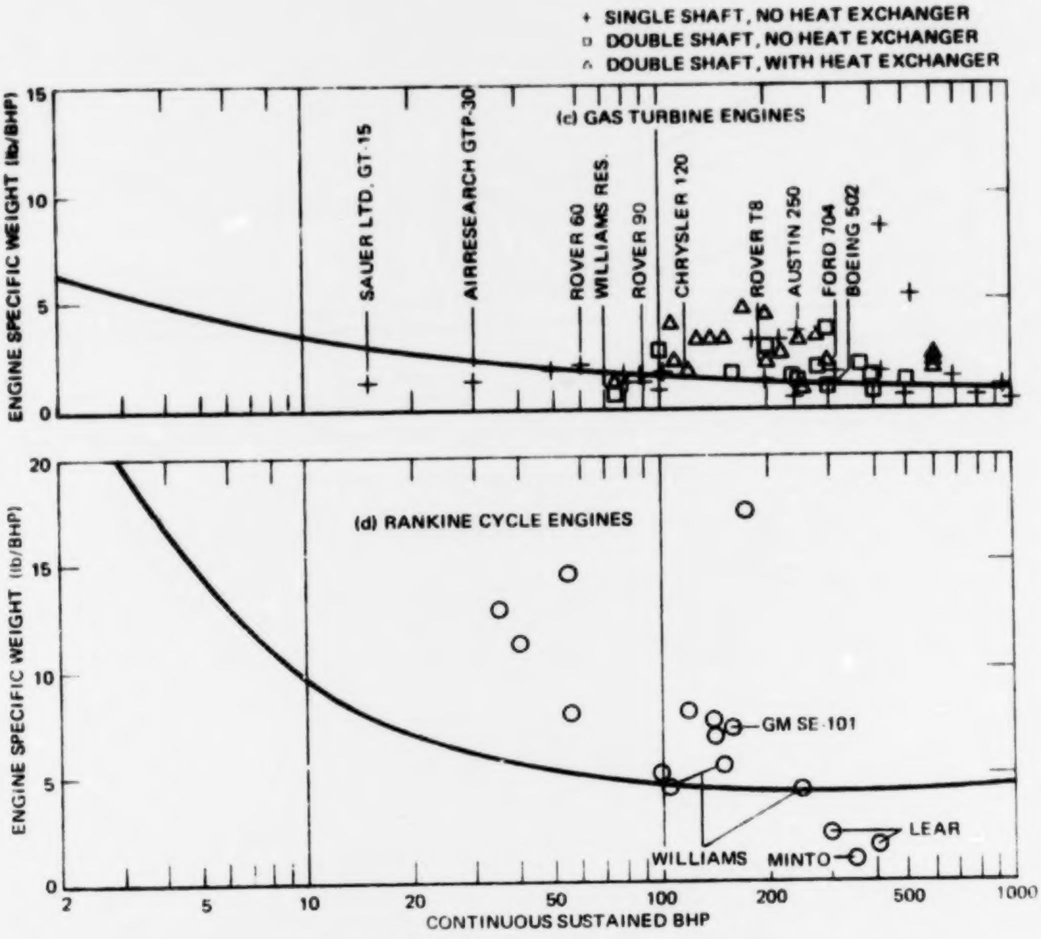

Fig. 5-4 (Cont'd) SPECIFIC WEIGHT VERSUS BRAKE HORSEPOWER FOR THE FOUR HEAT ENGINES

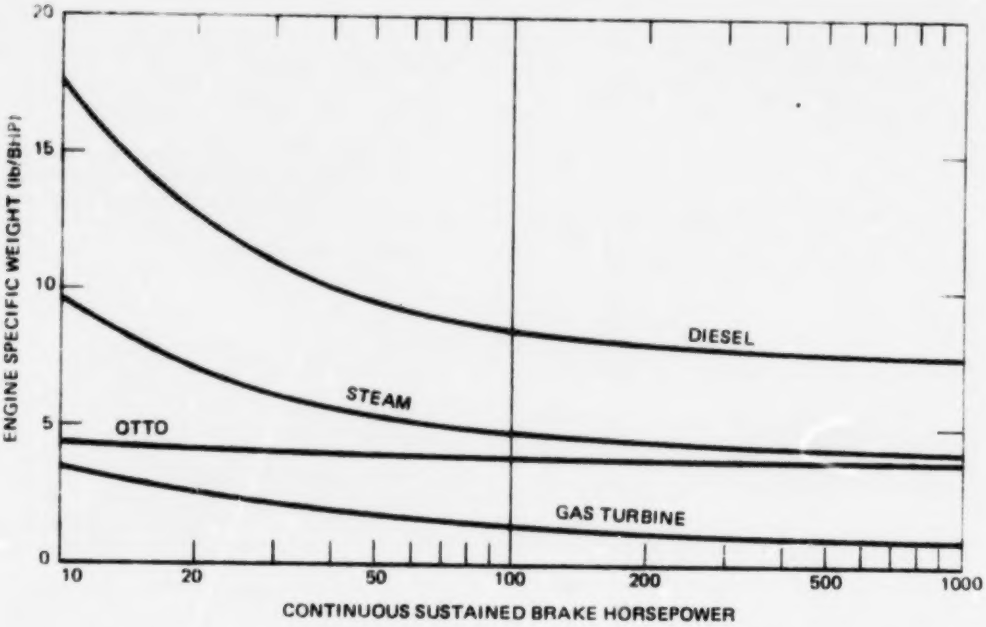

Fig. 5-5 COMPARISON OF SPECIFIC WEIGHTS OF THE FOUR ENGINES

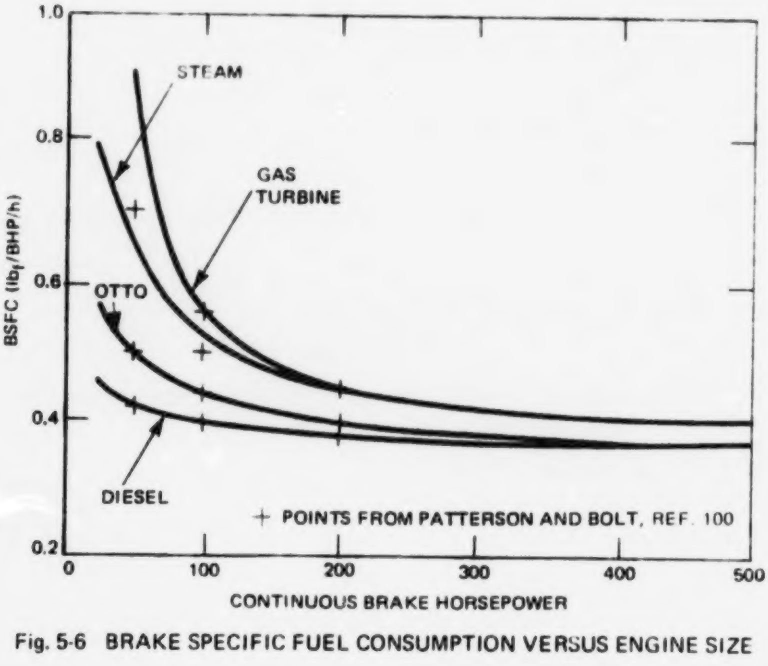

Fig. 5-6 BRAKE SPECIFIC FUEL CONSUMPTION VERSUS ENGINE SIZE

devices, cooling, exhaust system, fuel, etc.) For a given bhp the CIE is heaviest, followed by the SRE, SIE, and GT. For a 100-bhp engine, for example, the weights are 850, 460, 340, and 150 pounds, respectively.

The values for bsfc are more difficult to attain. No comprehensive listing for any of the powerplants was found. We are using the values reported in Ref. 100 and plotted in Fig. 5-6 with the resulting curves. The values are presumed to be minimum values for each engine and can probably be improved because of the operating mode (limited speed range at full load) envisioned for the hybrid application. The curves reflect the lower efficiencies for small engines. The gas turbine engines have the highest bsfc's in the smaller sizes and show the greatest improvement as size is increased. Following the GTE in order of decreasing bsfc are the steam, Otto, and diesel engines. At 100 bhp, for example, the Otto, steam, and gas turbine engines have fuel consumptions that are by 10, 33, and 40% higher, respectively, than the diesel engine values.

5.2.7 CLOSURE

A number of authors (e.g., Refs. 100 through 103) have attempted to compare various powerplants in terms of emissions, cost, size, performance, weight, feasibility, etc. The conclusions reached often depend solely on the assumptions advocated for a particular engine. They are subject to debate since the comparisons normally involve comparing a paper study engine to a mass-produced engine. In addition, it is difficult to make valid comparisons since the SI and CI engines are presently under intense study by automobile manufacturers as to methods of reducing emissions through engine redesign and/or emission control devices.

For the hybrid vehicles under study, it appears that for the commuter car, family car, and delivery van the SIE is the first-choice powerplant for a near-term vehicle (1975). For the bus, the diesel may be the first choice, but gas turbines also look very attractive. Smaller engines suffice for the hybrid vehicles as compared to their conventional current counterparts, but the relative specific fuel consumptions of the gas-turbine and Rankine cycle engines become even poorer in the small sizes. Oversize GTE's may be of interest to improve bsfc, as discussed in Section 5.5. The potential for lower emissions from current CI and SI engines may be enhanced by the proposed fixed-load operation. The GTE is a clear second choice for all hybrid vehicles in 1978-80, and the hybrid mode of operation might allow simplification of it, e.g., elimination of the second shaft and possibly the regenerator. Improvements in both weight and volume would appear to be needed for use of diesel or Rankine cycle engines in hybrid systems for the cars or the van, if appreciable weight or volume is to be left for a flywheel system by the approach described in the following subsections.

5.3 VEHICLE REQUIREMENTS AND WEIGHT AND VOLUME CONSIDERATIONS

A primary premise to the approach in this section is that it is desirable to maximize energy storage in order to provide significant flywheel-only (nonemitting) ranges for operation through cities. Therefore, the first step is to establish the weight W_s and volume Vol_s available for propulsion in each vehicle type, within limits specified by OAP (Ref. 104) at the outset of this study. Within these limits, some modifications are used on the basis of prior studies by others of present-day vehicles. The propulsion system weight results herein are conservative in two respects: they are generally below the OAP limits, and they could be further increased in proportion to total vehicle weight by increased use of lighter or more efficient materials (plastics and composites) in the bodies and accoutrements of future vehicles.

The next step is to break down W_s and Vol_s to determine the weight left for the flywheel subsystem itself

(W_{fwo}) or in the case of hybrid propulsion systems, the sum of the weights of the heat engine (W_e) and the flywheel subsystem (W_{fw}). In the latter case, the heat engine is sized by a certain critical performance requirement for each vehicle type (e. g. , maximum sustained cruise speed) and by interpolation of data for current engines to achieve that performance. Finally, assumptions on other parts of the flywheel subsystem lead to a value for the flywheel rotor weight W_r.

The situation is not really that simple, of course, because certain items (e. g. , fuel tank size) are iterated even in the present, relatively simple computer program, and many other items would be subject to iteration in the detailed design of a specific vehicle. The greatest uncertainties at present are flywheel containment weight (see Section 4. 4) and transmission weight, volume, and efficiency. In these preliminary baseline studies, transmission weights and volumes are assumed to be comparable to those of present-day automatic transmissions for given horsepower requirements and vehicle duties, and constant (average) efficiencies of 98. 5% for flywheel charging (engine to flywheel) and 73% for the drivetrain (flywheel to vehicle drive wheels) are used. For some of the cases covered, the transmission weight allowance may prove to be too optimistic, but such factors on the optimistic side are balanced somewhat by the aforementioned conservative approach to total propulsion system weight W_s.

5. 3. 1 VEHICLE SPECIFICATIONS AND RESULTING FLYWHEEL SUBSYSTEM WEIGHTS

The vehicle specifications supplied by OAP (Ref. 104) are listed in Table 5-1.

The total propulsion system is defined to include the engine, battery, radiator, exhaust system, loaded fuel tank, transmission, and driveline (propeller shaft and rear axle assembly). The values of W_s and Vol_s supplied

Table 5-1

Performance Specifications for the Four Vehicles

Parameter	Family Car[1]	Commuter Car	Bus	Van
V_{max} (mph)	80	70	40	40
V_{grade}, mph at Grade (%)	40 at 12	33 at 12	6 at 20	8 at 20
R_{grade} (miles)	8	4	0.5	0.5
$\bar{a}_{max}$ (mph/s)	4-6	5	3.2	4
Jerk Rate (mph/s)	6	5	2	4
R (miles)	200	50	18	60
W_c, Curb Weight (pounds)	3500(4300)	1400	20 000	4500
W_ℓ, Fully Loaded Weight (pounds)	4000(5000)	1700	30 000	7000
C_D, Drag Coefficient[2]	0.50	0.35	0.85	0.85
A, Frontal Area (ft^2)	25	18	80	42
HP_{acc} (with air conditioner)	12.6	5.7	39.3	2.3 (no A/C)
HP_{AC}, Air Conditioner (hp)	5.9	4.0	27.0	0

[1] These values were given in the summer of 1970 (Ref. 104). Current OAP specifications for the family car are much more complex and lead, among other things, to the higher weights shown in parentheses.

[2] Aerodynamic drag only. A tire resistance coefficient, $f = 0.01 + 1.1 \times 10^{-6} V^2$, where V is in mph, has been assumed to compute tire friction load (Ref. 108).

by OAP (Ref. 104) are listed in Table 5-2 and are based on two previous OAP-funded studies (Refs. 105 and 106). The values of W_s evidently are averages of the A. D. Little, Inc. weight estimates (Ref. 106) based on "conventional" and "lightweight" body construction (magnesium frames and plastic panels), which would permit higher W_s for a given vehicle curb weight W_c. The "conventional" construction weights from Ref. 106 were based on Hoffman's (Ref. 107) data for 1966 automobiles and estimated values for the van and bus. The Vol_s estimates for the commuter car and bus correspond to those from the Battelle study (Ref. 105).

The W_s values used herein are listed under "APL" in Table 5-2. For the cars they are based on Hoffman's (Ref. 107) average percentage weight distributions for 1966 cars of conventional construction. For the van, we have modified the Hoffman results to account for the lower powerplant mass fraction given for a van with the appropriate curb weight in Ref. 60. The bus weight fractions have been derived from a weight breakdown for the General Motors T8H-5305A model bus (Ref. 110). Table 5-3 shows the corresponding weight breakdowns for the four vehicles, and Tables 5-4 and 5-5 present breakdowns of W_s and Vol_s for the first- and second-choice powerplants. Radiator, exhaust system, and battery weights are related to engine weight and are based on Hoffman's values (Ref. 107 and the GM bus data (Ref. 110); corresponding volumes are based on data from Ref. 60 for the Diesel (CI) and Otto (SI) engines and from Ref. 74 for the gas turbine (GT) engine. The fuel tank is sized for the amount of fuel required to travel the specified range at V_{max} using gasoline with a density of 43 lb/ft^3. Transmission weights are assumed to be equivalent to those for present vehicles, and volumes have been derived from the Battelle study.

Tables 5-4 and 5-5 give the weights and volumes available for the flywheel subsystem (rotor, hub, shaft, seals, bearings, and case) for the hybrid (W_{fw} and Vol_{fw})

Table 5-2

Propulsion System Total Weight and Volume

Vehicle	W_c (pounds)	W_s, Total Propulsion System Weight (pounds)				Vol_s[1] (ft^3)
		Conventional	Lightweight	OAP	APL	
Family Car	3500	1250	1750	1500	1138	30. 9
Commuter	1400	500	700	600	455	16
Van	4500	1400	2000	1700	1323	42
Bus	20 000	5000	7000	6000	5940	175

[1] Vol_s = propulsion system total volumes (ft^3) suggested by OAP; the value for the family was originally 28 ft^3, but was raised by OAP to 30. 9 ft^3 in January 1971; the vans studied by Battelle (Ref. 105) gave 28 ft^3, but OAP raised this allowance to 42 ft^3.

Table 5-3

Vehicle Weight Breakdowns

	Commuter Car	Family Car	Van	City Bus
Body, Trim, etc.	706	1763	2407	10 400
Suspension	84	210	270	1040
Wheels	35	88	113	660
Tires	45	112	144	700
Brakes	53	133	171	1120
Steering	22	56	72	140
Propulsion, W_s	455	1138	1323	5940
Rear Axle	60	151	194	1280
Transmission	66	165	212	520
Powerplant (= W_{fwo})[1]	329	822	917	4140
Curb Weight, W_c	1400	3500	4500	20 000
Loaded Weight, W_ℓ	1700	4000	7000	30 000

---

[1] For hybrid vehicles, powerplant includes engine, radiator, loaded fuel tank, battery, and flywheel system weight (W_{fw}); for flywheel-only vehicles, entire weight is available for flywheel (W_{fwo}).

Table 5-4

Breakdowns of Propulsion System Weight W_s (pounds) for Hybrid Vehicles

	Bus 134 bhp[1]		Family 94 bhp		Commuter 33 bhp		Van 36 bhp	
	CI	GT	SI	GT	SI	GT	SI	GT
Engine	1102	164	357	131	131	70	142	72
Battery	95	42	31	34	11	18	12	19
Fuel Tank	143	178	115	147	29	67	64	143
Radiator	102	0	33	0	12	0	13	0
Exhaust	95	0	31	0	11	0	12	0
Transmission and Axle	--1800--		-- 316--		-- 126--		-- 406--	
Subtotal	3337	2184	883	628	320	280	649	640
OAP Allocation, W_s	--5940--		--1138--		-- 455--		--1323--	
Left for Flywheel, W_{fw}	2603	3756	255	510	135	175	674	683

[1] Engine shaft output bhp; engine sized to sustain V_{max} shown in Table 5-1.

Table 5-5

Breakdowns of Propulsion System Volume Vol_s (ft^3)

	Bus 137 bhp		Family 95 bhp		Commuter 34 bhp		Van 37 bhp	
	CI	GT[1]	SI	GT	SI	GT	SI	GT
Engine,[1] Radiator, and Battery[2]	31.6	5.4	15.0	4.2	11.1	2.3	13.6	2.3
Fuel Tank[3]	3.7	4.5	2.9	3.7	0.7	1.7	1.6	3.6
Exhaust[3]	1.9	0	0.6	0	0.2	0	0.2	0
Transmission[4]	-- 5.8		-- 1.1 --		-- 0.4 --		-- 1.4 --	
Rear Axle[3]	-- 12.8 --		-- 1.5 --		-- 0.6 --		-- 1.9 --	
Total	55.8	28.5	21.1	10.5	13.0	5.0	18.7	9.2
OAP Allocation, Vol_s	-- 175.0 --		-- 30.9 --		-- 16.0 --		-- 16.0 --	
Left for Flywheel, Vol_{fw}	119.2	146.5	9.8	17.5	3.0	11.0	23.3	32.8
Flywheel-Only Case, Vol_{fwo}	-- 156.5 --		-- 24.7 --		-- 14.7 --		-- 37.6 --	

[1] Average density of engines in Ref. 74, 31 lb/ft^3.

[2] CI and SI engine volumes increased by 10% to account for radiator.

[3] Assumed overall densities (lb/ft^3): fuel tank, 50; exhaust, 40; rear axle, 100.

[4] Bus, 90 lb/ft^3; others, 150 lb/ft^3 (Ref. 105).

and the flywheel-only (W_{fwo} and Vol_{fwo}) vehicles. It should be noted from Table 5-4 that the heat engine system subtotal weights for the GT and SI hybrid vans are almost equal, 640 and 649 pounds, respectively, even though the bare GT engine is 70 pounds lighter, because such a small gas turbine has a high bsfc (see Fig. 5-15) and requires a larger fuel load (more than double the SI powerplant) to attain the same range. The same characteristic is observed for the commuter car hybrids.

5.3.2 ROTOR WEIGHT AND FLYWHEEL SUBSYSTEM VOLUME

Let us represent the flywheel casing requirements as equivalent to a steel casing with a uniform thickness t_c in the circumferential direction, which is left as a free parameter. The top and bottom end plates, which are parallel to the plane of rotation, are assumed to be equivalent to 1/8-inch-thick steel plates for all cases. The rotor density is assumed to be 0.073 lb/in^3, representative of a composite structure. Clearances of 1/8 inch are allowed between the bar-shaped rotor and the casing. The weights of the shaft, seals, bearings, and support structure are assumed to be equal in total to 10% of the rotor weight.

Prior to settling on an equivalent to a disk configuration and a case thickness t_c of 3/8 inch, some parametric calculations were done for bar rotors. For various values of t_c, rotor half-width-to-radius ratio T/R, and $\ell (= 2R)$, the corresponding rotor weight W_r and total flywheel subsystem volume Vol_{fw} are calculated for a fixed flywheel subsystem weight W_{fw}. Some consequences of the foregoing assumptions for bar rotors are illustrated in Fig. 5-7. For a large W_{fw} (917 pounds), with T/R and t_c fixed at 0.125 and 0.25 inch, respectively, W_r and Vol_{fw} increase slowly as ℓ is increased, because the assumed fixed clearance and case thickness, as well as the volume and the weight of the can's end plates, have second-order

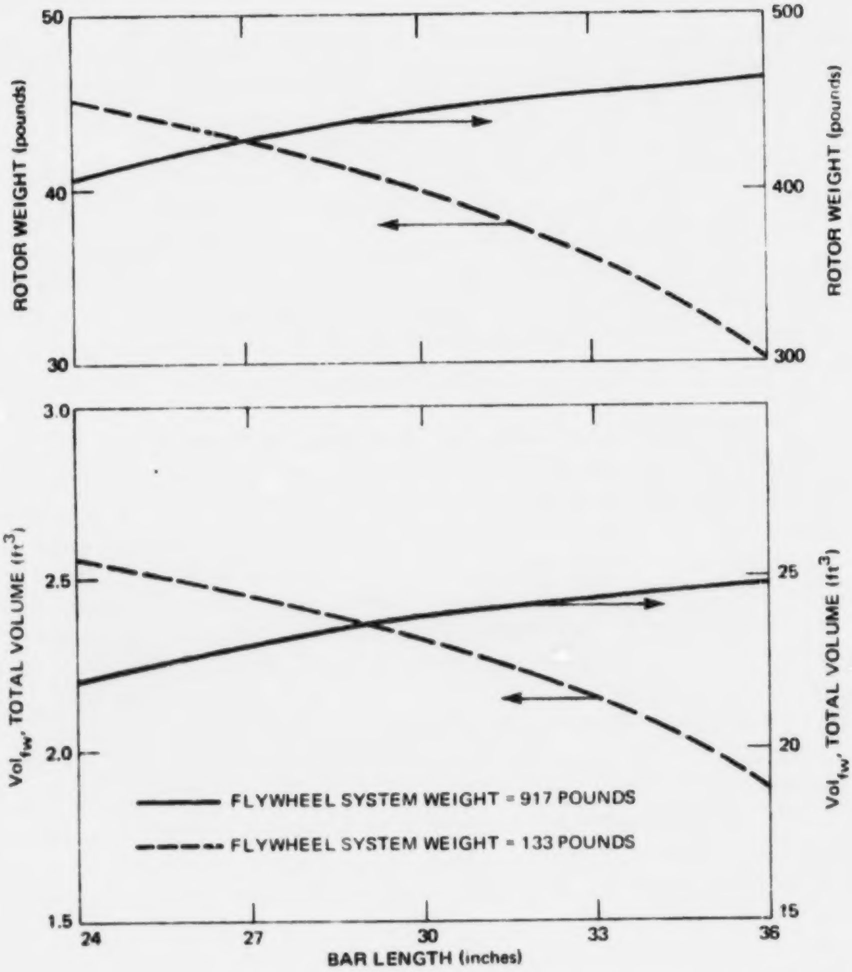

Fig. 5-7 EFFECT OF ROTOR LENGTH ON ROTOR WEIGHT AND TOTAL VOLUME, T_C = 0.25 INCH, T/R = 0.125

effects relative to W_{fw}. For a small W_{fw}, however, effects of these parameters become significant and result in reverse trends. (As ℓ increases here, can height h decreases.)

From such parametric studies, it has been concluded that bar configurations would not exceed the volume limits per se; however, the physical dimensions for very large bar rotors would present installation problems. For example, for the gas turbine/flywheel hybrid bus with a 2960-pound bar rotor, and with ℓ = 48 inches and T/R = 0.188, the required height for the flywheel system would be 9.8 feet. The corresponding disk rotor requires 2.1 feet. For the flywheel-only family car, with ℓ = 24 inches, heights of 4.0 and 1.5 feet result for the bar (T/R = 0.188) and disk, respectively; increasing ℓ to 36 inches would reduce these heights to 1.8 and 0.42 feet, respectively.

For these reasons, as stated in Section 5.1 (and supported by the material presented in Section 4.2, which was actually developed later in the program), the flywheel subsystem weights used in the system studies are equivalent to a disk configuration with a rated specific energy E/W_r of 32 W-h/lb. Because of the lack of a definitive case thickness design philosophy at this stage, a constant 3/8-inch wall thickness has been used. This approach may be considered compatible with a nominal casing design philosophy wherein the external loads are of primary concern. If further test results of the type described in Section 3.3.5, together with safety specifications, establish that a constant percentage of the total energy is to be contained, the case thickness requirements would increase with increasing rotor energy per unit depth. Thus for a disk configuration, t_c would be proportional to the square of the rotor diameter. (If a bar were used, e.g., in a commuter car, t_c would be directly proportional to the width and length of the bar.) The resulting flywheel system weights and volumes used in the performance studies are given in Table 5-6. It is noted again that the

Table 5-6

Flywheel Rotor Length ℓ, Rotor Weight W_r, Can Depth h, Can Volume Vol_{fw}, and Stored Energy E_O for Each System of Table 5-5[1]

Parameter	Bus			Family Car			Commuter Car			Van		
	FO	CI	GT	FO	SI	GT	FO	SI	GT	FO	SI	GT
ℓ (inches)	48	48	48	24	24	24	24	24	24	24	24	24
h (inches)	25.3	15.8	22.9	18.2	5.3	11.2	7.1	2.8	3.6	20.3	14.8	15.0
Vol_{fw} (ft^3)	27.6	17.2	25.0	5.2	1.5	3.2	2.0	0.8	1.0	5.8	4.2	4.3
W_r (pounds)	3278	2019	2964	584	163	353	217	74	103	655	474	481
E_O (hp-h)	1431	880	1293	25.5	7.1	15.4	9.5	3.2	4.5	28.6	20.7	21.0

[1] Equivalent of composite disk flywheel configuration assumed throughout, with equivalent steel case thickness t_c of 3/8 inch. These required volumes are smaller than the available volumes in Table 5-5. FO = flywheel only; first-choice powerplants for near term (CI or SI) and longer term (GT) are listed for hybrid system for each vehicle type (CI = compression ignition diesel, SI = spark ignition Otto, GT = gas turbine).

overall weight limitations assumed are below the NAPCA allowances (except for the bus), as was indicated in Table 5-2.

5.4 DRIVETRAIN CONSIDERATIONS

5.4.1 GENERAL CONSIDERATIONS

In current vehicles the operator directly controls the engine (hence the vehicle) via the throttle and manual or automatic transmission. Appropriate gears (3 to 15) are selected depending on the engine/tire speed ratio and torque requirements. Clutches (torque converter in the automatic) are used during the gear shifting to smooth the transition. A rear axle gear reduction is used, usually about 3.5:1, so that at cruise conditions the transmission speed ratio is essentially unity. The powerplant operates over a wide range of conditions, particularly to attain high accelerations. Current SI engines operate from 500 rpm at idle to 6000 rpm at maximum power (up to 300 bhp). Manual gear box efficiencies are 99% in high gear and 95% in low gear, and corresponding automatic transmission efficiencies are 93 and 87%, respectively (Ref. 109). Specific weights are near 1/2 $\mathrm{lb/bhp_{max}}$ for manual types and 1 $\mathrm{lb/bhp_{max}}$ for automatic types (Ref. 105). The efficiency of the rear axle gear reduction is about 98% at wide open throttle and varies from 85 to 95% at cruise conditions (Ref. 109).

In contrast to these variable input properties of current engines, a flywheel energy storage unit would run at nearly constant speed (in our applications it will slow down by 2 to 10% during one vehicular acceleration from 0 to 60 mph) and could not be used as a means of control. The transmission must, therefore, incorporate a control system as well as the added speed ratio range needed to make up for the essentially constant flywheel speed. Over a longer period the flywheel speed level will vary by a factor of two (for a 75% DOD[1] limit) or perhaps three (89% DOD), so that the transmission speed range must be able to accommodate this additional factor. To achieve these objectives, a controllable, continuously variable transmission (CVT) is required.

For hybrid systems (as well as flywheel-only systems), we assume that the vehicle is driven directly from the flywheel, with the heat engine supplying energy to the flywheel as needed. This approach may permit engine design and operation to reduce emissions[2]. The vehicle performance estimates presented herein are based on an overall engine-to-drive-wheels transmission efficiency of 72%. Overall transmission weights are assumed to be comparable to those for current automatic units and amount to 165 pounds for the family car and 66 pounds for the commuter car. These weights are optimistic for near-term systems, but again it is noted that we have used total propulsion system weights considerably below the OAP allowances for all vehicles except the bus.

An average regenerative recovery of 50% (of the kinetic energy to be removed during decelerations or downhill runs) is assumed for the bulk of these studies, based on a detailed study of the DHEW cycle (Section 5. 4. 7). It will be shown that this regenerative braking recovers some 14 to 17% of total urban cycle energy and thus compensates the lower energy transfer efficiency as compared to present automatic transmissions. Better CVT's should become available over a longer term, and the proposed programmer control (see Section 5.4.5), as opposed to unaided operator control on current vehicles, should lead to gains. In any event, these studies, in agreement with others (Refs. 10 and 111), indicate that the ultimate advantage of using a flywheel for energy storage will depend on the development of a suitable drivetrain with good transmission and dynamic braking efficiencies.

---

[1] DOD = depth of discharge, defined as percentage of total energy already extracted, relative to that contained at full rated speed and charge. In comparison, the DOD for long-life batteries seldom exceeds 10%.

[2] An alternative dual-drive arrangement would be advantageous for hybrid systems having relatively low energy storage capabilities (smaller flywheels, as suggested by Lockheed, Ref. 2) or limitations on energy withdrawal rate (batteries) and thereby requiring dual or combined drive systems (c. f., Ref. 19), but they require additional controls or couplings to accomplish the dual driving function.

5.4.2 ENGINE-TO-FLYWHEEL (CHARGE) TRANSMISSION

The engine-to-flywheel link may be as simple as a mechanical clutch, provided that (a) a 2:1 speed range for the engine (corresponding to flywheel speed range) can be tolerated without increasing emissions appreciably, and (b) a satisfactory solution to the problem of start-up when complete flywheel rundown (e.g., after several days of parking) has been allowed to occur. One approach would be to spin the flywheel up by an external electric motor. These concepts are assumed herein. (The 2:1 engine speed range might be a problem with gas turbine engines; it might be necessary to reduce the speed range to 1.33:1 by limiting the flywheel DOD to 44% instead of 75%, which would require a 70% increase in flywheel rotor weight to maintain a given flywheel-only range.)

If, however, it should prove that this energy transfer should be accomplished with a fixed engine speed to minimize emissions, a variable-speed transmission will be required. Since no external control is needed, a torque converter or fluid coupler would work, but the low overall efficiencies (60 to 70%) of these devices make them undesirable. Attainment of a high efficiency would require a second CVT transmission similar to the flywheel-to-wheels transmission discussed in the next section, but smaller, since only half the power level is required. This choice is undesirable because of the penalties in efficiency, weight, volume, and cost.

5.4.3 FLYWHEEL-TO-WHEELS DRIVE TRANSMISSION

The maximum requirements of the drive transmission are dictated by the vehicle acceleration requirements. The schedule of torque and power supplied to the wheels will depend on the particular capabilities of the transmission finally selected as well as specified vehicle performance requirements. Figure 5-8 shows some transmission output characteristics, during accelerations, for commuter and family cars using a simplified drivetrain consisting of a speed changer (yielding a 10:1 ratio for charging the flywheel, or a 1:10 ratio for driving from it) with 98% efficiency (in both directions), an undefined CVT with a constant 76% efficiency, and a rear axle (to give a 1:1 overall ratio at V_{max}) with 98% efficiency. The families of solid lines represent constant-output-torque (T_D). The effects of rotating inertia (i.e., power required to accelerate the vehicle components themselves) and road wheel slippage have been neglected. Auxiliary ordinate scales show transmission output speed W_D (top) and time scales (bottom) for acceleration from 0 to 60 mph at constant T_D and constant P_D. The dashed, constant-P_D line is at the level which does provide the specified acceleration and similarly the constant T_D is shown by a dashed curve (0 to 60 mph in 12 and 10 seconds for the commuter and family cars, respectively).

For the 32.5 W-h/lb flywheels assumed for these examples (73 pounds for the commuter car and 162 pounds for the family car), the variation in flywheel speed is small (3% decrease from full charge for both cases). However, if a small flywheel is used, the variation may be large (e.g., for a 20-pound, 0.64-kW-h wheel the input speed to the transmission would change by 52%). Figure

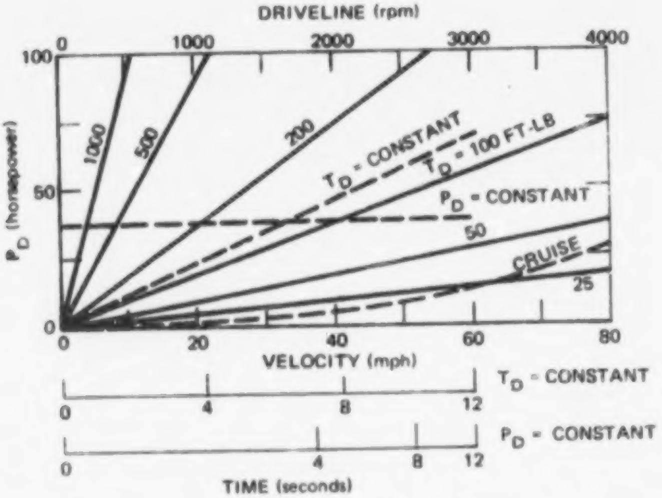

(a) COMMUTER CAR

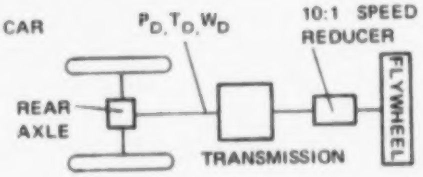
P_D, T_D, W_D
10:1 SPEED REDUCER
REAR AXLE
TRANSMISSION
FLYWHEEL

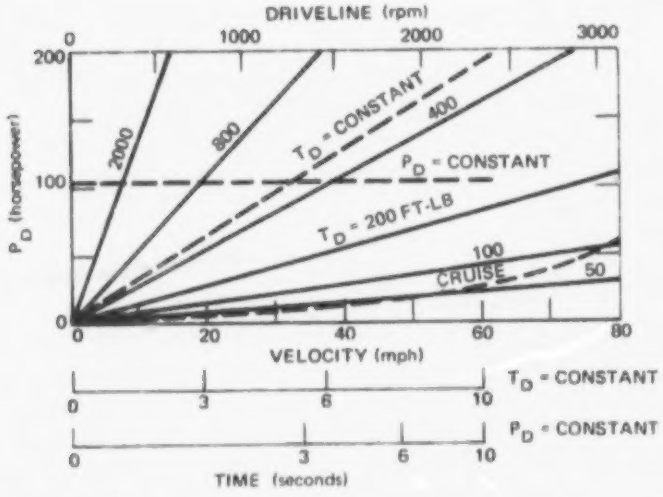

(b) FAMILY CAR

Fig. 5-8 TRANSMISSION OUTPUT CHARACTERISTICS

5-8 shows that 37 hp at the output is required for the constant-power acceleration of the commuter car, with high output torques (≥ 130 ft-lb) for the first 3 seconds (at high transmission speed ratios). In contrast, the constant torque output requires 134 ft-lb with higher powers (≥ 37 hp) during the last 6 seconds (at low transmission speed ratios). The cruise horsepower curves fall well below the acceleration requirements until the maximum cruise speed requirements are approached. The transmission requirements for the family car (Fig. 5-8b) are ~ 2.5 times the values of the commuter car, roughly in proportion to their loaded weights.

Figure 5-9 shows variations with time of velocity, acceleration, torque, horsepower, and transmission speed ratio (N_T) for the family car. The constant-torque acceleration curve is essentially flat (constant acceleration). The constant-power acceleration curve shows high initial accelerations (~ 10 mph/s or 0.5 g at 1 second), a situation characterized by "squealing rubber" and some passenger discomfort. Note that an N_T of 10 is required at 10 mph. If the flywheel were at near the rundown condition the N_T required at 10 mph would be ~ 5. The acceleration schedule and consequent "jerk rate" are dictated by the rate of change of N_T and would be controllable by the operator.

The overall requirements of the drive transmission may be summarized as follows:

1. Continuous variation over speed range,
2. 2:1 variation in input speed, but an essentially constant speed input at any time, e.g., during one acceleration period,
3. Output speed range to match vehicle velocity requirements, ~ 5:1 or higher,
4. Control must go through the transmission, to produce the required torque and speed,

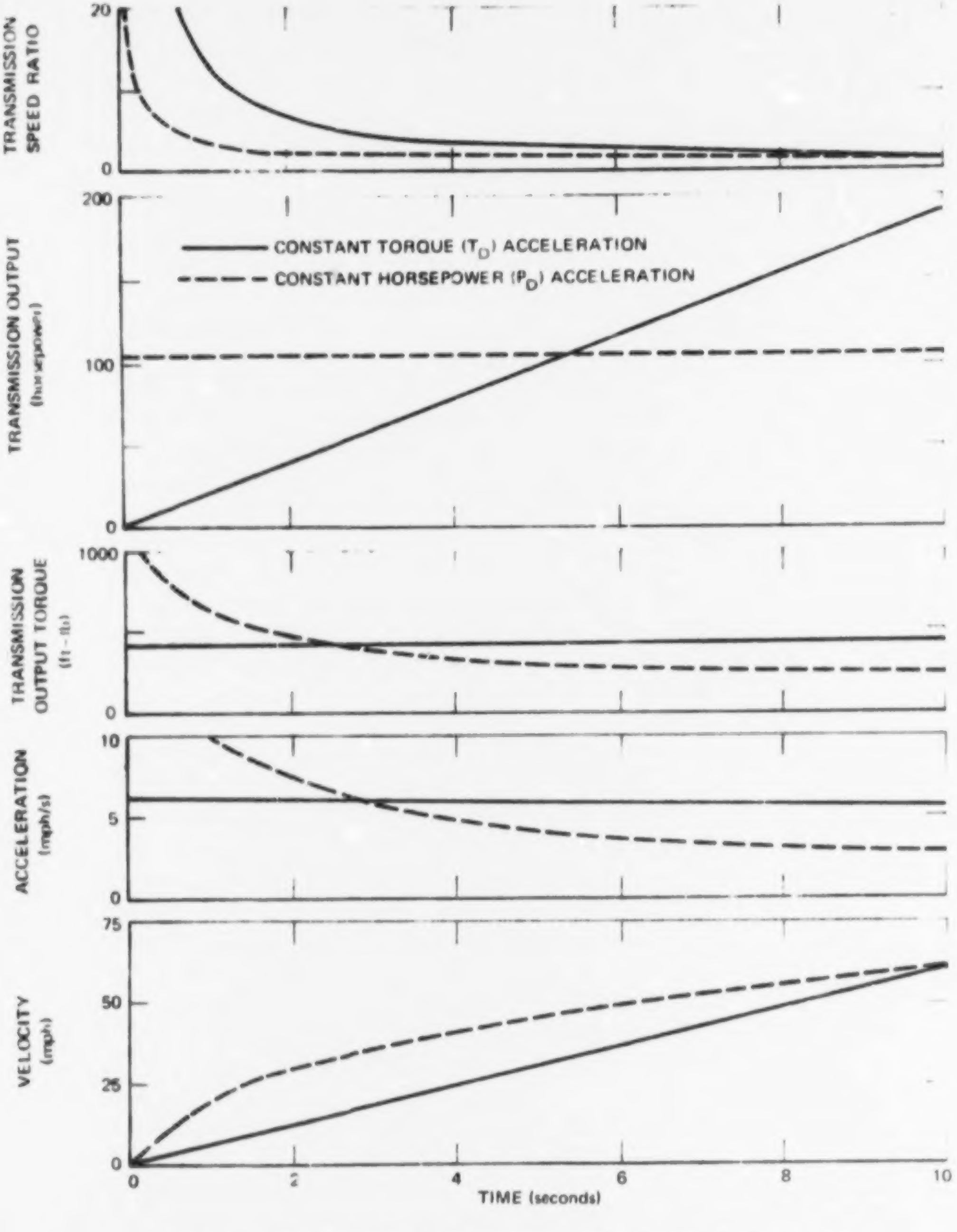

Fig. 5-9 ACCELERATION PARAMETERS VERSUS TIME, FAMILY CAR

5. Torque and horsepower requirements corresponding to vehicle acceleration requirements, and

6. High efficiency over operating range.

The limited use of CVT's in current vehicles is not due to a lack of ideas. The recent patent rate on transmission concepts has been near six per month, and a significant portion of these are CVT's. Use of a CVT in any automobile would allow the engine to operate in its minimum bsfc region, and would reduce the speed range required of the engine (Ref. 112). The present lack of a CVT for automobiles may mean mainly that the requirement has not been strong enough to force such an innovation with its production development and changeover costs. The general problem is low efficiency[1] at off-design, nonpeak-load conditions, because most of the vehicles under consideration seldom operate on the design curve (maximum cruise speed or maximum acceleration). However, further development may lead to more satisfactory CVT's.

A review of the literature on CVT's is given in Appendix D. For the commuter car the belt drive (Ref. 5) is a candidate, even though the combination of horsepower (~ 30 hp) and speed ratio (9:1) requirements is difficult relative to current belt applications, if one adheres strictly to the present commuter car performance specifications.

The needs of the family car, delivery van, and bus probably will be best satisfied by a power-dividing device.

---

[1] The transmission requirements for lower-energy flywheels than we consider, perhaps operating in a dual mode with the engine, would not be as stringent, but as noted earlier, lower-energy systems give up the advantage of flywheel-only (zero pollution) operating ranges to alleviate local, in-town, emission levels.

The development of a power-dividing, hydromechanical device [along the lines of Sundstrand's DMT (see, e. g., Ref. 4) which they are now producing for trucks] should be straightforward and appears promising for the van and bus because of their lower performance requirements and relatively higher propulsion system weight allowances. A CVT for the family car will require a greater effort in development because of the more stringent performance specifications; the mechanical drives (Toric (Ref. 15) and Beier (Ref. 16)) appear to warrant further investigation, and they may prove suitable. Pure electric or hydrostatic drives are least promising for any of the specified vehicles because of their high weights and low efficiencies.

5.4.4 OTHER DRIVETRAIN COMPONENTS AND DRIVETRAIN LAYOUT

A speed increaser (~ 1:10) will be needed to match the low-speed engines (i. e., all but the GTE) to the flywheel speed, and in all cases a speed reduction (~ 10:1) will be needed to couple the flywheel to the vehicle drive system. The capability for reverse operation must be included. The speed increaser and reducer functions can be incorporated in a single unit, possibly at a savings in weight and/or efficiency. Three clutches – engine/gearbox, flywheel/gearbox, and gearbox/drive-transmission – will be needed. A conventional drive axle (~ 3.5:1) is assumed. Provisions for external (emergency) flywheel charging must be made, and the ability to use the flywheel to start the engine, particularly in the case of a GTE, may be desired.

A brake-regeneration system, providing for an appropriate distribution of deceleration energy, must be incorporated. Finally, a control system is needed to: monitor flywheel speed, start and stop the engine, interpret and modulate driver commands, balance regeneration and brake energy distribution, and operate drivetrain clutches under appropriate conditions.

A drivetrain schematic incorporating the foregoing features is shown in Fig. 5-10. The power required for accessories (power steering, power brakes, air conditioning, fans, pumps, and lights) is taken from the central gearbox, and an input shaft is provided for externally supplying power to charge the flywheel in the event of rundown or while the vehicle is parked. The flywheel's clutch is disengaged whenever the vehicle is parked to conserve the stored energy. When the flywheel and drive clutches are engaged, power can be transmitted from the gearbox to the drive wheels, or vice versa (for regeneration).

The operator controls are analogous to those on present vehicles. An "ignition" switch engages the flywheel clutch, a selector lever positions the transmission for drive, neutral, or reverse, and accelerator and brake pedals command vehicle accelerations and decelerations. (A conventional parking brake, not shown, would be provided.) A central control box, called the power programmer, translates operator commands into the desired mechanical responses. Its inputs are flywheel speed, drive-wheel speed, and acceleration and deceleration rate commands from the operator. It combines this information to determine the appropriate, continuously varying transmission ratio. During deceleration it must also decide, based on the flywheel charge status and the braking rate demand, whether to use energy regeneration, the mechanical brakes, or a combination of both. It also controls the on-off operation of the powerplant and clutch to keep the flywheel speed within the design range. The same programmer, using feedback data, could provide antislip control of the brakes and drive wheels. It might also be practical to provide a gain control to adjust the vehicle response to operator preferences and driving conditions.

While the arrangement shown in Fig. 5-10, with the 10:1 speed changer between the flywheel and its clutch reduces the start-up clutching problem, it is undesirable from the viewpoint of rundown time. Since a method of

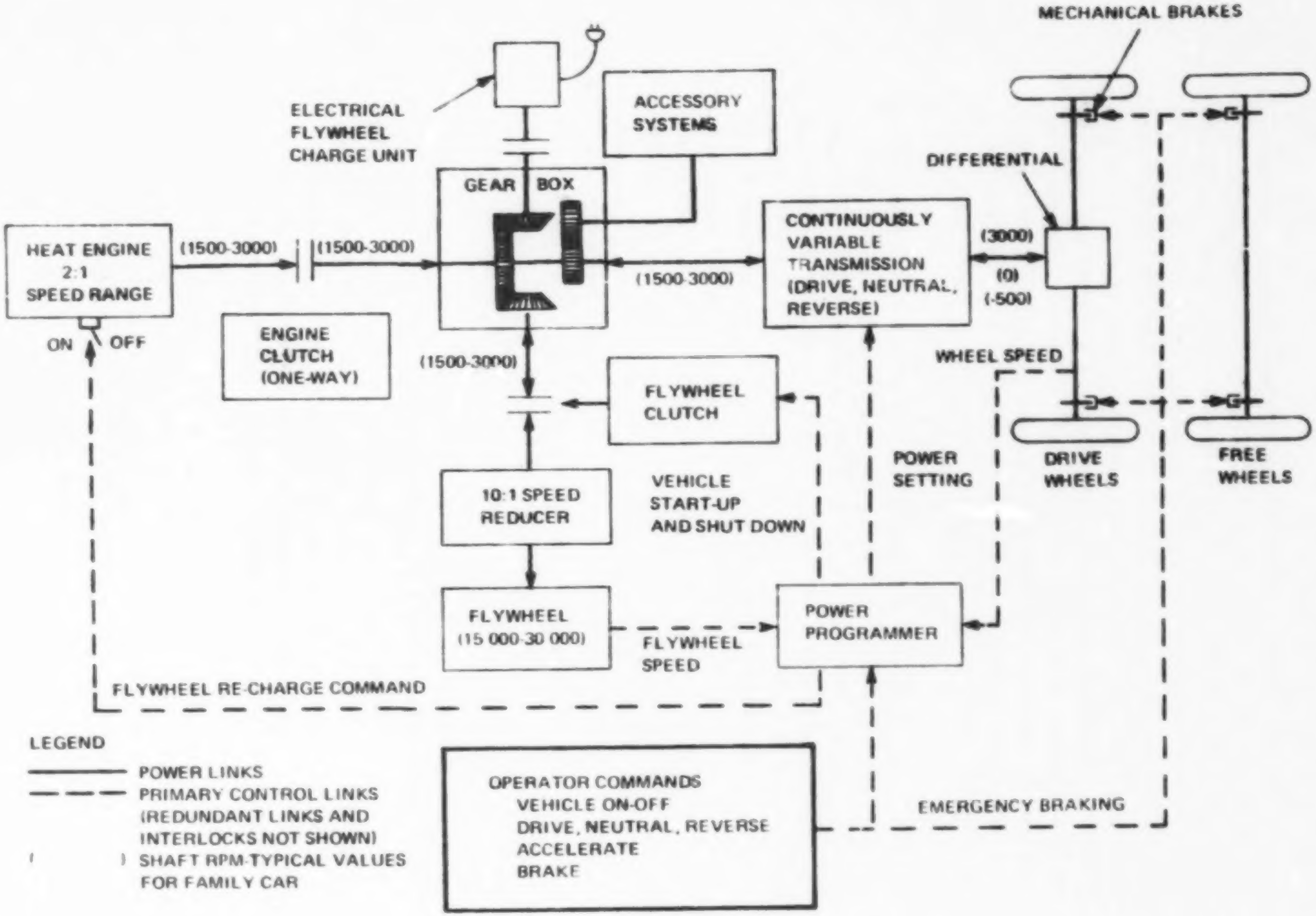
MECHANICAL BRAKES
ELECTRICAL FLYWHEEL CHARGE UNIT
ACCESSORY SYSTEMS
GEAR BOX
DIFFERENTIAL
HEAT ENGINE 2:1 SPEED RANGE
ON
OFF
(1500-3000)
(1500-3000)
(1500-3000)
CONTINUOUSLY VARIABLE TRANSMISSION (DRIVE, NEUTRAL, REVERSE)
(3000)
(0)
(-500)
ENGINE CLUTCH (ONE-WAY)
(1500-3000)
FLYWHEEL CLUTCH
WHEEL SPEED
DRIVE WHEELS
FREE WHEELS
POWER SETTING
VEHICLE START-UP AND SHUT DOWN
10:1 SPEED REDUCER
FLYWHEEL (15 000-30 000)
FLYWHEEL SPEED
POWER PROGRAMMER
FLYWHEEL RE-CHARGE COMMAND
LEGEND
POWER LINKS
PRIMARY CONTROL LINKS (REDUNDANT LINKS AND INTERLOCKS NOT SHOWN)
( ) SHAFT RPM-TYPICAL VALUES FOR FAMILY CAR
OPERATOR COMMANDS
VEHICLE ON-OFF
DRIVE, NEUTRAL, REVERSE
ACCELERATE
BRAKE
EMERGENCY BRAKING

Fig. 5.10 FLYWHEEL HYBRID POWER CONTROL SYSTEM

externally accelerating (via an electric motor) a rundown flywheel probably will be needed in any case, it may prove better to incorporate the speed changer within the gearbox and, for normal operation after short-term (< 18 hour) parking, use the engine to match the flywheel clutch speed within a few hundred rpm before engaging it at high speed.

As previously noted, we have assumed for the following studies an average overall (engine to wheels) efficiency of 72%, and this value is judged to be compatible with the average efficiencies for CVT's that could be developed in the short term for use with these systems. Over a longer term, better efficiencies should be achievable. The 72% value (which is used for all vehicle speeds and power levels) is realistic for cars on urban cycles but is pessimistic for freeway cruising at 40 to 70 mph. The transmission weights assumed herein, equivalent to current automotive transmissions, are optimistic for near-term flywheel-hybrid systems.

5.4.5 REGENERATION EFFICIENCY AND OPERATIONS ON THE DHEW CYCLE

A study (Ref.115) of driving habits of selected drivers indicated that of the total energy dissipated during decelerations on a 'trip', as much as 70% is dissipated by the brakes. The remaining 30% evidently is dissipated by vehicle drag (aerodynamic and frictional resistance) and engine braking. For a 60 to 0 mph deceleration, vehicle drag accounts for 3% (for a 3-second 'panic' stop) to 15% (for a 15-second 'leisure' stop) of the kinetic energy dissipation. If 10% is a reasonable average for vehicle drag, then a maximum of 90% could go back from the two drive wheels through the drivetrain to the flywheel at 73% transmission efficiency. Thus, based on this simple analysis, a maximum of 66% of all deceleration energy might be recoverable. A more detailed analysis follows.

To assess flywheel operation and regeneration on the DHEW (Department of Health, Education and Welfare) cycle, as detailed in the Federal Register (Ref. 113), a numerical analysis was done. The DHEW cycle, which is being used by OAP for emission measurements, is based on the accumulated experimental data for drivers in the Los Angeles (Ref. 114) area and is defined by 1372 velocity (V_i, mph)-time (t_i, second) points at 1-second intervals. The analytical approach herein is as follows.

The net power required at the wheels (P_{N_i}, hp) for mass acceleration during the i^{th} 1-second time step is computed from the equation of motion:

$$a_i = g(550)\left(\frac{3600}{5280}\right)^2 P_{N_i}/W_\ell \overline{V}_i = 8310\ P_{N_i}/W_\ell \overline{V}_i\ , \qquad (5\text{-}7)$$

where $\overline{a}_i$ and $\overline{V}_i$ are the arithmetic average acceleration (mph/s) and velocity (mph) for the step, g is the gravitational constant (32.17 ft/s^2), and W_ℓ is the loaded vehicle weight (pounds). (The change in W_ℓ because of fuel consumption on one 7.45-mile driving cycle is negligible.) Using the prescribed drag coefficient C_D and frontal area A for the vehicle (Table 5-1), and assuming a tire friction factor (f_t) relationship (Ref. 108) (footnote 2, Table 5-1), the horsepower supplied to the wheels during acceleration and cruise is given by:

$$P_W = P_N + P_D\ , \qquad (5\text{-}8)$$

where

$$P_D = (D + f_t\ W_\ell)V/375$$

$$= [0.00278\ C_D A V^2 + (0.01 + 1.1 \times 10^{-6} V^2)\ W_\ell]V/375, \qquad (5\text{-}9)$$

where $D = \frac{1}{2} \rho C_D A V^2$ is the aerodynamic drag force. During deceleration the power regenerated at the flywheel shaft is given by:

$$P_R = (P_N \eta_R) , \tag{5-10}$$

where η_R ($= \eta_D$) is the average regeneration transmission efficiency (0.73 herein).

A conceptual schematic of the flywheel-hybrid system analyzed is shown in Fig. 5-10. The engine is characterized by its shaft power P_{ES} and cooling fan power P_{CF}. The net flywheel charging power $P_{F_{in}}$ supplied by the engine to the flywheel shaft is:

$$P_{F_{in}} = (P_{ES} - P_{CF}) \eta_C , \tag{5-11}$$

where η_C is the charge transmission efficiency (0.985 herein). The net horsepower $P_{F_{net}}$ extracted from the flywheel shaft is the difference between the vehicle requirement ($P_{F_{out}}$) and the horsepower supplied by the engine:

$$P_{F_{net}} = P_{F_{out}} - kP_{F_{in}} = P_W/\eta_D + P_{AC} + P_{misc} - kP_{F_{in}} , \tag{5-12}$$

where η_D is the overall drivetrain efficiency from flywheel to wheels (includes speed reducer, CVT, two clutches, and rear axle); k = 0 if the engine is in the off mode and k = 1 during engine charging; and P_{AC} and P_{misc} are the powers required for the air conditioner and for the miscellaneous accessories — lights, radio, windshield wipers, etc.

The maximum (and reference) flywheel energy density E_O/W_r, maximum rotational speed ω_O, and rotor weight W_r are input as initial conditions. At each time step an energy balance is made at the flywheel

$$\Delta E_i = 550\ P_{F_{net}}\ \Delta t_i\ , \tag{5-13}$$

and the rotational speed is found from:

$$\omega_i = \omega_o (E_i / E_o)^{\frac{1}{2}}\ . \tag{5-14}$$

When ω_i has fallen to $\omega_o/2$ ($E_i = E_o/4$), the powerplant is turned on ($k = 1$), and when ω_i again reaches ω_o it is turned off ($k = 0$).

There is a fixed speed reduction ratio ($N_{FR} = 10$) between the flywheel and the main, variable speed transmission. The rear axle gear ratio N_A is based on the assumption of a main transmission speed ratio of unity ($N_t = 1$) at $\omega = \omega_o$ and $V = V_{max}$; thus:

$$N_A = \omega_o\ r_W / (14\ N_{FR} V_{max})\ , \tag{5-15}$$

where r_W is the drive-wheel radius (feet). The required speed ratio N_t of the infinitely variable main transmission is computed as a function of time from

$$N_t = \omega_i\ r_W / (14 V_i N_A N_{FR}) = (\omega_i / \omega_o)(\overline{V}_i / V_{max})\ . \tag{5-16}$$

The foregoing cycle calculations have been made for the family car and commuter car using SIE/flywheel hybrid propulsion. The input conditions not already given in Table 5-1 are shown in Table 5-7. The cycle is ~ 7.45 miles long with a time average velocity of 19.6 mph. Maximum accelerations and decelerations are 3.3 and -3.3 mph/s, respectively. A peak speed of 56.7 mph is attained, and 17.3% of the total time is spent at idle ($V = 0$). Each case was started with a fully charged flywheel and with all accessories and the air conditioner operating continuously at full load. For the family and commuter cars, the engines were on during 19.8 and 27.0%, respectively, of a flywheel cycle (one period each with k = 0 and k = 1). The ranges for a flywheel-only operation (k = 0 period, $E_o \rightarrow E_o/4$) were 6.0 and 5.5 miles for the family and commuter cars, respectively; without the air conditioner operating the corresponding ranges are approximately 8.8 and 10.1 miles. For the commuter car the air conditioner power requirement is a greater fraction of the total accessories load (0.85) than for the family car (0.62).

The computer printout for each 1-second interval shows time t, velocity V, acceleration a, distance R, flywheel shaft horsepower $P_{F_{out}}$, wheel gross horsepower ($P_W = P_N + P_D$), drag horsepower P_D, flywheel rotational speed ω, transmission speed ratio N_T, energy in flywheel E, and engine status (on or off). Figure 5-11 shows the variation of P_W, V, ω, and N_T for a 172 second sequence for the commuter car as an example. Note the very gradual decline in ω for the 73-pound rotor flywheel.

The resulting energy (W-h) balances are shown in Table 5-8 for the two cars with and without their air conditioners operating. The numbers in parentheses are percentages of total cycle energy. For the commuter car, 398 W-h (28.9% of the total energy) is used to accelerate the vehicle mass (excess over the external resistance), and this value also must represent the kinetic energy expended during decelerations. Figure 5-12 shows graphically the resulting energy balance for the commuter car. In a conventional vehicle this kinetic energy is dissipated through engine braking, mechanical brakes, and external resistance. Assuming a flywheel-to-wheels transmission efficiency during regeneration of 73% (i.e., $\eta_R = \eta_D$), 218 W-h (15.8% of the total energy cycle) is returned to the flywheel, while 100 W-h and 80 W-h are lost to

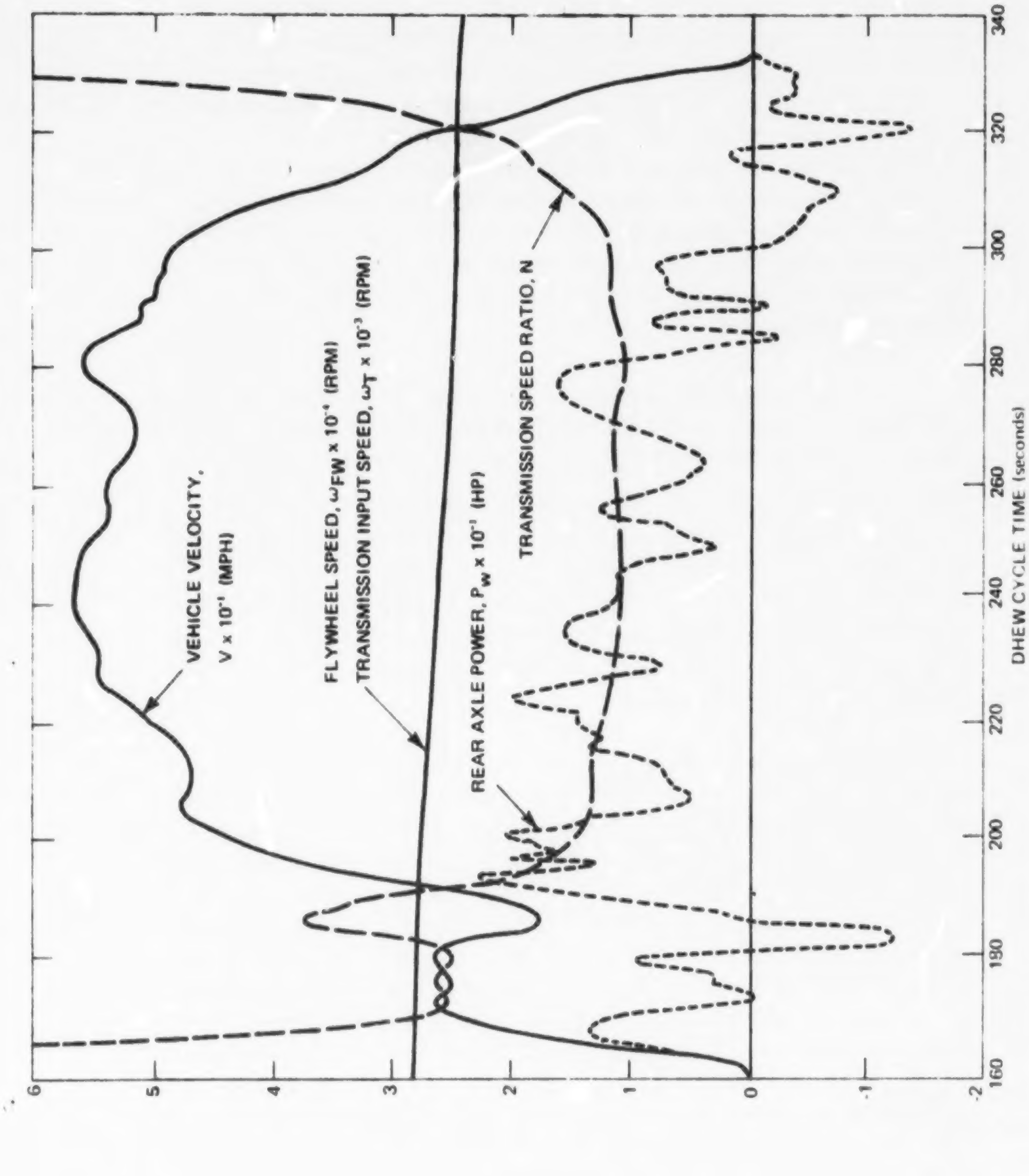

Fig. 5.11 COMMUTER CAR HYBRID OPERATING ON DHEW DRIVING CYCLE. FULL FLY WHEEL CHARGE AT START OF CYCLE; ENGINE IS OFF DURING THIS PORTION.

Table 5-7

Input Conditions for Family and Commuter Hybrid Vehicles (see also Table 5-1)

	Family Car	Commuter Car
Initial Energy Density E_o/W_r (W-h/lb)	30	30
Rotor Weight, W_r (pounds)	158	72
Maximum Rotational Speed, $\omega_{max} = \omega_o$ rpm	30 000	30 000
Drive Wheel Radius, r_w (feet)	1.5	1.0
Drive Efficiency, η_D (%)	73	73
Charge Efficiency, η_c (%)	98.5	98.5
Regeneration Efficiency, η_R (%)	73	73
Flywheel Speed Reduction, N_{FR}	10	10
Engine Shaft Horsepower, P_{ES} (bhp)	92	33
Miscellaneous Accessories Power, P_{misc} (bhp)	3.66	0.71
Engine Cooling Fan Power, P_{CF} (bhp)	3.0	1.0
Air Conditioner Power, P_{AC} (bhp)	5.89	4.0

Table 5-8

Energy Disposition on DHEW Cycle (7.5 miles)

Source	Energies[1] (W-h)			
	Family Car		Commuter Car	
	With A/C[2]	No A/C	With A/C[2]	No A/C
In				
Supplied by Powerplant	4875	3178	2313	1160
Regenerated	523	523	218	218
Total	5398	3701	2531	1378
Out	(%)[1]	(%)	(%)	(%)
Accessories	2712(50.2)	1040(28.1)	1338(52.9)	202(14.7)
Engine Transmission Losses	81(1.5)	56(1.5)	38(1.5)	21(1.5)
Main Transmission Losses	703(13.0)	703(19.0)	312(12.3)	312(22.6)
External Resistances (drag and friction)	954(17.7)	954(25.8)	445(17.[illegible])	445(32.3)
Acceleration (kinetic energy)[3]	948(17.6)	948(25.6)	398(15.7)	398(28.9)
External Resistance	232(4.3)	232(6.3)	100(3.9)	100(7.3)
Transmission Losses	193(3.6)	193(5.2)	80(3.2)	80(5.8)
Regenerated Energy	523(9.7)	523(14.1)	218(8.6)	218(15.8)
Total	5398	3701	2531	1378

---

[1] Numbers in parentheses are percentages.

[2] A/C = air conditioner, operated at 100% load continuously.

[3] Acceleration kinetic energy must equal the sum of external resistance, transmission losses, and regenerated energy during deceleration.

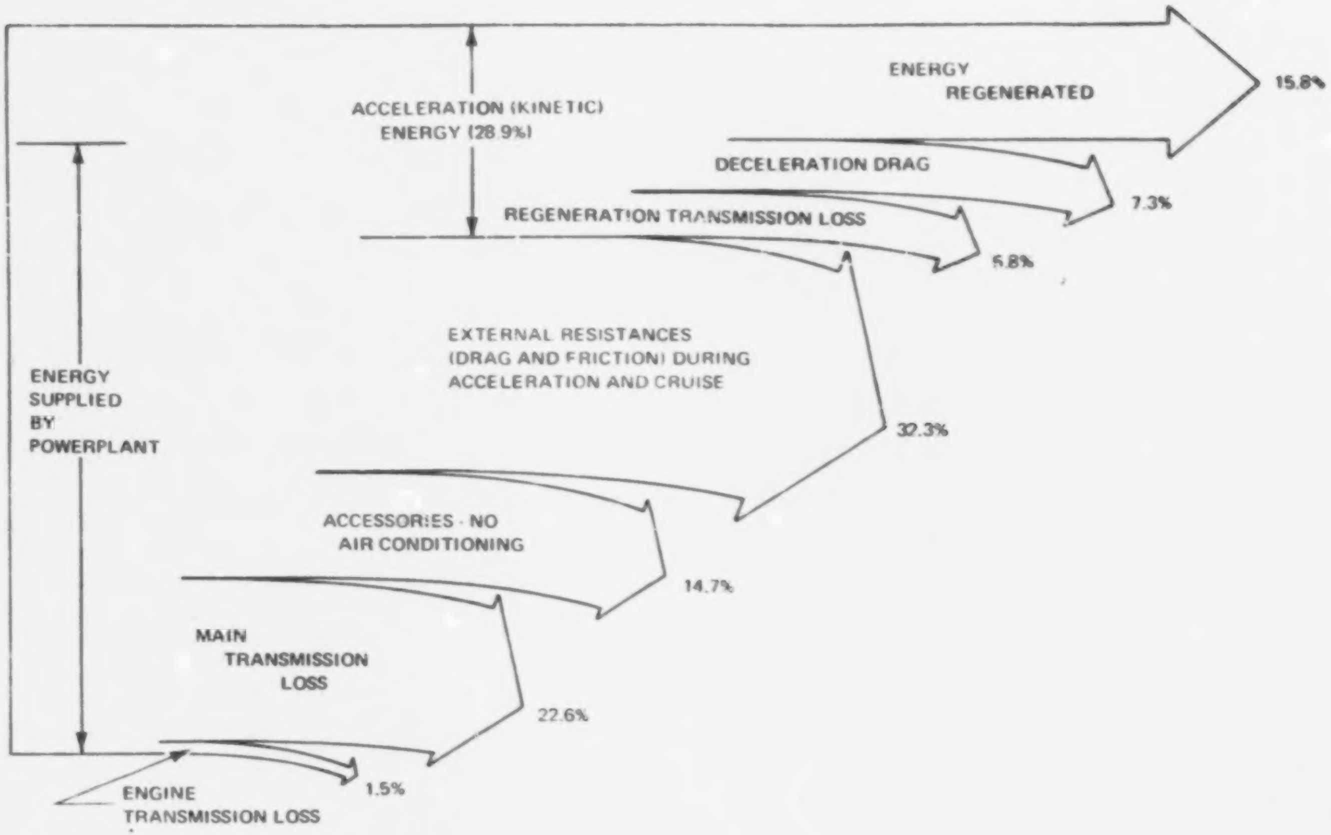
ENERGY REGENERATED
15.8%
ACCELERATION (KINETIC) ENERGY (28.9%)
DECELERATION DRAG
7.3%
REGENERATION TRANSMISSION LOSS
5.8%
EXTERNAL RESISTANCES (DRAG AND FRICTION) DURING ACCELERATION AND CRUISE
32.3%
ENERGY SUPPLIED BY POWERPLANT
ACCESSORIES - NO AIR CONDITIONING
14.7%
MAIN TRANSMISSION LOSS
22.6%
ENGINE TRANSMISSION LOSS
1.5%

Fig. 5-12 ENERGY DISPOSITION OF COMMUTER CAR ON DHEW CYCLE WITHOUT AIR CONDITIONER; 0.247 HP-H/MILE. (A 4-HP AIR CONDITIONER OPERATING CONTINUOUSLY REPRESENTS 32% OF ABOVE ENERGY)

external resistance and the transmission, respectively, during decelerations. Thus, the regeneration efficiency ϵ_R, defined as the recovery of kinetic energy during decelerations (or down-grade operation), is 218/398 = 0.55, or 55% for the commuter car. The same value is obtained for the family car: $\epsilon_R = 523/948 = 0.55$. This value compares with the maximum of 66% estimated earlier on the basis of a driver study (Ref. 115) and a range of external resistance losses for decelerations from 60 to 0 mph. For the broader but more simplified analytic studies presented hereinafter, we have assumed an ϵ_R of 50%.

5.4.6 CONCLUSIONS ON TRANSMISSIONS AND REGENERATION EFFICIENCY

State-of-the-art CVT's cannot meet the overall flywheel system requirements, but short-term development efforts probably would produce a satisfactory CVT, slightly less efficient (especially at off-design conditions) and heavier than current automotive transmissions. With substantial long-term development, more competitive CVT's could be developed. Mechanical or partly mechanical (power dividing) transmissions provide high efficiency and are the primary candidates.

The overall transmission efficiency (72%) and regeneration recovery (50%) values assumed herein seem compatible with development for low emission vehicles by 1975, especially for buses. Better efficiencies should be achievable over a longer term.

5.5 PERFORMANCE AND EMISSION ESTIMATES

5.5.1 INPUTS

Since the vehicles appear to be weight-limited, even when using bar-type flywheels, volumes are not considered herein. The propulsion-system/vehicle-curb-weight fractions (W_s/W_c) are 0.33, 0.29, and 0.30 for the cars, van, and bus, respectively; these fractions correspond to the "APL" propulsion system weights in Table 5-2. Equations (5-8) through (5-12) are used, with the vehicle characteristics given in Tables 5-1, 5-3, and 5-7. Figure 5-13 shows P_W versus V for the four vehicles. The ancillary requirements (P_{misc}, P_{CF}, and P_{AC}) in Table 5-7 were supplied by OAP (Ref. 104). The engine cooling fan is not included in the flywheel-only vehicles or the gas-turbine and steam-engine hybrids.

For each vehicle class, an appropriate driving "cycle" is represented as the sum of a number of discrete cruise, acceleration, and deceleration phases in terms of the percentage of time spent in each (Fig. 5-14). The operating mode of the flywheel-hybrid vehicles essentially decouples the engine operation from the time sequence of operation of the vehicle. The engine is either on (at full load and nearly fixed speed) to charge the flywheel (from ω_{min} to ω_o) or off. For the cars the high rotor energy density allows energy storage for at least seven accelerations from 0 to 60 mph, which, with regeneration, allows the vehicle to negotiate with ease a trip (of range R_T as defined later) on any of the cycles without the possibility of the energy use rate being greater than the charge rate. Therefore, the time sequence of the modes is immaterial, and the resulting performance and emission estimates are based on average horsepowers and velocities for the various phases.

Acceleration rates also are not of primary concern because, theoretically, energy can be extracted or supplied to the flywheel system at any power level. The power levels will be limited only by the powertrain (transmission) capabilities. The energy required for an acceleration is not strongly dependent on the rate (power) at which it is accomplished. The acceleration rates specified by OAP (Table 5-1) are used, and for the decelerations, rates 33% greater than these are used. The low average velocities for the bus and van reflect the

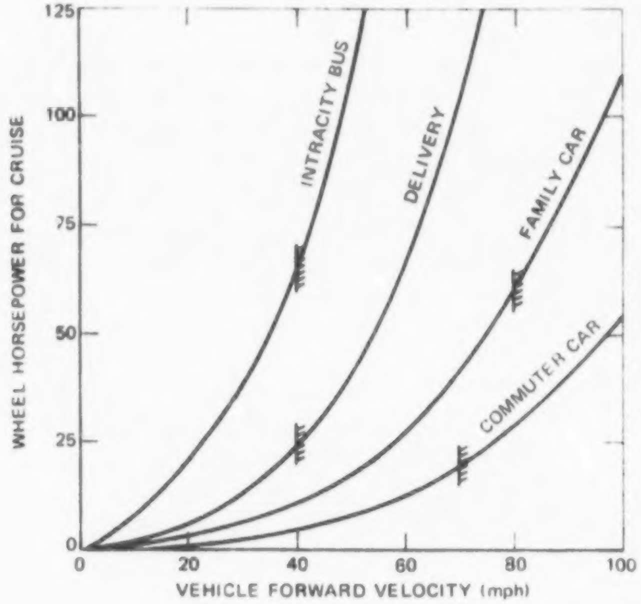

Fig. 5-13 STEADY-STATE WHEEL HORSEPOWER REQUIREMENTS FOR THE FOUR VEHICLES.

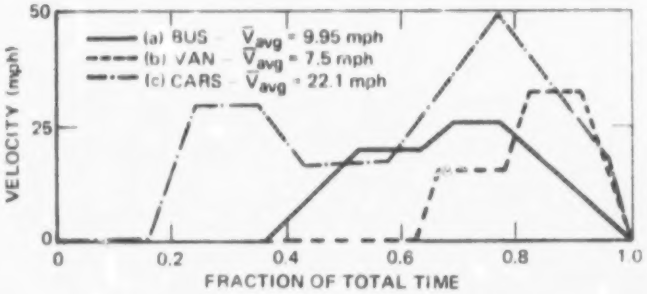

Fig. 5-14 DRIVING CYCLES

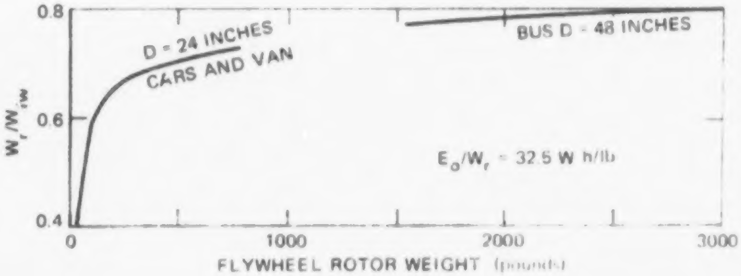

Fig. 5-15 FLYWHEEL ROTOR MASS FRACTIONS ASSUMED

large percentages of idling time (Fig. 5-14). The cycle for the commuter and family cars (Fig. 5-14c) is the California ten-mode cycle, which is normally referred to as the seven-mode cycle, since three of the modes are not used in measuring emissions.

Flywheel rotor weights are computed as described in Section 5. 3. 2, based on spin diameters (ℓ) of 48 inches for the city bus and 24 inches for the other vehicles. With E_o/W_r = 32. 5 W-h/lb, these sizes yield ω_o = 15 900 rpm for the bus and 31 900 rpm for the other vehicles. The resulting rotor mass fractions, W_r/W_{fw}, are plotted in Fig. 5-15 versus rotor weight W_r.

Emission results are nondimensionalized by dividing by appropriate future standard values (Table 5-9). For the light-duty vehicles ($W_c \leq$ 6000 pounds, van and cars) the 1975-76 standards (Ref. 3) are used, whereas for the intracity bus the proposed 1973 California Diesel Standards (Ref. 116) are used. The former are expressed in gm/mi; the latter in lb/bhp-h ($BSPE_x$).

Table 5-9

Light- and Heavy-Duty Vehicle Emission Standards

Pollutant	$W_c \leq$ 6000 pounds	$W_c >$ 6000 pounds[2]
	Emission standard, gm/mi	lb/bhp-h
CO	3. 40[1]	0. 0770
HC	0. 41[1]	0. 0077
NO_x (as NO_2)	0. 40[1]	0. 0088

[1] Federal standards for 1976 (gm/mi) (Ref. 9).

[2] Proposed 1973 California Diesel Standards (lb/bhp-h).

5.5.2 METHOD OF ANALYSIS

For each portion (mode) of a vehicle's cycle, average acceleration (or deceleration) velocities (mph) and horsepowers are defined by $\overline{V}_i = \Delta s/\Delta t$ and $\overline{P}_{w_i} = V_i F_w/375$, where F_w is the constant wheel force required for the acceleration or deceleration, s is the distance (miles), and t is time (hours). These wheel horsepowers are related to the flywheel shaft horsepower by the specified efficiencies with account taken for regeneration during deceleration. The average flywheel shaft output horsepower $\overline{P}_{F_{out}}$ for the cycle is found by time-averaging the shaft horsepowers over the modes,

$$\overline{P}_{F_{out}} = \sum_i \frac{t_i}{t_T} \overline{P}_{F_{out_i}} , \qquad (5\text{-}17)$$

where t_i is the time (hours) spent in the i^{th} mode and t_T is the trip time (hours). Similarly, the time average cycle velocity is:

$$\overline{V} = \sum_i t_i V_i / t_T . \qquad (5\text{-}18)$$

The total energy expended on the cycle at the flywheel shaft is:

$$E_{F_{out}} = 1.98 \times 10^6 \, t_T \, \overline{P}_{F_{out}} , \text{ ft-lb} . \qquad (5\text{-}19)$$

The total engine-on time t_{eo} (hours) is related to the fuel load W_f and engine output power ($P_E = P_{F_{in}}/\eta_C$) by:

$$t_{eo} = W_f/(P_E \cdot \text{bsfc}) , \qquad (5\text{-}20)$$

and the energy $E_{F_{in}}$ (ft-lb) delivered by the engine to the flywheel shaft is:

$$E_{F_{in}} = 1.98 \times 10^6 \, W_f \, \eta_C / \mathrm{bsfc} \; . \qquad (5\text{-}21)$$

The total trip time (hours) is then found by equating $E_{F_{in}}$ and $E_{F_{out}}$, yielding:

$$t_T = \eta_C \, W_f / \mathrm{bsfc} \; , \qquad (5\text{-}22)$$

and the total trip range (miles) is:

$$R_T = t_T \, \overline{V} \; . \qquad (5\text{-}23)$$

The fuel economy γ (mi/gal) is:

$$\gamma = R_T \, \rho_f / W_f \; . \qquad (5\text{-}24)$$

where ρ_f is the fuel density, 5.75 lb/gal (for gasoline). The available energy E_a (ft-lb) in a flywheel charge is 75% of the maximum stored energy:

$$E_a = 0.75 \, (2655.3) \, (E_o / W_r) W_r = 64\,730 \, W_r \; , \qquad (5\text{-}25)$$

where E_o / W_r is the rated flywheel energy-density (32.5 W-h/lb), and 2655.3 converts ft-lb to W-h. The number of flywheel charges during the trip is:

$$n = E_{F_{out}} / E_a \; . \qquad (5\text{-}26)$$

The flywheel-only (FO) range R_{FO} on a single charge is:

$$R_{FO} = R_T / n \; . \qquad (5\text{-}27)$$

Similar calculations are used to estimate ranges and fuel consumptions at constant speed or on a grade.

Emissions X_i (gm/mi; i = NO_x, CO, HC) are given by:

$$X_i = 453 \cdot BSPE_i \cdot P_E \cdot t_{eo} / R_T = 453 \cdot BSPE_i \cdot \overline{P}_{F_{in}} / \overline{V} \eta_C \, , \quad (5\text{-}28)$$

where $BSPE_i$ is the brake specific pollution estimate for species i and is related to the engine's full-load brake horsepower P_E from the curves supplied by OAP (Ref. 104). The HC and CO emissions are then increased for a 10-second period at the beginning of each of the n engine startups as discussed in Section 5.2.5 and ratioed to the appropriate emission standards.

5.5.3 RESULTS

For the majority of the OAP estimates, $BSPE_i$ is independent of horsepower, so that X_i is essentially independent of the engine size, but a second-order effect is introduced, in that as engine size (P_E, bhp) and weight are increased, W_r decreases, and therefore the number of flywheel cycles (hence engine startups and corresponding added emissions) on a fixed trip increases. In addition, for the smaller powerplants, thermal efficiencies decrease, thereby resulting in larger bsfc's and subsequent increase in emissions (gm/mi).

The results that are discussed in the following paragraphs do not include any credit for the fact that the engines are operated over much smaller ranges of conditions than conventional engines.

It should be noted, too, that the flywheel storage systems do not suffer from the limitations of battery storage systems (e.g., low depth of discharge for long cycle life, and low power densities) and have the theoretical potential for storing a larger amount of energy than with a battery system of comparable weight. Although they will not offer reductions in total emissions over multihour periods compared to battery systems (or lower energy flywheels used in parallel with heat engines), the relatively large flywheel energy storage systems do offer the possibility of operation for lengthy periods without the heat engines, allowing limited operation in densely populated areas (cities) with the flywheels only. The hybrid vehicles thus could serve as dual-mode vehicles, with external (electrical) charging of the flywheels in cities if necessary. The heat engines would be used for longer intercity trips or for recharging of the flywheels outside the restricted city regions.

For these reasons, we consider relatively high values of energy density and rotor weight to be desirable. As previously noted, the engines are sized in all cases to permit cruise at V_{des}, the maximum sustained velocity specified by OAP, with all accessories operating. Emissions, fuel economy, and ranges are quoted in Tables 5-10 through 5-13 without the air conditioner operating. The cruise range capabilities of the four flywheel-only vehicles, with and without the air conditioner operating are shown in Fig. 5-16. Results for each vehicle are discussed in the following paragraphs.

Commuter Car. Only three hybrids are presented in Table 5-10, because the diesel engine weight exceeded W_s. These hybrids have predicted emissions levels below the 1975-76 standards and can sustain the specified grade of 12%, and the flywheel-only vehicle attains the required 4 miles on a 12% grade. The fuel tanks of the hybrid vehicles have been sized for a 100-mile trip at 70 mph. (Larger fuel tanks could be provided at little penalty, of course.) The fuel consumption of the small (33-bhp) gas-turbine-engine (GTE) hybrid is high, almost three times that of the same-sized Otto engine (SIE) hybrid, reflecting the poor performance of small GTE's. A second larger GTE hybrid (represented by the numbers in parentheses) has been sized such that the fuel economy is equivalent to that of the SIE hybrid. This 80-bhp GTE leaves less weight for the flywheel,

Table 5-10

Results for Commuter Car Without Air Conditioner Operating

	Flywheel Only	Hybrids		
		Gas Turbine	Otto	Steam
Gross Engine Horsepower	--	32. 2(109)[1]	33. 2	32. 2
$W_{fw}/W_{(fw+E)}$	1. 0	0. 53(0. 33)	0. 41	0. 25
Flywheel Rotor Weight, W_R (pounds)	217	103(64)	74	35
W_{fw}/W_R (pounds)	112	72(45)	61	49
Fuel Economy at V_{max} (mpg)	--	10. 9(25. 5)	25. 5	17. 8
Flywheel Only Range at 40 mph (miles)	38. 3	18. 5(11. 5)	13. 1	6. 2
Flywheel Only Range on Grade (miles)	4. 9	2. 3(1. 4)	1. 6	0. 8
No. of Accelerations per Flywheel Charge	42	20(12)	14	6
Flywheel Charge Time (minutes)	--	6. 4(1. 2)	4. 6	2. 2
Cycle Performance				
Fuel Economy (mpg)	--	13. 0(30. 6)	30. 6	21. 2
HC Emission Ratio[2]	--	0. 01(0. 01)	0. 11	0. 20
NO_x Emission Ratio	--	0. 76(0. 76)	0. 67	0. 34
CO Emission Ratio	--	0. 10(0. 08)	0. 22	0. 24
Flywheel Cycles per 100 Miles	4. 7	9. 9(15. 8)	13. 8	28. 9
Flywheel Only Range (miles)	21. 5	10. 2(6. 3)	7. 3	3. 5
% Time Engine on	--	23. 1(6. 8)	23. 1	23. 1

[1] Numbers in parentheses are for a GTE sized for same fuel economy as Otto engine.

[2] Emissions ratioed to 1975-76 Federal Standards, listed in Table 5-9.

Table 5-11

Results for Family Car Without Air Conditioner Operating

	Flywheel Only	Hybrids		
		Gas Turbine	Otto	Steam
Gross Engine Horsepower	--	91.0(200.0)[1]	64.0	91.0
$W_{fw}/W_{(fw+E)}$	1.0	0.62(0.52)	0.31	0.27
Flywheel Rotor Weight, W_R (pounds)	584	353(289)	153	138
W_{fw}/W_R (pounds)	239	159(143)	92	85
Fuel Economy at V_{max} (mpg)	--	9.2(11.8)	11.8	10.0
Flywheel Only Range at 40 mph (miles)	42.3	25.6(21.0)	12.2	10.0
Flywheel Only Range on Grade (miles)	5.5	3.3(2.7)	1.7	1.3
No. Accelerations per Flywheel Charge	49	30(24)	13	11
Flywheel Charge Time (minutes)	--	7.7(2.9)	3.5	3.0
Cycle Performance				
Fuel Economy (mpg)	--	11.3(14.4)	14.4	12.2
HC Emission Ratio[2]	--	0.02(0.01)	0.31	0.46
NO_x Emission Ratio[2]	--	1.97(1.97)	1.73	0.38
CO Emission Ratio[2]	--	0.20(0.15)	0.55	0.57
Flywheel Cycles per 100 Miles	4.5	7.4(9.0)	15.0	18.9
Flywheel Only Range (miles)	22.4	13.5(11.1)	6.2	5.3
% Time Engine on	--	21.1(9.6)	21.1	21.1

---

[1] Numbers in parentheses are for a GTE sized for same fuel economy as Otto engine.

[2] Emissions ratioed to 1976 Federal Standards listed in Table 5-9.

Table 5-12

Results for Delivery Van with No Air Conditioner

	Flywheel Only	Hybrids			
		Gas Turbine	Otto	Steam	Diesel
Gross Engine Horsepower	--	34.3(110)[1]	36.3	34.3	36.3
$W_{fw}/W_{(fw+E)}$	1.0	0.75(0.72)	0.73	0.67	0.43
Flywheel Rotor Weight, W_R (pounds)	655	481(465)	474	430	266
W_{fw}/W_R (pounds)	263	203(196)	200	185	129
Fuel Economy at V_{max} (mpg)	--	5.3(11.9)	11.9	8.6	14.5
Flywheel Only Range at 40 mph (miles)	25.4	18.6(18.0)	18.4	16.7	10.3
Flywheel Only Range on Grade (miles)	2.4	1.7(1.6)	1.7	1.6	0.9
No. of Accelerations per Flywheel Charge	30	22(21)	21	19	12
Flywheel Charge Time (minutes)	--	28.0(8.4)	27.5	25.0	15.5
Cycle Performance					
Fuel Economy (mpg)	--	6.2(13.9)	13.9	10.0	16.9
HC Emission Ratio[2]	--	0.02(0.01)	0.20	0.28	0.76
NO_x Emission Ratio[2]	--	1.67(1.67)	1.50	0.75	1.77
CO Emission Ratio[2]	--	0.19(0.15)	0.44	0.40	0.18
Flywheel Cycles per 100 Miles	3.4	4.6(4.7)	4.7	5.2	8.4
Flywheel Only Range (miles)	29.6	21.7(21.0)	21.3	19.4	12.0
% Time Engine on	--	16.1(5.0)	16.1	16.1	16.1

[1] Numbers in parentheses are for a GTE sized for same fuel economy as Otto engine.

[2] Emissions ratioed to 1976 Federal Standards listed in Table 5-9.

Table 5-13

Results for Intracity Bus without Air Conditioner Operating

	Flywheel Only	Hybrids			
		Gas Turbine	Otto	Steam	Diesel
Gross Engine Horsepower	--	126.9(270.0)[1]	133.7	126.6	133.7
$W_{fw}/W_{(fw+E)}$	1.0	0.91(0.88)	0.81	0.81	0.63
Flywheel Rotor Weight, W_R (pounds)	3278	2964(2866)	2628	2628	2019
W_{fw}/W_R (pounds)	862	792(766)	717	717	583
Fuel Economy at V_{max} (mpg)	--	4.5(5.1)	5.1	4.7	5.6
Flywheel Only Range at 40 mph (miles)	43.9	39.7(38.4)	35.2	35.2	27.6
Flywheel Only Range on Grade (miles)	2.7	2.5(2.3)	2.1	2.1	1.6
No. of Accelerations per Flywheel Charge	38	34(32)	30	30	23
Flywheel Charge Time (minutes)	--	46.6(21.1)	41.3	41.3	31.7
Cycle Performance					
Fuel Economy (mpg)	--	3.3(3.8)	3.8	3.4	4.1
HC Emission Ratio[2]	--	0.002(0.001)	0.03	0.04	0.11
NO_x Emission Ratio[2]	--	0.23(0.23)	0.19	0.10	0.23
CO Emission Ratio[2]	--	0.02(0.01)	0.05	0.05	0.01
Flywheel Cycles per 100 Miles	3.2	3.5(3.6)	3.9	3.9	5.1
Flywheel Only Range (miles)	31.8	28.3(27.9	25.5	25.5	19.6
% Time Engine on	--	26.9(12.6)	26.9	26.9	26.9

[1] Numbers in parentheses are for a GTE sized for same fuel economy as Otto engine.

[2] Emissions ratioed to 1973 California heavy-duty vehicle standards.

with a resultant 38% decrease in stored energy capability compared to the 33-bhp GTE; nevertheless, the flywheel-only (FO) range is near that of the SIE hybrid. The fuel consumption of the steam-engine (SRE) hybrid is 44% greater than the SIE hybrid.

The commuter car specifications list a maximum trip range (range without supplementing the energy storage system of the vehicle) of 50 miles. Although the flywheel-only vehicle does not attain a 50-mile range on the 10-mode cycle trip, the 21.5-mile range that it does attain is still quite attractive for a specialized intracity vehicle. A range of 50 miles can be attained at 30 mph without the air conditioner operating (Fig. 5-16). A 50-mile range on the cycle could be provided by increasing curb weight W_c by ~1/3 (450 pounds).

For a life of 100 000 miles of driving on the 10-mode cycle, the total numbers of flywheel cycles vary from 4700 for the flywheel-only vehicle to 28 900 for the SRE hybrid; we would not expect these values to present problems in terms of cyclic fatigue. From 6 to 42 accelerations from 0 to 60 mph can be provided by one flywheel charge.

The flywheel-only, Otto-hybrid, and larger GTE-hybrid vehicles are the more promising commuter car configurations. The GTE would necessarily be considered a longer term (i.e., 1978 rather than 1975) choice. Note also the qualification about GTE speed range mentioned at the end of Section 5.4.3.

Family Car. Here, too, the Diesel engine is too heavy to allow for a flywheel system and is omitted from Table 5-11. The larger engine requirement for cruise places the minimum GTE in a more competitive position to the SIE, but its fuel consumption still is 20% greater than the SIE's. Again, a larger GTE (numbers in parentheses) should provide nearly equivalent fuel economy to the SIE at smaller engine weight, with still nearly twice the FO range. All of the hybrids can achieve the 12% grade with the powerplant. The flywheel-only vehicle attains 5.5 miles on the 12% grade, which is short of the required 8 miles. The NO_x emissions are approximately double the 1976 goal for the GTE and SIE hybrids; however, if the Aerospace projections (Ref. 97) are assumed, the NO_x emissions can be reduced by 60 and 67% for the SIE and GTE hybrids, respectively, and would result in emission levels below the 1976 goal. The flywheel-only vehicle cannot meet the specified cruise (200 mile) and grade (8 mile)ranges; however, as with the commuter car, ranges available are attractive for specialized intracity vehicles of this size.

The SIE would necessarily be the near-term engine choice for a hybrid, but its FO cycle range would be relatively low, so that the value of high energy storage would be questionable. (The energy density or flywheel rotor weight would have to be increased by a factor of three to result in a desirable 15 to 20 mile range for a dual-mode vehicle.) In this case, a smaller flywheel operating in parallel with the SIE simply to provide acceleration capability and smooth operation of an engine optimized for low emissions at the higher engine speeds, such as Lockheed (Ref. 2) has proposed, probably would be the correct choice. Nevertheless, the probable safety advantages of composite-type rotors (as opposed to all-metal rotors) could still dictate their choice.

Except for a doubt about NO_x emission levels and the aforementioned uncertainty about GTE speed range and consequent engine-to-flywheel transmission requirements, the GTE has the greatest potential as a long-term choice and does show promise for FO range. It is believed (see Section 7 and Appendix D) that NO_x emissions from GTE's can be further reduced by proper combustor design.

Delivery Van. With the exception of the CIE hybrid, all of the vehicles can attain approximately 20 miles of FO range on the cycle trip. The performance specifications are low when compared to the family car, thereby resulting in a small (34-bhp) engine requirement; the weight remaining permits packaging of a relatively large rotor. The powerplant alone can sustain a 15.4% grade at 8 mph, and the required range of 1/2 mile on the 20% grade can be achieved by all the vehicles with the flywheel alone. For a hybrid system, the SIE is the near-term engine choice because of its lower fuel consumption and low development costs. Again, a larger GTE (values in parentheses) appears to be a good long-term choice, because it could charge the flywheel in 8.4 minutes, and 21 miles of FO operation (~ 3 hours on the cycle) would then be available. This larger engine also would allow the van to cruise at 60 mph on freeways.

As with the family car the best-case OAP estimates for NO_x emissions (with no credit for engine optimization for hybrid use) are double the 1976 goal for all hybrids except the SRE. However, if the Aerospace projections can be attained through optimization, the 1976 goals can be met. The small GTE suffers from its high fuel consumption, and the CIE suffers from its weight, which reduces available FO range. The SRE hybrid, although it appears promising, is the least developed powerplant. The FO vehicle is attractive, since a cycle range of 29.6 miles is estimated. From Fig. 5-16 an FO range of 60 miles (the range requirement specified by OAP) is achievable at a constant speed of 15 mph. Many smaller vans (e.g., postal, florist, druggist, etc.) could be designed to achieve 60 miles on the van cycle if such ranges are needed.

Intracity Bus. The intracity bus appears as the most promising of the specified vehicles for a flywheel system. The relatively large engine size permits a GTE that is competitive with the CIE and SIE engines in terms of fuel consumption. The OAP range requirement of 18 miles can be met with all vehicles in the FO mode of

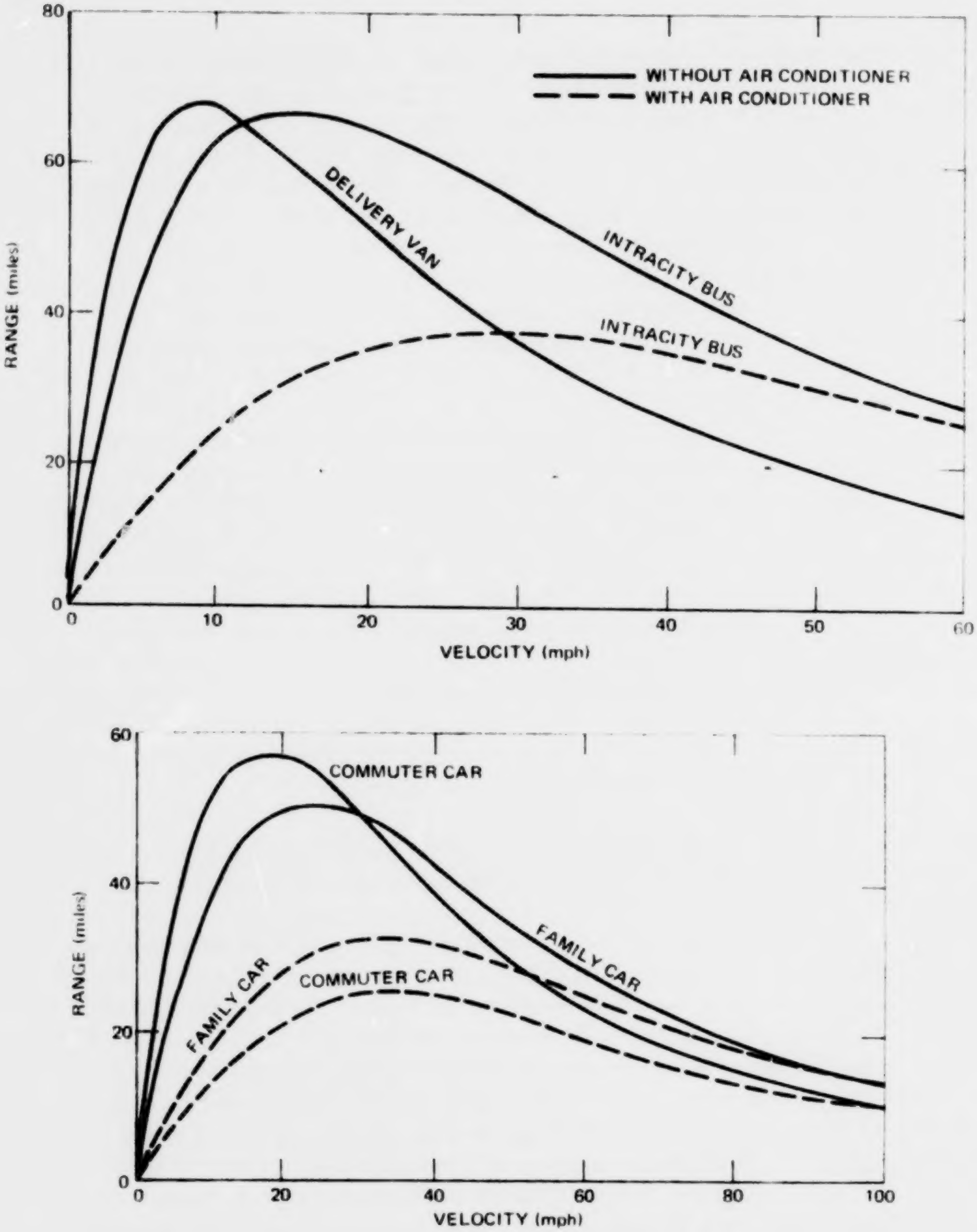

Fig. 5-16 FLYWHEEL-ONLY LEVEL ROAD CRUISE PERFORMANCE

operation. The FO vehicle attains a cycle range of 32 miles. For the hybrids, FO ranges of 26 (SRE) to 29 miles (GTE) are calculated. The larger GTE (values in parentheses) would be able to charge the flywheel in 21 minutes (while the driver takes a rest break at a suburban car barn having a high vent stack)* and would still give 27-mile FO range (2.7 hours of service on the cycle); this 270-bhp engine also would raise V_{des} to ~ 60 mph, making this city bus useful on freeways. Such GTE's are ready for introduction in heavy-duty vehicles before 1975 (Ref. 75).

The emissions for the bus, when compared to the 1973 Diesel proposed standards, are low; however, the proposed standards are not particularly stringent and can be met by the heat engines alone with the emission estimates used here (best OAP values). The grade length requirement of 0.5 mile can be met by all the vehicles with the FO. The SIE hybrid has slight advantages over the Diesel (CIE) in several parameters, but either would be a good second choice behind the large GTE. The CIE does, however, have an odor problem at present. The steam engine also looks good, but its lower state of development makes it an unlikely candidate.

5.5.4 SENSITIVITIES OF PERFORMANCE AND EMISSION ESTIMATES TO ASSUMPTIONS

The SIE hybrid commuter car was selected for the purpose of investigating the influence of variations in various parameters. The base case refers to the SIE hybrid reported in Table 5-10 without the air conditioner operating. The effects of vehicle (and engine) design speed V_{des}, and air-conditioner load, on FO range and fuel economy are shown in Fig. 5-17. Reducing the design speed to 60 mph results in a 48% increase in FO range (from 7.3 to 10.9 miles) with a 6% reduction in fuel economy as a result of the lower bsfc for the smaller engine. Since the $BSPE_i$ are assumed to be independent of

---

*The vent stack could be equipped with both catalytic converters and continuous monitoring instrumentation.

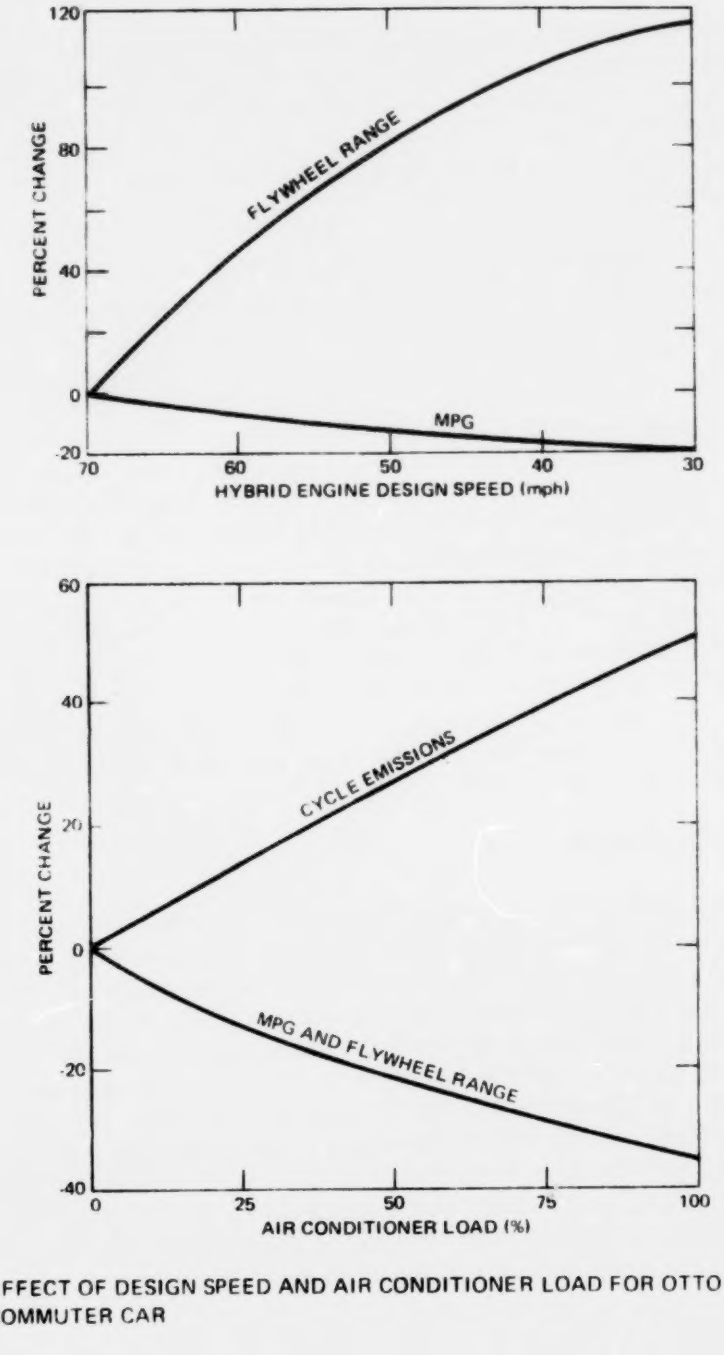

Fig. 5-17 EFFECT OF DESIGN SPEED AND AIR CONDITIONER LOAD FOR OTTO HYBRID COMMUTER CAR

engine size and the total energy required is fixed, the emissions will vary inversely with the fuel economy γ (mpg). Continuous operation of the 4-hp air conditioner (100% load) requires an energy increase of 54%. Accordingly, the emissions increase by 54%, while γ and FO range decrease by 35%.

Figure 5-18 shows that as W_r is increased, fuel economy decreases and total emissions increase due to the increased curb weight. The upswings in the HC and CO emissions for the smaller rotors are due to the effects of the start-up emission penalties. The FO range increases essentially directly with W_r. The effects of the drivetrain efficiencies and the external resistance D (drag and tire friction) on γ are shown in Fig. 5-19. (The emissions on a gm/mi basis vary inversely with γ.) Increasing the regeneration efficiency ϵ_R from 50 to 60% (+20%) results in a 12% increase in γ. The direct linear effects of drive and charge efficiencies are equivalent: a 10% increase in either results in a corresponding 10% increase in γ. Because of the nature of the cycle (small percentage of cruise time) the effects of drag variations are not pronounced. A 20% drag decrease results in a 6.2% increase in fuel economy.

5.6 CLOSURE

With the assumptions stated in Section 5.1, the bus is the only vehicle that literally meets the OAP specifications as an FO vehicle. The 22-mile range of the FO family car is far short of the required 200-mile range. The 21-mile range of the FO commuter car on the 10-mode cycle is 42% of the specified 50-mile range and might be adequate for the second car of many two-car families. A 20-mi/day average would be adequate for a large percentage of cases, and a 7-mile reserve range would always be there for emergency, since only 75% of E_o is used for 21-mile range. Likewise, for a van a 30-mile range would cover many types of delivery routes

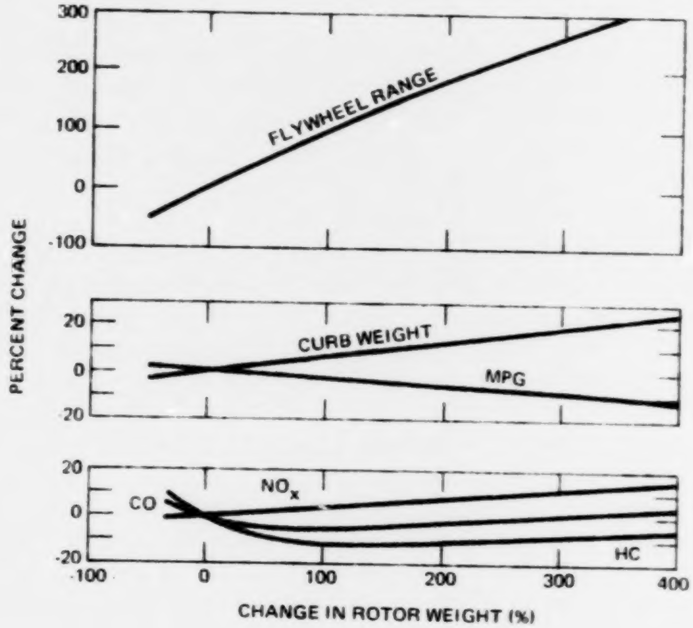

Fig. 5-18 EFFECT OF FLYWHEEL ROTOR WEIGHT FOR OTTO HYBRID COMMUTER CAR

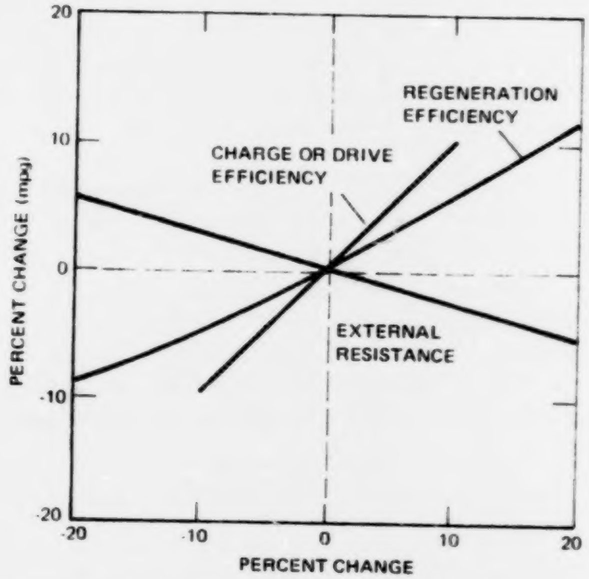

Fig. 5-19 EFFECT OF DRIVETRAIN EFFICIENCIES AND EXTERNAL RESISTANCE FOR OTTO HYBRID COMMUTER CAR

before recharging. Smaller-payload vans could be designed for 60-mile range if desired. A market certainly exists in Britain for this type of vehicle; more than 70 000 battery-powered milk, parcel, and delivery vans are on the road there (Ref. 117).

Heat-engine/flywheel hybrid propulsion looks promising for all of the vehicles and definitely merits further study. Estimated emissions based on the most optimistic OAP projections indicate that the hybrid 'light-duty' vehicles can meet the 1975 standards for CO and HC. The NO_x estimates for the SIE and GTE van and family car hybrids are above the 1976 goals; however, if the Aerospace projections (Ref. 97) for fixed-load, nearly-fixed-speed operation can be attained, the NO_x standard will be met. It should be emphasized that the OAP projections for emissions did not consider engine optimization for this type of operation. An SIE- or GTE-hybrid commuter car is attractive with 7 to 13 miles of emission-free urban driving, and these emission-free ranges could be doubled by allowing a 10% increase in curb weight. The GTE-hybrid bus looks very attractive, particularly if it is given an oversized (300-bhp) GTE to permit 20-minute flywheel recharging and 60-mph cruise on freeways.

These performance projections are based on a number of assumptions that will require detailed investigation. Answers to questions regarding flywheel rotor configuration, seals and bearings, gyroscopic forces, containment requirements, emission characteristics of powerplants optimized for fixed-load, nearly-fixed-speed operation, powertrain component efficiencies, and weights and volumes will have to await experimental investigations.

6. CONCLUSIONS AND RECOMMENDATIONS

6.1 GENERAL

The principal tasks of this program were an experimental proof-of-principle demonstration of the superflywheel concept and evaluation studies which considered a matrix of four vehicles fitted with flywheel-only or flywheel/heat-engine hybrid propulsion systems, and four heat-engine types.

Filamentary and composite rods of 30-inch length have been rotated to high speeds. Energy storage exceeded the goal of 30 W-h/lb of rotor material for small-scale rods of the better materials using the better experimental drive/mounting systems. Larger 1-pound specimens of glass and graphite/epoxy composite materials came within 7 and 13%, respectively, of the goal. There is good reason to believe that improved manufacturing controls for the composite materials will lead to significant improvements over these early experimental data.

High-speed motion pictures of the tests of the larger rods confirm the hypothesized mode of failure. The two halves of a failed composite rod were progressively abraded as they struck (end-on) and moved along opposite sectors (about 90°) of the steel containment ring, and this process was so rapid and complete as to minimize the energy transferred to the ring. This significant finding offers the promise of rotor containment with minimal system weight penalty. The most important task in the future is to develop and test a flywheel system, complete with vacuum capability, low-loss seals and bearings, containment structure, and power take-out.

The results of the evaluation studies indicate that the city bus is the primary candidate for use of a large, flywheel-only system. The delivery van, with reduced range, is a secondary candidate for flywheel-only propulsion. All of the hybrid-propulsion vehicles would meet all vehicle performance requirements and would meet or nearly meet the 1975-76 emissions standards, based on the "best" emissions estimates provided by OAP. However, studies have not taken into account the probable reductions in emissions by the use of hybrid systems in which the heat engine operates only under constant-load, nearly-constant-speed conditions. Investigation of the latter area merits high priority, because it is fundamental to the value of the hybrid propulsion for reducing air pollution.

A literature and technology review of transmissions has shown that there are a number of systems that could be developed to provide the continuously variable control required by the flywheel system. The success in developing such a system with a reasonable production cost is also fundamental to the acceptance of flywheel propulsion systems.

The following sections delineate specific conclusions of this program and the associated recommendations for future work to develop flywheel propulsion systems.

6.2 ROTOR CONFIGURATION AND MATERIALS

We have demonstrated 48 W-h/lb (without failure) with boron filaments, 36 W-h/lb at burst with small graphite/epoxy composite rods, and 31 W-h/lb at burst with small R-glass/epoxy composite rods. These materials are candidates for brush-rotor configurations (the glass composite should improve in strength by 15 to 20% with the substitution of S-glass), and the use of pure filaments or small-diameter, pultruded rods should insure the highest strength, uniformity,and freedom from surface flaws.

The larger 1-pound composite rods did not come up to expectations, showing only 28 W-h/lb (S-glass/

epoxy) and 26 W-h/lb (graphite/epoxy). Tensile tests show that the graphite/epoxy material was substandard, while the S-glass/epoxy bars had many surface defects. The supplier is confident that bars of this same type and material could be produced by a net-molding process (no surface machining and more consistent cure conditions) and would yield improvements in specific energy density to > 30 W-h/lb. The unidirectional laminae should be interspersed with angle plies to resist flaw propagation that can lead to an early catastrophic failure.

With respect to rotor configuration, the simple composite bar is still the most straightforward rotor design and is of interest for a commuter car application. The analysis of a pseudo-isotropic composite disk has shown outstanding potential for a compact, high-energy-density device. The validity of these results must be verified by experiment because of the lack of biaxial stress-strain data for these materials. Finally, two brush-type rotors comprising hubs and multiplicities of individual filaments or rods of glass or fused silica have been conceived. Since these configurations may offer the greatest safety in combination with good performance, they merit experimental evaluation.

RECOMMENDATIONS

1. Evaluate the dynamic fatigue (tension-zero-tension) and stress-rupture characteristics of various types of glass or fused-silica rods and of glass/epoxy composites in a vacuum environment. This will determine whether this low-cost, high-strength material is applicable for flywheel systems.

2. Fabricate and test larger bar-type rotors, using improved processing techniques.

3. Design, fabricate, and test a pseudo-isotropic, glass/epoxy composite disk.

4. Fabricate and test simulations of both circular brush and radially-fanned brush rotors to verify the performance of these configurations.

6.3 CONTAINMENT OF ROTORS

Experiments, both at APL and at NAPTC, have demonstrated that the filamentary and composite materials destroy themselves as they impact steel containing rings. Photographic data from NAPTC have shown that the destruction of 1-pound graphite/epoxy rods takes place in approximately 600 μs, less than the response time of the containment ring. Analyses by two methods have shown that on this test only 1 to 2% of the kinetic energy of the rod is transferred to the ring, the remainder being dissipated by pulverization of the rod itself. This is in direct contrast to the failure mode that has been observed for steel disk rotors, which generally fracture into a small number (usually 2 to 4) of relatively large segments that in turn transfer nearly all of their kinetic energy to the containment ring, as evidenced by the minimal plastic deformation of the segments and the severe distortions of the containment ring. Therefore a conclusion based on data that are presently available is that it should be much easier to contain the fragments of a composite material rotor than it is to contain the fragments of a steel rotor, and this should be particularly important for vehicular applications where public safety is involved.

RECOMMENDATIONS

1. Conduct an experimental program studying the containment of larger rotors in order to establish scaling laws for the ratio of containment weight to rotor weight, to permit design estimates for various rotor sizes of practical interest.

2. Study the containment of configurations such as the pseudo-isotropic, composite disk and the brush-type rotors.

3. Use computer programs that are available to correlate experimental data with empirical formulations of containment requirements.

6.4 FLYWHEEL SYSTEMS

The detailed study of system components such as bearings, seals, and auxiliary vacuum pumps was not included in the scope of the current program; however, cursory review of these items indicates that the problems are amenable to engineering development. The degree of success may dictate the size and type of flywheel rotor that can be used, which in turn will establish stress cycle limits for dynamic and static fatigue rating. Gyroscopic effects on vehicle ride and control were also outside the scope of this program, though a simple simulation was programmed as an example. Further studies of this area could lead to the establishment of limits on flywheel size for certain vehicles.

RECOMMENDATIONS

1. Conduct a detailed design, development, and testing program to qualify flywheel system components such as bearings, seals, and vacuum equipment. Integrate these items and a scaled-up rotor weighing ~ 20 pounds into a prototype demonstrator flywheel system (Fig. 6-1, described below). Selection of the material configuration for this rotor would be based on results of experimental work recommended under Sections 6.2 and 6.3 if time and funds permit. However, because an early demonstration of flywheel system performance, which also would illuminate areas needing greatest attention, is highly desirable, it is recommended that this work proceed immediately with either a graphite/epoxy or an S-glass/epoxy, bar-type rotor.

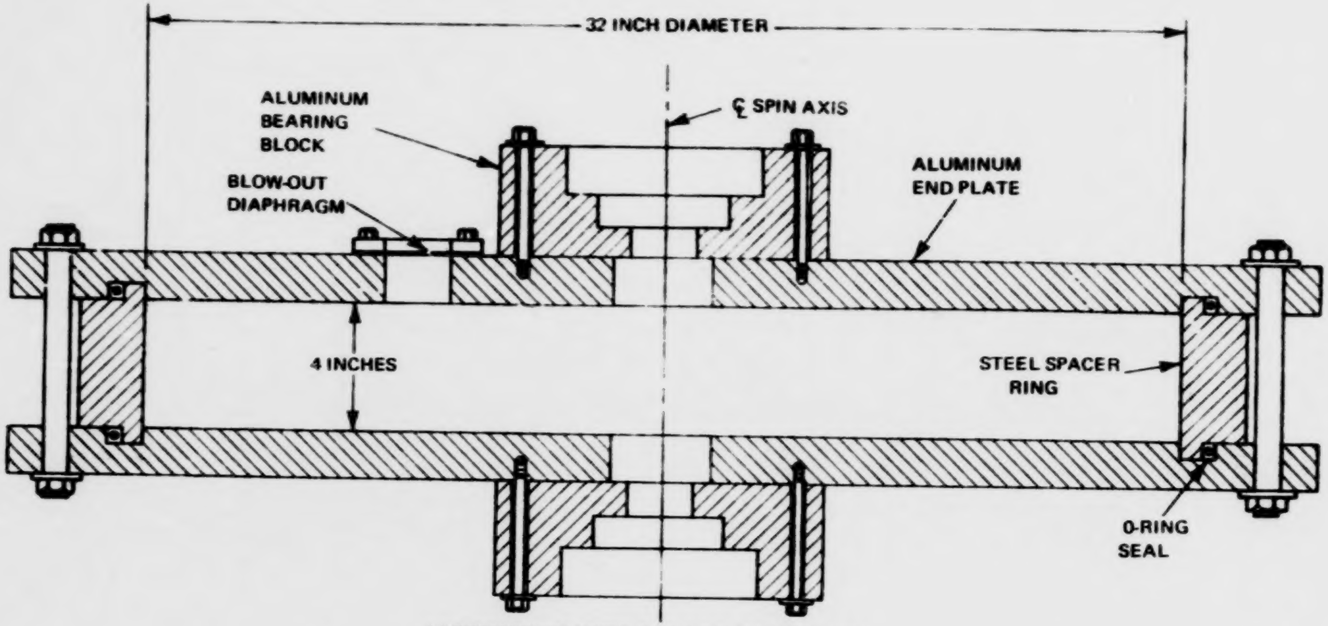
32 INCH DIAMETER
ALUMINUM BEARING BLOCK
℄ SPIN AXIS
BLOW-OUT DIAPHRAGM
ALUMINUM END PLATE
4 INCHES
STEEL SPACER RING
0-RING SEAL

(a) STRUCTURE SIZED FOR BAR ROTOR TESTS

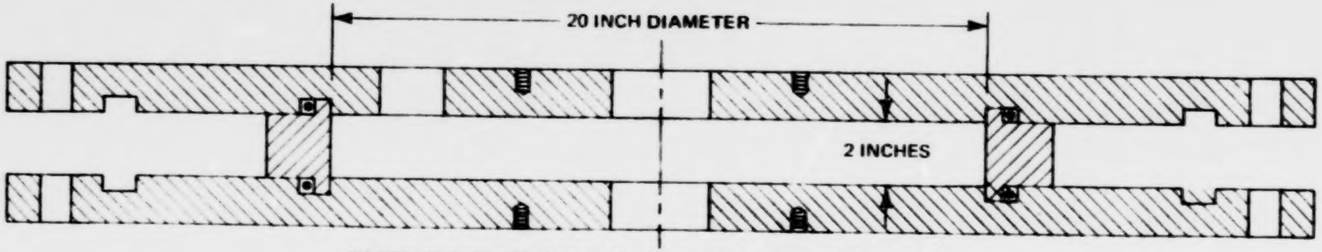
20 INCH DIAMETER
2 INCHES

(b) STRUCTURE MODIFIED FOR DISK OR CIRCULAR BRUSH TEST
(BOLTS AND BEARING BLOCKS NOT SHOWN)

Fig. 6-1 DETAILS OF RECOMMENDED WORKING PROTOTYPE STRUCTURE

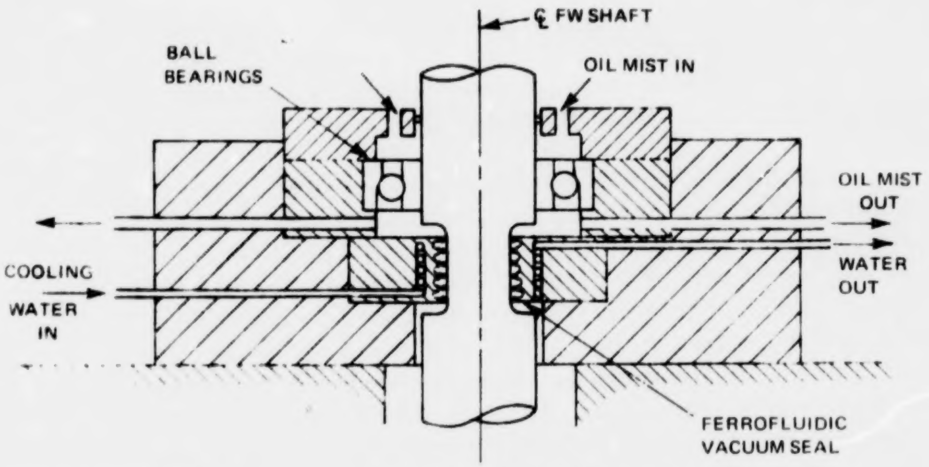
℄ FW SHAFT
BALL
BEARINGS
OIL MIST IN
OIL MIST
OUT
WATER
OUT
COOLING
WATER
IN
FERROFLUIDIC
VACUUM SEAL

(c) SEAL AND BEARING TEST BLOCK

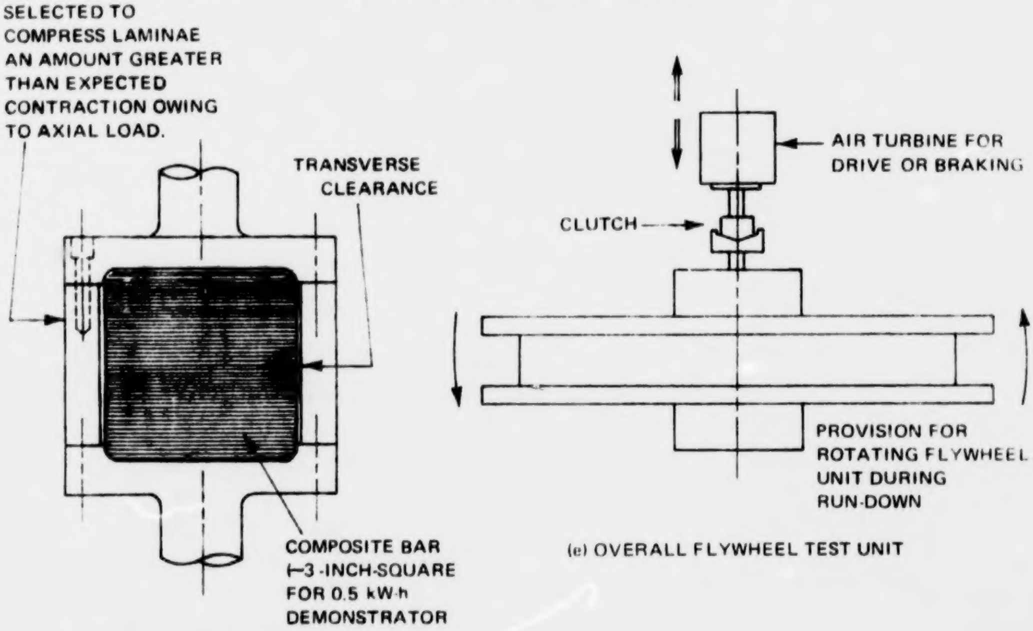
SIDE PLATE DIMENSIONS SELECTED TO COMPRESS LAMINAE AN AMOUNT GREATER THAN EXPECTED CONTRACTION OWING TO AXIAL LOAD.
TRANSVERSE
CLEARANCE
COMPOSITE BAR
~3-INCH-SQUARE
FOR 0.5 kW·h
DEMONSTRATOR
AIR TURBINE FOR
DRIVE OR BRAKING
CLUTCH
PROVISION FOR
ROTATING FLYWHEEL
UNIT DURING
RUN-DOWN

(e) OVERALL FLYWHEEL TEST UNIT

(d) HUB DETAILS FOR BAR ROTOR

Fig. 6-1 (Cont'd) DETAILS OF RECOMMENDED WORKING PROTOTYPE STRUCTURE

2. Conduct computer simulations of flywheel gyroscopic effects in a vehicle, including driver response functions, to assess any problems in ride comfort or control.

A concept for a flexible, working prototype model to permit realistic evaluation of different types of bearings, lubrication systems, shaft seals, and flywheel rotors is shown in Fig. 6-1. The vacuum chamber comprises two identical end plates separated by a cylindrical segment as shown in Fig. 6-1a; "O" rings provide vacuum seals between the parts and are mechanically positioned by grooves in the plates. Different size rotors, such as required for a disk or circular brush, may be accommodated by merely changing the cylindrical insert, as shown in Fig. 6-1b. In this way minimum radial and axial clearance can be maintained.

Figure 6-1c shows the conceptual layout of the bearing and seal attachment. A water-cooled ferrofluidic seal is used on a reduced-diameter section of the shaft, mounted inboard of the bearing. The bearing shown is the angular-contact ball type, supplied with positive lubrication. Thus the bearings and seals are accessible for inspection and replacement.

Figure 6-1d shows a cross section of the hub attachment of a bar rotor. Numerical stress analysis of the rotor has shown that the deformation near the hub is quite complex. There is a positive deformation in the direction of the fibers, and this creates a contraction (Poisson's ratio effect) in the transverse and spin-axis directions. However, in the transverse direction centrifugal forces create a positive component of deformation which, for wide bars, is greater than the contraction due to Poisson's ratio. The net result is that the bar will contract along the direction of the spin axis and contract, stay the same, or grow in the transverse direction depending on the bar aspect ratio. The hub attachment accommodates these deformations by (a) preloading the bar in the spin-axis direction (squeezing) enough to counteract the expected contraction, and (b) allowing the bar to expand or contract in the transverse direction without constraint.

The overall arrangement is shown in Fig. 6-1e with a bar-type rotor installed. The rotor is powered by an air turbine, and the conical friction clutch can be disengaged for free-wheeling operation. The flywheel unit can be tilted to produce gyroscopic torques and radial loads on the bearings. This working prototype system could be used to evaluate seals and bearings and to demonstrate flywheel run-down and power takeout.

6.5 EVALUATION STUDIES

The city bus is the only vehicle that can meet the vehicle performance specifications using a flywheel-only (FO) propulsion system. There still may be application for FO propulsion in certain classes of central business district delivery vans and for a small, personal runabout or limited-range commuter car. Heat-engine/flywheel hybrid propulsion systems satisfy the performance requirements of all four classes of vehicles — commuter car, family car, city bus, and van. The near-term choice of heat engine is the spark-ignition engine; however, the gas turbine offers the greatest promise for the future because of its low specific weight, its potential for minimizing emissions, and its operating speed, which is close to that of the flywheel.

The results of emissions analysis of the hybrid systems must be considered inconclusive because of the lack of data on the operation of engines at single design points or over a very limited speed range. It is expected, however, that restricted operation of a specially designed engine will result in significant reductions in emissions, and this mode of operation is recommended. The use of on-off engine operation and relatively large flywheel systems will permit dual-mode operation of the vehicle, with long periods of emission-free operation within congested areas. This remains an attractive concept and should not be discarded unless other studies show that a large flywheel is undesirable or that start-up and shut-down emissions are excessive.

RECOMMENDATIONS

1. Obtain emissions data for spark-ignition and gas turbine engines operating at selected design points. The engines, which should be of a size appropriate for use in a flywheel hybrid system, should then be modified (timing, carburetion, manifold design, etc., or corresponding features for gas turbines) to minimize emissions at the selected operating condition(s).

2. Conduct basic combustion research to determine NO concentrations as a function of distance from the luminous zone of a flat flame, thereby answering questions on the existence of "prompt NO" (see Appendix E) that could have a fundamental effect on the ability to meet the 1976 NO_x standards.

3. Develop a prototype continuously-variable transmission and integrate it with an improved heat engine (item 1 above) and a prototype flywheel system (see Section 6.4). This propulsion system then should be installed in a vehicle to demonstrate heat engine/flywheel hybrid propulsion.

APPENDIX A

FLYWHEEL SHAPE AND BIAXIAL STRESS CONSIDERATIONS

A.1 FLYWHEEL PERFORMANCE CHARACTERISTICS AND THE OPTIMAL SHAPE FOR A RIGID, UNI-AXIALLY LOADED ROD

A.1.1 Constant-Thickness Flywheels of Isotropic Material

As noted in Section 3, specific kinetic energy E/W of a rotor of radius R and weight W at rotational speed ω is given by:

$$\frac{E}{W} = \frac{I\omega^2}{2W} = k_I \frac{R^2\omega^2}{2g} \quad \text{where} \quad k_I = \frac{gI}{WR^2}, \qquad \text{(A-1)}$$

and I is the mass moment of inertia about the axis of rotation. If ω is specified (for a given R and W), maximum E/W can be achieved by using the flywheel configuration with the highest I, and a rim-type flywheel is best. However, if ω is allowed to vary, so that ω is, in effect, governed by the allowable stress of the material, it is not directly apparent from Eq. (A-1) which flywheel configuration is best.

In general, the stress in a rotating rigid body can be related to ω through the equilibrium stress balance in the radial direction. For conditions of plane stress in a constant thickness flywheel (Ref. 118):

$$\sigma_t - \frac{d}{dr}(r\sigma_r) - \rho r^2\omega^2 = 0 , \qquad \text{(A-2)}$$

where σ_t, σ_r are the tangential and radial stresses, $\rho (= \gamma/g)$ the material mass density, and r the radial coordinate. The last term represents the centrifugal (inertial) force component. Solution of this equation for particular configurations (using the appropriate boundary conditions) permits the determination of the maximum stress values for each configuration. Equating the maximum stress to the yield stress (allowable) σ_a, given by a suitable failure criterion – von Mises condition (Ref. 119):

$$\sigma_a^2 = \sigma_r^2 + \sigma_t^2 - \sigma_r \sigma_t \,, \tag{A-3}$$

determines the maximum speed allowable and, with Eq. (A-1), the energy storage capability.

As can be seen from dimensional considerations, solutions for ω^2 will be proportional to $\sigma_a / \rho R^2$, so that we can write:

$$\frac{E}{W} = k_I k \frac{\sigma_a}{\rho g} \qquad \text{where} \qquad k = \frac{\omega^2 R^2}{2\sigma_a / \rho} \,. \tag{A-4}$$

Solutions of Eq. (A-1) for various standard configurations, solid disk, disk with hole, thin rim, and slender, uniform rods are readily available, c.f., Ref. 118. For slender rods the terms involving σ_t in Eqs. (A-2) and (A-3) drop out. The use of the failure criterion (A-3) in these available solutions results in the performance characteristics shown in the upper portion of Table A-1. These computations assume that R and σ_a are specified. In particular, to determine the allowable ω for the solid disk and the disk with a center hole, the maximum-stress solutions given by Timoshenko (Ref. 118) were used. For the thin rim and the rod, solution of Eq. (A-2) follows directly. In all cases $\sigma_{max} = \sigma_a$ occurs at the innermost radius ($r = 0$ with no hole; $r = r_o$ with a hole). It is apparent from Table A-1 that the solid disk is the best constant-thickness flywheel configuration. For other payoff criteria or other specified parameters (such as the fixed-ω case mentioned above) the relative merits of these configurations would be different.

Table A-1

Effects of Shape on Flywheel Properties

Rotor Configuration	Rotational Speed[1] $\omega^2/(\sigma_a/\rho R^2)$	Moment of Inertia $I/(WR^2/g)$	Energy Storage $\frac{E_0/W}{(\sigma_a/\rho g)}$	Packaging Efficiency $\frac{E_0/V}{(\sigma_a)}$
Uniform thickness rod	2	1/3	1/3	0-0.02[2]
"Optimal" rod	→ ∞	→ 0	1/2	0-0.01[2,3]
"Constant-stress" family, $\alpha = 2$:				
With end mass	8	0.120	0.48	0-0.02[2,3]
Without end mass	8	0.117	0.46	0-0.02[2,3]
1-D wedge ($A \propto r$)	16/3	1/12	2/9(≈0.22)	0-0.4[4]
2-D wedge (pyramid) ($A \propto r^2$)	9	1/10	9/20(≈0.45)	0-0.05[4]
Uniform solid disk	2.42	1/2	0.605	0.605
Uniform rim $0 < r_{hole} < R$	1.21 → 1	1/2 → 1	0.30 → 1/2	0.3 → 0
Best constant-stress solid disk (theoretical limit)	→ ∞	→ 0	1	→ 0
Constant-stress disk, k = 4	8	0.231	0.925	0.23
Hyperbolic (rim, $\eta = 1$), best E/W, $\bar{r}_0 \approx 0.05$	4.37	0.351	0.77	0.07
Hyperbolic, best E/V, $\bar{r}_0 \approx 0.50$	1.31	0.58	0.38	0.19
Hyperbolic, $Z/z_1 = 4$, $\bar{r}_0 = 1/4$	1.87	0.42	0.41	0.15

[1] Equal to 2k or $2\alpha^2$.

[2] Based on a rod radius ≈ 0.15 R (R = arm length); E_0/W is degraded as E_0/V is increased (see Section A.2).

[3] Rod also tapers almost hyperbolically (Fig. A-2) but still must effectively occupy an almost drum-like packaging space.

[4] Based on a maximum half-width ≈ 0.15 R.

A.1.2 Optimal Rod Flywheels (Rotors) of Isotropic Material

Consider a slender rod of variable cross-sectional area, $A = A(r)$ spinning about its center point ($r = 0$), and having a specified $R(= r_1)$ and a given weight W. Because of the variable area, the overall weight must be specified as:

$$W = 2\rho g \int_0^R A dr , \qquad \text{(A-5)}$$

and the radial stress equation becomes:

$$\frac{d}{dr}(A\sigma_r) = -\rho\omega^2 rA, \quad \sigma(R) = 0 . \qquad \text{(A-6)}$$

The limiting stress relationship is $\sigma_r \leq \sigma_a$, and the energy to be maximized by optimization of $A(r)$ is:

$$E = \rho \int_0^R \omega^2 r^2 A dr , \qquad \text{(A-7)}$$

which is equivalent to maximizing E/W, since W is specified.

From the limiting stress relationship, $\sigma_r \leq \sigma_a$, it follows that the optimal configuration may consist of two segments: $\sigma_r < \sigma_a$ and $\sigma_r = \sigma_a$. The shape of the region where the inequality holds is not ascertainable, since the resulting Eq. (A-6) contains two unknown variables σ_r and A. When $\sigma_r = \sigma_a$, Eq. (A-6) yields:

$$A = A_0 e^{-\alpha^2 (r/R)^2}, \quad \text{where } \alpha^2 = \frac{\omega^2 R^2}{2\sigma_a/\rho} , \qquad \text{(A-8)}$$

and $A_0 = A(0)$, and the solution is specified when α, the dimensionless rotational speed, is specified. Physical reasoning suggests that the optimal rod should be in a state of maximum stress throughout, since, if this were not the case, some of the material existing in a region where $\sigma_r < \sigma_a$ could be redistributed and therefore effectively increase E/W. On the other hand, if $\sigma_r = \sigma_a$ over the entire rod the boundary condition $\sigma(R) = 0$ cannot be satisfied. Thus, the optimal rod is one wherein $\sigma_r = \sigma_a$ throughout except for a small segment at each end of length ΔR and mass m_e. This end segment may be of any shape as long as m_e is sufficient to give $\sigma_r = \sigma_a$ at $r = R - \Delta R$. (The end condition will be considered again below.) Moreover, to make m_e as small as possible, α^2 should be as large as possible. That this condition leads to the maximum payoff is borne out by the following constant-stress flywheel solutions.

Assume now that the size, mass and energy of the end mass are small. From Eqs. (A-7) and (A-8) it follows that:

$$\frac{W}{2\rho g A_0 R} = \frac{\sqrt{\pi}}{2} \frac{\mathrm{erf}(\alpha)}{\alpha} , \qquad \text{(A-9)}$$

$$\frac{E}{\rho A_0 R} = \frac{\sigma_a}{\rho\alpha} \left\{ \alpha^2 \frac{\sqrt{\pi}}{2} \mathrm{erf}(\alpha) - \sqrt{\pi} \left[\alpha \int_0^\alpha \mathrm{erf}(s)ds - \int_0^\alpha \int_0^t \mathrm{erf}(s)\,dsdt \right] \right\}$$

where s is a dummy variable, so that:

$$E/W = G(\alpha)\sigma_a/\rho g , \qquad \text{(A-10)}$$

$$G(\alpha) = \alpha^2 - \frac{2\alpha}{\mathrm{erf}(\alpha)} \int_0^\alpha \mathrm{erf}(s)ds + \frac{2}{\mathrm{erf}(\alpha)} \int_0^\alpha \int_0^t \mathrm{erf}(s)dsdt ,$$

again indicating the independence of E/W from the actual dimensions of the flywheel. $G(\alpha)$ can be evaluated directly using complementary error functions. In the limit as

$\alpha \to \infty$, $G(\alpha) \to 1/2$. Figure A-1 shows E/W referenced to E/W for the uniform rod (see Table A-1) versus α. The area distribution for various values of α from Eq. (A-8) is shown in Fig. A-2.

Although it would be difficult to construct the optimal rod flywheel, various approximations to the optimal, in the constant-stress family, $\alpha < \infty$, can perhaps be constructed. For reference, the optimal case as well as a possible approximation ($\alpha = 2$) are included in the lower portion of Table A-1. Other rod flywheels such as the double pyramid $[A/A_0 = (1 - r/R)^2]$ also approach the optimal.

To complete the analysis it is necessary to show that $m_e \to 0$ as $\alpha \to \infty$, i.e., the end mass is small for the optimal rod. Moreover, for the solutions to be valid for other values of α it must be demonstrated that the effects of the end mass can correctly be neglected. Consider for simplicity a concentrated end mass m_e located at $r = R$ (the subscript e refers to the end conditions at $r = R$). A simple force balance at this location results in:

$$m_e = \sigma_a A_e / \omega^2 R = \rho A_e R / 2\alpha^2 , \tag{A-11}$$

from which it is evident that as $\alpha \to \infty$, $m_e \to 0$. Using this relation and the area distribution, Eq. (A-8), it follows that:

$$\frac{W_e}{W} = \frac{m_e/g}{W} = \frac{1}{2\sqrt{\pi}} \frac{e^{-\alpha^2}}{\alpha \operatorname{erf}(\alpha)} ; \quad \frac{E_e}{W_e} = 2\alpha^2 \frac{\sigma_a}{2\rho g} ; \tag{A-12}$$

$$\frac{E_e}{W} = \frac{2}{\sqrt{\pi}} e^{-\alpha^2} \frac{\alpha}{\operatorname{erf}(\alpha)} \frac{\sigma_a}{2\rho g} . \tag{A-13}$$

Figure A-3 shows $(E_e/W)/(E/W)$ as derived from Eq. (A-13). For $\alpha \geq 3$ the concentrated-end-mass contribution is negligible. For the $\alpha = 2$ case shown in Table A-1, the end mass

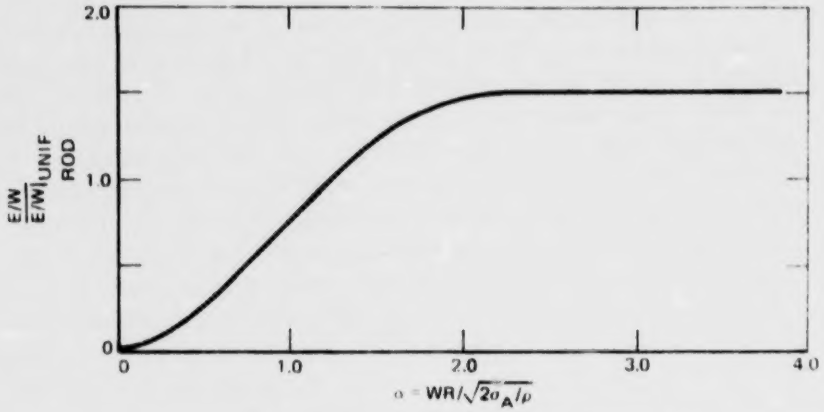

Fig. A-1 CONSTANT STRESS FLYWHEEL PERFORMANCE

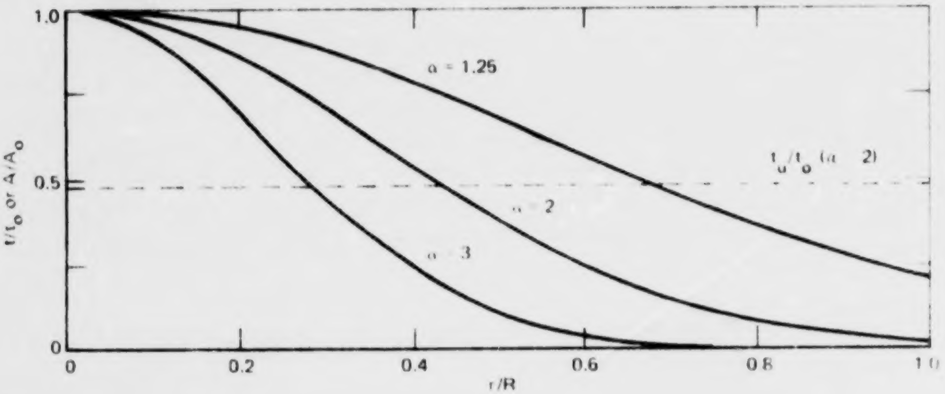

Fig. A-2 THICKNESS DISTRIBUTIONS FOR CONSTANT STRESS ROD FLYWHEELS. ($t_o/t_{\alpha=2}$ = THICKNESS OF UNIFORM ROD WITH SAME WEIGHT AS $\alpha = 2$ CONSTANT STRESS CASE.)

contains 4% of the total energy and about 0.3% of the mass. While the solutions for large α (including the optimal) are therefore valid, solutions for $\alpha < 2$ using small values are not, and a proper analysis of a rod for $\alpha < 2$ would entail a combined set of computations considering both the constant-stress portion of the rod and the end mass. Fortunately, such cases are of little interest. For large α the end mass becomes a very efficient energy storage portion of the flywheel [Eq. (A-13)], but the magnitude of E_e becomes very small. [Similar results can be obtained by considering the end mass to be finite in extent. In this case the constant-stress results would be somewhat in error, since the constant-stress region goes only to $r = R - \Delta R$. If $\Delta R/R$ is assumed small a mass balance at $R - \Delta R$ yields $\Delta R/R = 1/(2\alpha^2)$, confirming the conjecture. For $\alpha = 2$, $\Delta R/R = 12.5\%$; and α must be 5 to reduce $\Delta R/R$ to 2%. Thus, for end regions of finite length, the analysis is more in error than for the "concentrated" end mass case.]

The end mass given by Eq. (A-11) need not have any particular configuration so long as it is of a form which does not violate the boundary condition, $\sigma(R) = 0$; however, it must be present to give a constant stress throughout the remainder of the rod. The saving grace in the actual construction of such flywheels is the fact that the absence (or incorrect value) of the end mass at large α will only slightly alter the stress distribution throughout the rod and thus give an almost optimal value. This is illustrated by the stress distributions shown in Fig. A-4 and the final listing in Table A-1.

A.1.3 Theoretical Performance Capabilities for Isotropic Rotors

The optimal rod flywheel, while not feasible as an actual design, represents a basis for comparison of other candidate flywheel configurations. Using maraging steel as an example of current high strength isotropic materials, $\sigma_a = 400$ ksi, $\gamma = \rho g = 0.28$ lb/in^3, it follows that the best

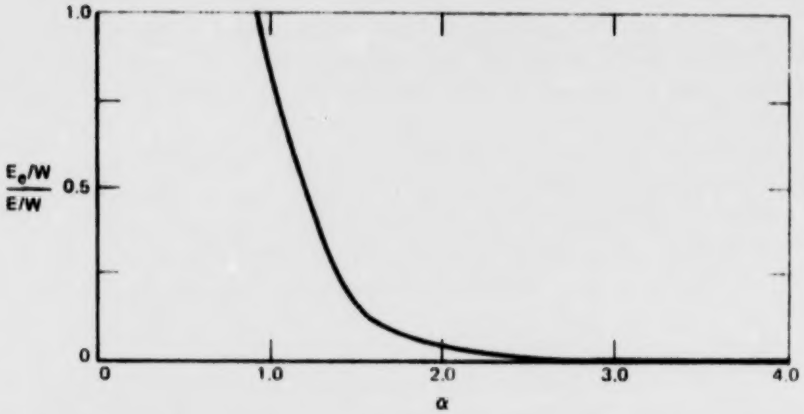

Fig. A-3 EFFECT OF END MASS ON CONSTANT STRESS FLYWHEEL PERFORMANCE

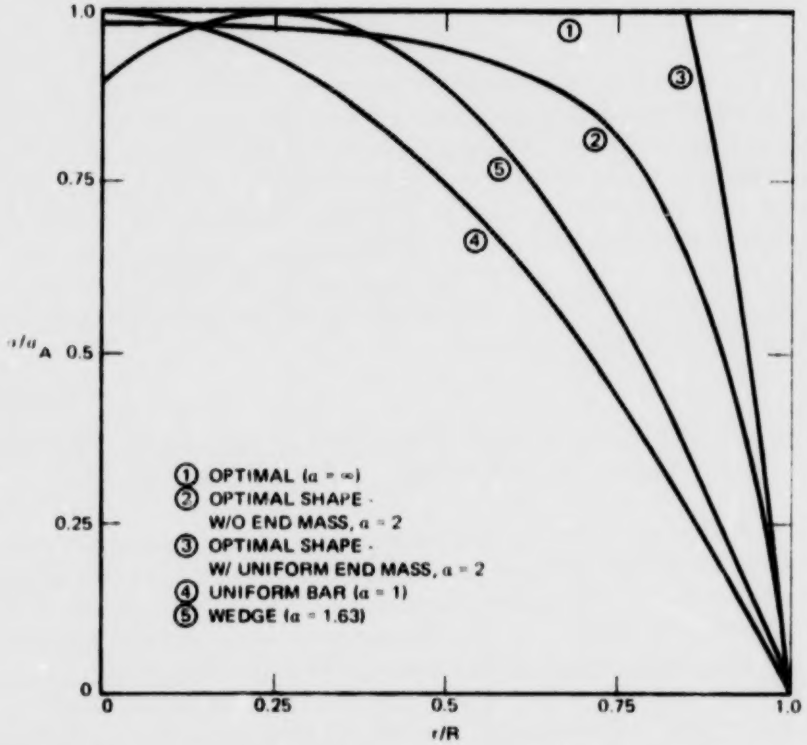

Fig. A-4 STRESS DISTRIBUTIONS IN VARIOUS ROD FLYWHEEL CONFIGURATIONS rod flywheel configurations would approach E/W = 59 600 ft-lb/lb = 22.7 W-h/lb, as compared to 15.3 W-h/lb for the uniform rod and 27.5 W-h/lb for the uniform disk. (For conventional steel σ_a = 140 ksi, $E/W|_{\text{opt. rod}}$ = 7.9 W-h/lb. Values for other configurations and properties can be computed using the information in Table A-1.) Further improvements using isotropic materials can be achieved using optimal (nonuniform) shapes for other flywheel configurations, e.g., the solid disk, as discussed in Section A-3.

It is desired to use the increased uniaxial stress properties of fibrous and fiber-composite materials in a flywheel composed of rod type elements. Since $E/W \propto \sigma_a/\rho$, a uniform rod composed of boron filaments, with σ_a = 400 ksi, and γ = 0.092 lb/in^3, will have an E/W of 38 W-h/lb, 1.67 times better than the maraging steel disk.

In practice practical effective stress values must be used. These design values must account for material degradation effects (fatigue, etc.), effective utilization stress (for composites or bundles of fibers) and appropriate factors of safety. In addition, the effects of other flywheel-system design considerations, such as bearing requirements, air drag, vacuum seals, starting and stopping considerations, and overall flywheel sizing and weight requirements or constraints must be taken into account.

A.2 ELASTIC ANALYSIS OF A ROTATING ANISOTROPIC BAR USING THE METHOD OF COLLOCATION

The gains to be derived from uniaxially loaded rod or bar flywheels of fiber-composite materials in comparison to more conventional flywheel configurations were mentioned in Section A.1. Because it is desirable from a packaging standpoint to have the greatest energy storage per unit volume, a bar-type flywheel should be as wide as practical. Therefore, the transverse properties of the fiber-composite material must be considered in determining the energy storage capability. In this section a method of solution based on collocation is used to provide approximate results for the biaxial stress field. Using Hill's yield criterion (Ref. 120) for anisotropic materials, limiting rotational speeds are determined as a function of bar aspect ratio (width/length) for several fiber-composite materials, and corresponding energy reduction factors are presented.

A.2.1 Method of Analysis

Among approximate analytical methods (Ref. 121), weighted residual techniques are very effective. A trial solution, in terms of undertermined parameters, is selected and the parameters are determined in such a way as to make a residual equation zero. Each method is classified according to the manner in which the residual equation is formed. One method in particular, collocation, is most direct, requiring only a substitution of the trial solution in the governing differential equation, whereas other methods require integrations. Collocation is analogous to curve-fitting with the assumed solution satisfying the governing equation at all collocation points. The accuracy attained depends critically on the selection of the form of the trial solution. Problems in heat conduction (Ref. 122) and elastic plate analysis (Ref. 123) have illustrated the ease in application of the collocation method.

The conditions of equilibrium for an element of the rotating bar in plane stress (Fig. A-5) are:

$$\frac{\partial \sigma_r}{\partial r} + \frac{\partial \tau}{\partial t} + \underline{\overline{R}} = 0 \qquad \frac{\partial \tau}{\partial r} + \frac{\partial \sigma_t}{\partial t} + \underline{\overline{T}} = 0 \; , \tag{A-14}$$

where σ_r, σ_t, and τ are the axial, transverse, and shear stress and $\underline{\overline{R}}$ and $\underline{\overline{T}}$ are components of the body-force caused by rotation. With the body-force field obtained as the gradient of a potential $\underline{\overline{V}}$:

$$\underline{\overline{R}} = \partial \underline{\overline{V}} / \partial r \qquad \underline{\overline{T}} = \partial \underline{\overline{V}} / \partial t \; . \tag{A-15}$$

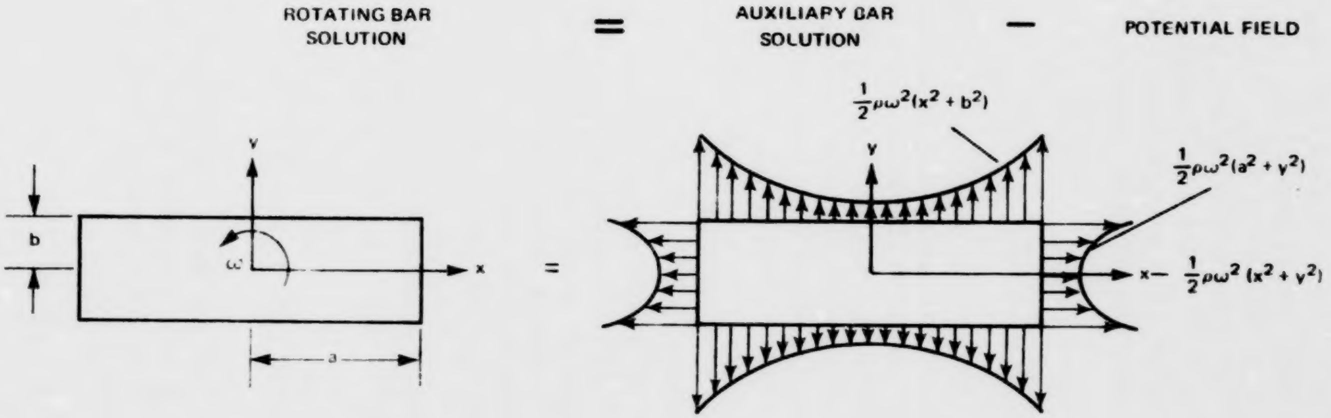
ROTATING BAR SOLUTION
=
AUXILIARY BAR SOLUTION
—
POTENTIAL FIELD
y
b
ω
x
a
=
$\frac{1}{2}\rho\omega^2(x^2 + b^2)$
y
$\frac{1}{2}\rho\omega^2(a^2 + y^2)$
x
$\frac{1}{2}\rho\omega^2(x^2 + y^2)$

Fig. A-5 FORMULATION OF ROTATING BAR PROBLEM. NOTE THAT THE THIN PLATE OR BAR IS IN PLATE STRESS

Equations (A-14) are identically satisfied when:

$$\sigma_r + \underline{\overline{V}} = \frac{\partial^2 \underline{\overline{\Psi}}}{\partial t^2}, \quad \sigma_t + \underline{\overline{V}} = \frac{\partial^2 \underline{\overline{\Psi}}}{\partial r^2}, \quad \tau = -\frac{\partial^2 \underline{\overline{\Psi}}}{\partial r \partial t} . \qquad \text{(A-16)}$$

where $\underline{\overline{\Psi}}$ is a stress function and:

$$\underline{\overline{V}} = \tfrac{1}{2}\rho\omega^2(r^2 + t^2) . \qquad \text{(A-17)}$$

For isotropic problems, the usual procedure is to substitute the stress-strain relations into the compatibility equation and use the definition of the stress function. When body forces are absent, the solution of a biharmonic equation for $\underline{\overline{\Psi}}$ is required. However, for the anisotropic problem with body forces, a slightly different approach will be used. The formulation follows from the use of an artifice discussed by Flügge (Ref. 124) known as Biot's Theorem. The particular solution $\underline{\overline{\Psi}} = 0$ of the biharmonic equation yields for the stresses:

$$\sigma_r = \sigma_t = -\underline{\overline{V}}, \quad \tau = 0 . \qquad \text{(A-18)}$$

This represents the solution if the boundary conditions specify the application of a normal pressure $\underline{\overline{V}}$ at all points of the boundary, which is in equilibrium with the body forces. Since forces different from this pressure are prescribed at the boundary (namely stress-free conditions), the solution is the sum of Eq. (A-18) and a stress system for zero body forces and an edge load equal to the normal tension $\underline{\overline{V}}$. Therefore, the stresses in a rotating plate (or bar) can be derived from an auxiliary stress field S_r, S_t, and S_τ for a plate without body forces subjected to a normal stress $\underline{\overline{V}}$ applied to all points of the boundary; the actual stresses are then:

$$\sigma_r = S_r - \underline{\overline{V}}, \quad \sigma_t = S_t - \underline{\overline{V}}, \quad \tau = S_\tau . \qquad \text{(A-19)}$$

The situation is illustrated in Fig. A-5. With the body forces removed, the equilibrium equations:

$$\partial S_r/\partial r + \partial S_\tau/\partial t = 0 \qquad \partial S_\tau/\partial r + \partial S_t/\partial t = 0\ , \tag{A-20}$$

are satisfied by:

$$S_r = \partial^2\Phi/\partial t^2,\ S_t = \partial^2\Phi/\partial r^2,\ S_\tau = -\,\partial^2\Phi/\partial r\partial t\ . \tag{A-21}$$

The stress-strain relations for an orthotropic plane stress material are:

$$\Sigma_r = (S_r - \nu_{rt}S_t)/E_r;\ \Sigma_t = (S_t - \nu_{tr}S_r)/E_t;\ \Gamma = S_\tau/G_{rt}\ , \tag{A-22}$$

where $\nu_{tr}\, E_r = \nu_{rt}\, E_t$, and the elastic constants E_r, E_t, G_{rt}, and ν_{rt} are the Young's Moduli in the principal directions, the shear modulus, and the major Poisson's ratio.

When the constitutive equations [Eqs. (A-22)] are substituted into the compatibility equation:

$$\partial^2\Gamma/\partial r\partial t = \partial^2\,\Sigma_r/\partial t^2 + \partial^2\Sigma_t/\partial r^2\ , \tag{A-23}$$

and the stress function is introduced via Eqs. (A-21), we obtain the following fourth-order equation:

$$L_4\Phi = \frac{\partial^4\Phi}{\partial r^4} + 2p\,\frac{\partial^4\Phi}{\partial r^2\partial t^2} + m\,\frac{\partial^4\Phi}{\partial t^4} = 0\ , \tag{A-24}$$

where $p \equiv m[n + \nu_{rt}(n-1)]$, $n \equiv E_r/2(1 + \nu_{rt})G_{rt}$, and $m \equiv E_t/E_r$. Note that for an isotropic material Eq. (A-24) reduces to the standard biharmonic form with $p = n = m = 1$.

In summary, to obtain the solution for the stress field in a rotating anisotropic bar: (a) Eq. (A-24) is solved according to the boundary conditions for the auxiliary problem, and (b) the stresses are determined by Eq. (A-19) as the superposition of the potential field on the stresses for the auxiliary problem, Eq. (A-21).

Some form must be assumed for the stress function. Referring to Fig. A-5, the distribution of boundary stresses on the auxiliary problem consists of a combination of uniform and parabolic components. A somewhat similar problem having a parabolic stress distribution on the boundaries $r = \pm R$ was solved by Rivello (Ref. 125) using both finite-difference and Rayleigh-Ritz solution techniques. (The Rayleigh-Ritz procedure uses energy principles to obtain approximate solutions.) This problem is illustrated in Fig. A-6 together with a comparison of the normal stresses given by each approximate solution. The finite-difference solution was based on a relatively crude mesh of 12 grid points, but more important, the Rayleigh-Ritz solution resulted from the following assumed form for the stress function:

$$\Phi = \frac{ct^4}{12} + (r^2 - R^2)^2 (t^2 - T^2)^2 (a_1 + a_2 r^2 + a_3 t^2) . \quad (A-25)$$

The first term satisfies the essential (force boundary) conditions, whereas the remaining terms are chosen to give no stresses on the boundary. Since the loading is symmetrical about the r- and t-axes, only even power terms were included in the polynomial series. Although each method produces an approximate solution to the problem, because of the form of Eq. (A-25), the Rayleigh-Ritz method gives exact results for σ_r stresses at $r/R = \pm 1$.

The similarity in boundary conditions between the problem of Ref. 125 and the auxiliary problem of the rotating bar suggests the choice of Eq. (A-25) for the assumed form of the stress function. To validate the collocation method of solution for the rotating bar, the problem of Ref. 125 was resolved by collocation, and the results were compared with the three-term Rayleigh-Ritz solution. For collocation, up to 11 terms were included in polynomial series:

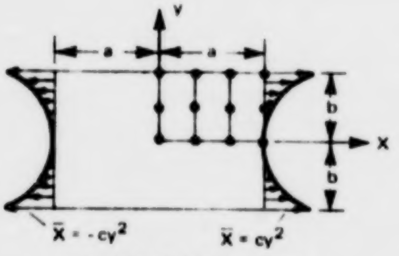

EXAMPLE PROBLEM

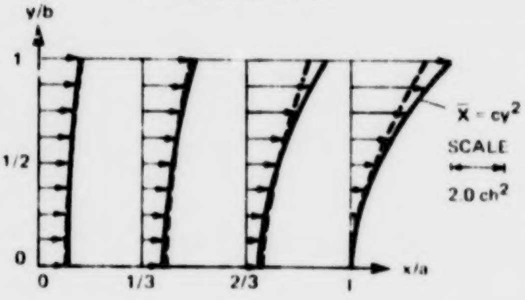

(a) σ_x

$\frac{b}{a} = \frac{2}{3}$

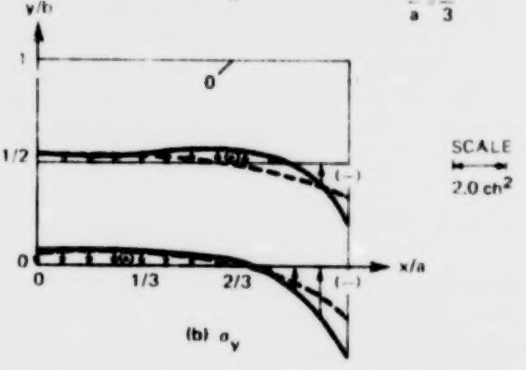

(b) σ_y

Fig. A-6 COMPARISON OF RAYLEIGH-RITZ SOLUTION WITH FINITE-DIFFERENCE SOLUTION. THE SOLUTION IS SHOWN AS A DASHED LINE (SYMMETRICAL ABOUT X AND Y AXES) (REF. 125)

$$F = a_1 + a_2 r^2 + a_3 t^2 + a_4 r^2 t^2 + a_5 r^4 + a_6 t^4$$
$$+ a_7 r^2 t^4 + a_8 r^4 t^2 + a_9 r^4 t^4 + a_{10} r^6 + a_{11} t^6 . \quad \text{(A-26)}$$

To apply the collocation method, we select as many locations* as there are undetermined parameters a_i, substitute Eq. (A-25) into the biharmonic equation and solve the linear algebraic system for the unknown coefficients a_i. For example, using the first four terms in the polynomial would require four locations to evaluate the biharmonic equation. Table A-2 summarizes the various solutions corresponding to a specific number of terms in the polynomial for several collocation patterns. Selected collocation solutions are compared with the three-term Rayleigh-Ritz solution in Table A-3. For the parabolic boundary stress distribution, very little accuracy is gained by including more than six terms in the collocation solution.

A. 2. 2 Results for Fiber-Composite Rotating Bars

Based on the foregoing results, a six-term polynomial was adopted in the solution for the stress-function to evaluate rotating anisotropic bars:

$$\Phi = \frac{1}{12} \rho\omega^2 (6R^2 t^2 + t^4 + 6T^2 r^2 + r^4) + (R^2 - r^2)^2 \times$$
$$(T^2 - t^2)^2 (a_1 + a_2 r^2 + a_3 t^2 + a_4 r^2 t^2 + a_5 r^4 + a_6 t^4). \quad \text{(A-27)}$$

The first term in Eq. (A-27) satisfies the stress boundary conditions of the auxiliary problem (Fig. A-5), whereas the remaining terms vanish on the boundary. Using the

---

*The collocation points, although arbitrary, should be uniformly distributed over the domain to insure the best possible results.

Table A-2
SUMMARY OF COLLOCATION FOR CHECK PROBLEM*

$$F = a_1 + a_2x^2 + a_3y^2 + a_4x^2y^2 + a_5x^4 + a_6y^4 + a_7x^2y^4 + a_8x^4y^2 + a_9x^4y^4 + a_{10}x^6 + a_{11}y^6$$

	COLLOCATION PATTERN	a_1 a_2 a_3	a_4	a_5 a_6	a_7 a_8	a_9	a_{10} a_{11}
A.	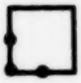	-0.06657 -0.03578 -0.00483	--	-- --	-- --	--	-- --
B.	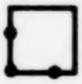	-0.06961 -0.04392 -0.00476	--	-- --	-- --	--	-- --
C.	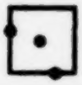	-0.0950 -0.03707 -0.00044	--	-- --	-- --	--	-- --
D.	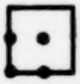	-0.06952 -0.04432 -0.00602	-0.01906	-- --	-- --	--	-- --
E.	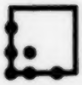	-0.06941 -0.04597 -0.005504	-0.01467	-0.007529 0.000161	-- --	--	-- --
F.	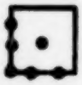	-0.07005 -0.04757 -0.005672	-0.01890	-0.006854 0.00030	-- --	--	-- --
G.	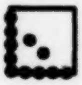	-0.06564 -0.03134 -0.004177	0.020693	-0.001248 0.000101	0.03611 0.07883	0.01896	-0.00990 0.00078
H.	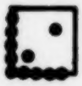	-0.070435 -0.04801 -0.006184	-0.02529	-0.00557 0.000219	-0.0130 0.00735	-0.01055	0.00218 0.000228
I.	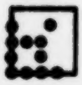	-0.070241 -0.04903 -0.005671	-0.02069	-0.00862 0.000262	-0.00230 -0.01246	-0.00480	0.000065 0.000033
J.	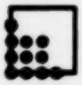	-0.070239 -0.049015 -0.005672	-0.02066	-0.00863 0.000260	-0.00235 -0.01237	-0.00444	0.000064 0.000035
K.	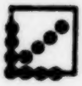	-0.06914 -0.05216 -0.003581	0.01765	-0.02040 0.000449	0.04154 -0.09131	-0.00972	0.00839 -0.00079

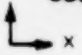

*NOTE: COEFFICIENTS A_i ARE NONDIMENSIONAL WITH RESPECT TO x = x/a, y = y/b.

Table A-3

Comparison of Collocation Solutions with the Three-Term
Rayleigh-Ritz Solution from Ref. 8[1]

	Rayleigh-Ritz	Collocation[2]				
		A	D	F	H	I
a_1	-0.0700	-0.0666	-0.0698	-0.070	-0.0704	-0.0702
a_2	-0.0557	-0.0358	-0.0443	-0.0476	-0.0480	-0.0490
a_3	-0.00769	-0.00483	-0.0060	-0.00567	-0.00618	-0.00576
$\sigma_x(0,0)$	0.1176	0.1141	0.1187	0.1195	0.1197	0.1198
$\sigma_y(0,0)$	0.0333	0.0385	0.0376	0.0365	0.0367	0.0361
$\sigma_x(0,1)$	0.1676	0.1906	0.1748	0.1763	0.1736	0.1756
$\sigma_y(1,0)$	-0.1986	-0.1618	-0.1804	-0.1967	-0.1994	-0.2020

Notes:

[1] Coefficients a_i are nondimensional with respect to $x = \bar{x}/a$, $y = \bar{y}/b$.

[2] All solutions, except A, have additional terms a_i; refer to Table A-2.

above assumed solution form, Eq. (A-24) was collocated on pattern (F) of Table A-2. The coefficients a_i were determined with different values of width to length ratio T/R for six fiber-composite materials. Table A-4 summarizes the properties corresponding to the indicated fiber volume percent (v_f). The stresses σ_r, σ_t, and σ_{rt} are the axial, transverse and shear strengths, while the strength/composite density parameter σ_r/ρ is proportional to E/W for the uniaxial composite rod.

The biaxial stresses in the anisotropic bar were computed, as discussed in Section A. 2. 1, by superimposing the stresses for the auxiliary problem on the potential field caused by the body forces. Typical nondimensionalized distributions are shown in Fig. A-7 for a high-strength graphite/epoxy (Hercules 2002T) composite for various aspect ratios. For a uniaxial rod the limiting axial stress is equal to $\frac{1}{2}\rho\omega^2R^2$, but for a biaxial situation, σ_r at the center of rotation > $\frac{1}{2}\rho\omega^2R^2$. The transverse and shear stresses are two orders of magnitude less than σ_r and reach their maximum values for $t/T > 0.50$. Increasing the aspect ratio T/R causes a moderate increase in the maximum axial stress*. However, an 80% increase in T/R causes more than three-fold increases in the transverse and shear stresses.

Since the stress distributions are nondimensionalized with respect to $\frac{1}{2}\rho\omega^2R^2$, they are independent of ω, but to evaluate the E/W capability, an ω must be specified to determine limiting stress conditions for the fiber-composite bar. For an orthotropic material in plane stress, a generalization of the von Mises isotropic yield criterion, known as the Hill criterion, has the following form:

---

*Note that as the aspect ratio increases the transverse distribution of the axial stresses becomes more nonuniform, tending to decrease along the boundary $t/T = 1$.

Table A-4

Properties of Fiber-Composite Materials

	E_1 E_2 G_{12} 10^6 psi	ν_{12} ν_f	σ_1 σ_2 τ_{12} 10^3 psi	σ_1/ρ 10^6 in
Boron/Aluminum	34.2 23.4 11.0	0.25 0.50	164 13.9 15.6	1.80
Boron/Epoxy (Hercules 2002B)	30.3 3.1 1.4	0.16 0.55	212 13 13.5	2.94
Graphite/Epoxy (Hercules 2002T)	21.5 1.44 0.61	0.25 0.59	204 11.8 14	3.78
Graphite/Epoxy (Hercules 2002M)	30.1 1.0 0.61	0.28 0.58	135 7.6 13.7	2.33
S-Glass/Epoxy (Hercules 828-5994)	7.65 2.24 0.78	0.27 0.60	264 7.5 8.5	3.67
E-Glass/Epoxy	8.0 2.7 1.25	0.25 ~0.60	157 4.0 6.0	2.20

$$\left(\frac{\bar{\sigma}_r}{\bar{\sigma}_1}\right)^2 - g\left(\frac{\bar{\sigma}_r}{\bar{\sigma}_1}\right)\left(\frac{\bar{\sigma}_t}{\bar{\sigma}_2}\right) + \left(\frac{\bar{\sigma}_t}{\bar{\sigma}_2}\right)^2 + \left(\frac{\bar{\tau}}{\bar{\sigma}_{12}}\right)^2 \leq 1. \quad \text{(A-29)}$$

where $g = \bar{\sigma}_2/\bar{\sigma}_1$, and $\bar{\sigma}_r$, $\bar{\sigma}_1$, etc., are actual stresses divided by $\frac{1}{2}\rho\omega^2R^2$. For a uniaxial rod the rotational speed (or specific energy) is directly obtained from the uniaxial strength as:

$$\omega_Q^{\,2} = 2\sigma_1/\rho a^2 . \quad \text{(A-30)}$$

However, for a rotating bar, ω is dependent upon the biaxial stress field through Eq. (A-29). That is, for a given aspect ratio, an ω must be determined such that the equality in Eq. (A-29) holds at some point in the bar. Computations show this point to be on the center of rotation. For example, the limiting rotational speed (specific energy storage) of a graphite/epoxy (Hercules 2002T) bar of aspect ratio 0.10, is $(94\%)^{\frac{1}{2}}$ of the ω computed on the uniaxial composite strength. The stress-distributions are presented in Fig. A-7. This reduction in ω may be viewed as an energy reduction factor owing to the biaxial loading condition on the bar. Such a factor may be determined for each fiber-composite material in Table A-4, as a function of aspect ratio. Figure 4-2 shows the dependence of E/W capability on aspect ratio for each composite material. The glass/epoxy bars suffer the greatest percentage degradations at large aspect ratios, while boron-composites are the least affected. In terms of the largest specific energy storage ($E/W \propto \sigma_a/\rho$) the high-strength graphite/epoxy is the superior composite material with a wide bar configuration ($T/R \rightarrow 0.18$), providing a σ_a/ρ in excess of 3×10^6 inches.

A.3 OPTIMIZATION OF DISK FLYWHEELS

Classically two special cases of variable-thickness disks have been studied (Refs. 126 and 127), the constant-

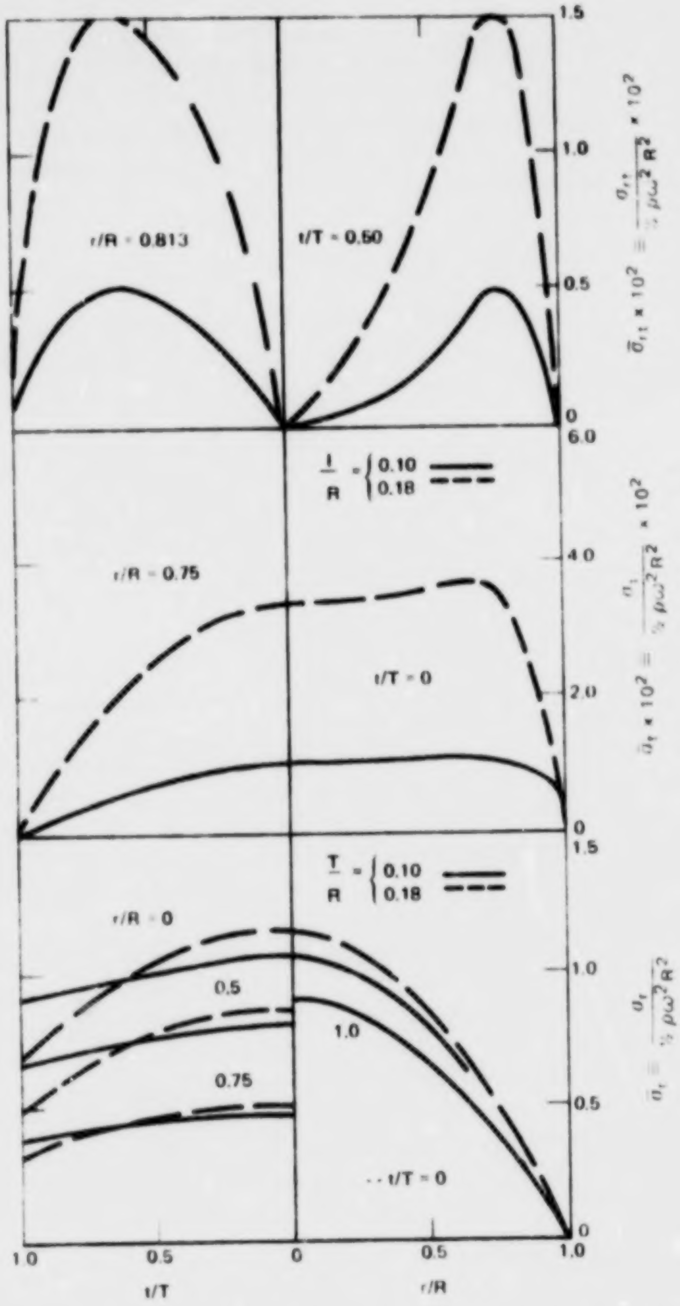

Fig. A-7 STRESS DISTRIBUTION FOR A GRAPHITE/EPOXY (HERCULES 2002T) BAR stress and the hyperbolic-thickness-variation cases, because the use of either of these assumptions permits the direct solution of the stress equilibrium equation(s), and probably also because the resulting solutions give a family of solutions which the designer can use to solve or "optimize" his problem.

A.3.1 Constant-Stress Solution for Disks

For a rotating, variable-thickness disk the stress equilibrium (radial direction component and compatibility (Hooke's law)) equations are (c.f., Ref. 126):

$$\frac{d}{dr}(z\, r\, \sigma_r) - z\, \sigma_t + z\, \rho\, \omega^2 r^2 = 0\,, \qquad \text{(A-31)}$$

$$\frac{d\sigma_t}{dr} - \mu \frac{d\sigma_r}{dr} + \frac{1+\mu}{r}(\sigma_t - \sigma_r) = 0\,, \qquad \text{(A-32)}$$

where the radial displacement has been eliminated from the radial and tangential stress-strain equations to give the stress compatibility relation, Eq. (A-32); σ_r and σ_t are the radial and tangential stresses, respectively, r is the radius, z is the thickness, and μ is Poisson's ratio. These equations contain three unknown variables (σ_r, σ_t, and z) and an unspecified constant ω. Generally, ω can be determined by the specification of an overall, i.e., integral, disk property such as W or σ_a, depending upon the specific problem; in any case solutions for the variables, as functions of r, can be made in terms of ω. An additional relationship is needed to permit solution for the three variables. Usually, as in most problems, this relation is supplied by the assumed failure criterion. By assuming that the stress is constant throughout the disk, i.e., $\sigma_r = \sigma_t = \sigma_a$, a direct solution of Eq. (A-31) is possible (Refs. 126 and 127), yielding:

$$z = Ze^{-k\bar{r}^2}\,, \qquad k = \rho\, \omega^2 R^2 / 2\sigma_a \; (= \alpha^2)\,, \qquad \text{(A-33)}$$

where Z is the innermost disk thickness, and $\bar{r} \equiv r/R$. Note that the compatibility equation is satisfied identically. This result is similar in form to the uniform bar case, as is the computation of E/W given below (which is in fact, somewhat easier, since odd powers of $\bar{r}$ appear in the I and W integrals, making their solutions straightforward; i.e., error functions are not needed). Using Eqs. (A-1), (A-4), and (A-33), it follows that the dimensionless weight, moment of inertia, and E/W are given by:

$$\frac{W}{2\pi g \rho Z R^2} = \int_0^1 \bar{r}\, e^{-k\bar{r}^2}\, d\bar{r} = -\frac{1}{2k}\left(e^{-i} - 1\right), \qquad \text{(A-34)}$$

$$\frac{I}{2\pi \rho Z R^4} = \int_0^1 \bar{r}^3\, e^{-k\bar{r}^2}\, d\bar{r} = \frac{1}{2k^2}\left(1 - (1 + k)e^{-k}\right), \qquad \text{(A-35)}$$

and

$$\frac{E}{W} = \frac{1 - (1 + k)e^{-k}}{(1 - 2^{-k})}\, \frac{\sigma_a}{\rho g}. \qquad \text{(A-36)}$$

As in the 1-D rod case, these solutions depend upon the value assigned to k, which in effect sets the remaining as yet unspecified geometric variable, say Z or W. Moreover, an end-mass problem (analogous to that in the 1-D rod problem) exists, since at $r = R$ the stress is not equal to σ_a unless $R \to \infty$. Because the end thickness becomes exponentially smaller as $r \to R$, the end mass is probably of no consequence for large k, as shown for the 1-D case. Evaluation of Eq. (A-36) shows that the maximum E/W is achieved for $k \to \infty$, which is the best value in the optimal family of constant-stress disks (discussed later) as well as for the rod. In this case as $k \to \infty$, $E/W \to 1 \cdot \sigma_a/\rho g$. With this use of σ_a, the allowable stress, the constant-stress assumption is tantamount to a failure criteria, and is similar to the 1-D failure criterion (also constant stress). In this case, however, it has not been fully demonstrated that the constant-stress-failure assumption is the most appropriate for 2-D problems (optimization or otherwise), but it is clear that the general result represents a possible, if not fully optimal, solution*.

To illustrate how closely more practical disk shapes can approach the best constant-stress values, a plot of dimensionless E/W and Z_u/Z versus k is shown in Fig. A-8, where Z_u is the thickness of the uniform-thickness disk having the same weight as the disk in question. For k = 4 [corresponding to the $\alpha = 2$ rod case Eq. (A-8)], $Z/Z_u = 4.07$, not too unreasonable a geometry, and E/W is 92.5% of the best value obtainable. This disk and even other less drastically shaped disks are significantly better than the uniform disk and 1-D rod cases (see comparisons in Table A-1). The packaging efficiency for constant-stress disks is given by:

$$E/V = [1 - e^{-k}(1 + k)] \sigma_a/k . \qquad (A-37)$$

These values are also shown in Fig. A-1. For the k = 4 case, $E/\sigma_a V = 0.227$ (see Table A-1).

A.3.2 Hyperbolic-Thickness-Variation Disks

The other case of classical interest, the assumption of a hyperbolic thickness variation, $z = z_1 \bar{r}^{-q}$ (where q is a positive number, and z_1 is a fixed edge reference thickness at $\bar{r} = 1$), when substituted into the combination of Eqs. (A-31) and (A-32) formed by eliminating σ_t, results in an integrable second-order differential equation in terms of the group $z\bar{r}\sigma_r$. The exact form of the results

---

*Constant σ corresponds to the Tresca failure condition and, in fact may be a suitable failure criterion (Ref. 119). To account for a more appropriate biaxial failure criterion an appropriate reduction (say, 10%) can be made in the allowable maximum in the constant-stress case, and correspondingly in the energy content levels (E/W, etc.) achievable.

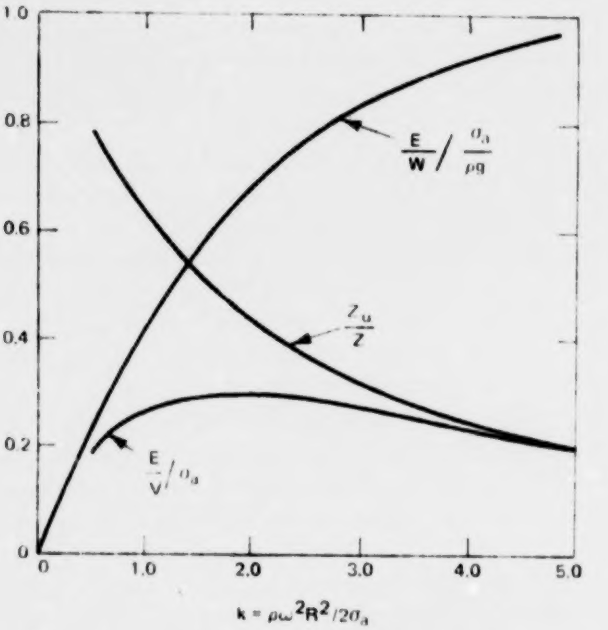

Fig. A-8 GEOMETRIC AND PERFORMANCE PARAMETERS OF A CONSTANT STRESS DISK FLYWHEEL

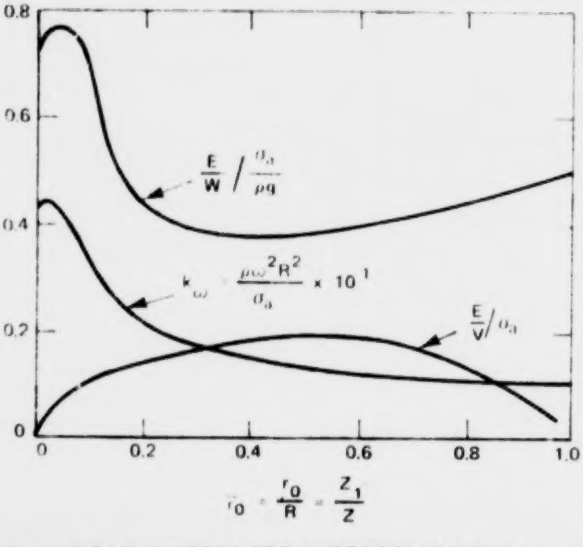

Fig. A-9 PERFORMANCE PARAMETERS FOR HYPERBOLIC DISKS (α = 1/2) WITH SMALL CENTRAL HOLE. INNER-TO-OUTER RADIUS RATIO EQUALS INNER-TO-RIM THICKNESS RATIO.

depends on the value of q (which can be chosen to give a desired thickness variation), and a family of solutions is obtained for each q selected. To maintain the hyperbolic shape there must be a central hole, for as $r \rightarrow 0$, $z/z_1 \rightarrow \infty$, thus hyperbolic solid disks are not possible. Thus, the members of each family are characterized by the yet to be specified inner radius ($\bar{r}_0$) and ω, which in turn are determined from the system parameters, such as W or σ_a, or other geometric parameters of interest. By assuming the von Mises failure criterion (Ref. 119), Eq. (A-3), the maximum E/W member of the family (variable $\bar{r}_0$) "ordinary" hyperbolas, $q = 1$, $z/z_1 = 1/\bar{r}$ was determined. This was done by finding the maximum stress point for each value of $\bar{r}_0$ by algebraically locating the maximum of Eq. (A-3) with respect to $\bar{r}$ and then numerically evaluating the expression for the maximum stress point, $\bar{r}_{max}$ at each $\bar{r}_0$. The location of this point yields the maximum stress in terms of ω, i.e., yielding k from Eq. (A-4), and permits evaluation of the flywheel performance. For the ordinary hyperbola:

$$I/(2\pi\rho R^4 z_1) = \int_{\bar{r}_0}^{1} \bar{r}^3 \bar{z} \, \overline{dr} = (1 - \bar{r}_0^{\,3})/3 \,, \qquad \text{(A-38)}$$

$$W/(2\pi\rho g R^2 z_1) = \int_{\bar{r}_0}^{1} \bar{r} \bar{z} \, \overline{dr} = (1 - \bar{r}_0) \,, \qquad \text{(A-39)}$$

$$\frac{E}{W} = \frac{1}{6} \frac{(1 - \bar{r}_0^{\,3})}{(1 - \bar{r}_0)} k \frac{\sigma_a}{\rho g} \,, \qquad \text{(A-40)}$$

$$\frac{E}{V} = \frac{1}{3} k \bar{r}_0 (1 - \bar{r}_0^{\,3}) \sigma_a \,. \qquad \text{(A-41)}$$

The computations for the maximum stress for each case (value of $\bar{r}_0$) have shown that, for all but the smallest inner hole (i.e., for $\bar{r}_0 > 0.05$), the maximum combined stress occurs at the center. These results for k_ω and consequently E/W and E/V from Eqs. (A-40) and (A-41) are shown in Fig. A-9. The best performance, $E/W \simeq 0.77\ \sigma_a/\rho V$ occurs with a small (nonzero diameter) central hole. The effect of the shift in the maximum stress point to the interior is reflected in the shape of the E/W curve at low $\bar{r}_0$. The packaging efficiency at the high E/W point is quite low, reflecting the large Z/z_1 ratio, where Z is the (maximum) thickness at the $r = r_0$ location. The best E/V occurs at $E/W \simeq 0.38\ \sigma_a/\rho g$ and $Z/z_1 = 2$. For $Z/z_1 = 4$, which equals the thickness ratio of the $k = 4$ constant-stress disk discussed above, $\bar{r}_0 = 1/4$, possibly a reasonable value, $E/W = 0.39\ \sigma_a/\rho g$, and $E/V = 0.15\ \sigma_a$. These results are included in Table A-1. Thus, within this family of hyperbolic flywheels, some reasonably performing shapes can be found, and the best approaches that of the best constant-stress case.

Other simpler shapes such as the wedge-shaped disk may prove advantageous, especially from the fabrication point of view, but the foregoing examples are deemed sufficient for the present exploratory studies.

A.3.3 Studies by Others of Optimal Disk Flywheels

Studies concerned with the optimization of flywheels are relatively recent (Refs. 128 through 130)*. In all cases, moreover, there are implicit assumptions or conditions, which result in an optimal-shape disk having a constant stress throughout, i.e., $\sigma_r = \sigma_t = \sigma$, with the resulting exponential thickness distribution. Ranta (Ref. 128) considered the optimal minimum-weight disk (presumably for any suitable operating condition, e.g., given ω) which was assumed to occur when the stress is uniform throughout. His analysis was concerned with showing that the assumption σ_t/σ_r = constant also leads to the constant-stress result; an assumption which has more validity when materials having nonlinear stress-strain relations are considered. This assumption also seems somewhat more appropriate for anisotropic materials, although in this case the constituitive equations themselves would also have to be modified. For shaped-disk flywheels, the deviations from the assumed 2-D stress distribution will increase as the thickness variation increases (i.e., with increased shaping), so that there may be an eventual trade-off between the losses due to the triaxial stress distribution and the geometric improvement of E/W. Ranta (Ref. 128) considered the 3-D stress-strain problem in the constant-stress (exponential thickness variation) disk and obtained estimates of the errors incurred by assuming a 2-D stress field. The final results are a function of the slope of the disk face [$\tan \beta = d(z/2)/dr$] and Poissons' ratio μ. For $0.145 \leq \mu < 0.5$, the maximum error is $0\,[2.72\,(1 + \mu)/(1 - \mu) \cdot \max\,(\tan^2 \alpha)]$ giving values of 15.6 and 3.8% for $\mu = 0.3$ and $\beta = 10°$ and $5°$, respectively. Obviously, the errors could be even larger if β or μ were greater (as the effective value may be for some anisotropic materials), or if the true anisotropic problem were considered.

---

*The only other optimization studies known to the writer are those of Seirig and Surana (Ref. 131), and Sulkin et al. (Ref. 132). The former numerically "optimizes" the thickness of a rotating disk by dividing the radial dimension into a finite number of subelements (rings) and applying a gradient technique to the resulting algebraic equations. Because the assumptions going into the stress analysis, the performance criteria chosen, and the numerical results themselves seem to be of dubious validity or relevance to practical applications, further discussion is not warranted. The North American (Ref. 132) study apparently is based on the constant-stress case but is difficult to follow.

Using the calculus of variations Chern and Prager (Ref. 129) derived the optimality condition (i.e., sufficiency condition) which gives the minimum-weight disk having a specified edge loading or displacement. This result, which is not completely relevant to the present objective, was applied to a disk having a specified edge displacement, and the resulting stress distribution (numerically computed) was shown to be far from constant and thus nonoptimal in this sense. Note that again σ = constant was assumed to be optimal, and that the analysis did not include a failure criterion as a constraint. Chern and Prager also showed that the von Mises yield limit for an elastic-plastic disk also results in the constant-stress solution; a result of possible relevance to anisotropic, composite materials.

Perhaps the study most relevant to the present objective is that of de Silva (Ref. 130), who formulated the minimum-weight problem in terms of Pontryagin's maximum principle. He included the Tresca yield condition as a problem constraint and proved that the configuration would have σ_r = constant (as opposed to σ_t or $\sigma_r - \sigma_0$ = constant, the other branches of the Tresca condition). This resulted in an exponential thickness distribution similar to the constant stress result, but here σ_t is a function of r:

$$z = Z \exp \left[\frac{b}{(1 + \mu)\sigma_a} r^{-(1+\mu)} - \frac{\rho\omega^2 r^2}{2\sigma_a} \right] , \qquad \text{(A-42)}$$

where Z and b are constants to be determined by the geometry or by minimum-thickness requirements. This result, which agrees with de Silva's previous numerical computations, can be used to compute E/W and E/V; a task which is at present not completed. His general approach can also be used to compute optimal shapes corresponding to other yield criteria, such as the von Mises condition, which may seem more appropriate, although for such cases analytic results may not be attainable.

A. 3. 4 Disk Flywheels Constructed from Anisotropic Materials

The properties of a flywheel constructed of an anisotropic material depend on the material's properties, its orientation, and the overall flywheel configuration. A flywheel comprising fibrous or filamentary materials which are structurally unbonded does not offer an attractive E/V, because σ_a will be significantly degraded by a relatively small lateral displacement of filaments from the center of rotation. However, circular brush (filaments bonded into a hub) or rim-wound configurations can also be analyzed using modifications of the closed-form flywheel results. For a quasi-isotropic material formed by alternating the layers of the oriented composite materials, the homogeneous solutions can be used. Although such a flywheel does not take full advantage of the high-strength filaments of which it is formed, the disk configuration does give a high E/V with a moderately good E/W(Table A-1).

APPENDIX B

THE DISK FLYWHEEL CONFIGURATION

B.1 CLASSICAL SOLUTION FOR AN ISOTROPIC MATERIAL

The equation governing the plane stress condition in a constant thickness disk flywheel was given in Section 1.1 of Appendix A as:

$$\sigma_t - \frac{d}{dr}(r\sigma_r) - \rho r^2\omega^2 = 0 \,. \qquad \text{(A-2)}$$

The solution to this equation for a solid disk flywheel is known and is:

$$\frac{\sigma_r}{\sigma_o} = \frac{3+\nu}{4}\left(1 - \frac{r^2}{R^2}\right) ,$$

$$\frac{\sigma_t}{\sigma_o} = \frac{3+\nu}{4}\left(1 - \frac{1+3\nu}{3+\nu}\ \frac{r^2}{R^2}\right) , \qquad \text{(B-1)}$$

where the reference stress $\sigma_o = \frac{1}{2}\rho\omega^2 R^2$. The maximum stress occurs at the center of the disk and depends solely upon the value of Poisson's ratio, ν. Examination of the failure condition [Eq. (A-3)] shows that at the center of the disk $\sigma_r = \sigma_t = \sigma_a$, and the maximum allowable speed is easily determined when ν, σ_a, ρ, and R are specified. For example, when $\nu = \frac{1}{3}$, $\sigma_r/\sigma_o = \sigma_t/\sigma_o = 0.833$. Therefore if $\sigma_a = 200$ ksi and $\rho = 0.30$,* the reference stress has a value of 240 ksi, from which $\omega = 1265/R$ rad/s. Because the isotropic-disk configuration presents a significantly better packaging efficiency than the rod or bar configuration (Table A-1), it is desirable to evaluate the use of fiber-composite materials in a disk-type configuration.

---

*Values representative of steel.

B. 2 PSEUDO-ISOTROPIC/LAMINATED DISK FLYWHEEL

B. 2. 1 Constitutive Relations

Consider a laminated disk constructed of several individual layers* (or laminas). Since, as shown in Fig. B-1a, the lamina principal axes (1, 2) are not coincident with the reference axes for the laminate, (x, y), each lamina constitutive relation must be transformed to the laminate reference axes. Then, for the kth lamina (Ref. 27):

$$\begin{Bmatrix} \sigma_x \\ \sigma_y \\ \tau_{xy} \end{Bmatrix}^k = \begin{bmatrix} \bar{Q}_{11} & \bar{Q}_{12} & \bar{Q}_{16} \\ \bar{Q}_{12} & \bar{Q}_{22} & \bar{Q}_{26} \\ \bar{Q}_{16} & \bar{Q}_{26} & \bar{Q}_{66} \end{bmatrix}^k \begin{Bmatrix} \epsilon_x \\ \epsilon_y \\ \gamma_{xy} \end{Bmatrix}^k , \qquad \text{(B-2)}$$

where the transformed lamina stiffnesses are given by:

$$\begin{aligned} \bar{Q}_{11} &= U_1 + U_2 \operatorname{Cos} 2\theta_k + U_3 \operatorname{Cos} 4\theta_k \\ \bar{Q}_{22} &= U_1 - U_2 \operatorname{Cos} 2\theta_k + U_3 \operatorname{Cos} 4\theta_k \\ \bar{Q}_{12} &= U_4 - U_3 \operatorname{Cos} 4\theta_k \\ \bar{Q}_{66} &= U_5 - U_3 \operatorname{Cos} 4\theta_k \\ \bar{Q}_{16} &= -\tfrac{1}{2} U_2 \operatorname{Sin} 2\theta_k - U_3 \operatorname{Sin} 4\theta_k \\ \bar{Q}_{26} &= -\tfrac{1}{2} U_2 \operatorname{Sin} 2\theta_k + U_3 \operatorname{Sin} 4\theta_k \end{aligned} \qquad \text{(B-3)}$$

---

*The laminate is midplane symmetric so that warping caused by inplane loads does not occur.

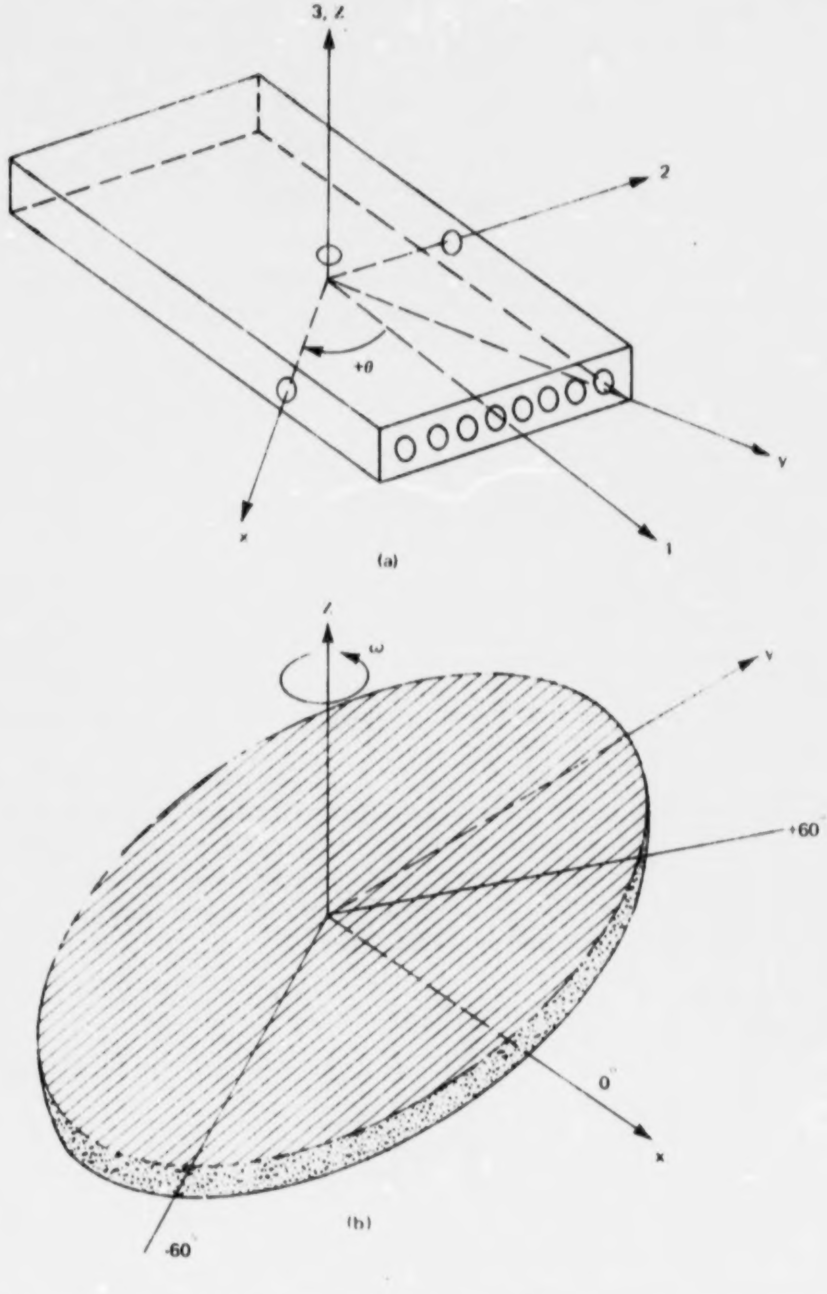
3, Z
2
+θ
y
x
1
(a)
Z
ω
y
+60°
0°
x
(b)
-60°

Fig. B-1 (a) LAMINA AXES ROTATION AND (b) PSEUDO-ISOTROPIC LAMINATED DISK

and
$$\begin{aligned} U_1 &= \tfrac{1}{8}\left(3Q_{11} + 3Q_{22} + 2Q_{12} + 4Q_{66}\right) \\ U_2 &= \tfrac{1}{2}\left(Q_{11} - Q_{22}\right) \\ U_3 &= \tfrac{1}{8}\left(Q_{11} + Q_{22} - 2Q_{12} - 4Q_{66}\right) \\ U_4 &= \tfrac{1}{8}\left(Q_{11} + Q_{22} + 6Q_{12} - 4Q_{66}\right) \\ U_5 &= \tfrac{1}{8}\left(Q_{11} + Q_{22} - 2Q_{12} + 4Q_{66}\right) \; . \end{aligned} \tag{B-4}$$

The unbarred quantities Q_{ij} are the stiffness coefficients in the lamina coordinate system and can be defined in terms of four elastic constants:

$$\begin{aligned} Q_{11} &= E_{11} / \left(1 - \nu_{12}\nu_{21}\right) \\ Q_{22} &= E_{22} / \left(1 - \nu_{12}\nu_{21}\right) \\ Q_{12} &= \nu_{21}Q_{11} = \nu_{12}Q_{22} \\ Q_{66} &= G_{12} \\ Q_{16} &= Q_{26} = 0 \end{aligned} \tag{B-5}$$

where E_{11} and E_{22} are the Young's moduli in the 1 and 2 directions, G_{12} is the shear modulus, and ν_{12} is the major Poisson's ratio.

The stresses in the laminated disk are evaluated by requiring the stress resultants to satisfy the governing equations. This leads to a resultant stiffness matrix for the laminate which is the weighted sum of each lamina over thickness of the laminate. That is:

$$\begin{Bmatrix} \sigma_x \\ \sigma_y \\ \tau_{xy} \end{Bmatrix} = \sum_{k=1}^{n} \int_{t_k} \begin{Bmatrix} \sigma_x \\ \sigma_y \\ \tau_{xy} \end{Bmatrix}_k dz \tag{B-6}$$

and

$$\bar{Q}_{ij} = \sum_{k=1}^{n} \left(\bar{Q}_{ij}\right)_k f_k \tag{B-7}$$

where f_k is the thickness fraction of the k^{th} lamina relative to the total laminate thickness. In general a laminated disk composed of arbitrarily oriented laminas or plies is inherently anisotropic. However, several specific lamina orientations will result in an equivalent isotropic disk with an effective allowable stress.

B. 2. 2 The Pseudo-Isotropic Disk

With reference to Fig. B-1b, the lamina orientations which produce pseudo-isotropic material properties are +60/0/-60, +45/0/90/-45, and +60/+30/0/90/-30/-60, where each lamina contributes equally to the overall laminate thickness. Furthermore, when the principal lamina strengths are resolved into the laminate coordinate system, an allowable laminate strength can be determined which is the same for all pseudo-isotropic laminates:

$$\begin{aligned}
\sigma_1 &= \sum_{k=1}^{n} \left(\sigma_1^k \cos^2\theta_k + \sigma_2^k \sin^2\theta_k + \tau_{12}^k \, 2\sin\theta_k \cos\theta_k\right) f_k \\
\sigma_2 &= \sum_{k=1}^{n} \left(\sigma_1^k \sin^2\theta_k + \sigma_2^k \cos^2\theta_k - \tau_{12}^k \, 2\sin\theta_k \cos\theta_k\right) f_k
\end{aligned} \tag{B-8}$$

and it follows that $\sigma_1 = \sigma_2 = \sigma_a$ for all laminate directions.

An energy storage capability can be computed for the pseudo-isotropic disk once the equivalent isotropic properties are determined. Table B-1 summarizes results for three fiber/epoxy laminated disks. For example, a laminated pseudo-isotropic disk constructed of graphite/

Table B-1

Energy-Storage Capability of Pseudo-Isotropic[1] Laminated Disks

Item	S-Glass/Epoxy (828-5994)	Boron/Epoxy (2002B)	Graphite/Epoxy (2002T)
Property: E_{11}	7.65×10^6	30.3×10^6	21.5×10^6
E_{22}	2.24×10^6	3.10×10^6	1.44×10^6
ν_{12}	0.27	0.16	0.25
G_{12}	0.78×10^6	1.4×10^6	0.64×10^6
Allowable Lamina Stresses: σ_1	264×10^3	212×10^3	204×10^3
σ_2	7.5×10^3	13×10^3	11.8×10^3
τ_{12}	8.5×10^3	13.5×10^3	14×10^3
Equivalent Isotropic Property: E	3.92×10^6	12.27×10^6	8.14×10^6
G	1.50×10^6	4.76×10^6	3.09×10^6
ν	0.308	0.288	0.315
$\frac{\sigma_r}{\sigma_o} = \frac{\sigma_\theta}{\sigma_o} = K(\nu)$			
when $r = 0$	0.827	0.822	0.829
Allowable Disk Stress	135.75×10^3	112.5×10^3	105.5×10^3
Ref. Stress $\sigma_o = \frac{1}{8}\rho\omega^2 a^2$	164×10^3	137×10^3	127×10^3
$\omega^2_{ply}/\omega^2_{iso}$:			
Aluminum Ref.[2]	6.33	5.30	6.55
Steel Ref.[3]	2.85	2.38	2.94

---

[1] Ply orientations +60/0/-60, +45/0/90/-45, and +60/+30/0/90/-30/-60 produce the same equivalent isotropic disk.

[2] $\sigma_y = 30$ ksi, $\rho = 0.1$ pci, $\nu = 1/3$.

[3] $\sigma_y = 200$ ksi, $\rho = 0.3$ pci, $\nu = 1/3$.

epoxy plies can store 2.94 times the energy of a steel disk and 6.55 that of an aluminum disk, with a specific energy of 37 W-h/lb.

APPENDIX C

ESTIMATES OF WINDAGE LOSSES FOR FLYWHEELS

C.1 INTRODUCTION

The purpose here is to present some gross trends of effects of rotor shape, size, and speed and operating pressure on P_{wind}, the power required to compensate the windage drag. For example, a cylindrical rod will have only 75% as much drag as a square bar of the same cross-sectional area, arm-radius, and material. An S-glass/epoxy rod having twice the energy density of a steel (music wire)/epoxy rod of the same size and shape would also have twice the windage loss, because both E_0/W and P_{wind} are proportional to ω^2, the square of the rotational speed. Since most of the length of the rotor will be moving at supersonic velocity relative to the surrounding gas, and since form drag at supersonic speed is proportional to the gas density, P_{wind} can be reduced by a factor of 10^6 by evacuating the container from 1 to 10^{-6} atmosphere.

It is emphasized that only the relative trends indicated herein should be given any weight, inasmuch as two major simplifying assumptions will be made:

1. The relative velocity between rotor and gas is equal to the rotor velocity; i.e., the gas sits still as the rotor spins. This is a conservative assumption, because for rotors enclosed in containers with appropriate clearance, the surrounding gas will rotate at some speed, too, thus reducing relative velocities and drag.
2. The degradation in allowable ω^2 as rotor width is increased (caused by biaxial stress effects; see Appendix A.3) will be neglected. This degradation will result in proportionate reductions in both E_0/W and P_{wind}.

Preceding page blank

The examples presented herein are based on uniaxially loaded rotors made of a composite material having an allowable working stress σ_a of 200 000 psi and a density ρg of 0.07 lb/in^3. For a rod or bar of uniform cross-sectional area A_0 (in^2), where the maximum loading F_{max} (lb$_f$) will occur at the spin axis and will be:

$$F_{max} = \sigma_a A_0 = 200\ 000\ A_0 . \qquad \text{(C-1)}$$

The mass (slug) of each arm of the bar (of radial length R) is:

$$m = A_0 R\rho = 0.0327\ A_0\ (\text{for } R = 15 \text{ inches}) \qquad \text{(C-2)}$$

For our reference case, the rotational speed ω that just provides a centrifugal force equal to F_{max} is:

$$\omega = (F_{max}/r_{cg}m)^{\frac{1}{2}} = 3130 \text{ rad/s} = 29\ 900 \text{ rpm}$$

$$(r_{cg} = R/2 = 0.625 \text{ foot}) . \qquad \text{(C-3)}$$

Here r_{cg} is the distance (feet) from the center of rotation to the center of gravity of the mass being spun (one arm of the total bar).

The maximum kinetic energy storage is:

$$E_0 = I\omega^2/2 , \qquad \text{(C-4)}$$

where I is the moment of inertia and varies with configuration.

C. 2 WINDAGE LOSS FOR BARS AND RODS

Let us consider a bar of rectangular cross-section with 2-to-1 proportion (2T/Z = 2). The half-width T is

2.3 inches (0.192 foot); the height Z of the flat face presented to the approaching airflow is 2.3 inches (0.192 foot). The arm length R is 15 inches (1.25 foot), so that $T/R = 0.153$, a reasonable value (see Appendix A.3); and A_0 for Eq. (C-2) is 10.58 in^2, yielding $m = 0.346$ slug for each arm. The rotor weight W (both arms) is 2mg, or 22.3 pounds.

For $\omega = 3130$ rad/s, the tip speed ωR is 3910 ft/s, and most of the length of the bar is in supersonic flow. For convenience, let us assume that the supersonic drag coefficient, $C_D = 1.84$, applicable for a flat, infinitely-long plate, face-on to the approaching flow (Ref. 108), can be applied for the entire length of each arm for this case. Then the drag force D (pounds) and moment M are:

$$D = 2\,C_D \int_0^R qz\,dr \qquad m = \int_0^R Dr\,dr\ , \tag{C-5}$$

where q is the dynamic pressure, $\rho_g V^2/2$, for a flow with local velocity V and gas density ρg. Using Eqs. (C-5) for the moment, we can find the horsepower required to overcome windage loss:

$$P_{wind} = \frac{\omega M}{550} = \frac{2C_D\omega}{550} \int_0^R qzr\,dr\ . \tag{C-6}$$

where ω is in rad/s, and ωr is the distance (feet) through which a local element of the drag force operates in 1 second; ωr also is the local velocity (ft/s) at the radial distance r. Hence, the local q is simply $\frac{1}{2}\rho_g(\omega r)^2$. For the rectangular bar, $\underline{z = Z}$ also is a constant; thus, integration yields

$$P_{wind} = \rho_g C_D Z R^4 \omega^3/2200 = 0.00204\, \rho_g \omega^3 Z$$

$$= \underline{28\,500 \text{ hp at 1 atmosphere}} \tag{C-7}$$

where ρ_g is 0.00238 slug/ft^3 for air at 59°F and 1 atmosphere. If we reduce the pressure from 1 atmosphere to 10^{-3} torr*, the air density becomes 3.13×10^{-9} slug/ft^3, and

$$P_{\text{wind}} = \underline{0.0375 \text{ hp at } 10^{-3} \text{ torr}} \text{ (2:1 bar)} . \qquad \text{(C-8a)}$$

If we replace the 2-to-1 rectangular bar by a square bar ($Z = 2T = 3.25$ inches) of the same cross-sectional area (10.58 in^2), the face height Z and the consequent P_{wind} will be multiplied by $\sqrt{2}$ for the same ω (3130 rad/s), or

$$P_{\text{wind}} = \underline{0.052 \text{ hp at } 10^{-3} \text{ torr}} \quad \text{(square bar)} . \qquad \text{(C-8b)}$$

The diameter d of a cylindrical rod of the same cross-sectional area will be $(4/\pi)^{\frac{1}{2}} Z = 1.128\, Z = 3.66$ inches. However, the high-speed C_D will be 2/3 that of a flat-faced wall of equal frontal area, as can be shown by integrating the Newtonian version of the expression for the local pressure distribution around a circular section (a result essentially confirmed by experiment) (Ref. 108). Thus, the rod's windage loss will be $(2/3)(1.128) = 0.752$ times the square bar's value,

$$P_{\text{wind}} \approx 0.039 \text{ hp at } 10^{-3} \text{ torr} \quad \text{(rod)} . \qquad \text{(C-8c)}$$

The cross-sectional shape does not affect the permissible rotation speed in Eq. (C-3) (neglecting transverse stress effects); all that matters is A_0, which is the same for all three configurations examined so far, hence the limiting ω is 3130 rad/s for all three. However, their energy-storage capabilities differ slightly, because their I's differ. For a 2:1 rectangular bar:

$$I = 2m(R^2 + T^2)/3 = 0.369 \text{ slug-ft}^2 \quad \text{(2:1 bar)} . \qquad \text{(C-9)}$$

---

* 1 torr = 1 mm Hg = 1/760 atmosphere = 0.001315 atmosphere.

Here 2m is the rotor mass (both arms), 0.692 slug. Using this I, and $\omega = 3130$ rad/s, Eq. (C-4) yields $E_0 = 1.804 \times 10^6$ ft-lb, or 680 Wh, and $E_0/W = 30.6$ Wh/lb.

For the square bar with its smaller T dimension, $I = 0.367$ slug-ft^2, and $E_0 = 1.79 \times 10^6$ ft-lb.

For the circular rod,

$$I = 2m(3d^2/16 + R^2)/3 = 0.365 \text{ slug-ft}^2 \quad \text{(rod, } R = 1.25 \text{ feet)} \qquad \text{(C-10)}$$

and $E_0 = 1.78 \times 10^6$ ft-lb.

If we reduce R for the rod from 15 to 12 inches (80%) but keep A_0 at 10.58 in^2, we have $2m = 0.554$ slug, and $r_{cg} = 0.5$ foot; the permissible ω per Eq. (C-3) is increased to 3910 rad/s. Note that the tip speed, ωR, remains the same, 3910 ft/s. Now we find $I = 0.188$ slug-ft^2, and $E_0 = 1.436 \times 10^6$ ft-lb, ~ 81% of the original value. The windage drag is 80% of the original value, hence:

$$P_{wind} = 0.031 \text{ hp at } 10^{-3} \text{ torr} \quad \text{(rod, } R = 12 \text{ inches)} \qquad \text{(C-8d)}$$

C.3 WINDAGE LOSS FOR A DISK OF ZERO THICKNESS IN FREE AIR

For a disk of zero thickness experiencing only skin-friction drag, the relation analogous to Eq. (C-6) is:

$$HP_{windage} = \frac{\omega M}{550} = C_M(\tfrac{1}{2}\rho_g R^5 \omega^3)/550 , \qquad \text{(C-11)}$$

where C_M is a nondimensional coefficient (including both sides of the disk). A chart has been prepared in Ref. 133 (see Fig. 17) to facilitate rapid estimation of the horsepower required to drive disks of various diameters at speeds from 100 to 40 000 rpm. A curve on this chart shows the combination of R and ω at which boundary layer transition from laminar to turbulent can be expected. It is evident from this curve that for the configurations and ω's of interest for superflywheels, the turbulent-boundary-layer analysis can be expected to apply. For a turbulent boundary-layer,

$$C_M = 0.146/\mathrm{Re}^{0.2} = 0.146/(\omega R^2 \rho_g/\mu_g)^{0.2} , \quad \text{(C-12)}$$

where Re is the Reynolds number and μ_g is the gas viscosity (3.78×10^{-7} slug/ft-s for air at 59°F). This result is confirmed by experiment (Ref. 134). Thus,

$$P_{\mathrm{wind}} = \frac{0.146}{(550)(2)} \rho_g^{0.8} R^{4.6} \omega^{2.8} \mu_g^{0.2} . \quad \text{(C-13)}$$

Let us consider a 15-inch-radius disk, rotating at 2333 rad/s, so that it will have the same E_0/W as the rod of the same R rotating at 3130 rad/s. Equation (C-13) gives:

$$P_{\mathrm{wind}} = 497 \text{ hp at 1 atmosphere, or } 0.0098 \text{ hp at } 10^{-3} \text{ torr.} \quad \text{(C-14)}$$

Thus, at 1 atmosphere the friction drag on the top and bottom surfaces of a disk is only 1.7% of the form drag on the rod for equal E_0/W, but at 10^{-3} torr it is 25%.

C.4 DEVIATIONS FROM SIMPLE FLOW PATTERNS

One thorough experimental investigation of disks rotating inside cylindrical containers (Ref. 135) showed that the thickness of the outer rimface of the disk has a strong influence on the drag, so that any formula based on the assumption of a vanishingly small disk edge is bound to underestimate the friction drag of a thick-rim design. In addition, surface roughness could raise the drag appreciably. However, the greatest factor (that is going to be ignored hereinafter) is the whirl-up of the body of air in the container. If s is the separation distance in the axial direction between the disk surface and the surface of the can on each side, and if s exceeds the sum of the boundary-layer thicknesses on the disk and can wall, the "core" gas between the boundary layers will rotate approximately as a solid body. The relative velocity between the disk and this core gas will be substantially less than the disk velocity itself. Theoretically (Ref. 136), an enclosed disk should have only 42.6% of the drag attributable to the same disk spinning in the open in the same fluid. [If s is much smaller than the sum of the boundary-layer thicknesses, on the other hand, the drag can exceed the free-air value (Ref. 137).] This finding of a constant fraction of free-air drag, when a can of sufficient size is provided, is used as the prime justification herein to ignore the presence of any container entirely and to quote drag results for the simpler condition of free-air operation.

C.5 EFFECT OF CHANGING THE GAS IN THE CONTAINER

Inasmuch as the drag of a rod or bar rotor is predominantly wave (form) drag, as opposed to skin friction drag, the effect of a gas change is simply accounted for by determination of the density ratio, which is proportional to the molecular weight ratio. Thus, replacement of air by hydrogen or by helium, under standard conditions, results in lowering the windage loss by a factor of 2/29 or 4/29, respectively.

In contrast, for a disk-type flywheel, the drag is primarily due to skin friction, and P_{wind} will vary with the product $\rho^{0.8}\mu^{0.2}$, as shown in Eq. (C-13), so that the reduction factor produced by a change from air to hydrogen is: $(2/29)^{0.8}(1.80/3.78)^{0.2} = 0.102$, where the μ's are in 10^{-7} slug/ft-s. Similarly, the reduction factor attainable by supplanting air with helium is 0.208.

C. 6 RUNDOWN TIME CAUSED BY WINDAGE LOSS ALONE

The P_{wind} requirement can be used to make a rough estimate of rundown time caused by windage loss alone (neglecting seal or bearing friction loss). The rate of decrease of energy can be expressed as a function of time by differentiating Eq. (C-4):

$$dE/dt = -I\omega(d\omega/dt) \ . \qquad \text{(C-15)}$$

where I is a constant for a given configuration. According to Eq. (C-7), P_{wind} is proportional to ω^3 for a given system; i. e.,

$$P_{wind} = C\omega^3 \ . \qquad \text{(C-16)}$$

Equating (C-15) and (C-16) we obtain:

$$C\omega^3 = -I\omega(d\omega/dt) \ , \qquad \text{(C-17)}$$

which we can integrate between any two values of t, t_1, and t_2:

$$\int_{t_1}^{t_2} dt = \Delta t_{wind} = -\frac{I}{C}\int_{\omega_1}^{\omega_2} \frac{1}{\omega^2}\, d\omega$$

$$\Delta t_{wind} = -\frac{I}{C}\left|-\frac{1}{\omega}\right|_{\omega_1}^{\omega_2} = \frac{I}{C}\left(\frac{1}{\omega_2} - \frac{1}{\omega_1}\right) \ . \qquad \text{(C-18)}$$

Now if we multiply and divide by $\omega_1{}^3/2$, we obtain

$$\Delta t_{wind} = \frac{2(I\omega_1{}^2/2)\omega_1}{C\omega_1{}^3}\left(\frac{1}{\omega_2} - \frac{1}{\omega_1}\right) = \frac{2E_1}{P_{wind_1}}\left(\frac{\omega_1}{\omega_2} - 1\right) \ , \qquad \text{(C-19)}$$

where E_1 and P_{wind} are in consistent units, e. g., ft-lb and ft-lb/s. For rundown to half speed ($\omega_1/\omega_2 = 2$, $E_1/E_2 = 4$); this reduces to:

$$\Delta t_{wind} = 2E_1/P_{wind_1} \qquad (\omega_1/\omega_2 = 2) \qquad \text{(C-20)}$$

For the 2:1 bar, starting from a full charge ($E_1 = E_0$) and using results from (C-8a) and (C-9), this gives:

$$\Delta t_{wind} = 2(1.804 \times 10^6 \text{ ft-lb})/(0.0375 \cdot 550 \text{ ft-lb/s})$$

$$= 1.75 \times 10^5 \text{ s, or 49 hours}$$

Starting from half speed ($\omega_1 = \omega_0/2$, $E_1 = E_0/4$, and $P_{wind_1} = P_{wind_0}/8$) and running down to one-quarter speed ($\omega_1/\omega_2 = 2$ again), Δt_{wind} would be twice as great, or 98 hours, because E_1/P_{wind_1} would be twice as great. The total time from full speed to 1/4 speed would be 49 + 98 = 147 hours, or 6^+ days, neglecting seal and bearing losses. Again, it should be remembered, as noted in Section C.4, that the true windage loss probably will be about half as large as the estimates given here, because the air will tend to turn with the rotor, reducing the air drag.

C.7 WINDAGE LOSSES FOR PYRAMIDAL AND HALBERD CONFIGURATIONS

As was shown in Appendix A, Table A-1, a rotor comprising two square-based pyramids base-to-base would have 4.5 times the allowable ω^2 compared to a rod of the same material and would thereby provide 35% more specific energy capability, even though the moment of inertia is considerably lower for the pyramidal configuration. Some rather complicated analytic geometry and integration were required to resolve velocity vectors and forces relative to the advancing sloped and tapered face, and these details will not be given here. The basic principle indicated by Eq. (C-6) was retained. However, some results of comparisons between bars, pyramids, and cones of equal volumes and equal R's (20 inches for these examples) may be summarized as follows:

1. At a given ω, a double pyramid with 2:1 base dimensions (narrower dimension facing the wind) would have 33% of the drag of the corresponding 2:1 bar.
2. However, at the higher permissible ω for the pyramid, it would have 3.2 times the drag of the 2:1 bar.
3. A square-based pyramid would have 1.46 times the drag of the 2:1 pyramid, or 3.3 times the drag of the corresponding square bar.
4. A double-cone rotor of the same volume would have 75% of the drag for the square-based double-pyramid rotor, just as the rod had 75% of the drag of the square bar. The energy density for the cone would be 5% less than that of the square pyramid.
5. If the square-based pyramid is rotated through 45° to present a wedge profile to the wind, its drag will be reduced by 50%. This result implies that the drag of bar rotors also might be halved by presenting wedge profiles to the wind, but no specific calculations were made.

An interesting concept for low drag is to form a halberd design by using a stack of thin bars and staggering them like a fanned deck of cards. By sweeping the upper half of the set one way and then reversing the sweep on the lower half, a wedge profile with a sharp leading edge can be developed on each side of the spin axis. A halberd configuration with a 7.8° half-angle would have only 8.6% of the drag of the corresponding 2:1 bar of the same total material volume.

APPENDIX D

SURVEY OF AVAILABLE TRANSMISSIONS AND PROPOSED CONCEPTS

The information presented here has been gathered from technical literature. Further information, especially regarding recent developments and research on transmissions, can only be obtained from the manufacturers, and it often is proprietary.

D.1 CONTINUOUSLY VARIABLE TRANSMISSIONS (CVT's)

The large number of CVT concepts can be categorized broadly as to their method of attaining the variability: mechanical (belt or other friction types), electrical, hydrostatic, hydrokinetic, and aerodynamic torque converters. In addition, combinations of these can be used as discussed later. At the outset let us note that the use of a CVT in present day vehicles could provide smoother performance and improved thermal efficiency, a fact recognized by automobile manufacturers (Ref. 14). However, to the authors' knowledge, only two production vehicles have been sold with a CVT: a Hayes friction drive was used on Austin cars in 1932-1936 (Ref. 138), and a belt drive is still in production by DAF (Ref. 5). In general, the CVT's have not attained a sufficient combination of reliability, durability, efficiency, and power capabilities in combination with acceptable size, cost, and weight, to displace the current well-developed automatic transmissions. The emerging importance of control of emissions may change this picture.

D.1.1 Mechanical (Belt or Friction) CVT's

There are many schemes for attaining a variable speed drive with belts (Ref. 16). In general, however, belt drives are restricted to the low horsepower (< 30) regime. Variable speed is obtained by variable-pitch pulleys, and speed adjustment can only be made while the drive is running. When both pulleys have variable pitch, speed changes up to 9:1 are possible. The major advantages to belt drives are low cost and simplicity. The major problems normally associated with them for high-horsepower (>25), and high-rpm (>3000) CVT's are short belt life, poor speed regulation under varying load, and high maintenance requirements. Regenerative braking is inherently possible with all mechanical CVT's.

Belt drives are widely used in snowmobiles and other small equipment (Ref. 16). The only production automobile currently sold with an "infinitely variable drive" – a belt drive with a 4.2:1 speed ratio – is the DAF, manufactured in Holland. The DAF models vary in curb weight from 1460 to 1700 pounds with powerplants rated from 32 bhp_{max} at 4200 rpm to 66 bhp_{max} at 5600 rpm. The manufacturer suggests that the belts be changed whenever tires are changed and inspected every 2000 miles. Two belts are used, one per drive wheel, and the transmission is bulky, occupying a large portion of the rear of the automobile.

General Motors, in a small (950-pound) experimental urban car (Ref. 139), used a variable-ratio, V-belt transmission and a two-cylinder SI engine rated at 13.9 bhp_{max}. The car had a top speed of 25 mph and an average acceleration rate of 1.6 mph/s from 0 to 30 mph.

Of the many variations of friction drives (Ref. 16) only two will be considered here. The Toric (Ref. 15) drive, known previously as the Perbury (Ref. 140) or the Hayes (Ref. 138) transmission, was first patented in 1899 by W. D. Hoffman. The drive uses disks with toroidal surfaces on the input and output shafts with speed variation by control of tiltable roller disks between the shaped shaft disks (Fig. D-1). Power is transmitted through the oil film separating the surfaces and controlled by axial loading. The Hayes transmission was fitted to the Austin

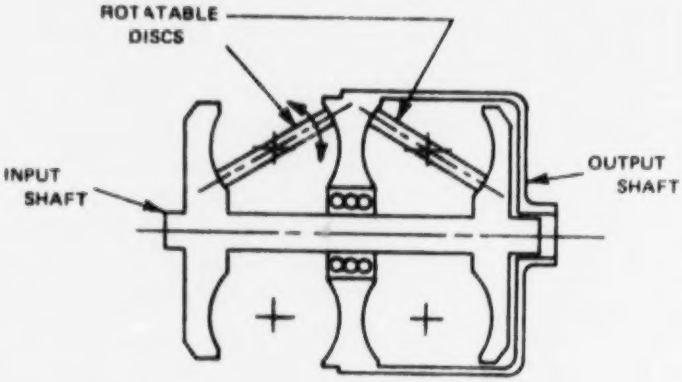
ROTATABLE
DISCS
INPUT
SHAFT
OUTPUT
SHAFT

(a) PRINCIPLE OF OPERATION OF PERBURY, HAYES, AND TORIC TRANSMISSIONS

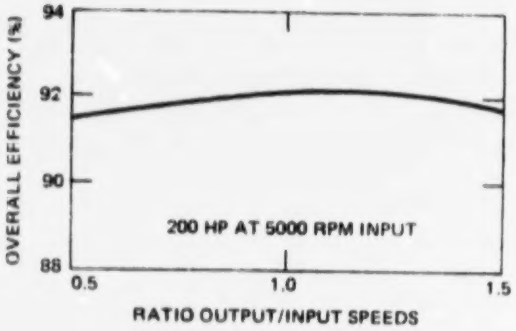

(b) EFFICIENCY VERSUS SPEED RATIO, PERBURY CVT (REF. 140)

Fig. D-1 PERBURY, HAYES, OR TORIC TYPE CVT'S car in 1933 and evidently was abandoned in 1936, "owing to teething problems" (Ref. 141), i.e., bugs. Recent interest (1956-1964) has resulted in the Perbury transmission, actually built from old Hayes parts. Laboratory tests were conducted for a test unit designed for a nominal 100 hp and reported in Ref. 140. Figure D-1 shows the results for 200-hp input at 5000 rpm (input torque = 210 ft-lb); efficiencies from 91 to 92% are attained over a 3:1 speed ratio. A hypothetical automotive Perbury transmission with clutch, gearbox, and Perbury drive was outlined in Ref. 140. Further studies were to be conducted on the life of the unit; however, we have found no more recent information in the literature.

General Motors' Toric transmission (Ref. 15) is a further development of the Perbury drive. Reference 15 quoted 96% efficiency, 800 ft-lb of torque and 275 hp. A visit to G.M. produced some additional general information but relatively little in the way of design information. Mr. Paul Vickers and other members of the Research Laboratories indicated that the unit is capable of a 6:1 (possibly 7:1) speed variation, and useful efficiencies are nearer 92% and evidently do not include oil pumping requirements. One main problem has been to obtain satisfactory hardened materials that could be produced at acceptable cost, but some progress has been made in recent years, and use in less capital-cost-critical applications (buses with GT's) may be approaching. The unit has been fitted to the experimental GM steam car (the SE 101) and a gas-turbine-powered bus, the RTX. No published information is available on size, weight, or durability as a function of power requirements. The GM Research people suggested that information for a specific requirement might be provided on request to the Transmission Division, to whom all GM work on the Toric has been transferred.

The second friction-type CVT under consideration is the Beier drive, in which many tapered disks are spring-mounted on a rotating drive shaft (Fig. D-2). The

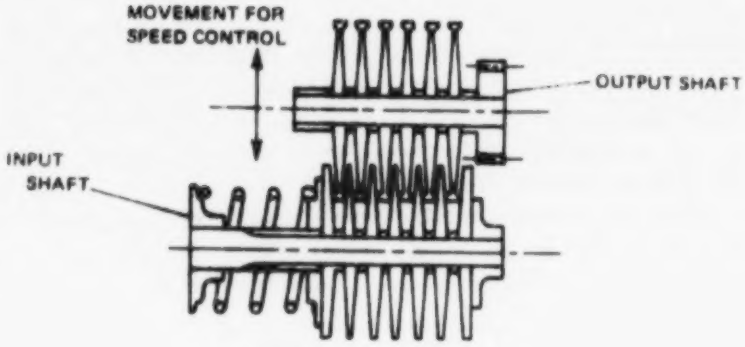
MOVEMENT FOR
SPEED CONTROL
OUTPUT SHAFT
INPUT
SHAFT

(a) PRINCIPLE OF OPERATION

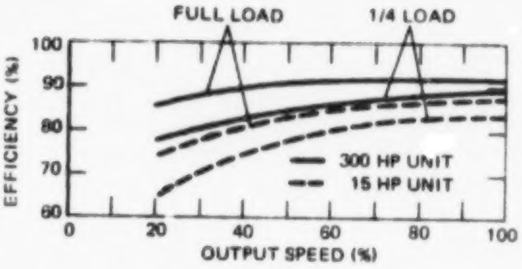

(b) EFFICIENCIES (REF. 16)

Fig. D-2 BEIER CVT'S

driven shaft is fitted with flanged disks, and speed control is obtained by varying the depth to which the flanged disks are inserted into the tapered disks. Power is transmitted by the viscous drag of thin oil films between the disks. Metal-to-metal contact (hence wear) of the power transmitting surfaces is prevented. Catalogued industrial units employ a 4:1 speed ratio with minimum output speeds of 650 rpm, and a maximum input speed of 1800 rpm. Units up to 300-hp capacity are available. Efficiency (Fig. D-2) increases with the power capability and ranges from 85% at the low speed ratio (4:1) to 91% at 1:1 for a 300-hp unit. The Beier transmission evidently was under development (1957) in Germany as an automobile transmission (Ref. 16); however, no further information has been located. No information is available as to size and weights.

D.1.2 Electric CVT's

The application of electric transmissions to electric vehicles was analyzed at length in the A. D. Little, Inc. study (Ref. 106). What follows here is largely a summary of those results, as related to our interests. (Reference 106 did not discuss the potential of high-energy-density flywheels or flywheel-hybrids.) The electric transmission as applied to a flywheel hybrid comprises a generator to convert the shaft mechanical energy to electrical energy, a motor to convert the electrical energy to mechanical energy, and a controller. Numerous controllers are available for each type. Losses in electrical machinery are due to bearing losses, windage losses of the rotor, and I^2R losses. Overall efficiency increases as power rating increases.

A DC motor provides the required high performance and is easier to control than an AC motor, but has brush-wear problems and is heavier. A DC motor provides essentially a constant horsepower throughout its speed range. DC motors have been used in electric locomotives and have been selected for the drives of a number of proposed urban transportation systems. Regenerative braking can be accomplished with both AC and DC motors. DC motors were selected for the vehicle drives in Ref. 106. To reduce weight, high-speed (13 000 to 16 000 rpm) motors were assumed, hence speed reducers were required in the drives. For the generators, however, AC units were selected because they have no brush maintenance, can be run at high speeds, are compact, and are mass-produced now (alternators); consequently, AC/DC rectifiers also were required.

Table D-1 shows the estimates from Ref. 106 for the electrical transmissions as applied to the commuter and family cars. It was not stated whether the quoted efficiencies were maximum values or averages over a driving schedule. Inclusion of the motor speed reducers and generator efficiencies would result in an overall drive transmission efficiency η_D of $\sim$ 70% in contrast to the 73% we are presently assuming. The weights in Table D-1 are larger by factors of 2.7 and 2.25, respectively, for the family and commuter cars than the values we have assumed in the analytic studies.

General Motors, under contract to the U.S. Army Tank Automotive Command, has equipped a 2½-ton M-35 Army truck with an all-electric drive system (Ref. 142). A six-cylinder, 140-net-hp, SI engine drives a 15 000-rpm, 75-hp, brushless homopolar induction alternator. The six motors (one per wheel) are brushless synchronous units rated at 20 hp each over a 16:1 speed range (1000 to 16 000 rpm) with 33/9:1 gear reducers from motor to wheel. Overall efficiencies are not given. Specific weight for the complete drive train (alternator, motors, and controls) is 19.1 lb/hp. After installation of the electric drive train the "electric drive test bed is 873 pounds heavier than the original M-35 truck with mechanical drive."

An excellent discussion of the various types of electrical devices available for power transmissions can be found in Ref. 143.

Table D-1

Electric Drivetrain Characteristics (Ref. 106)

Parameter	Family Car	Commuter Car
Maximum Output of Hybrid Power Source (hp)	114	39
Curb Weight (pounds)	3500	1400
Weight of Generator, Rectifiers, Speed increaser and Voltage Regulator (pounds)	70	30
Maximum Power Delivered to Wheel Speed Reducers (hp)	94	30
Motor Weight (pounds)	228	66
Motor Efficiency (%)	88	86
System Voltage, v	500	250
Controller Weight (pounds)	50	30
Controller Efficiency (%)	93	91
Weight of Speed Reducers (pounds)	15	6
Weight of Cables, Mounting, etc. (pounds)	45	12
Weight of Cooling System (pounds)	10	4
Overall Efficiency (Excluding Speed Reducers and Generator) (%)	82	77
Overall Weight of Electrical System (pounds)	418	148
Specific Weight (lb/hp)	3.68	3.80

D.1.3 Hydrostatic Drives

A hydrostatic transmission consists basically of a pump mounted on the input shaft that converts mechanical power to hydraulic power and a motor on the output shaft that converts hydraulic power to mechanical power. The pump and motor are positive displacement devices (they trap and discharge fluid in discrete segments). They are classified as to their method of fluid displacement (piston or rotary) and their controllability (constant or variable displacement). The piston type is better developed because of its high efficiency, ease of controllability, and capability of operating at high pressures. Figure D-3 depicts one with a variable-displacement axial piston pump and a fixed-displacement axial piston motor. The pump (input) consists of axial pistons mounted on a plate (swashplate) attached to the input shaft. The pistons and cylinder block rotate with the shaft, and through suitable porting valves at the cylinder base, fluid is pumped under pressure from the 'low' end to the 'high' end. Defining the displacement D of a pump or motor as the volume of fluid (in^3) displaced per revolution of the shaft, the fluid delivery Q (in^3/min) for a given shaft speed N (rpm) is

$$Q = D N .$$

For an ideal pump the mechanical power input (torque x rpm) equals the hydraulic power output (delivery x pressure). The torque (in-lb) is then given by:

$$T = pD/2\pi ,$$

and the horsepower by:

$$P = p\, D\, N/396\,000.$$

Speed control is accomplished by varying the piston stroke, i.e., swashplate angle, to vary Q. Pressure levels are dictated by the power input and can be monitored compared to a reference pressure determined by operator controls.

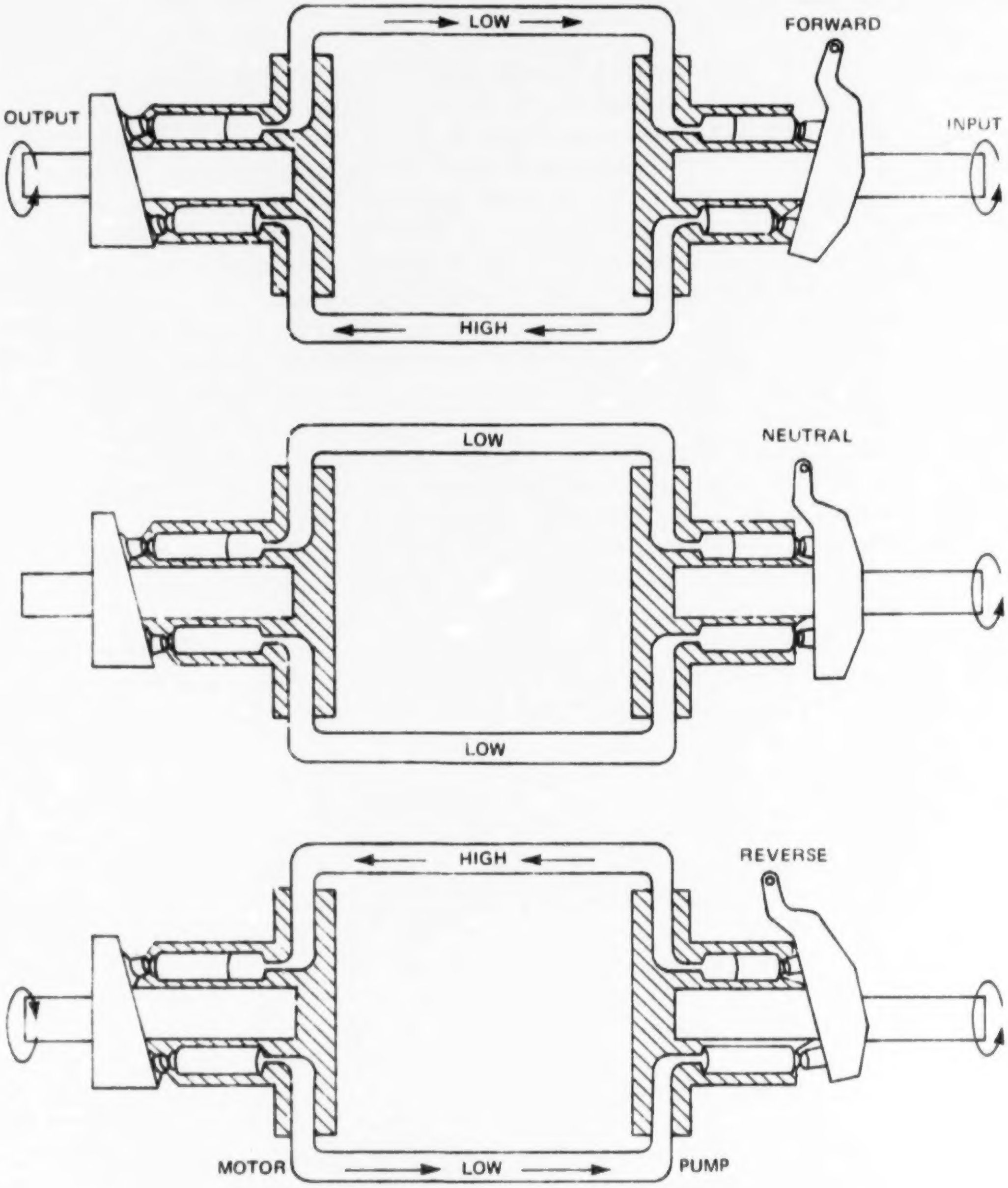
LOW
FORWARD
OUTPUT
INPUT
HIGH
LOW
NEUTRAL
LOW
HIGH
REVERSE
MOTOR
LOW
PUMP

Fig. D-3 HYDROSTATIC TRANSMISSION

If the pressure is used to adjust the swash-plate angle, control is effectively established. Such a system has been proposed for vehicle control. The motor operates on the same principle as the pump.

Neutral with a hydrostatic transmission (Fig. D-3) is not free-wheeling (i. e., the tractive wheels are not disconnected from the power train). To permit free-wheeling, say for towing, a special provision must be made, connecting the high- and low-pressure motor parts. Otherwise, the unit must be disconnected from the drive wheels or the pump will be damaged.

The advantages claimed for hydrostatic drive are: (a) infinite and smooth variability from full design speed in one direction, down to zero speed and to full design speed in the reverse direction, (b) precise controllability, (c) flexibility of installation and capabilities for (d) extremely fast acceleration or deceleration, (e) dynamic or regenerative braking, (f) developing a constant-torque or constant-power output, and (g) developing a constant speed independent of the load. Offsetting these features are its high specific weight (lb/hp) and volume, low overall efficiency, noise, cost, close manufacturing tolerances, and cooling requirements.

The earliest reference to an application was in a 1908 White Motor Co. truck (Ref. 144). No hydrostatic drive has, to our knowledge, been offered on a production automobile, although its applicability has been suggested (Ref. 145). Current usage is centered in industrial vehicles, e. g., grade and power rollers (Ref. 60) and farm tractors (Ref. 146). A hydrostatic drive has been proposed for a 6000-pound-loaded-weight vehicle in a mass transportation system. The top speed is 27.5 mph with a 2.75 mph/s acceleration capability. The proposed hydrostatic unit is estimated to weigh 320 pounds with an η_D of 65%.

Some characteristics of three catalogued units are listed in Table D-2. The "48-hp"* Sta-Rite unit is a compact, integral, motor-pump transmission. An efficiency map, computed from data in Ref. 147, at an input speed of 2800 rpm is shown in Fig. D-4a. The unit is too small to meet the acceleration requirements specified by OAP for the 1400-pound commuter car; its maximum output power actually is 32 hp at ~1.2:1 speed ratio. Maximum acceleration would occur along the 3000-psia line with an average efficiency of ~ 70%, which would be further reduced by inclusion of rear axle and speed-reducer efficiencies. The efficiency map of the "120-hp" Hydreco model 60 (Ref. 148) is shown in Fig. D-4b at an input speed of 2800 rpm. Its peak output power actually is 77 hp at ~1.5:1 speed ratio, and its efficiencies are somewhat poorer than those of the smaller Sta-Rite unit. Its acceleration capability exceeds the requirement for the commuter vehicle, but is inadequate for the family car. In addition to the pump and motor weight of 220 pounds, another 100 pounds or so will be required for controls and cooling.

Hydrostatic transmissions evidently are noisy (Ref. 149), possibly caused by fluid vaporization, which would be evident at high rotational speeds and high pressures. Current units operate at pressures up to 5000 psia. Maximum rotational speeds are limited by cavitation problems, and catalogued units operate at 3000 rpm. High power capability is obtained by increasing the size of the unit (i.e., Q). One manufacturer offers a 4000-hp unit with Q = 2300 gal/min at 4000 rpm (Ref. 150). As noted above, hydrostatic transmissions are relatively inefficient, and because of hydraulic fluid temperature limitations must be cooled to remove the lost power.

---

*Discussion with Sundstrand representatives brought out the fact that ratings are based on "corner horsepower," i.e., the result of maximum torque and maximum speed. The units are incapable of operating over a speed range at this power.

Table D-2

Characteristics of Catalogued Hydrostatic Transmissions

Manufacturer	Sta-Rite	Hydreco	Hydreco
Model Number	C3	60	110
Displacement (in^3/rev)	1.8	6	11
Input Power: Maximum (hp)	48	120	175
Continuous (hp)	--	80	125
Weight, Dry (Pump and Motor) (pounds)	50	220	482
Maximum Pressure (psia)	3500	5000	5000
Continuous Pressure (psia)	3000	--	--
Maximum Input Speed (rpm)	3000	2800	2500
Maximum Output Speed (rpm)	3000	3200	3200
Maximum Output Torque (ft/lb)	83	370	685

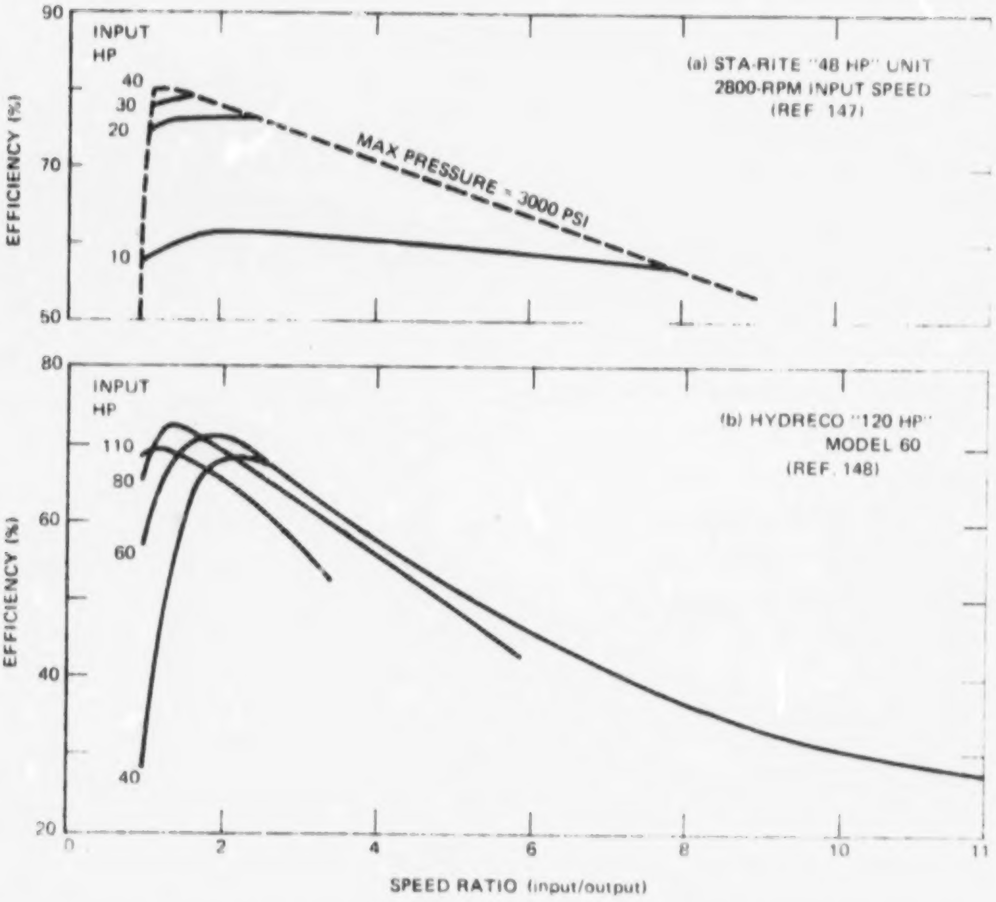

Fig. D-4 EFFICIENCIES FOR CATALOGUED HYDROSTATIC TRANSMISSIONS AT 2800 RPM INPUT SPEED

Battelle Memorial Institute, under contract to the U.S. Army Tank-Automotive Command, is investigating the possibility of developing a 600-hp, variable-displacement vane-type pump (Ref. 151) for possible use in a turbine-powered vehicle. Because of its high speed (22 000 rpm), it may be suitable for direct connection to the flywheel shaft. Discussions with Battelle personnel, however, disclosed that development effort is minimal, and the desired goals have not yet been attained in a test unit.

D.1.4 Hydrokinetic Drives

Hydrokinetic devices (Ref. 150) comprise an impeller (pump) connected to the drive shaft and a turbine (motor) connected to the driven shaft, between which is a viscous fluid, oil. The impeller causes fluid to travel radially under centrifugal forces and thence into the turbine. The angular momentum imparted to the fluid by the impeller is transferred to the turbine. Two types of drives are considered: (1) variable speed hydraulic couplings and (2) torque convertors. Variable speed is attained by controlled slip, an inefficient method of control that is analogous to using a resistor in an electric motor for speed control; hence, waste heat rejection is a design consideration.

A hydraulic coupling is depicted in Fig. D-5. Since the velocities leaving and entering the impeller are the same as those entering and leaving the turbine, respectively, the torque is the same on the impeller and turbine, i.e., output torque is equal to input torque. The transmission of torque depends on slippage; for zero slippage, no torque is transmitted as the centrifugal forces in the turbine are equal to the centrifugal forces in the impeller (i.e., pressures are equal), thereby preventing the circulation of fluid. The normal slip loss is 2 to 4% at the maximum turbine speed and torque. Speed control of the turbine is accomplished by bleeding fluid from the unit, thereby reducing the quantity of fluid circulated. This, however, also results in a lower capacity for torque

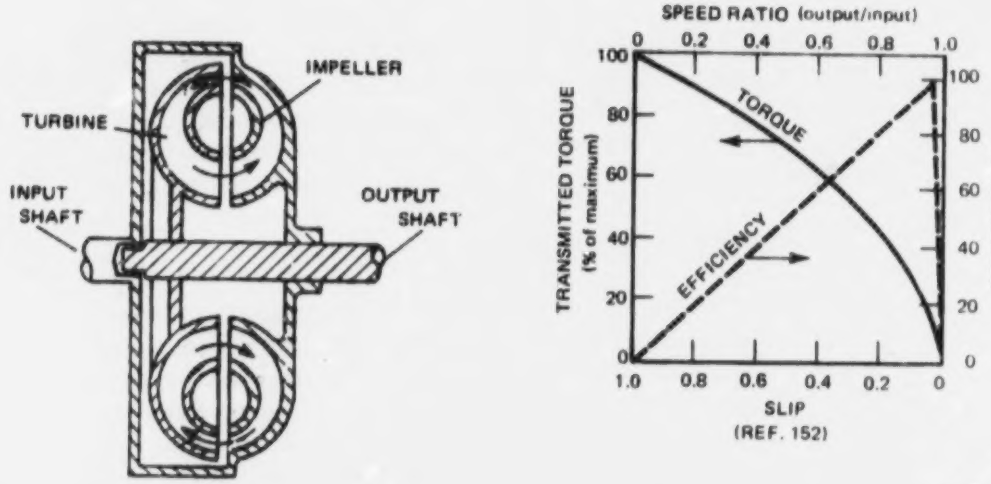
IMPELLER
TURBINE
INPUT SHAFT
OUTPUT SHAFT
SPEED RATIO (output/input)
0
0.2
0.4
0.6
0.8
1.0
TRANSMITTED TORQUE (% of maximum)
100
80
60
40
20
0
TORQUE
EFFICIENCY
EFFICIENCY (%)
100
80
60
40
20
0
1.0
0.8
0.6
0.4
0.2
0
SLIP
(REF. 152)

Fig. D-5 FLUID COUPLING DIAGRAM AND CHARACTERISTICS

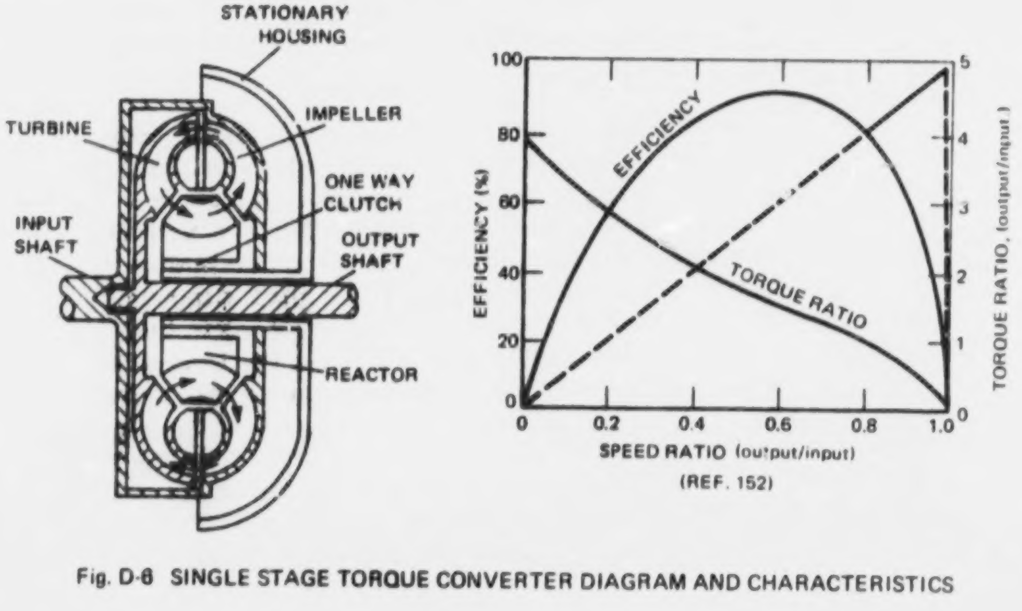
STATIONARY HOUSING
TURBINE
IMPELLER
ONE WAY CLUTCH
INPUT SHAFT
OUTPUT SHAFT
REACTOR
EFFICIENCY (%)
100
80
60
40
20
0
EFFICIENCY
TORQUE RATIO
TORQUE RATIO, (output/input)
5
4
3
2
1
0
0
0.2
0.4
0.6
0.8
1.0
SPEED RATIO (output/input)
(REF. 152)

Fig. D-6 SINGLE STAGE TORQUE CONVERTER DIAGRAM AND CHARACTERISTICS transmission. Torque and efficiency curves for a typical unit with a fixed impeller (input) speed are shown in Fig. D-5.

In a torque converter, a stationary "reaction member" (stator) is inserted between the impeller and turbine for torque multiplication (Fig. D-6). For steady flow the torques acting on the device must sum to zero; i. e., the output torque equals the input torque plus the torque developed on the reaction member. Maximum 'stall torque' (i. e., stationary output shaft) varies from 2:1 to 6:1 depending on the design. The efficiency of a single-stage (one set of blades on the turbine) torque converter as a function of speed ratio is shown in Fig. D-6 (Ref. 152) as the bell-shaped curve. Mounting the reactor on a one-way clutch, thereby allowing the reactor to rotate freely in one direction, converts the torque converter into a fluid coupler. At the high-speed ratios the forces on the reactor reverse and it therefore rotates with the impeller. The higher efficiency of the fluid coupler results. Figure D-6 shows the release (coupling) point occurring at the speed ratio where the torque converter and fluid coupler efficiencies cross. This type of unit is referred to as a 'converter-coupler'.

D.1.5 Aerodynamic Torque Converter

An aerodynamic torque converter (ATC) is presently under development by Power Technology Corp. (Refs. 153 and 154). The first unit tested (100-hp capacity) resulted in a peak efficiency of 77%. The ATC is, in principle, similar to a hydraulic torque converter except that a compressible fluid is used as the working fluid, with control accomplished by the fluid density. The unit is envisioned as operating with a GT, whereby the fluid for the ATC is bled from the turbine compressor output and then returned to the main GT flow, thereby recovering a portion of the transmission losses. This recovery capability has not been considered in the reported 77% efficiency. For a GT-flywheel hybrid vehicle, the ATC may be suitable for the drivetrain from the GT to the flywheel. However, with our present hybrid concept of on-off operation of the engine, use of an ATC for the main transmission is not feasible.

D.2 POWER-DIVIDING TRANSMISSIONS

Attempts have been made to alleviate the deficiencies of CVT's by dividing the power between two subsystems, one of which (e.g., a hydrostatic subsystem) generally performs the control function, the other (e.g., mechanical gearing) giving a high efficiency power transfer. The power split is generally a function of the speed ratio and power level. It is obviously desirable to transmit most of the power through the high efficiency unit.

The hydromechanical transmission invented by Ebert (Ref. 150) in Germany incorporates hydrostatic circuits in combination with constant-mesh gearing. It was (1964) under development under the name DB "Transmatic" for cars, buses, and trucks by David Brown Industries Limited in England. One unit for a car was designed to fit in the same volume as the standard gearbox. A 6:1 maximum torque ratio is claimed, of which one unit is mechanical and five units are hydrostatic. At the 1:1 speed ratio the drive is purely mechanical. The transmission uses a small variable-displacement pump and three small variable-displacement motors operating at less than 3000 psi. Features claimed are $\eta_D > 90\%$, reduction in noise levels, and small size. Prototype units evidently have been built and tested in trucks. It has been heard* that the Army Automotive Tank Command has supported effort on development of this unit, but its status is uncertain; further information is being sought.

A hydro-mechanical transmission now under development for large trucks by the Sundstrand Corp., called the Dual Mode Transmission (DMT) (Ref. 4), uses a variable-displacement pump and a fixed-displacement motor in combination with gears. During startup, all power is transmitted hydraulically. At a fixed, preset, power level the mechanical gears are placed in, so that for high-speed cruise, most of the power is transmitted mechanically. Control is obtained through this hydrostatic unit (see Section D.1.3). The prototype units (1968) used aircraft-type (expensive) materials and construction, were rated at 250 hp input, and weighed 225 pounds. The DMT 250 production units scheduled for 1972 also will be rated at 250 hp input but will weigh 675 pounds when made of conventional materials. The transmission is advertised for both on- and off-highway vehicles. Full-load efficiencies (acceleration) are shown in Fig. D-7. Efficiencies during cruise are expected to be somewhat lower. Sundstrand representatives* feel that the concept can ultimately be applied to flywheel vehicles, but that their current DMT design is not ideally suited for FW systems, and that significant development efforts will be necessary. The main problem areas of the simple hydro-mechanical transmission are weight and low efficiency at low vehicle speeds (< 25 mph) encountered over most of the typical operating cycles. A simple hydro-mechanical transmission adapted for a family car FW system (Ref. 155) is estimated to weigh ~ 280 pounds and would have peak efficiencies similar to those shown in Fig. D-7. Advanced design concepts such as multimechanical modes are possible, but have not been demonstrated.

---

*Private discussions with Sundstrand Corp. representatives.

General Electric, under sponsorship of the Army Tank-Automotive Command, is developing a hydromechanical transmission (Ref. 13) called the XM1. It has been

---

*A cursory study of the applicability of their hydromechanical transmission design concept to the APL flywheel vehicle systems was performed by Sundstrand Corp. as a result of their interest and our informal request at a recent meeting.

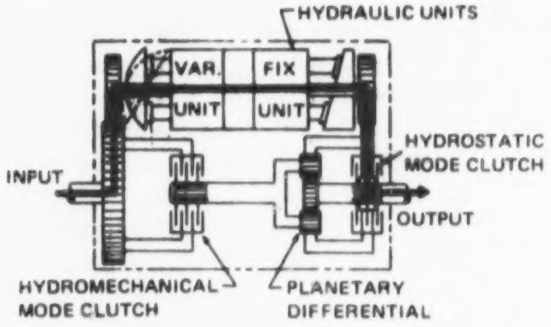
HYDRAULIC UNITS
VAR. UNIT
FIX UNIT
HYDROSTATIC MODE CLUTCH
INPUT
OUTPUT
HYDROMECHANICAL MODE CLUTCH
PLANETARY DIFFERENTIAL

HYDROSTATIC MODE

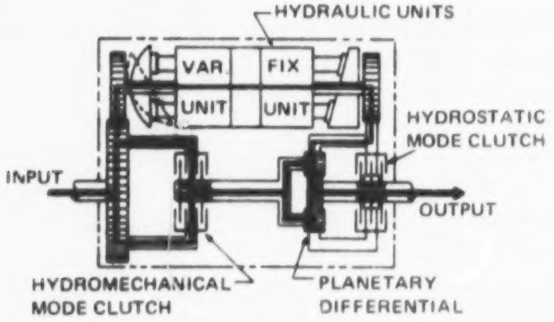
HYDRAULIC UNITS
VAR. UNIT
FIX UNIT
HYDROSTATIC MODE CLUTCH
INPUT
OUTPUT
HYDROMECHANICAL MODE CLUTCH
PLANETARY DIFFERENTIAL

HYDROMECHANICAL MODE

SCHEMATIC DIAGRAM

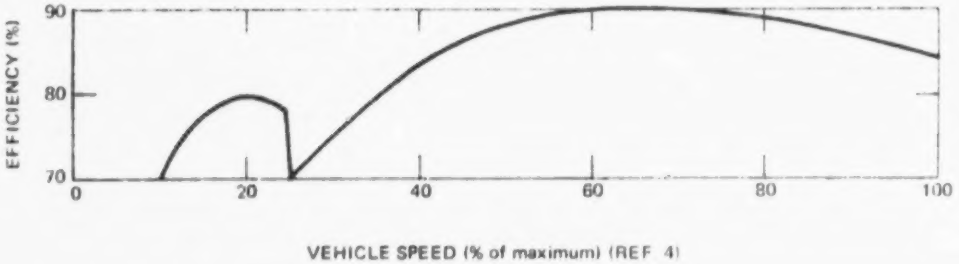

Fig. D-7 (a) SCHEMATIC DIAGRAM AND (b) WIDE-OPEN THROTTLE (ACCELERATION) EFFICIENCY OF SUNSTRAND DUAL-MODE, INFINITELY VARIABLE RATIO TRANSMISSION tested in the M113A1 Armored Personnel Carrier, a tracked vehicle, and it is claimed that the concept can be applied to wheeled vehicles as well. Performance characteristics of the XM1 have not been reported. A "revolutionary new car transmission" has been tested successfully by the National Engineering Laboratory in Glasgow, Scotland, in a small family car (Ref. 156). It is not clear whether the unit uses power-splitting or is a pure hydrostatic. It is claimed that the unit "produces a tiny power loss and can be mass-produced economically." No other information on this unit has been located.

An electromechanical transmission (EMT) for a hybrid battery vehicle is under development by TRW, Inc. (Ref. 17). It is a parallel-type configuration and operates in two modes. Mode 1 is used for urban operation, with the powerplant operating at fixed load and fixed speed, providing the average power needed on the cycle. Extra power for acceleration is supplied by the batteries, and excess power during idle is used to charge the battery. Mode 2 is used for highway cruise. The engine is directly coupled to the rear wheels,and the engine is throttled (speed change) to maintain the desired cruise condition. The transmission is capable of regeneration in mode 1, and the batteries are not used in mode 2. Dynamometer emission measurements of a breadboard proof-of-principle model were performed on the LA-4 driving route and compared to those for two standard automobiles – a 1970, 6-cylinder, 120 hp, 3000-pound car, and a 1969, V8, 190 hp, 3500-pound car – driven on the same schedule. The emissions reported for the two test comparisons showed reduction factors of 2.7 and 3.1 for HC, 10.4 and 6.0 for CO and 6.2 and 3.2 for NO_x, all for hot starts. Fuel economy of the EMT was 4% poorer than that of the 6-cylinder car – but 27% better than that of the V8 car. The fixed-speed EMT engine was operated lean at $a/f \approx 18$, and it was necessary to operate the engine at a power level approximately twice that of the road power demand because of the low overall EMT efficiency (< 50%). They (Ref. 17) concluded that regenerative braking does not contribute substantially to the total charging process, but they believe that the transmission efficiencies can be improved significantly by design refinement.

D. 3 THE GYREACTA MECHANICAL TRANSMISSION

The Gyreacta (Ref. 10) transmission was developed and tested by Clerk, King, Poynter & Co., Ltd. specifically for a flywheel-hybrid vehicle and is discussed separately, since it is a unique unit. It is a purely mechanical drive using meshing gears and clutches. Speed control is accomplished by the spark ignition engine with appropriate gear shifting to cover the operating range. The unit has provisions for regenerative braking, charging the flywheel, and powering from the power plant and/or flywheel. Efficiencies of 98.5% are claimed. Because of the method of control, i.e., via the powerplant, the unit is not suitable for the mode of operation presently under consideration, i.e., a hybrid using a constant-speed powerplant and capable of flywheel-only operation in congested areas.

D. 4 SPEED REDUCERS

A speed reducer is required between the flywheel and the transmission. The current state-of-the-art should be adequate. Garrett/Airesearch, for instance, uses a speed reducer of $\sim$20:1 from the high-speed (58 000 rpm) TSE 36-1 gas turbine that develops 240 shaft horsepower (Ref. 157).

Catalogued (Ref. 158) herringbone units with 15:1 reduction and pitchline velocities of 30 000 ft/min are quoted as 98% efficient at rated power with the efficiencies decreasing at less than full power.

Rear axle reduction boxes operate nominally at a 3.1:1 ratio and use planetary gear configurations.

Figure D-8 shows the rear axle efficiency of an installed unit (Ref. 109) operating at wide-open throttle (i.e., acceleration) and road load conditions. Note that at low cruise speed, 20 mph, the efficiency is reduced to 87%. The low efficiency under light load is attributed to seal friction, oil churning losses, and bearing losses.

A new development in planetary speed reducers is the roller traction type of device (Refs. 159 and 160) which is more efficient, reliable, durable, and quieter than planetary gears. Figure D-9 shows its significant efficiency advantage at part load. It is suited to high-speed (and high-power) applications. Tests on a 500-hp, 35 000-rpm unit and a 5-hp, 480 000-rpm unit are reported in Ref. 159. Weights and volumes are claimed to be equivalent to planetary gear trains.

A unique speed reduction mechanism is the harmonic drive (Ref. 161). The units use a "deflection wave transmitted to a nonrigid member to produce a high mechanical advantage between concentric parts." Advantages cited are high speed ratios, high efficiencies, low weight, and hermetic sealing. The last feature is particularly attractive for flywheels in evacuated cases. Maximum shaft-to-shaft efficiencies of 90% are reported. The units are employed where high reduction ratios are required, i.e., greater than 60:1. For a 30 000-rpm fully charged flywheel speed and a 60:1 reduction, input transmission speeds would vary from 250 to 500 rpm requiring high levels of input torque. For speeds $\geq$ 20 mph at low flywheel charge, the transmission would be required to operate at over 1:1 speed ratio, reaching 1:5 at 80 mph.

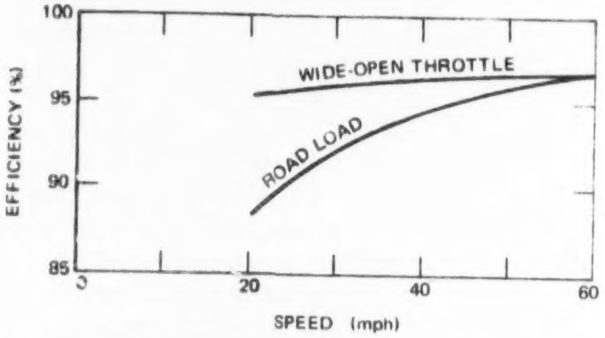

Fig. D-8 REAR AXLE EFFICIENCY AT WIDE-OPEN THROTTLE AND ROAD LOAD (REF. 109)

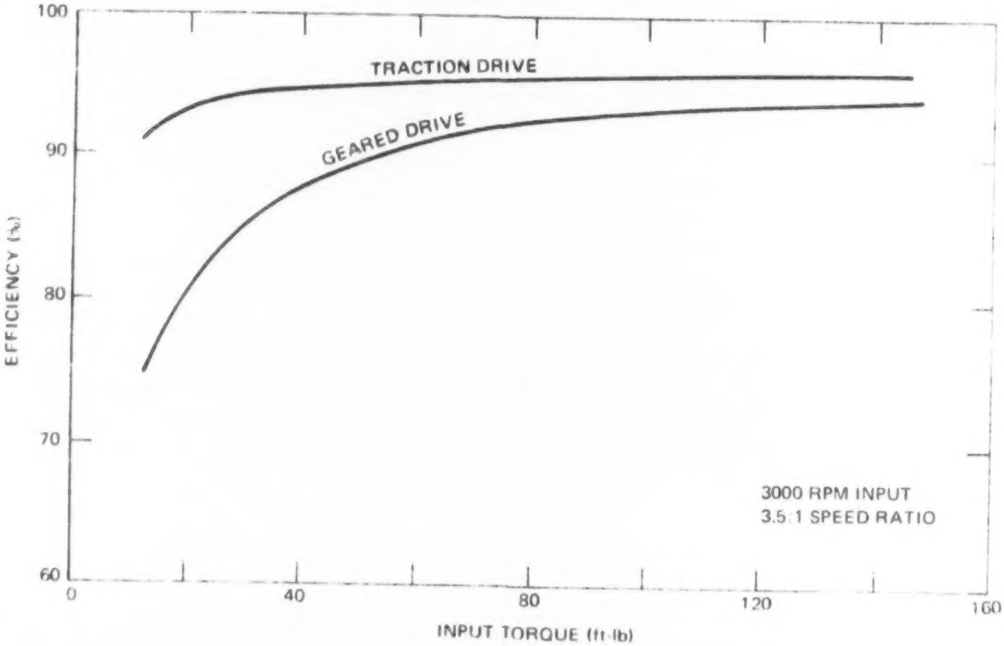

Fig. D-9 OVERALL EFFICIENCY COMPARISONS OF ROLLER TRACTION VERSUS GEARED PLANETARY DRIVE UNITS (REF. 160)

APPENDIX E

TIRE AND WIND RESISTANCE OF AUTOMOBILES

The major external resistance to vehicle propulsion are the aerodynamic resistance and the rolling contact resistance between the tires and the road. The aerodynamic drag force D is related to the drag coefficient C_D by:

$$D = \tfrac{1}{2}\rho V^2 C_D A = 0.00257\, C_D A V^2 \text{ , pound} \qquad \text{(E-1)}$$

where sea-level density has been assumed, A is in ft^2 and V in mph. The rolling friction F_F is related to the rolling resistance coefficient f (lb/lb) by:

$$F_F = f\, W_\ell \, , \qquad \text{(E-2)}$$

where W_ℓ is the loaded vehicle weight. With the forces given in pounds and the velocities in mph, the conversions to horsepower are given by:

$$P_D = DV/375 \qquad P_F = F_F V/375 \, . \qquad \text{(E-3)}$$

The values given by Eqs. (E-1) - (E-3) are wheel forces. To relate these to the powerplant shaft requires consideration of the driveline efficiency.

E.1 AERODYNAMIC DRAG COEFFICIENT

Bowman (Ref. 162) reported wind-tunnel measurements of 21 models of automobiles, 17 of which were "precise scale duplicates of production vehicles" ranging in size from subcapacity and small, high-performance racing coupes to the large high-production volume sedans. Three were models of production car proposals, and one was a "highly streamlined experimental body shape" (Ref. 162, p. 609). The measured C_D's are listed in Table E-1.

Hoffman (Ref. 107) plots drag force at 60 mph (88 ft/s) versus W_ℓ for 1960 automobiles. In Fig. E-1, force is shown on the right-hand scale, and the left-hand scale shows the corresponding drag coefficients for vehicles with 25-ft^2 frontal areas per Eq. (E-1).

In the North American study (Ref. 132), values of $C_D = 0.45$ for "conventional 1960 cars" and $C_D = 0.25$ for "advanced vehicles" were used.

Hoerner (Ref. 108) reports values of C_D for a number of production vehicles of 1920-1950 vintage. In addition, values for smooth wind-tunnel models are also documented. These values are given in Table E-2.

The Battelle (Ref. 105) and Little (Ref. 106) studies "employed optimistic values for the drag coefficients" (Ref. 106, p. 15). The values used (along with frontal areas) for a small commuter car and a family car are shown in Table E-3. Also shown in Table E-3 are the corresponding values proposed by OAP for the hybrid-flywheel vehicle specification.

E-2 ROLLING RESISTANCE COEFFICIENT

Experimental values of the rolling resistance coefficient, f, as a function of speed (0 to 70 mph), tire pressure (25 and 30 psi) and material (nylon and rayon cords) for 8.00-15 4-ply passenger tires are reported in Ref. 163. The results are shown in Fig. E-2.

Various equations have been proposed by tire manufacturers, automobile manufacturers, and analysts. A number of these are:

Table E-1

Measured Frontal Areas and Drag Coefficients from Bowman

Specimen	Make[1]	$A(ft^2)$	C_D
A	Ford Fairlane-500 (1963)	21.55	0.529
B	Anglia (English Ford)	16.95	0.508
C	1955 Ford	24.80	0.508
D	Unknown	20.8	0.502
E	1965 Ford	23.7	0.500
F	Unknown (no photo)	24.2	0.499
G	Datsun	18.5	0.473
H	1962 Ford	24.1	0.466
I	Edsel	22.3	0.458
J	Volkswagen	19.65	0.445
K	1960 Ford Falcon	20.75	0.445
L	Ford Station Wagon (1962)	24.70	0.4307
M	Unknown	20.1	0.429
N	Vauxhall	20.0	0.4258
O	Unknown	17.3	0.3996
P	Renault Dauphine	17.8	0.3938
Q	Unknown	18.9	0.369
R	Unknown	14.7	0.324
S	Proposed	17.56	0.307
T	Proposed	17.15	0.288
U	Experimental, highly streamlined vehicle	21.53	0.272

---

[1] Photographs were shown in Ref. 162, but the makes were not specified; the identifications listed here are opinions of "car buffs" at APL.

Table E-2

Vehicle Drag Coefficients from Hoerner (Ref. 108)

Car or wind-tunnel model	C_D
1920 open car	0.95
1940 German DKW	0.64
1949 Chrysler Windsor	0.60
1949-53 Hudson	0.51
1949 Nash	0.45
Box shape	0.86
Basic car body with sharp lateral edges	0.24
With sharp edged windshield	0.35
With long tapering tail	0.12
Streamline car shape	0.16
Extreme streamline shape	0.13

Table E-3

Vehicle Drag Coefficients Assumed for Recent Studies

Vehicle	W_ℓ(pound)	A(ft^2)	C_D(Ref. 106)	C_D(OAP)
Family Car	3500	28	0.35	0.50
Commuter Car	1400	18	0.25	0.35

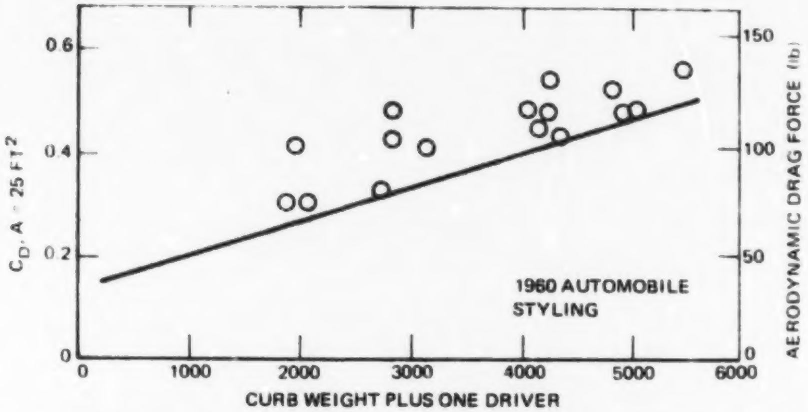

Fig. E-1 VEHICLE DRAG COEFFICIENTS FOR A FRONTAL AREA OF 25 FT^2, AND DRAG FORCES AT 60 MPH (REF. 107)

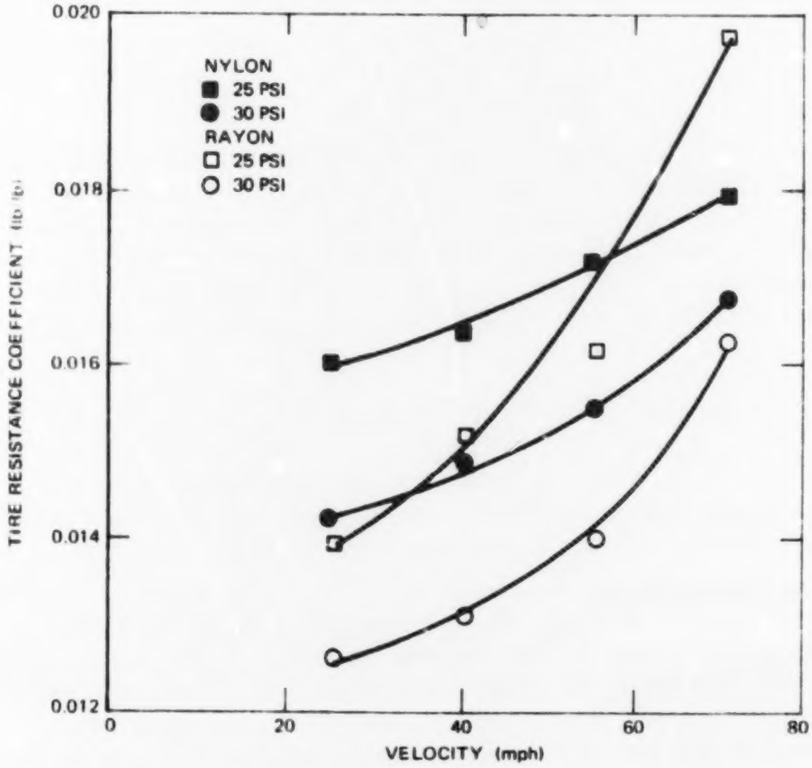

Fig. E-2 EXPERIMENTAL ROLLING RESISTANCE COEFFICIENTS (FROM REF. 163)

	Reference
$f = 0.0120$	57
$f = 0.0148$	57
$f = 0.0168 + 139.5 \times 10^{-6} V$	57
$f = 0.0116 + 165.0 \times 10^{-6} V$	57
$f = 0.0146 + 100.0 \times 10^{-6} V$	132 ("conventional 1966 cars")
$f = 0.0061 + 36.0 \times 10^{-6} V$	132 ("advanced vehicles")
$f = 0.01 + 50.0 \times 10^{-6} V$	107
$f = 0.02 + 28.0 \times 10^{-6} V + 0.24 \times 10^{-6} V^2$	106 (includes bearing and axle losses)
$f = 0.005 + \frac{0.15}{P} + \frac{35}{P} \times 10^{-6} V^2$	108 (P = tire pressure in psia)

where V is in mph. Values of the rolling resistance coefficient were not specified by OAP for the current study; however, it was recommended that current values only be used*. Current APL studies use the equation given by Hoerner (Ref. 108), with a tire pressure $P = 30$ psia (last equation in list above), as used in Eq. (5-9).

E.3 DISCUSSION AND CONCLUSIONS

It can be seen that the drag coefficients and rolling resistance quoted and measured by various authors differ by factors of 7 and 2.7 respectively ($0.13 \leq C_D \leq 0.89$ and

---

*"Any calculations of rolling resistance caused by tires should be made on the basis of currently available tires and include the effect of tire width. Decreasing the rolling resistance caused by the tires by assuming a type of tire that has unsafe traction characteristics by virtue of low rolling resistance is not allowed" (Ref. 104).

$0.0065 \leq f \leq 0.0182$ at 10 mph). The drag coefficients are mainly a function of body styling. Current values of production vehicles vary from 0.4 to 0.5 (independent of frontal area); the attainment of $C_D \simeq 0.3$ seems feasible. Rolling friction coefficients are sensitive to tire material, construction, and pressure. Advanced projections based on higher pressures and more favorable construction and materials seems tenuous. The arguments advanced in Ref. 106 for discarding highly optimistic values of f are of interest.

> "We have taken a cautious approach for the following reasons: (1) much of the reduction in rolling resistance of improved tires is lost if correct inflation pressures are not maintained; (2) a soft ride may be demanded by buyers of automobiles, and on rough roads this would require that energy be absorbed either in the tires or by the suspension system; (3) Federal safety requirements for tires cannot at present be met by tires with very low rolling resistance" (Ref. 106, p. 17).

Based on the above considerations the following ranking of values seems appropriate:

	C_D	f
Conservative	0.50	$0.0168 + 139.5 \times 10^{-6} V$
Optimistic	0.30	$0.010 + 50.0 \times 10^{-6} V$
Highly Optimistic	0.20	$0.00612 + 36 \times 10^{-6} V$

Steady state horsepower requirements based on the above assumptions are plotted in Fig. E-3 for a 1400 pound (curb weight) commuter automobile. Also shown for comparison are the values currently in use. ($C_D = 0.35$ and Hoerner's equation for the resistance with P = 30 psia.) It can be summarized that the values currently in use can be considered as reasonably optimistic.

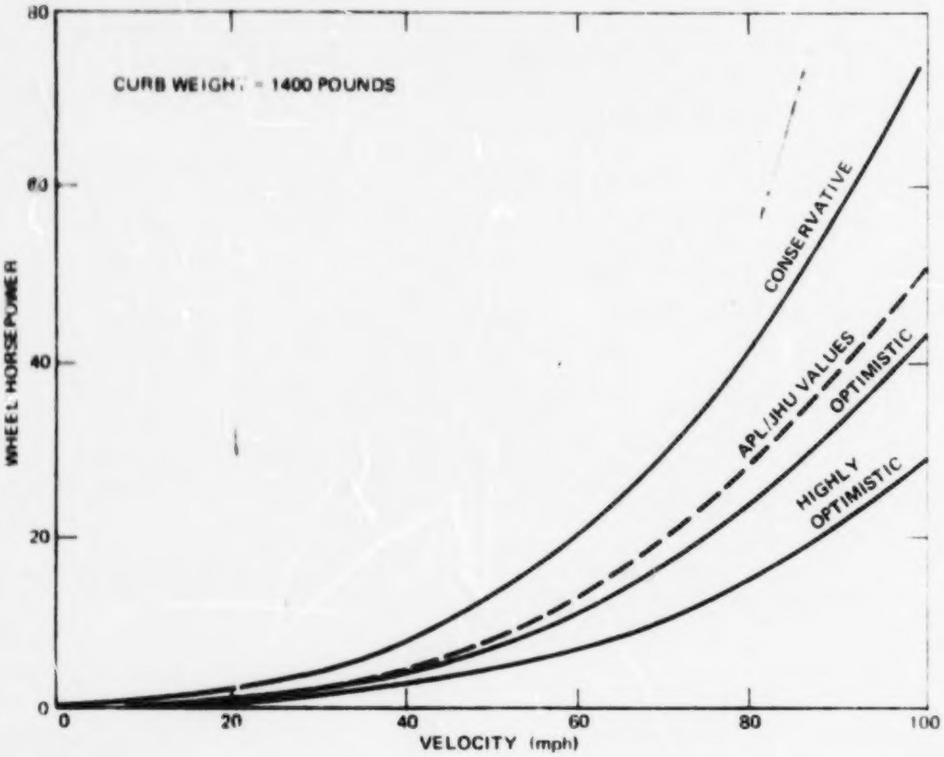

Fig. E-3 STEADY HORSEPOWER REQUIREMENTS FOR VARIOUS DRAG AND FRICTION ESTIMATES

REFERENCES

1. A. M. Lovelace and W. Tsai, "Composites Enter the Mainstream of Aerospace Design," Astronautics and Aeronautics, July 1970, p. 56.

2. L. J. Lawson, "Design and Testing of High Energy Density Flywheels for Application to Flywheel/Heat Engine Hybrid Vehicle Drives," Intersociety Energy Conversion Engineering Conference, SAE Paper No. 719150, Boston, Mass., 1971.

3. Statements by Government officials suggesting a potential need for limiting the number of polluting vehicles in certain cities
    a. W. D. Ruckelshaus, Keynote Address to the Air Pollution Control Association, 64th Annual Meeting, Journal of APCA, Vol. 21, No. 8, 1971, p. 470.
    b. J. M. Callahan, "An Interview with Eric O. Stork," Automotive Industries, Vol. 145, No. 6, 15 September 1971, pp. 21-22.

4. R. H. Guedet and J. E. Louis, "Dual Mode Hydromechanical Transmission as Applied to Gas Turbines," ASME Paper No. 69-GT-13, March 1969.

5. DAF 750 and Daffodil, Automobile Engineer, Part I, September 1962, pp. 342-349; Part II, December 1962, pp. 494-500; Part III, January 1963, pp. 26-32.

6. K. J. Springer and C. T. Hare, "Four Years of Diesel Odor and Smoke Control Technology Evaluations – A Summary," ASME Paper No. 69-WA/APC-3, 1969.

7. D. W. Rabenhorst, "New Concepts in Mechanical Energy Storage," Intersociety Energy Conversion Engineering Conference, Las Vegas, Nevada, 1970.

8. D. W. Rabenhorst, Primary Energy Storage and the Super Flywheel, APL/JHU TG 1081, September 1969.

9. "Exhaust Emission Standards and Test Procedures," Federal Register, Vol. 36, No. 128, Part II, 2 July 1971.

10. R. C. Clerk, "The Utilization of Flywheel Energy," Trans. SAE, Vol. 72, 1964, pp. 508-543.

11. A. E. Wetherbee, Jr. and A. Svensson, Jr., "Feasibility of Flywheel High-Energy Storage, Final Report," Pratt & Whitney Aircraft PWA-3676, East Hartford, Conn., April 1969.

12. R. R. Gilbert, et al., "Flywheel Feasibility Study and Demonstration," Lockheed Missiles and Space Company, Final Report, LSMC-D007915, 30 April 1971.

13. R. L. Rio, "XM1 Hydromechanical Transmission," Automotive Industries, 1 January 1971, pp. 38-41.

14. J. G. Giles, "Gears and Transmissions," Automotive Technology Series, Vol. 4, London, ILIFFE Books, Ltd., 1969.

15. "Toric Transmission Smooths Vehicles' Power," Product Engineering, 2 June 1969, pp. 72-73.

16. P. Cahn-Speyer, "Mechanical Infinitely Variable Speed Drives," Engineers' Digest, Survey No. 1, Vol. 18, No. 2, February 1957, pp. 41-65.

17. G. H. Gelb, et al., "An Electromechanical Transmission for Hybrid Vehicle Power Trains – Design and Dynamometer Testing," SAE Paper No. 710235, January 1971.

18. "Transmission for Heat Engine/Flywheel Propulsion System," Environmental Protection Agency, RFP EPAR 71-Neg. 128, 15 March 1971.

19. D. W. Lapedes and J. Meltzer, "An Evaluation of Hybrid Heat Engine/Electric Systems for Low Exhaust Emission Potential in Automotive Application," 1971 Intersociety Energy Conversion Engineering Conference, SAE Paper No. 719151, Boston, Mass.

20. C. A. Brown, "Performance of Hybrid Flywheel Vehicles," Urban Technology Conference, AIAA Paper No. 71-509, New York, May 1971.

21. E. J. Brunelle, "The Super Flywheel: A Second Look," manuscript Submitted to Journal of Basic Engineering, May 1971.

22. A. S. Martino and G. J. Mangano, "Rotor Burst Protection Program, Phase V – Final Report," Naval Air Propulsion Test Center, NAPTC-AED-1901, May 1969.

23. R. B. McCallum, J. W. Leech, and E. A. Witmer, "On the Interaction Forces and Responses of Structural Rings Subjected to Fragment Impact," Aeroelastic and Structures Research Laboratory, Massachusetts Institute of Technology ASRL-TR-154-2 (NASA CR-72801), September 1970.

24. P. G. Hodge, Jr., Plastic Analysis of Structures, McGraw-Hill, New York, 1959.

25. W. Goldsmith, Impact, the Theory and Behavior of Colliding Solids, Edward Arnold Publishers, Ltd., London, 1960.

26. M. F. Jacobson, "Acoustic Fatigue Design Information for Fiber Reinforced Structures," Northrop Corporation, for Air Force Flight Dynamics Laboratory AFFDL-TR-68-107, July 1968.

27. J. E. Ashton, J. C. Halpin, and P. H. Petit, Primer on Composite Materials: Analysis, Technomic Publishing Co., Inc., Stamford, Conn., 1969.

28. S. W. Tsai and N. J. Pagano, "Invariant Properties of Composite Materials," Air Force Materials Laboratory, Wright-Patterson Air Force Base, Ohio, AFML-TR-67-349, March 1968.

29. H. H. Coe, H. W. Scibbe, and W. J. Anderson, "Evaluation of Cylindrically Hollow (Drilled) Balls in Ball Bearings at DN Valves to 2.1 Million," Lewis Research Center NASA TN D-7007, March 1971.

30. R. Cohen, H. Means, and P. Heyl, "Brayton-Cycle Turbomachinery Rolling-Element Bearings," United Aircraft Corp. NASA CR-1229, January 1969.

31. R. E. Cunningham and E. J. Gunter, Jr., "Critical Speeds of a Rotor in Rigidly Mounted, Externally Pressurized, Air-Lubricated Bearings," Lewis Research Center NASA TN D-6350, May 1971.

32. "SKF Engineering Data," SKF Industries, Inc., Philadelphia, Pa.

33. K. H. Boller, "Fatigue Strength of Plastic Laminates Reinforced with Unwoven "S" Glass Fibers," Forest Products Laboratory, U. S. Department of Agriculture AFML-TR-64-403, May 1965.

34. "Structural Design Guide for Advanced Composite Applications," Advanced Composites Division, AFML, Wright-Patterson Air Force Base, January 1971.

35. "Advanced Composites Technical Data," Hercules, Incorporated, Wilmington, Delaware, ACM-7, Vol. 1.

36. M. J. Salkind, "Fatigue of Composites," ASTM Second Conference on Composite Materials: Testing and Design, Anaheim, California, April 1971.

37. K. H. Boller, "Stress-Rupture Evaluation of Glass-Reinforced Plastic Laminates," U. S. Department of Agriculture, Forest Products Laboratory, No. 2228, December 1961.

38. F. Y. Soliman, "Creep and Rupture of Graphite-Epoxy Composites," *Composite Materials: Testing and Design*, American Society for Testing and Materials, Philadelphia, Pa.

39. T. T. Chiao and R. L. Moore, "Stress-Rupture of S-Glass/Epoxy Multifilament Strands," *J. Composite Materials*, Vol. 5, January 1971, p. 2.

40. M. P. Hanson, "Static and Dynamic Fatigue Behavior of Glass Filament-Wound Pressure Vessels at Ambient and Cryogenic Temperatures," Lewis Research Center NASA TN D-5807, May 1970.

41. S. M. Wiederhorn, "Environmental Stress Corrosion Cracking of Glass," National Bureau of Standards Report 10565, April 1971.

42. B. A. Proctor, I. Whitney, and J. W. Johnson, Proc. Royal, Vol. 297A, 1967, p. 534.

43. N. V. Gulia, personal communications received by D. W. Rabenhorst, including a report entitled: "High-Energy Mechanical Accumulator," by N. V. Gulia and V. P. Rabinovich.

44. G. D. Andreyevskaya, "Nonfabric Glass Plastics," Translation from: Nelkanyze Stekloplastiki, 1967.

45. Handbook of Fiberglass and Advanced Plastics Composites, edited by George Lubin, Van Nostrand Reinhold Co., New York, 1969.

    a. J. C. Bowman and J. W. Brannan, "Graphite Reinforcement for Plastic Composites," p. 237.

    b. L. E. Line, Jr. and U. V. Henderson, Jr., "Boron Filament and Other Reinforcements Produced by Chemical Vapor Plating," p. 201.

    c. J. V. Milewski, et al., "Whiskers and Their Composites," p. 255.

46. B. A. Proctor, "The Effects of Hydrofluoric Acid Etching on the Strength of Glasses," Rolls Royce, Ltd.

47. H. A. Perry, "Surface-Compression Strengthened Glasses: Some Properties," Naval Ordnance Laboratory, White Oak NOLTR 71-21, Silver Spring, Md., March 1971.

48. W. B. Hillig, "The Factors Affecting the Ultimate Strength of Bulk Fused Silica," General Electric Research Laboratory.

49. "DuPont's New High-Modulus Fiber PRD 49 Type 1," E. I. du Pont de Nemours and Co., Wilmington, Delaware.

50. G. J. DeSalvo, "Theory and Structural Design Applications of Weibull Statistics," Westinghouse Astronuclear Laboratory WANL-TME-2688, April 1970.

51. L. J. Broutman and S. Sahu, "A New Theory to Predict Cumulative Fatigue Damage in Fiber Reinforced Plastics," ASTM Second Conference on Composite Materials: Testing and Design, Anaheim, California, April 1971.

52. R. R. McHenry and N. J. Delays, "Vehicle Dynamics in Single Vehicle Accidents," Cornell Aeronautical Lab., Inc. CAL No. VJ-2251-V-3, December 1968.

53. R. S. Rice, Vehicle Research Dept., Cornell Aeronautical Lab., Inc., personal communication to L. L. Perini (APL/JHU) with enclosures containing test data.

54. G. P. Peterson, "Development and Performance of Advanced Composite Structures," AIAA/ASME 12th Structures, Structural Dynamics, and Materials Conference, Anaheim, California, April 1971.

55. J. Andon and I. R. Barpal, "Emission Optimization of Heat Engine/Electric Vehicle," Minicars, Inc., EHS 70-107, Goleta, California, January 1971.

56. W. F. Marshall and R. W. Hurn, "Experience in Modifying Diesel Engine Operating Parameters to Reduce Emissions," presented at 1971 Intersociety Energy Conversion Engineering Conference, Boston, Mass., 3-6 August 1971.

57. E. F. Obert, *Internal Combustion Engines*, 3rd Edition, International Textbook Co., Scranton, Pa., 1970.

58. C. W. King, et al., "Electric-Wheel Vehicle Propulsion System," SAE Paper No. 69071.

59. F. S. Wright, W. P. Lear, G. D. Kitteridge, R. F. Sawyer, H. J. Wood, and A. F. Underwood, The Potential of Gas Turbine Vehicles in Alleviating Air Pollution, Panel Discussion, ASME 91st Winter Annual Meeting, New York, 1 December 1969.

60. *Automotive Industries*, Chilton Co., 15 March 1970.

61. "Performance Data for New Passenger Cars and Motorcycles," Vol. 1, No. 1, U.S. Dept. of Transportation, January 1970.

62. *Automobile Year*, No. 15, edit a S. A. Lausanne, Switzerland, 1967-1968.

63. G. W. Kahle, "The Turbine Powered Vehicle Promiser or Profit," *SAE Trans.*, Vol. 75, Sec. 2, 1967, pp. 12-23.

64. J. H. Weaving, "Small Gas Turbines," Proceedings of the Institution of Mechanical Engineers (Automobile Div.), No. 6, 1961-62, Discussion in Derby, p. 259.

65. R. F. Sawyer and E. S. Starkman, "Gas Turbine Exhaust Emissions," SAE Paper No. 680462, 1968.

66. A. A. Westenberg, "Kinetics of NO and CO in Lean, Premixed Air Flames," *Combustion Science and Technology*, Vol. 4, Hydrocarbons, 1971, p. 59.

67. C. G. Haupt, "Exhaust Emission by a Small Gas Turbine," SAE Paper No. 680463, May 1968.

68. M. W. Korth and A. H. Rose, Jr., "Emissions from a Gas Turbine Automobile," SAE Transactions, Vol. 77, Sect. 2, 1968, pp. 1327-1338. (Also SAE Paper No. 680402.)

69. H. B. Moore and J. A. Royer, "Exhaust Emissions from Williams Research Corporation Gas Turbine Engines," Williams Research Corp., Walled Lake, Mich., Report No. WR-ER-8T, 18 April 1970.

70. E. S. Starkman, "Theory, Experiment and Rationale in the Generation of Pollutants by Combustion," Twelfth Symposium (International) on Combustion, The Combustion Institute, Pittsburgh, 1968, pp. 593-601.

71. R. F. Sawyer, D. P. Teixeram and E. S. Starkman, "Air Pollution Characteristics of Gas Turbine Engines," Transactions of the ASME, Journal of Engineering for Power, October 1969, pp. 290-296.

72. D. C. Hammond, Jr., and A. M. Mellor, "A Preliminary Investigation of Gas Turbine Combustor Modeling," Combustion Science and Technology, Vol. 2, Nos. 2 and 3, 1970, pp. 67-80.

73. H. K. Newhall and M. Sahed, "Kinetics of Nitric Oxide Formation in High-Pressure Flames," Thirteenth Symposium (International) on Combustion, The Combustion Institute, Pittsburgh, 1971, pp. 381-389.

74. F. L. Schwartz, "Vehicular Gas Turbines," in Gas Turbine Engineering Handbook, J. W. Sawyer, Ed., Gas Turbine Publication, Inc., Stamford, Conn., 1966, pp. 271-280.

75. R. H. Eshelman, "Ford Sets Turbine Date," Automotive Industries, Vol. 144, No. 1, 1 January 1971.

76. I. M. Swatman, "Development of the Ford 704 Gas Turbine Engine," SAE Trans., Vol. 70, 1962, pp. 109-121.

77. G. J. Huelmer, Jr., "The Chrysler Gas Turbine Study," Proceedings In Mech. Engrs., 1964-65, Vol. 179, Pt2A, No. 9, pp. 257-279.

78. O. Ulrich, "Problems Related to the Development of a Gas Turbine in the 10-30 HP Class," ASME Paper No. A66-26992, 1966.

79. S. Williams, Williams Research Corp., Walled Lake, Michigan, News Release, 7 May 1971.

80. J. H. Keenian and F. G. Keyes, Thermodynamic Properties of Steam, John Wiley & Sons, Inc., New York, 1956.

81. V. Millman, "Advanced Technology Applied to the Stream Powered Vehicle," SAE Paper No. 931A, 1964.

82. The Automobile and Air Pollution – A Program for Progress, Part I and II, Report of the Panel on Electrically Powered Vehicles, U. S. Government Printing Office, Washington, D. C., October 1967.

83. P. T. Vickers, et al., "The Design Features of the GM SE-101 – A Vapor Cycle Powerplant," SAE Paper No. 700163, 1970.

84. P. T. Vickers, et al., "General Motors Steam Powered Passenger Cars – Emission, Fuel Economy, and Performance," SAE Paper No. 700670, 1970.

85. "The Search for a Low Emission Vehicle," staff report Prepared for the Committee on Commerce, U. S. Senate, 91st Congress, 1st Session, Committee Print, U. S. Government Printing Office, 1969.

86. Automotive News, 11 January 1971, p. 24.

87. T. O. Wagner, "Fuels and Lubricants for Steam Propulsion Systems," SAE Paper No. 700662, 1970.

88. D. T. Morgan, et al., "Organic Rankine Cycle with Reciprocating Engine," from 4th Intersociety Energy Conversion Engineering Conference, Paper No. 699001, 1969.

89. D. T. Morgan and R. J. Raymond, "Conceptual Design Rankine-Cycle Power System with Organic Working Fluid and Reciprocating Engine for Passenger Vehicles," Thermo-Election Corp., Report No. TE4121-133-70, Waltham, Mass., June 1970.

90. P. J. Marteney, "Analytical Study of the Kinetics of Formation of Nitrogen Oxide in Hydrocarbon Air Combustion," Combustion Science and Technology, Vol. 1, 1970, pp. 461-469.

91. W. Cornelius and W. R. Wade, "The Formation and Control of Nitric Oxide in a Regenerative Gas Turbine Burner," General Motors Emission Research Dept., Report GMR-994, Warren, Mich., 27 July 1970.

92. C. V. Burkland, et al., "Study of Continuous Flow Combustion Systems for External Combustion Vehicle Powerplants," The Marquardt Corp., prepared for NAPCA, Contract CPA 22-69-128, Van Nuys, Calif., June 1970.

93. J. P. Tomany, "A Survey of Nitrogen-Oxides Control Technology and the Development of a Low NO_x Emissions Combustor," ASME Paper No. 70-WA/Par 2, 1970.

94. H. K. Newhall and J. A. El Messiri, "A Combustion Chamber Designed for Minimum Engine Exhaust Emissions," SAE Paper No. 700491, 1970.

95. D. A. Trayser and F. A. Creswick, "Effect of Inductive System Design on Automotive Engine Emission," ASME Paper No. 69/WA/APC-7, 1969.

96. R. M. Campau, "Low Emission Concept Vehicles," SAE Paper No. 710294, published in "A Cooperative Research Program for Automotive Emission Control," Society of Automotive Engineers Publication SP-361, January 1971.

97. "Hybrid Heat Engine – Electric Systems Study, Briefing and Progress to Date," The Aerospace Corp., 21 October 1970.

98. W. C. Strock, "Condensers and Boilers for Steam-Powered Cars – A Parametric Analysis of Their Size, Weight, and Required Fan Power," NASA TN D-5813, Washington, D. C., May 1970.

99. "Control Techniques for Carbon Monoxide, Nitrogen Oxide, and Hydrocarbon Emission from Mobile Sources," NAPCA, U.S. Dept. of HEW, U.S. Government Printing Office, March 1970.

100. D. J. Patterson and J. A. Bolt, "Low Pollution Heat Engines," from 3rd Intersociety Energy Commission Engineering Conference, Paper No. 689107, 1968.

101. R. V. Ayres, "Alternative Non-polluting Power Sources," SAE Journal, Vol. 76, No. 12, December 1968.

102. W. E. Fraipe and R. K. Lay, A Survey of Propulsion Systems for Low-Emission Urban Vehicles," ASME Paper No. 70-Tran-49, 1970.

103. C. J. Heltemis, Jr., and C. A. Vansant, "Power Sources for Vehicles – 1966 Status Report," from 1st Intersociety Energy Commission Engineering Conference, 1966.

104. K. H. Hellman, letters to Dr. G. L. Dugger (APL/JHU) from Dept. of HEW, National Air Pollution Control Administration, 3 August 1970, with vehicle specifications, 28 May 1970 with attachment, "Heat Engine/Mechanical Energy Storage Hybrid Propulsion Systems for Vehicles."

105. J. A. Hoess, et al., "Study of Unconventional Thermal, Mechanical, and Nuclear Low-Pollution-Potential Power Sources for Urban Vehicles," Battelle Memorial Institute, NAPCA Pub. No. APTD 69-51, October 1969.

106. J. H. B. George, et al., "Prospects for Electric Vehicles. A Study of Low Pollution Potential Vehicles – Electric," Arthur D. Little, Inc., Cambridge, Mass., C-69260, Clearinghouse PB 193254, 15 May 1968.

107. G. A. Hoffman, "Systems Design of Electric Automobiles," *Transportation Res.*, Vol. 1, 1967, pp. 3-19.

108. S. F. Hoerner, *Fluid Dynamic Drag*, published by author, 1958.

109. C. E. Burke, et al., "Where Does all the Power Go?" *SAE Transactions*, Vol. 65, 1957, pp. 713-738.

110. P. T. Vickers, personal communications, General Motors T8H-5305A Weight Breakdown, General Motors Research Center, Detroit, Michigan.

111. J. P. Wilcox, "Flywheel Energy-Storage Systems for Transit Buses," Battelle Project G-8532, Monograph No. 12, Contract No. H-778 (HUD), Battelle Memorial Institute, Columbus, Ohio, October 1967.

112. P. M. Heldt, "Torque Converters or Transmissions," 4th Ed. 1951, New York.

113. "Control of Air Pollution from New Motor Vehicles and New Motor Vehicle Engines," *Federal Register*, Dept. of HEW, Washington, D. C., Vol. 35, No. 219, Part II, Tuesday, 10 November 1970.

114. G. C. Hass, M. P. Sweeney, and J. N. Pattison, "Laboratory Simulation of Driving Conditions in the Los Angeles Area," SAE Paper No. 660546, August 1966.

115. D. K. Mackenzie, et al., "Car Brake Usage and Test Schedules," Institute of Mechanical Engineers, Proceedings Automotive Discussion, No. 1, 1955-1956.

116. R. C. Bascom and G. C. Hass, "A Status Report on the Development of the 1973 California Diesel Emissions Standards," SAE Paper No. 700671, August 1970.

117. "The Liberators," Company brochure, i-space Inc., Washington, D. C.

118. S. Timoshenko, *Strength and Materials. Part II: Advanced Theory and Problems*, Van Nostrand, N. Y., 1956.

119. A. Mendelson, *Plasticity: Theory and Application*, MacMilliam Co., N. Y., 1968.

120. S. W. Tsai, "Mechanics of Composite Materials, Part I – Introduction," AFML-TR-149, Part I, June 1966.

121. S. H. Crandall, *Engineering Science – A Survey of Numerical Procedures*, McGraw-Hill, 1956.

122. R. O. Weiss, "A Comparison of Approximate Analytical Techniques in Heat Conduction," Journal Spacecraft and Rockets, Vol. 7, No. 2, February 1970, pp. 212-214.

123. N. I. Robinson, "Elastic Analysis of a Plate with an Edge Column Using the Method of Collocation and an Extended Method of Images," Commonwealth Scientific and Industrial Research Organization, Australia, Div. Bldg. Res. Tech. Paper No. 26, 1970.

124. W. Flugge, editor, Handbook of Engineering Mechanics, McGraw-Hill Book Co., Inc., New York, 1962.

125. R. M. Rivello, Theory and Analysis of Flight Structures, McGraw-Hill Book Co., Inc., New York, 1969.

126. J. P. Den Hartog, Advanced Strength of Materials, Chapter II, McGraw-Hill, 1952.

127. A. Stodola, Steam and Gas Turbines, Vol. I, Chapter V, McGraw-Hill, 1927.

128. M. A. Ranta, "On the Optimum Shape of a Rotating Disk of Any Isotropic Material," Int. J. Solids Structures, Vol. 5, 1969, p. 1247.

129. J. M. Chern and W. Prager, "Optimal Design of Rotating Disk for Given Radial Displacement of Edge," J. Optimization Theory and Application, Vol. 6, No. 2, 1970, p. 161.

130. B. M. E. de Silva, "Application on Pontryagins Principle to a Minimum Weight Design Problem," Journal of Basic Engineering, 1970, p. 245. J. Optimiz. Theory & App., Vol. 6, No. 2, 1970, p. 161.

131. A. Seireg and K. S. Surana, "Optimum Design of Rotating Disks," Journal of Engineering for Industry, Vol. 1, 1970, p. 1.

132. Sulkin, et al., "Frontiers of Technology Study. Implementation," Vol. III, North American Rockwell Corp. Report No. PB 178 272, 5 January 1968.

133. T. Theodorsen and A. Reiger, Experiments on Drag of Revolving Disks, Cylinders, and Streamline Rods at High Speeds, NACA Report No. 793, Washington, 1944.

134. W. Schmidt, Ein Einfaches Messverfahren fur Drehmomente, Zeitschrift des Vereins der destschen Ingenieure, Vol. 65, 1921, p. 441.

135. J. W. Dailey and R. E. Nece, "Roughness and Chamber Dimension Effects of Induced Flow and Frictional Resistance of Enclosed Rotating Disks," Massachusetts Institute of Technology, Department of Civil and Sanitary Engineering, Hydrodynamics Laboratory, Technical Report No. 27, May 1958.

136. F. Schultz-Grunow, Der Reibungswiderstand rotierender Scheiben in Genausen, Zeitschrift fur angewandte Mathematik and Mechanik, Vol. 15, 1935, p. 191.

137. H. Schlicting, Boundary Layer Theory, First English Edition, McGraw-Hill Book Co., New York, 1955, p. 446.

138. M. W. Bourdon, "Hayes Continuously Variable Transmission now Offered Optionally on Austin Sixteen," Automotive Industries, Vol. 69, 18 November 1933, pp. 604-607.

139. J. J. Gumbleton, et al., "Special Purpose Urban Cars," SAE Paper No. 690461, 1969.

140. T. G. Fellows, et al., "Perbury Continuously Variable Ratio Transmission," from Advances in Automobile Engineering II, Carter (Ed.), Vol. 5, MacMillan Co., 1964.

141. C. K. J. Price and S. A. Beasley, "Hydrostatic Transmissions," from Advances in Automobile Engineering II, Carter (Ed.), Vol. 5, MacMillan Co., 1964.

142. C. W. King, et al., "Electric-Wheel Vehicle Propulsion System," SAE Paper No. 690071, presented at Inter Auto. Engineering Congress, Detroit, Mich., 13-17 January 1969.

143. E. R. Laithwaith, "Electrical Variable-Speed Drives," Engineers' Digest, Survey No. 17, Vol. 25, No. 10, October 1964, pp. 113-165 (see also Survey No. 2, Vol. 18, No. 12, December 1957, pp. 533-568).

144. P. C. Mortenson, "Hydrostatic Transmissions," SAE Transactions, Vol. 68, 1970, pp. 243-247.

145. E. H. Bowers, "Hydrostatic Transmissions for Vehicles," SAE Transactions, Vol. 68, 1960, pp. 248-256.

146. R. H. Eshelman, "Hydro-Tractors: Reality in Iron," Automotive Industries, Vol. 143, No. 7, 1 October 1970.

147. Hydraulics, C3 Series Hydrostatic Transmissions, Sta-Rite Industries, Inc., Racine, Wis., Bulletin FP 26-2, April 1969.

148. "Application Engineering Manual for Dynapower Hydrostatic Transmission Systems," Hydreco, General Signal Corp., Kalamazoo, Mich., Report No. 9-602-13.

149. J. H. Hobbs, "The Small Car – Why Not Automatic," *Advances in Automobile Engineering II, Carter (Ed.), Vol. 5, MacMillan Co., 1964.*

150. C. V. Lezard, "Hydraulic Variable-Speed Drives," Engineers' Digest Survey No. 18, *Engineers' Digest*, Vol. 25, No. 12, Decemb*er 1964.*

151. J. C. Swain, et al., "A Turbine-Speed Pump for Vehicle Transmission Use," SAE Paper No. 670954, 1967.

152. R. L. Dougherty and A. C. Ingersoll, *Fluid Mechanics*, McGraw-Hill Book Co., N. Y., 1954.

153. C. C. Hill, "Aerodynamic Torque Converter from Gas Turbines," ASME Paper No. 69-GT-108, 1969.

154. C. C. Hill, et al., "Design and Test of the First Aerodynamic Torque Converter for Gas Turbines," ASME Paper No. 69-GT-109, 1969.

155. T. E. Ramsey, Sundstrand letter to Dr. A. Brandt APL/JHU), Sundstrand Aviation, Rockford, Ill., AE No. 421-78, 28 December 1970.

156. *Industrial Research*, December 1970, p. 17.

157. "Turboshaft Engines," Garrett Airesearch Manufacturing Co. of Arizona, Phoenix, Arizona, Product Literature, MS 2101, 20 March 1970.

158. "1970 Fluid Power Reference Issue," *Machine Design*, Vol. 42, No. 22, 10 Septemb*er 1970.*

159. A. L. Nasvytis, "Multiroller Planetary Friction Drives," SAE Paper No. 660763, October 1966.

160. L. O. Hewko, "Roller Traction Drive for Quiet, High-Speed Power Transmission," SAE Paper No. 690572, September 1969.

161. "Harmonic Drive, Mechanical Power Transmission Systems," Harmonic Drive Division, United Shoe Machinery Corp., Beverly, Mass., Sales Brochure.

162. W. D. Bowman, "Generalizations on the Aerodynamic Characteristics of Sedan Type Automobile Bodies," SAE Trans., Vol. 75, Sect. 2, SAE Paper No. 660389, 1967, pp. 608-620.

163. R. D. Stiehler, et al., "Power Loss and Operating Temperature of Tires," Journal of Research of the NBS, C. Engineering and Instrumentation, Vol. 64C, No. 1, January-March 1960.

ACKNOWLEDGMENT

The authors would like to acknowledge the contributions of the many persons associated with this program and to others who gave freely of their knowledge and experience. In particular, we acknowledge the support and program guidance of Dr. Jalal Salihi, Mr. David Dawson, and Dr. Karl Hellman of the Office of Air Programs, Environmental Protection Agency; the experimental techniques for rotating the rod flywheels and photographing the failure process developed by Mr. Guy Mangano of the Naval Air Propulsion Test Center; the efforts of Mr. Robert Randolph and Mr. James Burns of Hercules, Inc., in developing the processes required to fabricate the 1-pound test rods; the cooperation of AVCO Corp., General Technology Corp., Fothergill and Harvey, Ltd., PPG Industries, Hamilton Standard Corp., Corning Glass, Columbia Products Co., and the Whittaker Corp., for furnishing test samples of filamentary and composite materials; the information and suggestions offered by Mr. D. M. Latson of the U.S. Army Tank Automotive Command and Mr. R. H. Guedet of Sundstrand Corporation in the field of transmission design; the analysis of rotor drag and windage losses conducted by Mr. R. H. Cramer of APL; and the counsel and guidance of Dr. W. H. Avery and Messrs W. B. Shippen and R. W. Blevins of APL, and the experimental assistance of Mr. A. J. Klaunberg, Jr., of APL.

Preceding page blank